

Hasselt University, Campus Diepenbeek.  
Institute for Materials Research (IMO-IMOMECE)

Thesis to obtain the degree of Doctor in Sciences: Physics  
("Doctor in de Wetenschappen: Richting Natuurkunde"):

**Probing the electronic transport properties of  
individual fullerene-DNA complexes**

By

Kathia Lorena Jiménez Monroy

Promotor: Prof. Dr. Patrick H. Wagner

Copromotor: Prof. Dr. Hans-Gerhard Boyen

# Jury

- Chair: Prof. Dr. Karin Coninx  
Hasselt University, IMO
- Promotor: Prof. Dr. Patrick Wagner  
Hasselt University, IMO-IMOMECC
- Co-promotors: Prof. Dr. Hans-Gerhard Boyen  
Hasselt University, IMO-IMOMECC
- Members of the jury: Prof. Dr. Chris Van Haesendonck  
KU Leuven
- Prof. Dr. Ferdinand C. Grozema  
Technische Universiteit Delft
- Prof. Dr.-Ing. Michael J. Schöning  
Aachen University of Applied Sciences, INB
- Prof. Dr. Wanda Guedens  
Hasselt University, IMO-IMOMECC
- Prof. Dr. Bart van Grinsven  
Universiteit Maastricht
- Dr. Patricia Losada-Pérez  
Hasselt University, IMO-IMOMECC

## Acknowledgements

Seven years ago I left my country on the pursuit of happiness, starting first my master studies in Germany and then continuing my studies in Belgium as a PhD student. Every step involved rich experiences and lessons, for example regarding the academia, I learned that nobody has all the answers. Instead a dynamic flow of ideas within a multidisciplinary group can lead to solutions and eventually to answers. It was my good luck to arrive at the Biosensors group with: Lars, Bart, Thijs, Jan, Kasper, Matthias, Mohammed and Marloes as colleagues (all of them are now doctors and some even professors). Later, new colleagues arrived, like Patricia, Evelien, Andy, Yasin, Mehran, Gideon, Inge and Christopher adding fresh spice to the original mix. An advice I would like to give to the new students: science is great but it is even better when you can share day-to-day experiences with people that are not only of your group, as I had with Wiebke, Farnoosh, Yaso, Emilie, Ilaria, Stoffel, Matthew, Jeroen Drijkoningen and Giedrius Degutis.

I want to thank my supervisor, Prof. Dr. Wagner for accepting me into his group and for his trust on me. He gave me freedom to experiment without any type of pressure. For this reason, I can be a doctoral candidate at this moment. Also I thank my copromotor Prof. Dr. Boyen and members of the jury for the fruitful comments and interest. Special thanks to Prof. Dr. Grozema and Dr. Renaud because without their help, I would be still stumbling in the dark.

The length of this book would not be enough to acknowledge all the people who had an influence on this stage, because you were always kind and friendly to me (even in the most stressful times), every single one of you gave me a piece of knowledge or advice when I needed it. Therefore some of you will have to forgive me and I will mention some, like: Koen Schouteden, Alexander Volodine, Prof. Dr. Jean Paul Noben, Prof. Dr. Ken Haenen, Christel Bocken, Matthias Bäcker, Huguette Penxten, Wouter Dierckx, Alfred Kick and Prof. Dr. Mertig. Also thanks to the excellent team of IMO: Ellen, Marina, Relinde, Christel, Hilde and

Johnny because in a matter of minutes, they turned "impossible missions" into a piece of cake. I was also lucky to have Jeroen De Neve and Senne Seneca as my bachelor students, whose enthusiasm and initiative was a refreshing boost of mind.

I also learned that friendships are very hard to keep but I am happy to count amongst them: David, Paty, Loesje, Rafa, Dianita, Alan, Febri and Carlos. I thank you all for taming me and viceversa, quoting my favorite book in this sense: "It is the time that you spend on your "rose" that makes it so special... You are responsible for ever for those you have tamed."-A. Saint-Exupery-

Muchas gracias a mi familia por estar a mi lado en este largo camino, en especial a mi tías Rosita y Luchita, tíos Jacques y Honorio, Pablito, Sol, Honi, Araceli, Francis, Yvette, abuelita Luchita, sobrinitas y sobrinitos. Ik wil ook Magniela, Roger, Boccia, Ludo, Antonello en Lieve bedanken om mij te ontvangen als een nieuw lid van hun familie. Ik ben zeker dat er nog meer gelukkige tijden zullen komen voor ons om te delen.

Especialmente gracias a las personas más importantes de mi vida: mis padres Miguel y Catita, porque aún a la distancia siempre han estado conmigo, consolándome y dándome energías para afrontar los nuevos retos en mi vida. Gracias por confiar en mí, por apoyarme y por la fortaleza que han tenido para dejar a sus pollitos volar por sus sueños y buscar su felicidad. A mis queridos hermanos: Cynthi y Miguel, porque aún con nuestras diferencias, ustedes siempre me han motivado a ser una mejor persona y profesionista. Soy muy afortunada por ser parte de esta maravillosa familia, en vias de crecimiento gracias al fabuloso Dr. Heikkilä y mi hermoso sobrinito Aleksí Miguel Heikkilä.

Finally but not less important, to David, who not only is my best friend but also my partner. I thank you for teaching me the lessons that really matter in life:

"Life has taught us that love does not consist of gazing at each other, but in looking outward together in the same direction" -A. Saint-Exupery-  
"The thing that counts the most in the pursuit of happiness is choosing the right companion"-Anonymous-

# Table of Contents

<b>Acknowledgements .....</b>	<b>I</b>
<b>Table of contents .....</b>	<b>III</b>
<b>Abstract .....</b>	<b>IX</b>
<b>Nederlandse samenvatting .....</b>	<b>XI</b>
<b>Chapter 1, Introduction .....</b>	<b>1</b>
1.1 Motivation .....	1
1.2 Context.....	4
1.3 Molecular electronics .....	7
1.4 Molecular devices .....	9
1.4.1 Self assembly and self-assembled monolayers .....	10
1.4.2 Single molecules .....	11
1.4.2.1 Diodes and rectifiers .....	11
1.4.2.2 Switches and transistors.....	16
1.4.2.3 Nanowires and molecular wires .....	20
1.5 State of the art in computational electronics.....	22
1.5.1 Single electron transistors .....	22
1.5.2 Quantum cellular automata .....	23
1.5.3 Chemically assembled electronic nano-computers .....	25
1.5.3.1 Molecular computation .....	25
1.6 Objectives.....	26
1.7 Conclusions .....	28
1.8 References .....	29
<b>Chapter 2, Components of Molecular Devices .....</b>	<b>35</b>
2.0 Introduction to chemical bonds .....	35
2.1 Organic molecules.....	38
2.1.1 Molecular resistors .....	38
2.1.2 Rectifiers.....	39
2.1.3 Switches and memories .....	42
2.1.4 Molecular wires .....	44

---

2.2 Deoxyribonucleic acid (DNA).....	44
2.2.1 DNA structure.....	45
2.2.1.1 <i>A-DNA</i> : underwinding for replication .....	47
2.2.1.2 <i>B-DNA</i> : the standard form .....	47
2.2.1.3 <i>Z-DNA</i> : the left handed structure.....	48
2.2.2 DNA electronics .....	49
2.2.2.1 Conducting and semiconducting behaviour.....	50
2.2.2.2 Insulating behaviour .....	55
2.2.2.3 Applications .....	62
2.3 Conclusions .....	63
2.4 References .....	63
<b>Chapter 3, Charge Transport in DNA .....</b>	<b>71</b>
3.1 Theoretical framework .....	71
3.2 Sequential tunneling (unistep charge transfer or coherent tunneling)...	77
3.2.1 Steady states for sequential tunneling .....	80
3.3 Multistep hopping.....	82
3.3.1 Kinetics of hole transport .....	83
3.3.2 Steady states for multistep charge hopping .....	86
3.4 Conclusions .....	88
3.5 References .....	88
<b>Chapter 4, Experimental Techniques .....</b>	<b>93</b>
4.1 Physico-chemical techniques.....	93
4.1.1 Electromagnetic Radiation .....	93
4.1.1.1 Optical Spectroscopy.....	95
4.1.1.1.1 Ultraviolet-visible Spectroscopy .....	97
4.1.1.1.2 Infrared Spectroscopy .....	101
4.1.1.1.3 Raman Spectroscopy .....	105
4.1.2 Electrophoresis .....	108
4.2 Scanning Probe Microscopy .....	110
4.2.1 Scanning Tunneling Microscopy.....	110
4.2.2 Atomic Force Microscopy .....	112
4.2.2.1 Contact-Probe AFM .....	114

---

4.2.2.2 Conductive-Probe AFM.....	116
4.3 Conclusions .....	119
4.4 References .....	120

**Chapter 5, Synthesis and characterization of DNA-fullerene complexes**  
.....123

5.1 Why fullerenes to prepare single DNA molecules .....	123
5.1.1 Single molecules and contact with metallic surfaces .....	124
5.1.2 Electron-donor acceptor pairs .....	125
5.1.3 Absence of interference with DNA structure .....	126
5.2 Optimization of chemical functionalization .....	127
5.2.1 Protocol 1 .....	128
5.2.2 Protocol 2 .....	129
5.2.3 Characterization of DNA-fullerene complexes.....	129
5.2.3.1 UV-vis .....	129
5.2.3.2 FT-IR .....	132
5.2.3.3 Hybridization and electrophoresis .....	134
5.2.3.4 Raman spectroscopy .....	135
5.3 References .....	136

**Chapter 6, Sample preparation for electronic transport studies on DNA-fullerene complexes** .....141

6.1 Substrate selection.....	141
6.1.1 Nanocrystalline Diamond.....	141
6.1.2 Homemade flame annealed gold samples.....	143
6.1.2.1 AFM characterization before annealing.....	143
6.1.2.2 AFM characterization after flame annealing .....	143
6.1.2.3 After annealing and DNA-fullerene deposition.....	146
6.1.3 Commercial ultra-flat gold samples (Platypus) .....	147
6.1.3.1 Imaging of DNA-fullerene deposition on gold .....	148
.....	148
6.2 Elastic modulus and conductivity tests with the Park NX10 AFM .....	148
6.2.1 Conductive AFM on silicon-gold sample .....	148
6.3 Protocol 2. Park AFM.....	153

6.3.1 DNA-fullerene (type 1, 27 bp) on ultra-flat gold .....	153
6.4 Conductivity test with optimal molecule arrangement and gold AFM tip .....	155
6.5 Additional characterization of fullerene-DNA molecules on mica .....	159
6.5.1 C-AFM on mica .....	159
6.5.2 NC-AFM on mica .....	160
6.6 AFM studies on longer DNA fragments .....	163
6.6.1 Fullerene-DNA (102 bp) on ultra-flat gold.....	163
6.7 Conclusions .....	164
6.8 References .....	165

## **Chapter 7, Electronic transport studies on DNA-fullerene complexes**

.....	167
7.1 I-V measurements on DNA-fullerene (type 2) .....	167
7.1.1 I-AFM experiments on ultra-flat gold .....	169
7.1.2 I-AFM experiments on ultra-flat gold with desalted DNA-fullerene molecules.....	174
7.1.3 Scanning Tunneling Microscopy.....	176
7.2 Comparison with theoretical models .....	178
7.2.1 Coherent charge transport by tunneling (sequential tunneling) ....	180
7.2.2 Kinetic scheme for multistep charge hopping (incoherent tunneling) .. ..	182
.....	182
7.3 Conclusions .....	186
7.4 References .....	188

## **Chapter 8, DNA-fullerene complexes as anticancer photoactivable drugs**

.....	191
8.1 Introduction .....	191
8.1.1 Conformation vs. pH.....	193
8.1.2 Cellular uptake .....	194
8.1.3 Toxicity of fullerene nanoparticles .....	195
8.1.3.1 MTT reduction assay .....	196
8.1.3.2 Alamar blue redox assay .....	196



---

8.2 Experimental design .....	197
8.2.1 PDT treatment and cell viability assays .....	197
8.2.1.1 MTT assay .....	198
8.2.1.2 Alamar blue assay .....	200
8.3 Conclusions .....	202
8.4 References .....	203
<b>Chapter 9, General conclusions and outlook .....</b>	<b>207</b>
<b>Chapter 10, AFM-Imaging for contributed publications .....</b>	<b>211</b>
10.1 Introduction.....	212
10.2 Applications.....	214
10.2.1 Single nucleotide polymorphisms in DNA fragments.....	214
10.2.2 Specific cell detection.....	217
10.2.3 Specific detection of small molecules ( <i>e.g.</i> histamine) .....	219
10.2.4 Detection of phase transitions on supported lipid vesicle layers ...	221
10.3 References .....	224
<b>Appendix 1: Publications and Conference contributions .....</b>	<b>227</b>
<b>Appendix 2: List of abbreviations .....</b>	<b>231</b>

“As I look back on my life I realize that every time that I thought I was being rejected from something good, I was actually being re-directed to something better” –S. Marab

“A goal without a plan is just a wish” –A. Saint-Exupery-

## Abstract

Technology is facing a challenge in adapting to the new miniaturization strategies with the current trend of incorporating more computing processes in smaller electronic devices. In this context, we present here an environmentally friendly solution: the use of DNA as electrical nanowires for developing even more complex integrated circuits. The fact that DNA is composed of carbon, phosphorus and sugar (deoxyribose), readily available in our daily life makes them an environmentally friendly option. Additionally, the length and complexity of the structure can be easily controlled and, besides DNA in dry state is a very stable molecule. Thus, replacement of semiconductor interconnections (wires) by DNA nanowires would result in a more ecological and cost-effective solution.

However, DNA wires are not yet featured to assemble complex circuits because the nature of electronic transport through DNA is not fully understood. Extensive efforts have been done in this matter without a clear consensus whether DNA behaves as an insulator, conductor or semiconductor. The structural conformation of DNA is believed to play a key role on its electrical behaviour. Thus, keeping the *B-DNA* structure (native DNA) in dry state is of great importance due to the favourable  $\pi$ -pathway that is formed along the helix, which does not take place in other DNA conformations. Another key factor is the selection of a small electron donor-acceptor group that could aid on the direct flow of charges through the DNA helix, without interfering with the structure. If this group has a strong adsorption to the surface and allows the production of homogeneous molecules (preferably single molecules), then electrical measurements can be performed in a reproducible way.

In this thesis, stable single fullerene-DNA molecules that transport electrical charges exclusively along the DNA have been produced. When charges are injected on DNA [from -1 V to +1 V] a symmetrical-semiconductor I-V profile is displayed, indicating that charges hop along the DNA towards the fullerene ends. A marked tendency was observed, where conductance changed accordingly from semiconductor to conductor, when the DNA distance with

---

respect to the fullerene group was large (194.75 Å) and slowly diminishing to zero.

In addition, the production of single DNA wires connecting gold nanostructures in a dry state, that work at low voltage ranges, could result on more complex integrated circuits (small DNA wires = more interconnections) with a lower range of power supply. This implies that fullerene-DNA molecules could be used for the assembly of a new generation of DNA chips that require only a prior chemical synthesis and direct deposition of molecules on top of tiny gold nanostructures.

Furthermore, another interesting property of these molecules is that fullerenes attached to DNA can display features oriented in nanomedicine, such as photoactivable drugs in photodynamic anticancer therapies, where their on/off switching mechanism could be directly influenced by the charges hopping along the molecule in an aqueous solution.

## Nederlandstalige samenvatting

De huidige technologieën voor de productie van elektronische circuits ondervinden steeds meer problemen om zich aan te passen aan de huidige trend van miniaturisatie. Het uitbreiden van het computationeel vermogen in kleinere elektrische toestellen wordt steeds belangrijker.

Om deze problematiek aan te pakken stellen we hier een milieuvriendelijke oplossing voor: namelijk het gebruik van DNA als elektrische "nanowires" voor de ontwikkeling van nog complexere geïntegreerde circuits. Het feit dat DNA opgebouwd is uit koolstof, fosfor en suiker (deoxyribose), allen beschikbaar in onze naaste omgeving, maakt het een ecologisch verantwoorde kandidaat. Bijkomende voordelen zijn dat de lengte en complexiteit van deze "DNA wires" gemakkelijk te controleren zijn en dat DNA in droge toestand een zeer stabiel molecule is. Men kan dus stellen dat "DNA wires" een ecologisch en goedkoop alternatief bieden voor de huidige halfgeleidende verbindingen.

Momenteel worden "DNA wires" nog niet gebruikt voor de productie van complexe circuits omdat er nog geen consensus is over het elektrisch gedrag van DNA. Ondanks uitgebreid onderzoek hieromtrent is men er nog niet uit of DNA zich gedraagt als een isolator, een geleider of een halfgeleider.

Men neemt aan dat de structurele conformatie van DNA een sleutelrol speelt in diens elektrisch gedrag. Het is daarom belangrijk om de *B-DNA* conformatie (natief DNA) in droge toestand te behouden, omwille van het gunstig  $\pi$ -pad gevormd langs de helix. Dit  $\pi$ -pad is afwezig in de andere conformaties van DNA. Bijkomend is de keuze van een kleine elektron donor-acceptor groep belangrijk. Deze moet de stroom van elektrische ladingen langs de DNA-helix vergemakkelijken, zonder de DNA-conformatie te verstoren. Indien deze groep sterk adsorbeert aan een oppervlak en de productie van homogene moleculen

(liefst enkelvoudige moleculen) toelaat, kunnen elektrische metingen op een reproduceerbare manier uitgevoerd worden.

In dit project werden stabiele individuele fullerene-DNA moleculen aangemaakt die elektrische ladingen uitsluitend langs de DNA molecule transporteren. Een symmetrisch-halfgeleider I-V profiel wordt bekomen wanneer ladingen geïnjecteerd worden in DNA [van -1 V tot +1 V] hetgeen erop wijst dat de ladingen langs het DNA molecule naar het fullerene-uiteinde "springen" of "hoppen". Er kon opgemerkt worden dat de geleidende eigenschappen veranderden van halfgeleidend naar geleidend, wanneer de afstand op het DNA tot de fullerene langzaam verkleind werd van 194.75 Å tot 0 Å.

De productie van enkelvoudige "DNA wires", verbonden met gouden nanostructuren in droge toestand, die werken op een laag spanningsbereik kan leiden tot complexere geïntegreerde circuits (kleine "DNA wires" = meer verbindingen) met een kleinere stroomvoorziening. Dit impliceert dat fullerene-DNA moleculen gebruikt kunnen worden voor de productie van een nieuwe generatie DNA chips. Deze DNA chips zouden enkel een voorafgaande chemische synthese en een rechtstreekse depositie op gouden nanostructuren vereisen.

Een bijkomende interessante eigenschap van deze fullerene-DNA moleculen is dat ze ook gebruikt kunnen worden in de zogenaamde "nanogeneeskunde". Meer bepaald als fotoactiveerbaar geneesmiddel in fotodynamische antikanker therapieën, waar hun aan/uit mechanisme rechtstreeks beïnvloed kan worden door de ladingen die langs de molecule "hoppen" in een waterige oplossing.

# Chapter 1

## Introduction

The aim of this chapter is to place the reader within the context of technological advances, especially in the electronics field. Outbreaks are strongly linked to the society needs and at this point, advances in the production of smaller intelligent electronic devices are reaching its limitations. The field of molecular electronics is a suitable candidate to continue with the miniaturization trend, where quantum computers represent the most popular envisioned application. The objective of this thesis is to refuel interest on producing nano-devices based on molecular wires, composed of single fullerene-DNA molecules because of the advantages that DNA and fullerenes offer, besides representing a practical application while other subfields in molecular electronics are still on development.

### 1.1 Motivation

It was the year of 1941 when the german inventor Konrad Zuse developed "Z3" (**Fig. 1.1**), the world's first programable computer based on a binary system. The machine weighted about 1000 kg, contained vacuum tubes and had a memory capacity of 64 words with a length of 22 bits [1]. Computers were gradually commercialized and they occupied large areas (even complete rooms) until the vacuum tubes were finally replaced for transistors, in the late 50's of the twentieth century. With the development of integrated circuits, computers followed a tendency to shrink on size, facilitating its commercialization for research and general public. Nowadays, we count with multicore processors and a variety of programming languages targeted to satisfy a growing technological driven society.

Smartphones, tablets, cameras and personal computers are product of these tendency to incorporate more processes on miniaturized chips. These chips are

produced with semiconductor materials, many of them derived from non-sustainable resources.

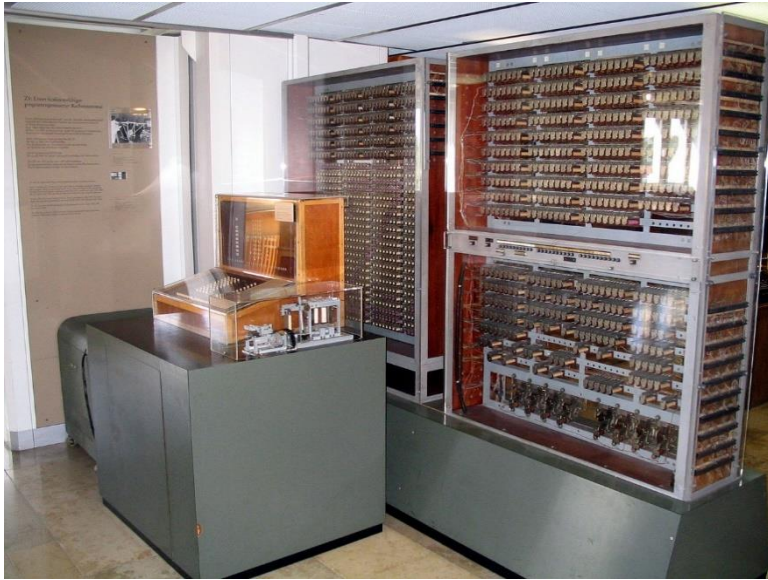


**Figure 1.1.** Replica of Zuse Z3 displayed at the Deutsches Museum in Munich [2].

For the logic board components, gold and the three T's (Tantalum, Tungsten and Tin) are extracted in their mineral form. Several other components of portable devices (see **Fig. 1.2**) are known to be toxic and therefore their use has started to be regulated towards environmentally friendly materials.

In addition, these natural resources for the semiconductor industry become more and more scarce (**Fig. 1.3**) and a reliable supply is not always guaranteed, therefore scientists look intensely to alternative materials. Along this thesis, we present a possible option: the use of deoxyribonucleic acid, which can be classified as a wire type of molecule.

It is composed of carbon, phosphorus and a sugar (deoxyribose), readily available on our daily life. The length and complexity of the structure can be easily controlled, besides DNA in dry state is a very stable molecule. Thus,



replacement of semiconductor interconnections (wires) for DNA nanowires would result in a more cost effective solution.



**Figure 1.2:** Apple's 2015 report on environmental responsibility. Toxic components discarded from the traditional production of portable devices [3].

However, DNA wires are not yet featured to assemble complex circuits because the electrical nature of DNA is not fully understood. Extensive efforts have been done in this direction without a clear consensus on if DNA behaves as insulator, conductor or semiconductor.

The structural conformation of DNA is believed to play a key role on its electrical behaviour. Thus, keeping the *B-DNA* structure (native DNA) in dry state is of great importance due to the favourable  $\pi$ -pathway that is formed along the helix. Another key factor is the selection of a small electron donor-acceptor group that could aid on the direct flow of charges through the DNA helix, without

interfering with the structure. If this group has a strong adsorption to a metallic surface and allows the production of homogeneous molecules (preferably single molecules), then electrical measurements can be performed in a reproducible way. As a consequence, if all these parameters could be controlled, then cost-effective DNA wires could be produced in large quantities, with the same characteristics, serving as novel small ecological interconnections for electronic chips.

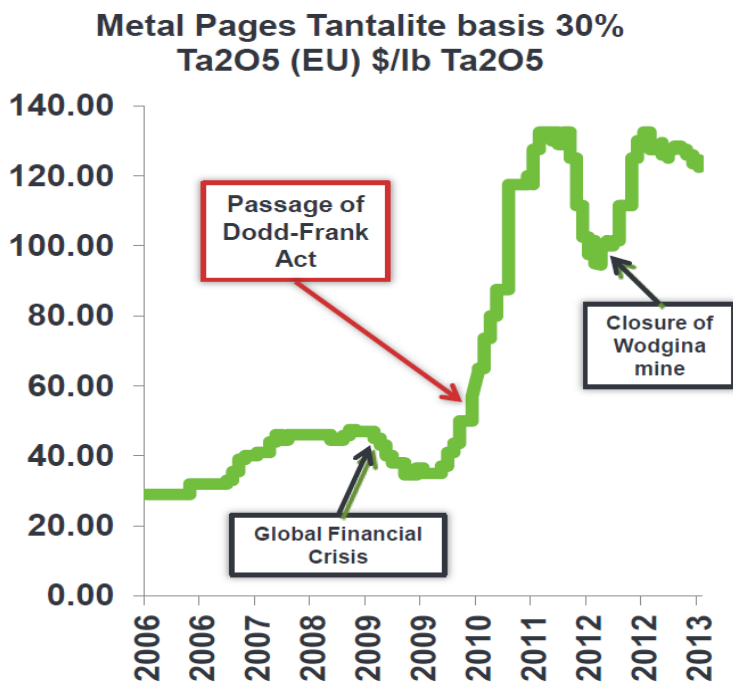


**Figure 1.3.** Record of tantalite metals price since 2006 until 2013 [4].

## 1.2 Context

Seen in perspective, human greatest achievements have been pushed forward by means of technological changes. These changes or revolutions are usually associated with higher work productivity and efficiency, while improving human life quality, reshaping culture, society and even human nature at the same time.

In general terms, a technological revolution can be classified in two categories [5]: *i)* Sectoral (changes in one region or sector) and, *ii)* Universal (interconnected radical changes in more sectors, *i.e.* science, industry, etc.).

During the modern era in western culture, the universal technological revolutions have been categorized as [6]:

- 1600-1740: Financial-agricultural revolution
- 1780-1840: Industrial revolution
- 1880-1920: Technical revolution
- 1940-1970: Scientific-technical revolution
- 1985-2000: Information and telecommunications revolution

With the advent of 21th century, nanotechnology has burst into a wave of sectoral technologies, such as materials, biotechnology and computation. Moreover, the main factors that impulse developments in nanotechnology, depend greatly on the costs vs social and ethical acceptance (**Fig. 1.4**), which has lead us to a "high-growth development" [7]. We can see this in various sectors such as aerospace, transport, defense, consumer products, environment, agriculture, pharmaceuticals, biotechnology, medical devices, energy generation and storage, electronics, *etc.* In this context, this thesis targets to contribute to the fabrication of molecular wires to build nano-scaled electronic devices.

Particularly, advances in computation have been possible thanks to the use of complementary metal-oxide semiconductor (CMOS)-based integrated circuits. This technique implements a "top-down" approach, where a number of lithographic and etch techniques are used to create a pattern in a substrate ("chip"). Nevertheless, this technique is reaching its limitation on the quest to cope with the challenge of scaling down the interconnections or "wires" between transistors with the final purpose of producing more complex integrated circuits.

As a consequence, scientists have oriented their attention to alternative technologies [8], for example the molecular electronics field. Here, molecules are synthesized from the "bottom-up" approach, where the physical and

electronic properties of organic molecules are engineered to produce small-self assembled structures at the atomic or molecular device level.

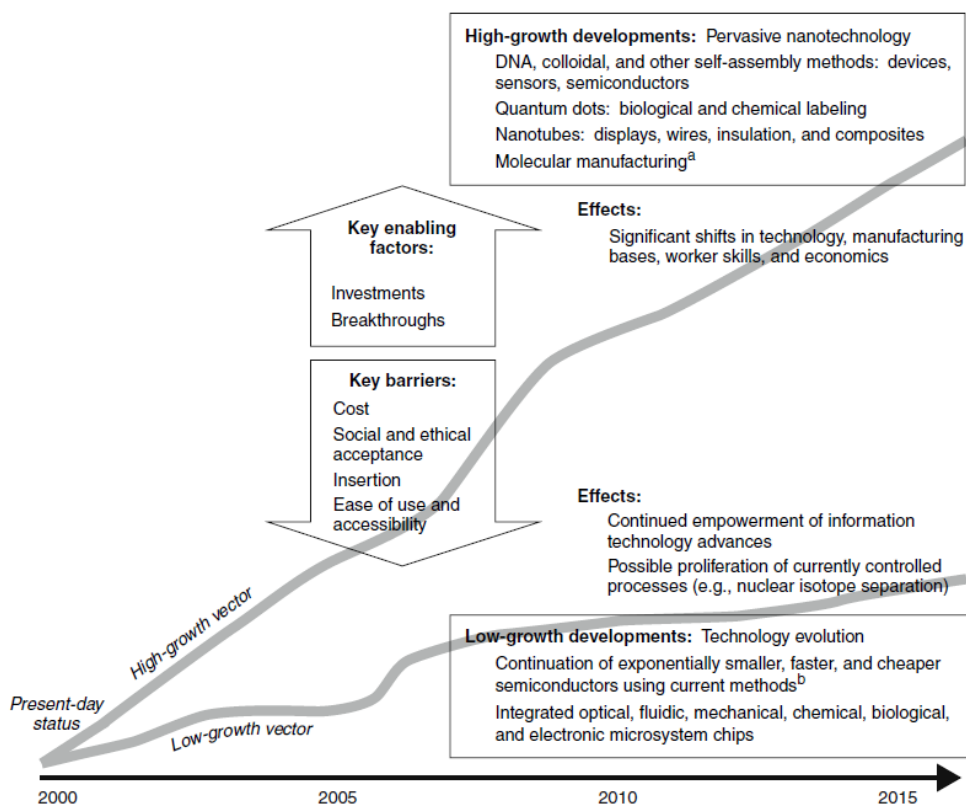


**Figure 1.4.** Range of perspective developments, restrains and effects of nanotechnology, that lead to a high- or low growth development. Note that in both scenarios, for today, the year 2015 improvements in computational technologies (devices/semiconductors) are expected [7].

The advantage of using this kind of synthetic chemistry is the possibility to use a large amount of small and homogeneous molecules in a cost-effective manner as compared to the CMOS technique. Additionally, some of the ongoing research topics are: *i*) single electron transistors [9], *ii*) quantum cellular automata [10] and *iii*) molecular computation [11], which will be explained at the end of this chapter.

### 1.3 Molecular electronics

The challenge of scaling down manufacture and architecture of electronic components has resulted on the increase of research oriented on nanofabrication of computational devices. Along this line, the field of molecular electronics emerged. It can be defined as a subfield of nanotechnology that use single molecules, or small groups of molecules, as components in electronic applications, such as transistors, sensors and circuits [12]. An example is the use of small organic compounds to operate as logic switches. After an organized chemical assembly of these compounds, a type of computer is formed [7].

Moreover, the factors that contributed to the history of molecular electronics started since the middle-sixties and it can be summarized by three major events oriented on the development of molecular scale systems for electronic and optoelectronic applications [12].

First, the revolution on microelectronics and computer changed drastically the way we live and work. Its success is largely attributed to the ability to shrink the size of transistors with the CMOS-based integrated circuits down to small dimensions (currently  $\sim 40$  nm), thus allowing an exponential growth in computing power as the number of transistors increase [13]. As a matter of fact, in 1965 Gordon E. Moore succeeded to observe this trend and enunciate his empirical law, stating that the number of transistors per square centimeter increase by two-fold in integrated circuits, approximately every two years [14].

Later in 1974, Norio Taniguchi used for the first time the term "Nanotechnology" to define a process related to the separation, consolidation and deformation of materials by one atom or one molecule, coining already the name of a bottom up approach [15]. It was not until the invention of the Scanning Tunneling Microscope (STM) by Binnig and Rohrer in 1981 that made this possible. Afterwards, Binnig, Gerber and Quate developed the first Atomic Force Microscope (AFM) in 1986 [16].

Then, Donald J. Cram, Jean-Marie Lehn and Charles J. Pedersen shared the Nobel Prize in Chemistry (1987) for their pioneering work in supramolecular chemistry. In this lecture, Lehn used the term “molecular wires” to describe polyolefinic chains “wiring” electron transfer through membranes. He also suggested that developments in molecular and supramolecular design could provide molecular photonic, electronic and ionic devices. Components such as molecular wires, diodes and resistors among others, might be assembled in nanocircuits to form a system capable of performing functions as detection, storage, processing, transfer of signals and information by means of various mediators (*e.g.* photons, electrons, *etc.*) [17]

Since Moore’s law, experts in the computational field already recognized the challenge on the miniaturization process. In 2010, Moore declared in an interview that the current “top down” miniaturization process (*i.e.* lithography), is reaching its limitations [18].

Moreover, it is just during the last decades that we became aware on the range of possibilities and tools required to engineer and measure atoms and molecules. Especially in this context, scientists have turned their attention to nanoscale processes with the final purpose to fulfill the needs of the current technological society, where molecular devices may play a key role (**Fig. 1.5**). A major breakthrough was achieved in the nineties, when conductance was able to be measured through single molecules. This thesis is situated precisely on this type of experiments at the single molecule level, oriented to contribute to the field of nanoelectronic components.

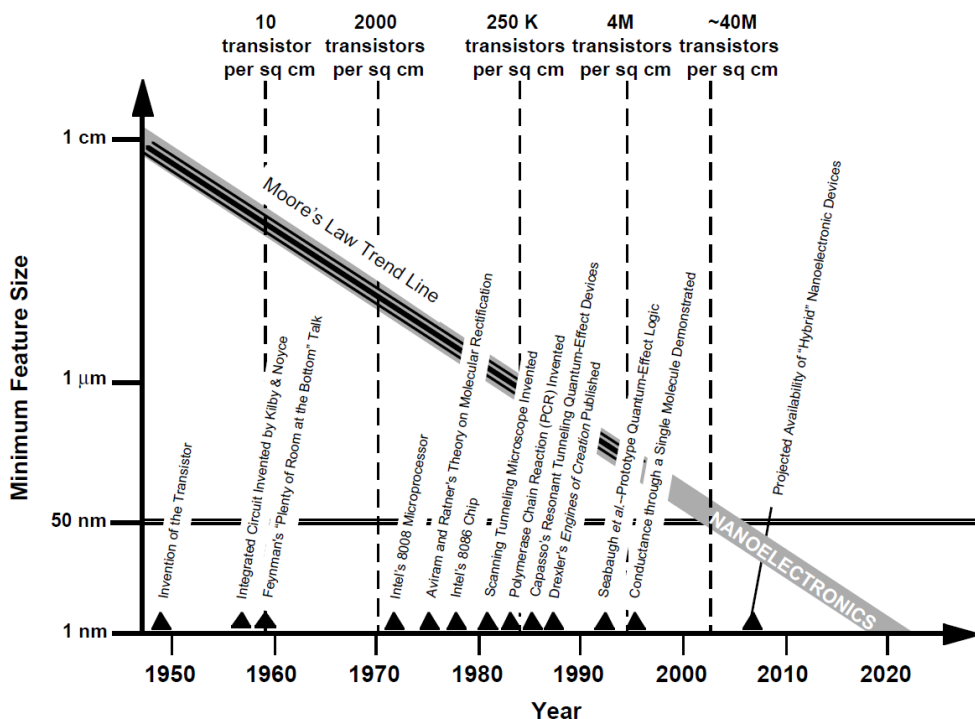


**Figure 1.5.** Timeline of key nanotechnological events versus time, aligned with the Moore's law trend [19].

#### 1.4 Molecular devices

From the chemical perspective, molecular devices can be seen as organized structures containing functional chemical groups, leading to supramolecular architectures [19, 20]. Therefore, one or few molecules can be integrated into a device, where they can be contacted between electrodes. The biggest challenge for this technology is the part of reliably connecting and integrating molecules into complex circuits [12]. A simple way to control the amount of molecules to be integrated in the device is the preparation step, where the predominant methods are: *i*) Self-assembled monolayers and, *ii*) Single molecules.

### 1.4.1 Self-assembly and self-assembled monolayers (SAMs)

The term "self-assembly" is given to a spontaneous organization of disordered components into ordered patterns by non-covalent interactions and without human intervention [21, 22]. Furthermore, it is not enough to direct atoms and molecules to form larger entities (*i.e.* precipitation). In order to belong to a self-assembled process, the system must also fulfill the following criteria:

- Higher order. The resulting self-assembled structures must be more ordered than the isolated components.
- Non-covalent interactions play a key role. Van der Waals,  $\pi$ - $\pi$  orbital stacking and hydrogen bonds form part of these weak interactions.
- Building blocks variety. This means that not only atoms and molecules can be used as building blocks but also nano- and macroscopic-particles can be used. Some natural examples are lipid bi-layers, nucleic acids and polypeptides folding into biologically functional structures.

In this category we find the Self-Assembled Monolayers (SAMs). They are defined as self-assembled organic thin-films, on the nanometer scale (thickness  $\sim$ 1-3 nm). This film is composed of gaseous or liquid material that spontaneously organizes itself onto a surface. The content of the molecules, define the arrangement of the layer on a given surface. Metallic bare surfaces for example, tend to adsorb organic materials to lower their free energy. These adsorbates have the ability to tune the reactivity and electrical characteristics of the surface. The most studied class of SAMs are the alkanethiols on top of gold and other noble metals due to the high affinity of thiol groups for metallic surfaces. Preparation of SAMs does not require specialized equipment [22]. The most common techniques to prepare SAMs are: Langmuir-Blodgett method, microcontact printing (stamps), nanoplotters, and even simple deposition. Commonly, the monolayers are assembled on top of electrodes and then their electronic properties are studied electrochemically [23–26] and more recently, with Conductive Probe Atomic Force Microscopy (I-AFM) [27–30].



### 1.4.2 Single molecules

Single molecules are ideal systems to investigate charge transport at the molecular scale, which is a topic of high interest for fundamental physics, oriented to unveil the charge transport phenomena at the molecular scale, and equally well for its practical applications [31]. Devices in general can be separated into active or passive types. An active device contains components with the ability to electrically control electron flow, *e.g.* batteries, transistors and tunnel diodes. In contrast, a passive device does not control current by means of another electrical signal, *e.g.* transformers and capacitors. Using this criteria, single molecules characteristics are mainly related to active devices, illustrated below.

#### 1.4.2.1 Diodes and Rectifiers

A diode is defined as an electrical device (voltage operated) that allows current to move in one direction easier than in the other. The most common kind of diode in circuit design is the semiconductor diode, although other diode technologies exist. If a diode is placed in a battery-lamp-circuit (**Fig. 1.6**), the polarity of the battery will lead to the diode type. Forward-biased diode indicates that electrons are allowed to flow through the diode (lamp on, **Fig. 1.6a**) and reverse-biased is when the battery is inverted and the diode blocks current (lamp off, **Fig. 1.6b**) [32]

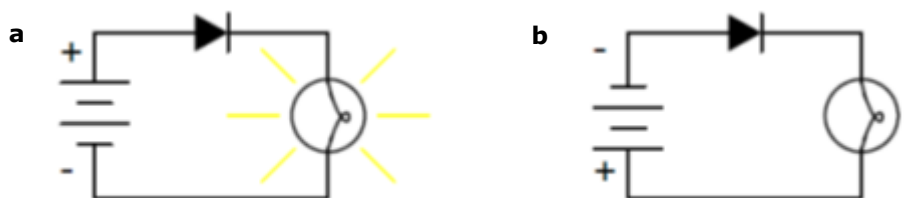


**Figure 1.6. Diode operation (a)** Current flow is permitted: forward-biased, **(b)** Current flow is prohibited: reverse-biased [32].

Diodes are essentially voltage-operated devices. The essential difference between forward-bias and reverse-bias is the polarity of the voltage dropped

across the diode. A forward-biased diode conducts current and drops a small voltage across it, leaving most of the battery voltage dropped across the lamp. If the battery's polarity is reversed, the diode becomes reverse-biased, and drops all of the battery's voltage, leaving none for the lamp. This forward-bias voltage drop exhibited by the diode is due to the action of the depletion region formed by the P-N junction under the influence of an applied voltage (**Fig. 1.7**). If no voltage applied is across the semiconductor diode, a thin depletion region exists around the region of the available charge carriers, and acts as an insulator.

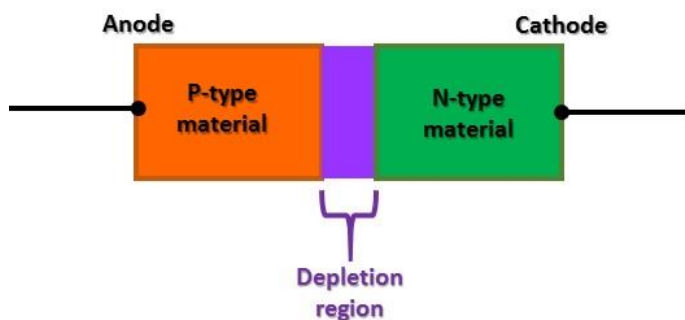


**Figure 1.7. Diode representation.** P-N junction model, where P- and N-type materials contain positive (holes) or negative (electrons) charge carriers, respectively.

If a reverse-biasing voltage is applied across the P-N junction, this depletion region expands, further resisting any current through it (**Fig. 1.8a**). On the other hand, if a forward-biasing voltage is applied across the P-N junction, the depletion region collapses becoming thinner (**Fig. 1.8b**). The diode becomes less resistive to current through it. In order to obtain a sustained current that flow through the diode, the depletion region must be fully collapsed by the applied voltage. This takes a certain minimum voltage to accomplish, called the forward voltage. For silicon diodes, the nominal forward voltage is 0.7 V, as exemplified here (**Fig. 1.8b-c**). Lower voltages generate partial forward-biased diodes, with thin depletion regions [32, 33].

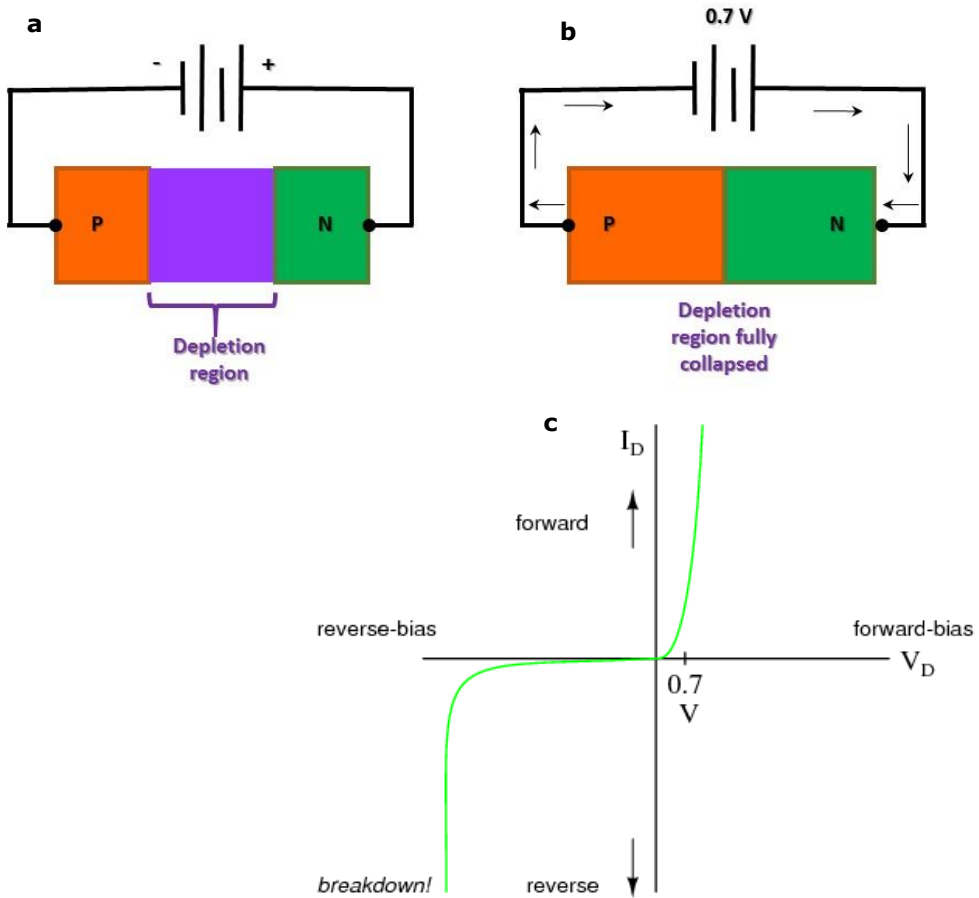


**Figure 1.8. Diode representation.** (a) Depletion region expands with reverse bias, and (b) Decrease or complete collapse of the depletion region with forward bias. (c) I-V curve representing the voltage value where forward current flow is observed for a silicon diode [32].

Rectification is the most popular application of a diode. A rectifier circuit converts alternating current (AC) that periodically reverses direction, to direct current (DC), meaning that the device will only allow one way of electrons flow. An example of a half-wave rectifier circuit is displayed in **Figure 1.9**, where the circuit only allows one half-cycle of the AC voltage waveform to be applied to the load, resulting in one non-alternating polarity across it. The resulting DC delivered to the load “pulsates” significantly. A full-wave rectifier is a circuit that converts both half-cycles of the AC voltage waveform to an unbroken series of voltage pulses of the same polarity [32].

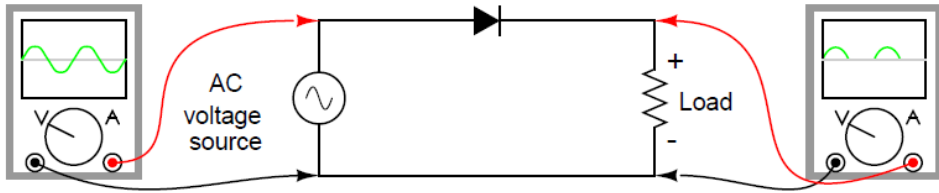


**Figure 1.9. Half way rectifier circuit** [32].

However, for most power applications, half-wave rectification is insufficient for the task. Generally, if we need to rectify AC power to obtain the full use of both half-cycles of the sine wave, a different rectifier circuit configuration must be used. This circuit is a full-wave rectifier. A common example is the four-diode bridge configuration, also called full-wave-bridge (**Fig. 1.10**).

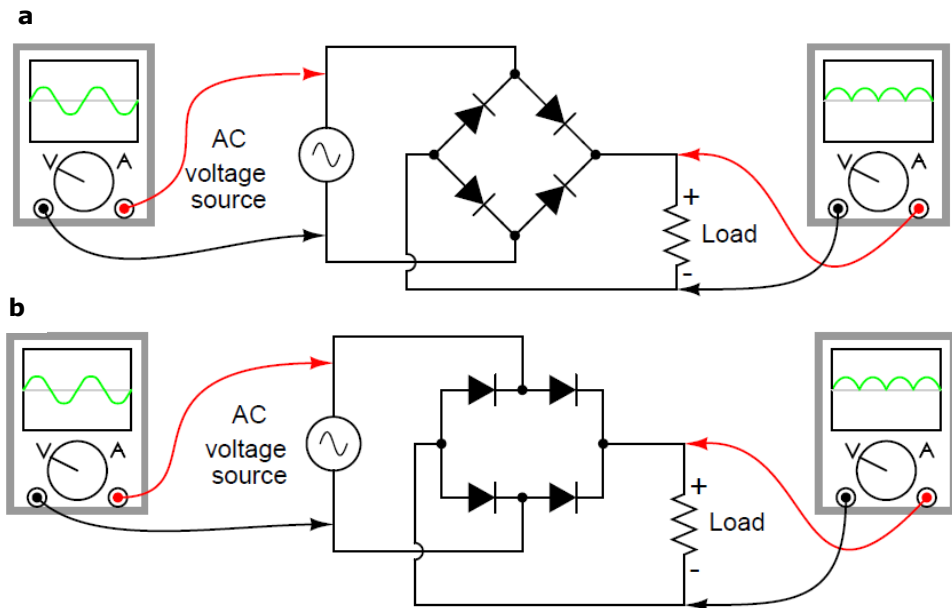


**Figure 1.10. Full-wave bridge rectifier.** Two styles to represent the same circuit, starting with an AC sinus voltage (left multimeter) rectified into a DC waveform (right multimeter). **(a)** Layout 1 is used to easily represent the current flow direction and, **(b)** Layout 2, the common diagram for bridge rectifier circuits [32].

The direction of current flow for the full-wave bridge rectifier circuit is illustrated in **Fig. 1.11a** for positive half-cycle and **Fig. 1.11b** for negative half-cycles of the AC source waveform. Regardless the polarity of the input, the current flows in the same direction through the load. That is, the negative half-cycle of source is a positive half-cycle at the load. The current flow is through two diodes in series for both polarities.

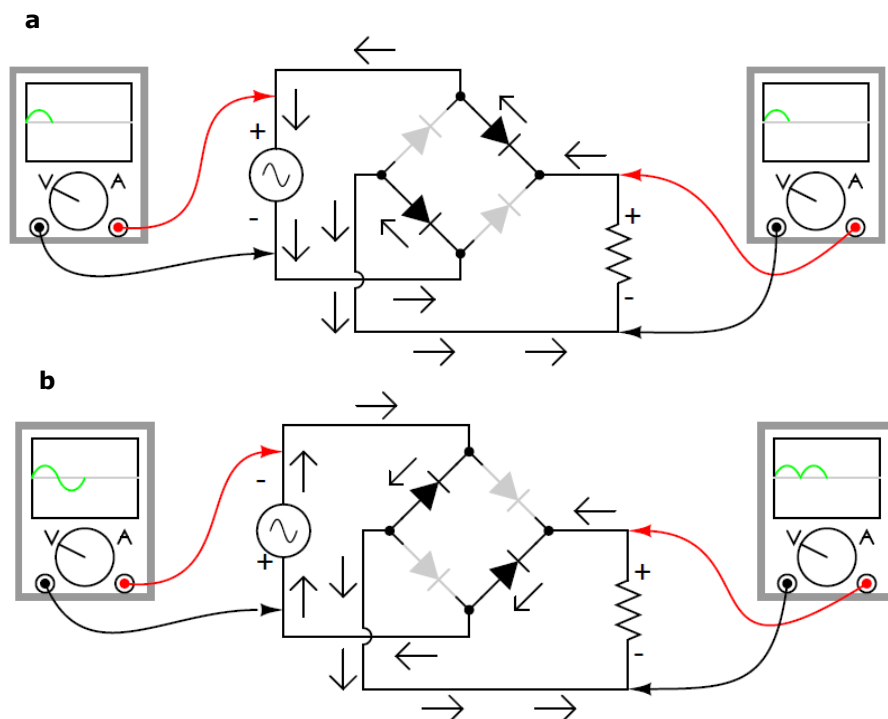


**Figure 1.11. Full-wave bridge rectifier Layout 1 (a)** Electron flow for positive half-cycles, **(b)** Electron flow for negative half-cycles [32].

The method of rectification can be referred as counting the number of DC “pulses” output for every  $360^\circ$  of electrical “rotation”. For instance, a single-phase, half-wave rectifier circuit can be called a 1-pulse rectifier, because it produces a single pulse during the time of one complete cycle ( $360^\circ$ ) of the AC waveform. Then a full-wave rectifier would be called a 2-pulse rectifier, because it outputs two pulses of DC during one AC cycle’s worth of time.

In 1974 Aviram and Ratner became the pioneers in the field of rectifiers and single molecules when they proposed first the feasibility to use a single molecule

as a molecular rectifier, carefully controlling the donor-space-acceptor functionality in the system (P-N junction) [34]. Two decades later, Joachim *et al.* [35] succeeded to measure changes in the virtual tunneling of adsorbed fullerenes on top of clean Cu (111).

Other research groups followed with the conductance measurement through benzene-dithiol molecules in a break junction device [36] and the rectification experiments on Aviram-Ratner type of molecules (or P-N junction molecules, **Fig 1.12**) [37], among others.

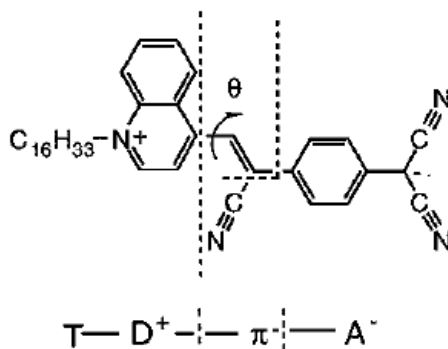


**Figure 1.12. Example of a rectifier molecule.** "T" stands for hexadecyl tail ( $C_{16}H_{33}$ ),  $D^+$  is the quinolinium moiety,  $\pi$  is the  $\pi$ -electron bridge, and  $A^-$  is the tricyanoquinodimethane moiety [37].

#### 1.4.2.2 Switches and transistors

The main characteristic for a switch is the ability to be kinetically stable between two or more states. Generally, molecular switches change from "on" (conducting state) to "off" (non-conducting state) depending on pH, light, temperature and electrical current [8, 12, 38, 39]. The development of molecular switches is envisaged for production of new molecular memories and logic devices.

This is the case of the bistable molecular memory controlled by voltage changes [40] where the "1" state could reverse spontaneously to "0" with a time constant of 760 s at 260 K. Therefore, the drawback on molecular switches is the electron transfer, where the charge separation competes with the reversibility of the switching mechanism, making further development

necessary. A remarkable example on the latest advances is illustrated in **Fig. 1.13**, where the electrical switching of polychloro-triphenyl-methyl (PTM) molecules is confirmed by optic (UV-vis spectra) and magnetic (electronic paramagnetic resonance, EPR) reading [41].

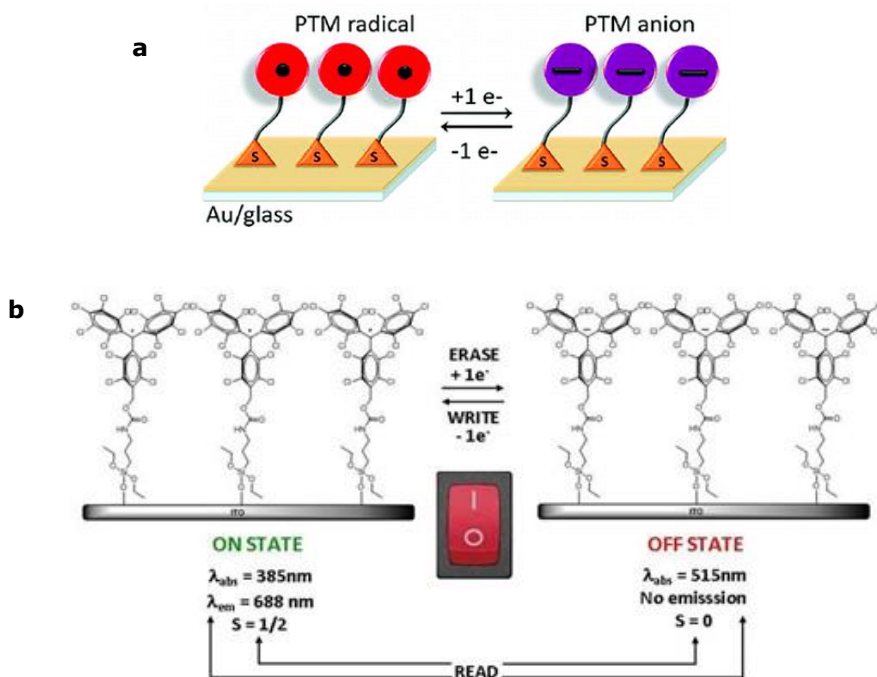


**Figure 1.13. Example of a switch molecule.** (a) General scheme of the switching mechanism and, (b) Detailed view, where “On state” stands for the polychloro-triphenyl-methyl (PTM) radical. In presence of an electron, the PTM radical switches to the anion form or “Off state” [41].

Bulk transistors on the other hand control the flow of charge carriers through semiconductor substances and is mainly represented by the Field Effect Transistors (FET). FET is a unipolar (single-carrier type) device that conducts current using only one kind of charge carrier, either an electron or a hole. If an N-type of semiconductor is used, the carriers are electrons. On the other hand, a P-type based device will use only holes [32]. The device consists of an active channel where charge carriers (electrons or holes) flow from the source to the drain. In more detail, the components are [42]:

- Source (S), area where the charges enter the channel. Current entering at S is defined as  $I_S$  (source current)
- Drain (D), area where the charges leave the channel. Current entering at D is named  $I_D$  and drain-to-source voltage is called  $V_{DS}$  and,
- Gate (G), it is the terminal that modulates the channel conductivity. Voltage applied at G ( $V_G$ ), modulates  $I_D$ .

Note that the source and drain terminal conductors should be connected to the semiconductor through Ohmic contacts. Thus, the conductivity of the channel is a function of the potential applied across the gate source terminals. The best known examples of FET devices are the Metal-Oxide-Semiconductor FET (MOSFET), which compose the main type of transistors in digital integrated circuits for high gate input resistance.

In a MOSFET, the source and drain terminals are connected through metallic contacts to n-doped regions linked by an n-channel. The gate is also connected to a metal contact surface but remains insulated from the n-channel by a very thin silicon dioxide ( $\text{SiO}_2$ ) layer (**Fig. 1.14**). Now, the name metal-oxide-semiconductor FET is more obvious: "metal" for the drain, source and gate connections to the proper surface, "oxide" for the silicon dioxide insulating layer and, "semiconductor" for the basic structure on which the n- and p-type regions are diffused. [33]. As a matter of fact, is for these type of transistors that Moore's Law postulated to decrease on size every 18 months. Thus, MOSFET p- and n-channel are used as building blocks of digital CMOS-circuits.

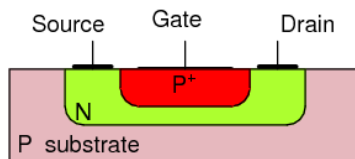


**Figure 1.14. Diagram of a MOSFET.** Bold black lines at the S, G and D represent the metal contact. The gate is heavily doped ( $P^+$ , red area) in order to diffuse holes into the P substrate (pink area) for a large depletion region (N, green area) [32].

Particularly, FET-like modulation in single molecules has been achieved using different gate configurations where the back- and electrochemical gate are the



most studied ones. However, it has been difficult to demonstrate a FET behaviour because the difficulties of placing the gate electrode close to the molecule for effective gate control.

The back-gate consists on a pair of electrodes (source and drain) on a solid substrate, (Si or Al) [43]. Then the Si substrate is heavily doped to serve as a back gate, with a thin oxide layer that separates the Si or Al from the source and drain electrodes (**Fig. 1.15a**) e.g. experiments on a single carbon nanotube showed a FET-type of behaviour [44]. On the other hand, for an electrochemical gate a  $V_G$  is applied between the source and gate electrode, within an electrolyte media. Since the gate voltage falls across the double layers at the electrode-electrolyte interfaces, the effective gate thickness is of the order of a few solvated ions, which results in a large gate field (redox switch of molecules, **Fig 1.15b**).

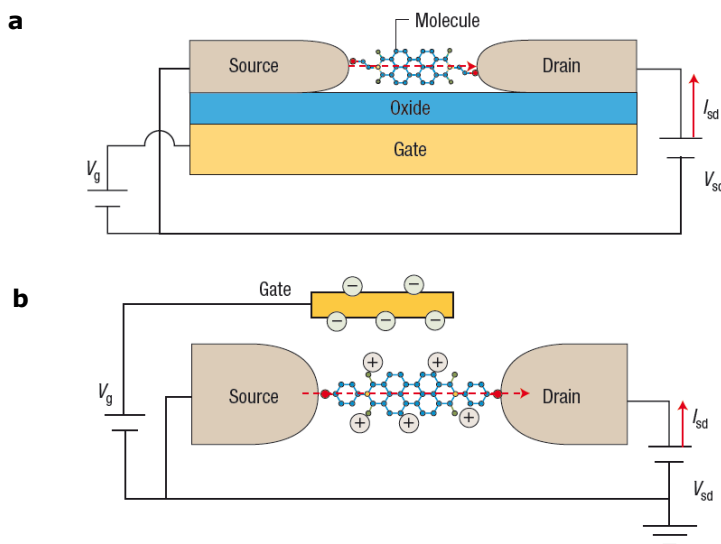


**Figure 1.15. Use of different gate approaches to control current through a molecule. (a)** Back-gate, with a molecule attached between a source and drain electrode on top of an oxidised metal or heavily doped Si gate (substrate) and, **(b)** Electrochemical-gate, a molecule is bridged between the source and drain electrodes, in an electrolyte, in which a gate field is applied by a third electrode inserted in the electrolyte. In many cases, a reference electrode can be used for a proper potential control (not shown) [43].

## 1.4.2.3 Nanowires and molecular wires

Nanowires can be described as nano-crystalline structures with a large length/diameter ratio, which can be used as both, interconnectors and functional components in the fabrication of nano-size electronic and optoelectronic devices [45].

It is important to mention that changes between several micro/nano-wires and single molecules are evident in their conducting properties, due to the size effect on the conductivity. In almost all cases, a semiconducting character in the single crystals is also kept in the micro/nano-wires. The growing direction of micro/nano-wires (length) usually corresponds to the stacking direction of donor or acceptor molecules, so the highest conductivity is observed along this direction. An example is shown in **Fig. 1.16**, where the donor molecules are EDT-TTF (ethylene-dithio-tetrathiafulvalene) and TIE (tetra-iodoethylene) are neutral molecules, assembled through coordination with anions of  $\text{Br}^-$  and  $\text{I}^-$ . Here the supramolecular structure  $(\text{EDT-TTF})_4\text{BrI}_2(\text{TIE})_5$  is formed, where  $\text{Br}^-$  and  $\text{I}^-$  and TIE contribute to the formation of a 3D network [46, 47].

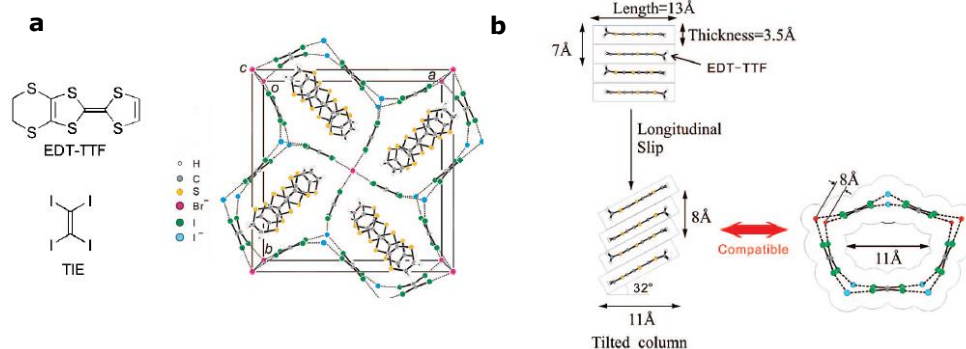


**Figure 1.16. Representation of composition and stacking in nanowires:** (a) EDT-TTF is the donor, TIE is a neutral molecule and  $\text{BrI}_2$  provide coordination anions for formation of the 3D crystalline structure (right) (b) Dimensions of the crystalline donor column, with (above) and without (below) the presence of TIE and comparison with experimental values. Tilted donor columns allow the assembly with TIE and anions, forming pentagonal shaped supramolecular channels (view from above the nanowire) [47].

Single crystals contain more defects in a larger size than in a smaller size. Since the smallest possible single crystals assemble into micro/nano-wires, the number of defects is supposed to be smallest, giving an ideal molecular conducting wire [45]. The field of nanowires can be divided into nanotubes (*e.g.* carbon nanotubes), molecular wires (*e.g.* butadiyne-linked porphyrin polymer) and quantum wires (*e.g.* GaAs/AlGaAs).

In this thesis, we are interested in molecular wires, which are connectors or junctions allowing electron flow to take place between different parts of a system. Furthermore, the criteria that a molecule needs to fulfill before being considered a molecular wire are [20]: *i)* Content of an electron-conducting chain and *ii)* Possession of a terminal electroactive and polar groups for reversible electron exchange.

Organic molecules are the preferred material to produce molecular wires because they allow control over the structural and electronic properties of the wire. For example, the wire rigidity can be modulated with the type of bonds present in the chain: single bonds present more flexible structures (higher rotational conformational freedom) than the more rigid double and triple bonds [48, 49]. Besides, organic molecules can be designed to self-assemble into supra-molecular structures appropriate for charge transport [49, 50].

Moreover, the study of charge transport through these type of molecules can be grouped as: *i)* Trapping molecules between electrodes (*e.g.* between break junctions) and, *ii)* Photoinduced electron transfer, using a donor-bridge-acceptor system (*e.g.* Time-resolved spectroscopy) [49]. Finally, the first molecule to be studied as a molecular wire was the natural compound, caroviologen (**Fig. 1.17**) [20], and later on, other organic molecules were tested, including polythiophenes [23, 50] and biomolecules, such as Deoxyribonucleic Acid (DNA) [51] and peptides [52].

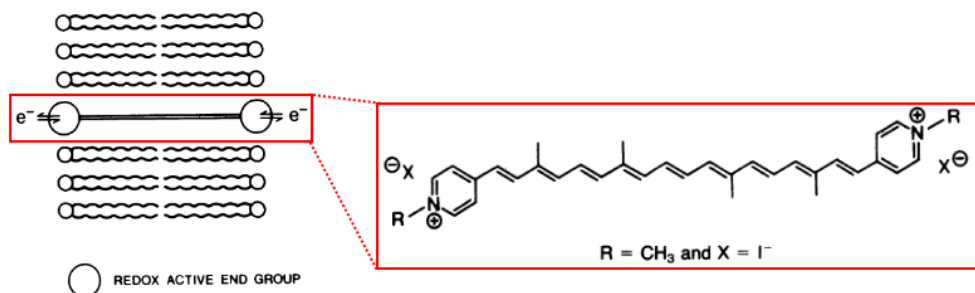


**Figure 1.17. Example of a molecular wire as transmembrane electron channel.** Diagram of a Bis(4-pyridinium) polyene molecule inserted in between a phospholipid bilayer [20].

## 1.5 State of the art in Computational Electronics

Currently, there are several advances in computational electronics. Here an overview of the competing fields with molecular wires are mentioned, such as: *i*) single electron transistors, *ii*) quantum cellular automata and, *iii*) chemically assembled electronic nanocomputers, best represented by means of molecular computation.

### 1.5.1 Single electron transistors

This is a theoretical approach, studied by Chen *et al.* [9] It aims to control the motion of single electrons in solid state structures, consisting of conducting "islands" separated by tunnel barriers. There are two possibilities:

- Single-electron logic (SEL), where digital bits are processed in the form of single electrons, trapped on conducting islands.
- Single-electron transistor (SET) or single-electron charging, where using only an inner three-terminal device or transistor. This transistor could be used in digital circuits where binary operations (0 and 1) are represented as usual by two different levels of voltage. **Fig. 1.18b**, shows a complementary buffer/inverter stage similar to the accepted configuration for CMOS technology (**Fig. 1.18a**). The input signal voltage changes the background electrostatic potentials of the middle

electrodes of the two SET and thus the distribution of the bias voltage  $2V_B$  across them.

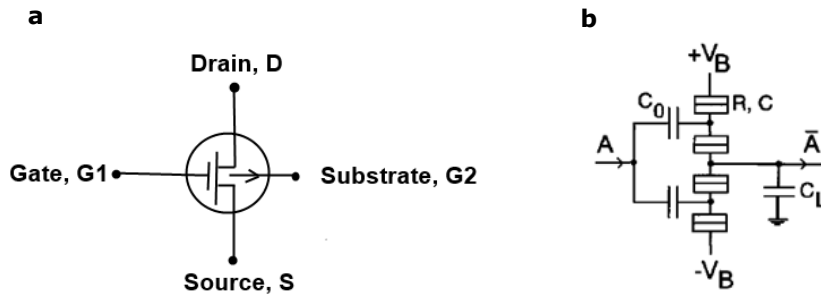


**Figure 1.18. Simplified diagram of a circuit. (a)** CMOS-FET basic components compared to **(b)** Three-terminal device with two SET electrodes [9].

From this analysis, it was concluded that a typical SET geometry would need to meet the following criteria: i) the conducting islands formed inside the  $\text{SiO}_2$  matrix should have a minimum feature size of about 2 nm, while being separated by  $\sim 1$  nm wide tunnel gaps, ii) the spatial pitch should be about 40 nm per transistor, which would allow high density integrated circuits of about  $\sim 10^{11}$  transistors per  $\text{cm}^2$ .

The downside of this technology is that it cannot be implemented for multi-input functions because SETs cannot be open in as wide a range of gate voltage as their FET counterparts. Also a SET requires low temperatures ( $T = 20$  K) to perform and the need to add a cryo-coolant to allow the heat removal when all transistors are activated. On the other hand, computer chips operate at temperature ranges between 0-85°C (based on calculation of the junction temperature or highest operating temperature of the semiconductor on the chip).

### 1.5.2 Quantum cellular automata (QCA)

In 1994, Tougaw *et al.* proposed the idea of QCA [53]. This is an array of quantum-dot cells, connected (locally) by interactions of the electrons in each

cell. The quantum state of each cell can be used to encode binary information. In addition, a Coulomb interaction connects the state of one cell to the state of its neighbours. As a consequence, problems related to small output currents and parasitic capacitances of connecting wires do not occur. Moreover, binary wires composed of linear arrays of cells have been considered as effective system to transmit information from one place to another. In order to prepare a QCA, it is necessary to maintain the double charging of each cell using an insulated top gate, also a conducting substrate to supply the electrons and a thin tunnel barrier between the cells and the substrate to stabilize the charge at integer values (**Fig. 1.19**). At that time, QCA was predicted to be able of performing all three of the basic Boolean operations (AND, OR and NOT) [53].

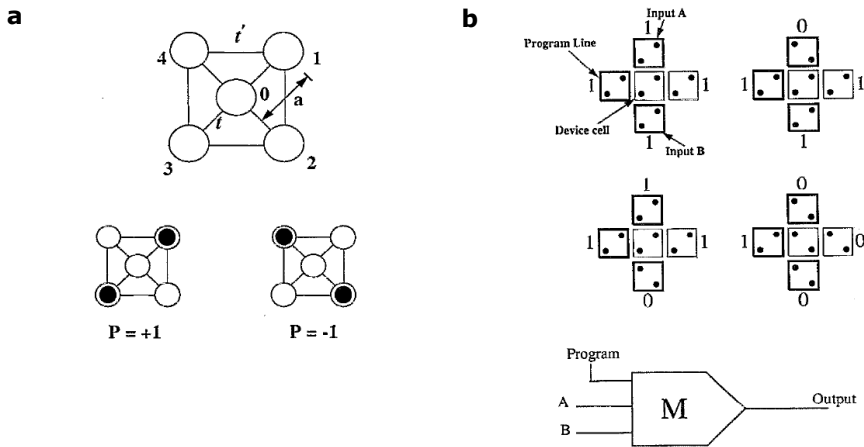


**Figure 1.19. Theoretical approach to QCA. (a) Above:** Scheme of the geometry of a five-site cell. The tunneling energy between the middle- and outer-site is designed by  $t$ , while  $t'$  is the tunneling energy between two outer sites. **Below:** Coulombic repulsion causes the electrons to occupy antipodal sites within the cell. These two bistable states result in cell polarizations of  $P = +1$  and  $P = -1$ . **(b) Above:** A programmable AND/OR gate. **Middle:** The program line is set to one in each system, so the gate is displaying OR logic. All four combinations of the non-program line inputs are shown. The cells with bold borders have fixed charged distributions. Any of the three inputs could be the program line. **Below:** schematic symbol for the programmable AND/OR gate [53].

Later in 1996, Amlani *et al.* achieved the construction of a logic gate consisting of a quantum dot cell. Moreover, this cell was composed of four dots connected in a ring by tunnel junctions and two-single dot electrometers, where the logic AND and OR operations were successfully verified [10]. The most remarkable achievement was in 1998, when Loss and Di Vincenzo proposed a semiconductor-based quantum computer [54]. However, the main disadvantage of the QCA is its dependence on nanolithography techniques to implement quantum dot cells in small metallic islands [53].

### 1.5.3 Chemically assembled electronic nano-computers (CAENs)

A general concept of a chemical computer is a device that processes information by making and breaking chemical bonds, storing logic gates or information in the resulting chemical structures. It is expected to selectively perform operations among molecules at the nano-scale [19].

#### 1.5.3.1 Molecular computation

Molecular computation emerged with the idea of computing directly on (bio)molecules [11]. In this study, Adleman used 50 picomol of small DNA fragments (20-mer) to encode a graph and solve a seven-point Hamiltonian path.

The encoded data consisted on a directed graph  $G$  with designated vertices  $v_{in}$  and  $v_{out}$  and is said to have a Hamiltonian path, if and only if there exists a sequence of compatible "one-way" edges  $e_1, e_2, \dots, e_z$  (= a path) that begins at  $v_{in}$ , ends at  $v_{out}$ , and enters every other vertex exactly once. **Figure 1.20** illustrates a graph that for  $v_{in}= 0$  and  $v_{out}= 6$  has a Hamiltonian path, given by the edges  $0 \rightarrow 1, 1 \rightarrow 2, 2 \rightarrow 3, 3 \rightarrow 4, 4 \rightarrow 5, 5 \rightarrow 6$ .

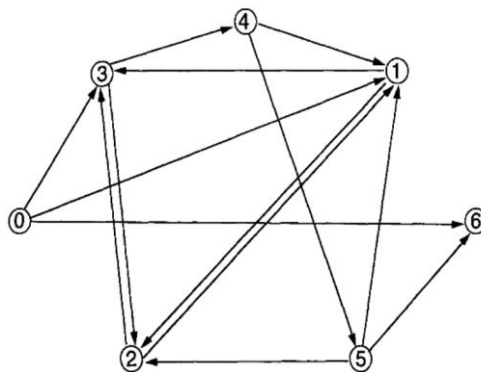


**Figure 1.20. Hamiltonian graph.** Directed graph. When  $v_{in} = 0$  and  $v_{out} = 6$ , a unique Hamiltonian path exists, where  $0 \rightarrow 1, 1 \rightarrow 2, 2 \rightarrow 3, 3 \rightarrow 4, 4 \rightarrow 5, 5 \rightarrow 6$  [11].

Furthermore, the operations of this computation were performed with standard protocols and enzymes (*e.g.* polymerase chain reaction). Later developments, proved that DNA computers can simulate Boolean circuits [55]. Finally, in 2004 Shapiro *et al.* successfully built a molecular computer that perform logic analysis of mRNA disease indicators in vitro and controls the administration of biologically active ssDNA molecules, including drugs (*e.g.* diagnosing prostate cancer in a cell) [56].

## 1.6 Objectives

The aim of this thesis is to study the feasibility of producing a molecular wire based on DNA. In other words, if DNA can be used as a connector allowing the flow of electrons between different parts of a system. According to the molecular wires criteria, DNA must fulfill the following requirements:

- Content of an electron-conducting chain: *B-DNA* (or native DNA) contains a  $\pi$ -conjugated system in its helical inner core, very similar to other conducting materials (*e.g.* graphene, discotic liquid crystals). Moreover, electron flow along DNA (*i.e.* charge transport mechanism) is not fully understood.
- Possession of a terminal electroactive and/or polar groups for reversible electron exchange: For this purpose, it was necessary to covalently



functionalize DNA with an electroactive group (fullerene), avoiding interference on the DNA structure. Therefore, we studied fullerene-DNA molecules as prospective molecular wires.

DNA is a promising molecule because it is a natural occurring wire able to perform self-assembly, rendering highly reproducible double stranded helical wires. As a consequence, it can generate single to supra-molecular structures (*e.g.* DNA origami [57]–[59]). Additionally, DNA is a stiff natural polymer (persistence length= 50 nm) capable of compacting or folding into tiny areas at physiological conditions due to the action of electrostatic forces (*e.g.* charge repulsion) and base pair interactions (*e.g.* stacking compression) [60]. This means that DNA's rigidity can be modulated depending on its environment and application.

The novelty in the present work consist in: *i)* the stringent elucidation of DNA's charge transport mechanism with, *ii)* the use of fullerene groups covalently attached to DNA, working as contacts between the metal electrodes.

Chapter 2 is a solid state physics compilation, related to the theoretical interpretation of DNA charge transport mechanisms (sequential tunneling or multistep charge hopping).

In Chapter 3, the different types of molecular wires are explained, starting from small organic molecules to DNA.

The experimental techniques used along these project, are described in Chapter 4 with their fundamental principles and setup description.

Chapter 5 presents the chemical characterization of the synthesized DNA-fullerene molecules. Then, Chapter 6 describes the different approaches to prepare DNA-fullerene molecules and study their electronic properties.

After optimization of all parameters, Chapter 7 shows the electrical transport on DNA-fullerene molecules was experimentally measured and analysed in the light

of the most accepted theoretical models, reaching to the conclusion that DNA-fullerene molecules present a multistep charge hopping mechanism.

Prospective experiments of fullerene-DNA complexes for photoactivatable anticancer drug applications are discussed in Chapter 8.

Chapter 9 gives a general conclusion of this research and possible work perspectives for the future. Finally, Chapter 10 shows an overview of the contributed imaging work for publications.

## 1.7 Conclusions

- The effects of nanotechnology as a technological revolution is part of life nowadays, with the release of new cosmetics, detergents, medicines, smart clothes, environmental treatments (*e.g.* nanopores) based on nano-components. Moreover, the area of electronic components on the nanoscale is of interest in this chapter.
- Nanoelectronics, is a field that targets to replace the typical top-down approach to build smaller electronic components. In this context, molecular devices are the ultimate goal, resulting from the assembly of nanoelectronic components.
- The bottom-up approach to produce these components is mainly based on SAMs and synthesis of single molecules. Some of their electrical characteristics are those of rectifiers, switches, transistors and molecular wires.
- Our objective is to understand the type of charge transport in DNA with perspectives to use DNA-fullerene molecules as wires to connect electrically circuits based on molecular devices.

## 1.8 References

- [1] P. Salz Trautman, "A computer pioneer rediscovered, 50 Years On," *The New York Times*, 20-Apr-1994. [Online]. Available: <http://www.nytimes.com/1994/04/20/news/20iht-zuse.html>.
- [2] Venusianer, "Replica of the Zuse Z3 in the Deutsches Museum in Munich, Germany," *Wikipedia: Z3 (computer)*, 2006. [Online]. Available: "Z3 Deutsches Museum" by Venusianer at the German language Wikipedia. Licensed under CC BY-SA 3.0 via Wikimedia Commons-[http://commons.wikimedia.org/wiki/File:Z3\\_Deutsches\\_Museum.JPG#media/File:Z3\\_Deutsches\\_Museum.JPG](http://commons.wikimedia.org/wiki/File:Z3_Deutsches_Museum.JPG#media/File:Z3_Deutsches_Museum.JPG). [Accessed: 18-May-2015].
- [3] Environmental responsibility, "We leave some important things out of our products. With a good reason", *Apple Inc*, 2015. [Online]. Available: <http://www.apple.com/environment/toxins/>. [Accessed: 11-Aug-2015].
- [4] J. P. Sykes, "Structural changes in mine supply: Case studies in tin and tantalum demand," Shanghai, China, 2013.
- [5] N. Bostrom, "Technological revolutions: Ethics and policy in the dark," *Nanoscale Issues Perspect. Nano Century*, vol. 1, no. 2006, pp. 129–152, 2007.
- [6] C. Perez, "Technological revolutions and techno-economic paradigms," *Technol. Gov. Econ. Dyn.*, no. 20, pp. 1–26, 2009.
- [7] P. S. Antón, R. Silbergliitt, and J. Schneider, *The global technology revolution. Bio/Nano/ Materials trends and their synergies with information technology by 2015*. Santa Monica, California, USA: RAND (National Defense Research Institute), 2001.
- [8] C. P. Collier, "Electronically configurable molecular-based logic gates," *Science*, vol. 285, pp. 391–394, 1999.
- [9] R. H. Chen, A. N. Korotkov, K. K. Likharev, R. H. Chen, A. N. Korotkov, and K. K. Likharev, "Single electron transistor logic," *Appl. Phys. Lett.*, vol. 68, no. 14, pp. 1954–1956, 1996.
- [10] I. Amlani, A. Orlov, G. Toth, G. H. Bernstein, and G. Snider, "Digital logic gate using quantum-dot cellular automata," *Science*, vol. 284, pp. 289–291, 1999.
- [11] L. M. Adleman, "Molecular computation of solutions to combinatorial problems," *Science*, vol. 266, no. 5187, pp. 1021–1024, 1994.

- [12] M. Zwolak and M. Di Ventra, "Molecular electronics," in *Introduction to Nanoscale Science and Technology*, 1st ed., M. Di Ventra, S. Evoy, and J. R. Heflin Jr., Eds. New York, USA.: Springer US, pp. 261–282, 2004.
- [13] C. Nguyen, "Molecular electronics: An overview," *Perspective on Science '07*, vol. 1. New Haven, U.S., pp. 1–24, 2007.
- [14] G. E. Moore, "Cramming more components onto integrated circuits," *Proc. IEEE*, vol. 86, no. 1, pp. 82–85, 1998.
- [15] N. Taniguchi, "On the basic concept of 'Nano-Technology,'" in *Proc. Intl. Conf. Prod. Eng. Tokyo, Part II*, 1974.
- [16] G. Binnig and C. F. Quate, "Atomic force microscope," *Phys. Rev. Lett.*, vol. 56, no. 9, pp. 930–933, 1986.
- [17] J.-M. Lehn, "Supramolecular chemistry-scope and perspectives molecules-supermolecules-molecular devices," *J. Incl. Phenom.*, vol. 6, pp. 351–396, 1988.
- [18] M. Dubash, "Moore's Law is dead, says Gordon Moore," *techworld*. [Online]. Available: <http://www.techworld.com/news/operating-systems/moores-law-is-dead-says-gordon-moore-3576581/>. [Accessed: 16-Feb-2015].
- [19] M. S. Montemerlo, J. C. Love, G. J. Opiteck, D. Goldhaber-Gordon, and J. C. Ellenbogen, "Technologies and designs for electronic nanocomputers," MITRE Corporation, McLean, Virginia, 1996.
- [20] T. S. Arrhenius, M. Blanchard-Desce, M. Dvolaitzky, J. M. Lehn, and J. Malthete, "Molecular devices: Caroviologens as an approach to molecular wires-synthesis and incorporation into vesicle membranes.," *Proc. Natl. Acad. Sci. U. S. A.*, vol. 83, no. 15, pp. 5355–5359, 1986.
- [21] G. M. Whitesides and B. Grzybowski, "Self-assembly at all scales," *Science*, vol. 295, pp. 2418–2421, 2002.
- [22] J. C. Love, L. A. Estroff, J. K. Kriebel, and R. G. Nuzzo, "Self-assembled monolayers of thiolates on metals as a form of nanotechnology," *Chem. Rev.*, vol. 105, no. 4, pp. 1103–1169, 2005.
- [23] S. Sek, A. Sepiol, A. Tolak, A. Misicka, and R. Bilewicz, "Distance dependence of the electron transfer rate through oligoglycine spacers introduced into self-assembled monolayers," *J. Phys. Chem. B*, vol. 108, no. 24, pp. 8102–8105, 2004.
- [24] T. Morita and S. Kimura, "Long-range electron transfer over 4 nm governed by an inelastic hopping mechanism in self-assembled

- monolayers of helical peptides," *J. Am. Chem. Soc.*, vol. 125, no. 29, pp. 8732–3, 2003.
- [25] S. J. Tans, R. Miedema and C. Dekker, "Electrical transport in monolayers of phthalocyanine molecular two electrodes wires and AFM imaging of a single wire bridging," *Synt. Met.*, vol. 84, pp. 733–734, 1997.
- [26] Y. Shirai, L. Cheng, B. Chen, and J. M. Tour, "Characterization of self-assembled monolayers of fullerene derivatives on gold surfaces: Implications for device evaluations," *J. Am. Chem. Soc.*, vol. 128, no. 41, pp. 13479–89, 2006.
- [27] D. J. Wold and C. D. Frisbie, "Fabrication and characterization of metal-molecule-metal junctions by conducting probe atomic force microscopy," *J. Am. Chem. Soc.*, vol. 123, no. 23, pp. 5549–56, 2001.
- [28] L. Reggiani, J.-F. Millithaler, and C. Pennetta, "Microscopic modeling of charge transport in sensing proteins," *Nanoscale Res. Lett.*, vol. 7, no. 1, p. 340, 2012.
- [29] V. B. Engelkes, J. M. Beebe, and C. D. Frisbie, "Length-dependent transport in molecular junctions based on SAMs of alkanethiols and alkanedithiols: Effect of metal work function and applied bias on tunneling efficiency and contact resistance," *J. Am. Chem. Soc.*, vol. 126, no. 43, pp. 14287–96, 2004.
- [30] T. Lee, W. Wang, J. F. Klemic, J. J. Zhang, J. Su, and M. A. Reed, "Comparison of electronic transport characterization methods for alkanethiol self-assembled monolayers," *J. Phys. Chem.B.*, vol. 108, pp. 8742–8750, 2004.
- [31] H. Song, M. A. Reed, and T. Lee, "Single molecule electronic devices.," *Adv. Mater.*, vol. 23, no. 14, pp. 1583–608, 2011.
- [32] Tony R. Kuphaldt, *Lessons in electric circuits, volume III-semiconductors*, 5th Ed., Open Book Project hosted by ibiblio, 2009.
- [33] R. Boylestad and L. Nashelsky, *Electronic devices and circuit theory*, 7th Ed, vol. 29, no. 8. Columbus, Ohio: Prentice Hall International Inc., 1996.
- [34] A. Aviram and M. A. Ratner, "Molecular rectifiers," *Chem. Phys.Lett.*, vol. 29, no. 2, pp. 591– 595, 1974.
- [35] C. Joachim, J. Gimzewski, R. Schlittler, and C. Chavy, "Electronic transparency of a single C60 Molecule," *Phys. Rev. Lett.*, vol. 74, no. 11, pp. 2102–2105, 1995.

- [36] M. A. Reed, "Conductance of a molecular junction," *Science*, vol. 278, pp. 252–254, 1997.
- [37] R. M. Metzger, B. Chen, U. Höpfner, M. V. Lakshmikantham, D. Vuillaume, T. Kawai, X. Wu, H. Tachibana, T. V. Hughes, H. Sakurai, J. W. Baldwin, C. Hosch, M. P. Cava, L. Brehmer, and G. J. Ashwell, "Unimolecular electrical rectification in hexadecylquinolinium tricyanoquinodimethanide," *J. Am. Chem. Soc.*, vol. 119, no. 43, pp. 10455–10466, 1997.
- [38] R. M. Metzger, "Unimolecular electronics and rectifiers," *J. Mater. Chem.*, vol. 18, pp. 4364–4396, 2008.
- [39] I. Diez-Perez, Z. Li, J. Hihath, J. Li, C. Zhang, X. Yang, L. Zang, Y. Dai, X. Feng, K. Muellen, and N. Tao, "Gate-controlled electron transport in coronenes as a bottom-up approach towards graphene transistors.," *Nat. Commun.*, vol. 1, no. 3, p. 31, 2010.
- [40] M. A. Reed, J. Chen, A. M. Rawlett, D. W. Price, and J. M. Tour, "Molecular random access memory cell," *Appl. Phys. Lett.*, vol. 78, no. 23, pp. 3735–3737, 2001.
- [41] C. Simão, M. Mas-Torrent, J. Veciana, and C. Rovira, "Multichannel molecular switch with a surface-confined electroactive radical exhibiting tunable wetting properties," *Nano Lett.*, vol. 11, no. 10, pp. 4382–4385, 2011.
- [42] J. Millman and C. C. Halkias, *Electronic devices and circuits*, International Edition, Kōgahusha, Tokyo: McGraw-Hill Inc., 1967.
- [43] N. J. Tao, "Electron transport in molecular junctions.," *Nat. Nanotechnol.*, vol. 1, pp. 173–181, 2006.
- [44] S. J. Tans, A. R. M. Verschueren, and C. Dekker, "Room-temperature transistor based on a single carbon nanotube," *Nature*, vol. 393, pp. 49–52, 1998.
- [45] T. Sugimoto, H. Tanaka, D. de Caro, and L. Valade, "New development in the preparation of micro/nano-wires of molecular (magnetic) conductors," *Materials*, vol. 3, pp. 1640–1673, 2010.
- [46] H. M. Yamamoto, J. I. Yamaura, and R. Kato, "Multicomponent molecular conductors with supramolecular assembly: Iodine-containing neutral molecules as building blocks," *J. Am. Chem. Soc.*, vol. 120, no. 24, pp. 5905–5913, 1998.
- [47] H. M. Yamamoto, Y. Kosaka, R. Maeda, J. I. Yamaura, A. Nakao, T. Nakamura, and R. Kato, "Supramolecular insulating networks sheathing

- conducting nanowires based on organic radical cations," *ACS Nano*, vol. 2, no. 1, pp. 143–155, 2008.
- [48] R. Breslow and S. T. Schneebeli, "Structure–property relationships in molecular wires," *Tetrahedron*, vol. 67, no. 52, pp. 10171–10178, 2011.
- [49] L. D. A. Siebbeles and F. C. Grozema, *Charge and exciton transport through molecular wires*. Weinheim, Germany: Wiley-VCH Verlag and Co. KGaA, 2011.
- [50] F. J. M. Hoeben, P. Jonkheijm, E. W. Meijer, and A. P. H. J. Schenning, "About supramolecular assemblies of pi-conjugated systems," *Chem. Rev.*, vol. 105, no. 4, pp. 1491–1546, 2005.
- [51] D. Porath, A. Bezryadin, S. de Vries, and C. Dekker, "Direct measurement of electrical transport through DNA molecules," *Nature*, vol. 403, pp. 635–638, 2000.
- [52] J. Gao, P. Müller, M. Wang, S. Eckhardt, M. Lauz, K. M. Fromm, and B. Giese, "Electron transfer in peptides: The influence of charged amino acids," *Angew. Chem. Int. Ed. Engl.*, vol. 50, no. 8, pp. 1926–30, 2011.
- [53] P. D. Tougaw and C. S. Lent, "Logical devices implemented using quantum cellular automata," *J. Appl. Phys.*, vol. 75, no. 3, pp. 1818–1825, 1994.
- [54] D. Loss and D. P. DiVincenzo, "Quantum computation with quantum dots," *Phys. Rev. A*, vol. 57, pp. 120–126, 1998.
- [55] M. Ogihara and A. Ray, "Simulating boolean circuits on a DNA computer," *Algorithmica*, vol. 25, pp. 239–250, 1999.
- [56] Y. Benenson, B. Gil, U. Ben-Dor, R. Adar, and E. Shapiro, "An autonomous molecular computer for logical control of gene expression," *Nature*, vol. 429, no. 6990, pp. 423–429, 2004.
- [57] N. C. Seeman, "Nucleic acid junctions and lattices," *J. Theor. Biol.*, vol. 99, pp. 237–247, 1982.
- [58] N. C. Seeman, "Biochemistry and structural DNA nanotechnology: An evolving symbiotic relationship," *Biochemistry*, vol. 42, no. 24, pp. 7259–7269, 2003.
- [59] F. Fischer, A. Henning-Knechtel, and M. Mertig, "Investigating the aggregation behaviour of DNA origami frames," *Phys. Status Solidi Appl. Mater. Sci.*, 2015.

- 
- [60] A. Savelyev, C. K. Materese, and G. A. Papoian, "Is DNA ' s rigidity dominated by electrostatic or nonelectrostatic interactions?," *J. Am. Chem. Soc.*, vol. 133, pp. 19290–19293, 2011.



## Chapter 2

### Components of Molecular Devices

This chapter begins with a basic introduction to chemical bonding, in order to establish the fundamentals on how to control the properties of organic molecules with the ultimate goal of producing molecular devices (rectifiers, switches, molecular wires). Our interest is to generate novel molecular wires based on DNA, thus it is important to have an overview on topics related to DNA structure and charge transport properties. Finally, some of the DNA applications as a molecular wires are briefly presented.

#### 2.0 Introduction to chemical bonds.

In organic systems, the nature of chemical bonding influence the behaviour of the molecules. The way that molecules bond is classified as: "*localized*" and "*delocalized*". "*Localized chemical bonding*" is a bond where electrons are shared by only two nuclei. This can be explained with a quantum mechanical model that describes the behaviour of an electron in an atom using a wave equation (Schrödinger equation). For instance, **Equation 2.1** depicts the wave equation for a one-electron system [1]

$$\frac{\delta^2\psi}{\delta x^2} + \frac{\delta^2\psi}{\delta y^2} + \frac{\delta^2\psi}{\delta z^2} + \frac{8\pi^2m}{h^2}(E - V)\psi = 0 \quad (\text{Equation 2.1})$$

Here  $m$  is the mass of the electron,  $E$  is its total energy,  $V$  is its potential energy and,  $h$  is Planck's constant. When a wave equation is solved, it is called a wave function, or orbital, and is denoted by the Greek letter psi ( $\psi$ ). Also, the plot of  $\psi^2$  in a three-dimensional space, describes the electron density or the volume around a nucleus that an electron is most likely to occupy (**Fig. 2.1**) [1, 2].

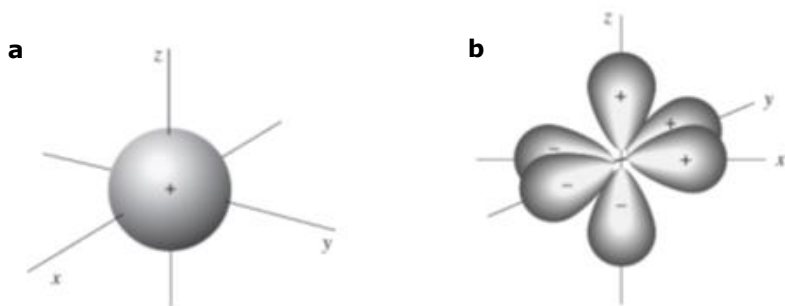


**Figure 2.1** Examples of atomic orbitals **(a)** The 1s orbital and **(b)** the three 2p orbitals [1].

Atomic orbitals ( $s$ ,  $p$ ,  $d$  and  $f$ ) are organized into different electronic shells, centred on the nucleus, increasing size and energy successively. In accordance to Pauli's exclusion principle, no more than two electrons can be present in any orbital, and they must have opposite spins. Thus, the first shell contains only a single  $s$  orbital, named 1s and it can only hold 2 electrons. The second shell contains: 2s orbital and 2p orbitals = 8 electrons, etc. The three different  $p$  orbitals within a given shell are oriented in space along mutually perpendicular directions, denoted  $p_x$ ,  $p_y$  and  $p_z$ . In addition, from **Fig. 2.1b**, a region where the two lobes of each orbital are separated by a region of zero electron density, is called a "node". The lobe signs, + and -, do not refer to positive or negative charges (electron cloud must be negatively charged) but are related to chemical bonding and reactivity [2].

The valence-bond theory describes this by using 2s orbital combined with only two of the three available 2p orbitals. This results in the formation of three  $sp^2$  hybrid orbitals and one orbital, 2p, remains unchanged. In addition, the  $sp^2$  orbitals lie in a plane at angles of  $120^\circ$  to one another, with the remaining p orbital perpendicular to the  $sp^2$  plane. When two carbons with  $sp^2$  hybridization approach each other, they form a strong  $\sigma$  bond by  $sp^2$ - $sp^2$  head-on-overlap. At the same time, the non-hybridized p orbitals interact by sideways overlap to form what is called a pi ( $\pi$ ) bond. The combination of a  $sp^2$ - $sp^2$   $\sigma$  bond and a 2p-2p  $\pi$  bond results in the sharing of four electrons and the formation of a carbon-carbon double bond [2].

Moreover, for the molecular-orbital concept bonding is considered to arise from the overlap of atomic orbitals. This is a number of atomic orbitals combine to form an equal number of new orbitals, namely molecular orbitals. For example, an  $H_2$  molecule has an H-H bond, resulting from the overlap of two hydrogen 1s orbitals seen in **Fig. 2.2** as a cylindrical shape. Bonds formed by the overlap of two atomic orbitals along a line drawn between the nuclei are called sigma ( $\sigma$ ) bonds [2]. Here, the clouds surround two or more atoms, different from atomic orbitals. In localized bonding, the overlapping atomic orbitals are two (each with one electron), so that the molecular orbitals are generated. Then, the bonding orbital has a lower energy than the original atomic orbitals, contrary to the antibonding orbital, which has a higher energy. The greater the overlap, the stronger the bond will be, while a total overlap is forbidden due to repulsion [1].

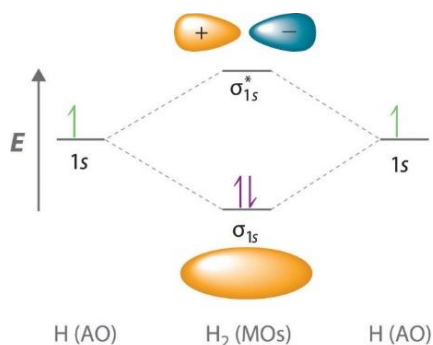


**Figure 2.2.** Overlap of two 1s orbitals gives rise to a binding ( $\sigma$ ) and a antibonding ( $\sigma^*$ ) orbital [1].

"*Delocalized chemical bonding*" is in the other hand useful to describe bonding that cannot be merely explained with localized bonding. In this type, one or more bonding orbitals are not restricted to two atoms, but they spread out over three or more, thus they are "delocalized". In the valence-bond method, an average of several Lewis structures (canonical forms, where valence electrons in lone pairs are represented as dots and shared pairs in a chemical bond are depicted as lines) are used to draw the molecule, called resonance (*i.e.* benzene). If we look at benzene by this method qualitatively, we see that each carbon atom, being connected to three other atoms, uses  $sp^2$  orbitals to form  $\sigma$  bonds, so that all 12 atoms are in one plane (**Fig. 2.3**).

Each carbon has a  $p$  orbital (containing one electron) remaining and each of these can overlap equally with the two adjacent  $p$  orbitals. This overlap of six orbitals produces six new orbitals, three of which are bonding. These three (called  $\pi$  orbitals) all occupy approximately the same space. One of the three is of lower energy than the other two, which are degenerate. They each have the plane of the ring as a nodal plane and so are in two parts, one above and one below the plane. The two orbitals of higher energy also have another node. The six electrons that occupy this torus-shaped cloud are called the aromatic (or conjugated) sextet [1].

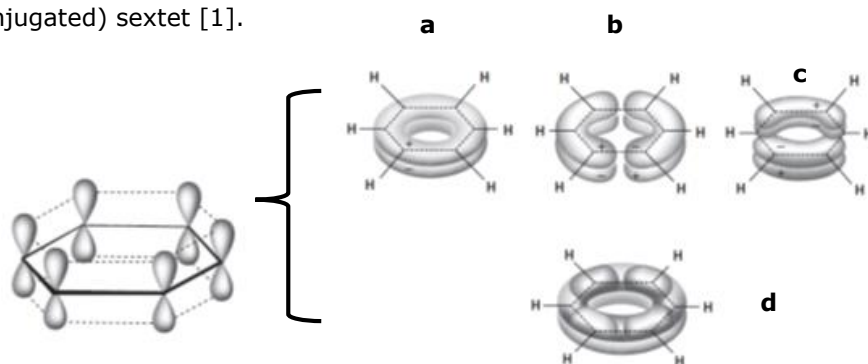


**Figure 2.3.** The six  $p$  orbitals of benzene overlap to form three bonding orbitals, (a), (b), and (c). The three orbitals superimposed are shown in (d) [1].

## 2.1 Organic Molecules

Returning to the components of molecular devices, organic molecules can behave in electrical terms as: *i*) Molecular resistors, *ii*) Rectifiers, *iii*) Switches and memories and *iv*) Molecular wires [3].

### 2.1.1 Molecular resistors

For a chemist, it is empirically known that saturated alkyl-chains conduct less than unsaturated poly-alkenes or poly-conjugated aromatic hydrocarbons. This was confirmed in 1969 by Taube *et al.* [4], where he observed a slower charge transfer along saturated alkyl-chains as compared to the unsaturated ones. Later on, with the break junctions technique [5], resistance measurements on the single-molecule level were easier to perform, where the tunneling charge transport is the main effect (Landauer quantum conductance,  $G_L \equiv 2e^2/h$ ).

In this context, the tunneling decay constant for N-alkanedithiols was determined to be  $1.0 \pm 0.1$  per carbon atom, and the resistances were of  $10.5 \pm 0.5$ ,  $51 \pm 5$ ,  $630 \pm 50$  and  $103 \pm 0.1$  M $\Omega$  for hexanedithiol, octanedithiol, decanedithiol and, 4,4' bipyridine respectively [6]. After years of research, an overview of the results indicates [3–8]:

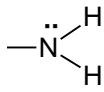
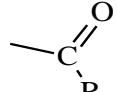
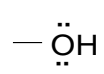
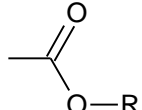
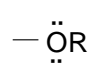
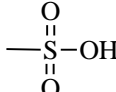
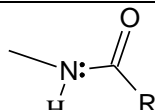
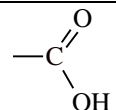
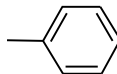
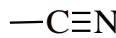
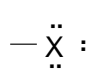
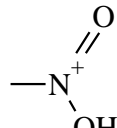
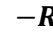
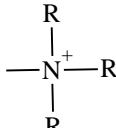
- Saturated molecules present higher resistances than their corresponding unsaturated relatives. Also, for the same unsaturated molecule, an increase of length (more carbon atoms) increases the resistance on the molecule.
- Conjugated aromatic molecules show lower resistances than conjugated non-aromatic molecules with similar structure. The more conjugated groups, the higher will be the molecule's conductivity. Moreover, a twist or conformational change can produce a decrease in conductivity.
- Higher conductivities are observed when the molecule is covalently bound to both electrodes.

### 2.1.2 Rectifiers

Rectification is a type of asymmetrical conduction and was the first envisioned molecular device. Typical bulk rectifiers are based on P-N junctions. A P-N junction is composed with both, a P-type (holes or positive charge carriers) and N-type (electrons or negative charge carriers) region in proximity at a junction [9]. This means that in order to use an organic molecule as a rectifier, it should contain P-N junction properties [10].

The synthetic control of the substituent groups on aromatic systems allows the modulation of the pi electron density within the organic molecule, and therefore to create relatively electron-poor (p-type) or electron-rich (n-type) aromatic molecular subunits. In chemistry, electron-withdrawing substituents cause their subunit to raise its electron affinity, making it a good electron acceptor. On the other hand, electron-releasing substituents cause a decrease in the ionization potential, generating a good electron donor subunit (see **Table 2.1** for representative chemical groups) [10].

**Table 2.1** *Left column:* Electron donating groups contain atoms attached to the ring with lone pairs, aryl or alkyl groups. *Right column:* Electron withdrawing groups have atoms attached to the ring that have either, double or triple bond to an oxygen or nitrogen, or have positive charges on them [11].

Electron donating groups (donor)	Electron withdrawing groups (acceptor)
	
	
	
	
	
	
	

In order to build a molecular rectifier, it is necessary to connect the donor and acceptor  $n$  subunits with a sigma-electron system ("insulator" bridge that provides depletion region similar to semiconductors). For instance, **Fig. 2.4a**

depicts hemiquinone, the most simple example and **Fig. 2.4b**, the first Aviram-Ratner type of rectifier (molecule arranged as P-N junction) that was experimentally measured [12]. Note that the  $\sigma$ -bridge should not be too long (between 2-6 C atoms) in order to allow rectification to occur [3, 8].

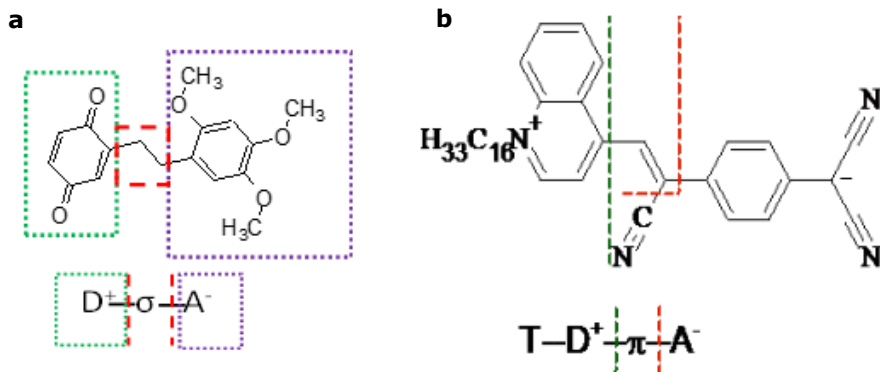


**Figure 2.4.** (a) Hemiquinone, where 2,5-cyclohexadiene-1,4-dione represents the donor, separated by an ethyl group, connected to the acceptor (2,4,6-cyclohexadiene-1,3,4-trimethoxy) [10]. (b) Hexadecylquinolinium tricyanoquinodimethanide rectifier molecule [12].

Further advances the field, allow to identify some of the best uni-molecular rectifiers (**Fig. 2.5**) that have been prepared by Langmuir-Blodgett monolayers and sandwiched between two metal electrodes of the same type (Al or Au).

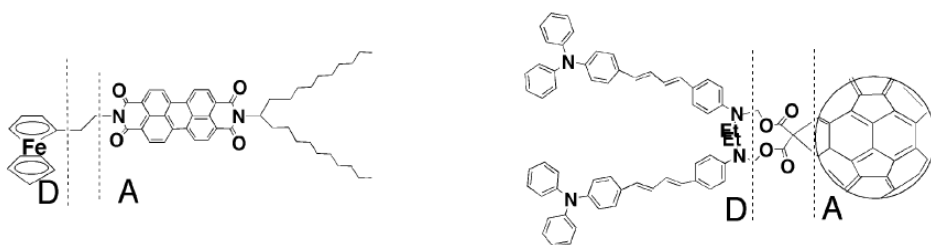


**Figure 2.5.** Example of molecular rectifiers, where the donor and acceptor moieties are marked as "D" and "A" respectively [3].

According to this metal-molecule-metal approach, if a molecule is centered in the gap, tunneling conduction across the molecules should decrease exponentially (gap width increase) and a sigmoidal I-V curve is observed,

passing through the origin [3, 8]. This is shown in **Fig. 2.6** for the molecular rectifier based on carbon nanotubes [13]

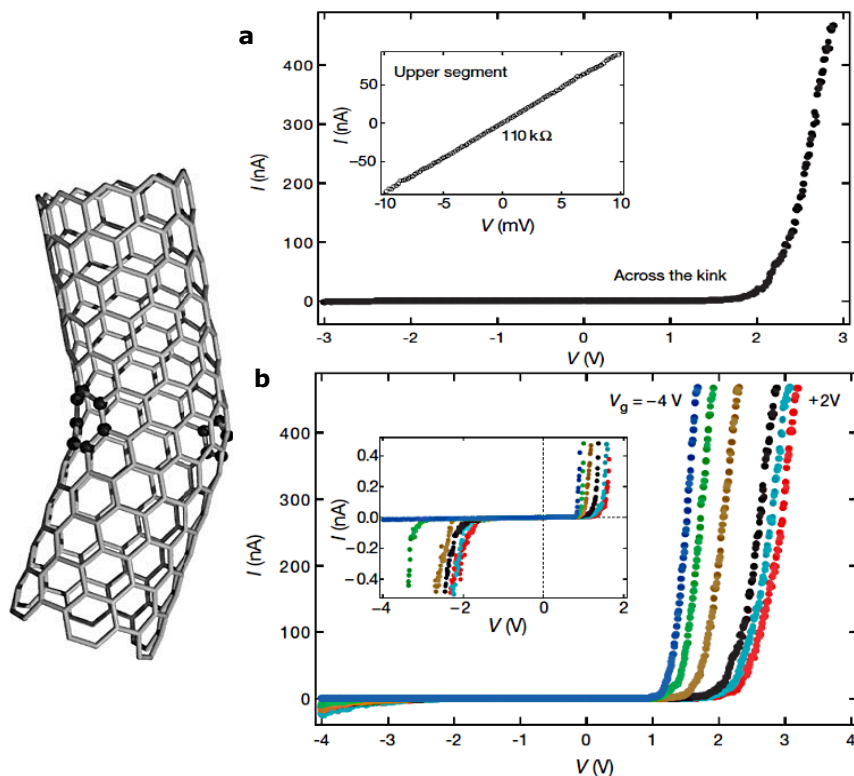


**Figure 2.6. Molecular rectifier based on a carbon nanotube kink. (a)** Measurements at 100 K. I-V plot with voltage changes between  $-4$  to  $+2$  V, where a semiconductor-metallic heterojunction is observed for the kink. Inset shows a metallic behaviour above the kink and, **(b)** Gate voltages are from right to left 2 V, 1 V, 0 V, 1 V, 2 V and  $-4$  V respectively. The inset shows an expanded view of the small-current region which shows more clearly the onset of conduction for both bias polarities [13].

### 2.1.3 Switches and memories

Here, the goal is to obtain molecules that can be switched to a different electronic state within a nanosecond or less, but this presents a problem because the charge separation must compete with its back-reaction (*i.e.*  $D - A \rightarrow D^+ - A^-$ ). Switches can be used in either way, isolated or in an array of



multiple switches to implement logic operations [14]. Currently, the most efficient switch type of molecules are seen in the plants photosynthesis (photosystem-II), where a set of acceptor neighbouring molecules, allows a process  $[D - A A_2 A_3] \rightarrow [D^+ - A^- A_2 A_3] \rightarrow [D^+ - A A_2^- A_3] \rightarrow [D^+ - A A_2 A_3^-]$  which is rapid and irreversible [3]. Redox-active rotaxanes (**Fig. 2.7a**) sandwiched between two metal electrodes, are a good example of switches. In the "closed" state, resonant tunneling dominates the current flow while in the "open" state, no current is observed. When a number of these switches are assembled together, it results into "AND" (**Fig. 2.7b-c**) and "OR" logic gates [15].

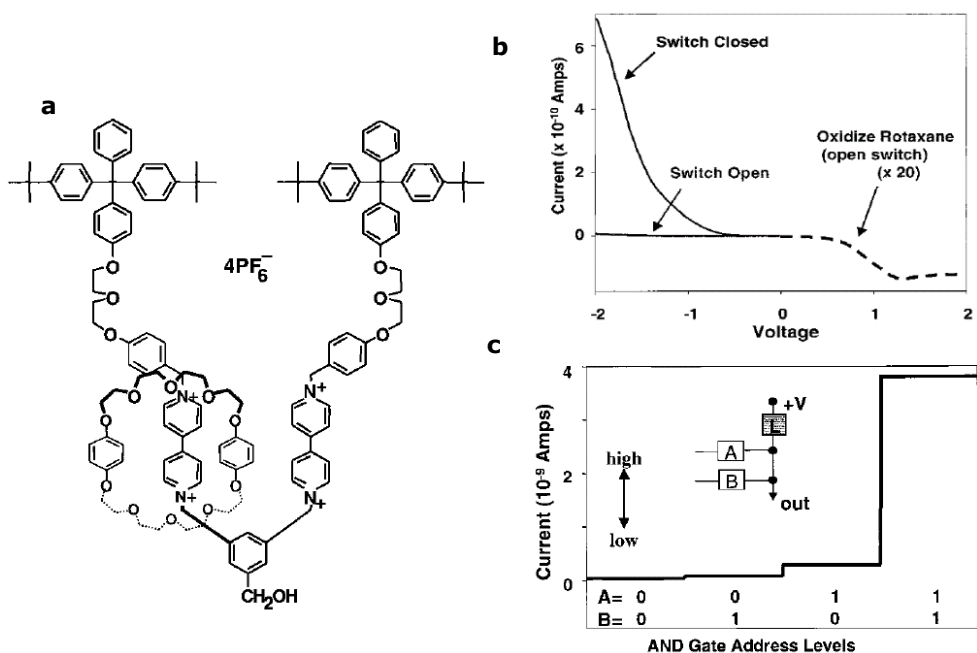


**Figure 2.7.** (a) Representation of a rotaxane molecule (b) The I-V plot shows that for the "closed" state, the device is probed by applying a negative voltage to the bottom electrode. After oxidation, the switches are "opened" by oxidizing the molecules at voltages above + 0.7 V. (c) Experimentally measured truth table for logic gates configured from linear arrays of molecular switch junctions. A low input is held at ground potential and a high input is held at +2V. Arbitrary high and low output current levels are assigned on each plot. The inputs are labeled alphabetically, and one device, labeled L, was configured as a load impedance on the gate. Here a two-terminal AND gate are represented as a function of input address with an accompanying schematic of how the device was configured [15].

### 2.1.4 Molecular wires

In order to connect single-molecule electronic devices, it is necessary to contact them by conducting wires of the same dimensions. Moreover, conjugated molecular wires can be composed of analogous polymers used for organic electronics. A synthetic control over structure and properties of a molecule is a great advantage for the production of molecular devices oriented to a specific function [14]. Examples of prospective molecules are shown in **Fig. 2.8**.

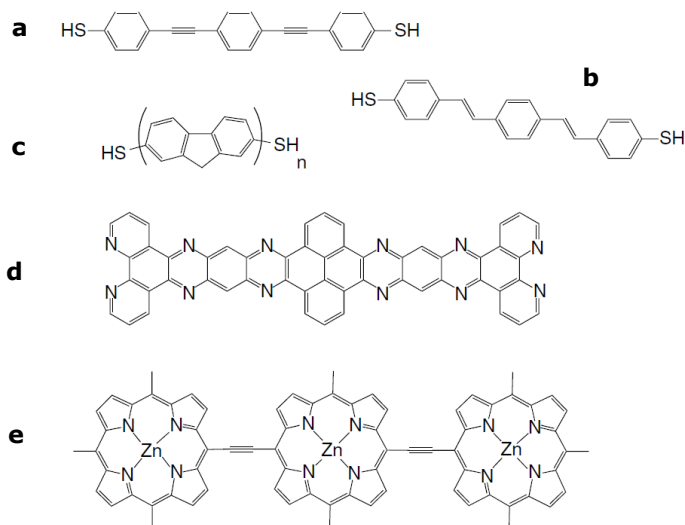


**Figure 2.8.** (a-e) Different molecular wires, ranging from less flexible to more rigid structures [14].

## 2.2 Deoxyribonucleic acid (DNA)

DNA constitutes a natural occurring molecular wire. It has a key role in encoding genetic information in living organisms. DNA's structure and biological function have been widely demonstrated but its electronic and assembly properties have been of great interest in different fields due to the implications it may have [16]. In this section, the structure of DNA and contradictory electronic results in prior literature will be described, together with some experiments and current advances in the DNA electronics field.

The composition of DNA is based on monomers of purines (adenine 'A' and guanine 'G') and pyrimidines (thymine 'T' and cytosine 'C'), also called nucleotides [17]. These nucleotides are attached to a 2'-deoxyribose (5-carbon sugar) and the sugar groups link to each other through a phosphodiester link (phosphate-sugar backbone). A given sequence of bases can form a single strand of DNA (ssDNA) [16]. During hybridization, two ssDNA coil around the same axis and bases will pair with its specific complement via hydrogen bonds and  $\pi$ - $\pi$  stacking, thus an A base will pair with a T base (two hydrogen bonds) and G will pair with C (three hydrogen bonds). It is important to mention that Watson and Crick already noticed that this nucleotides pairing could be part of the copying mechanism for the genetic material [18].

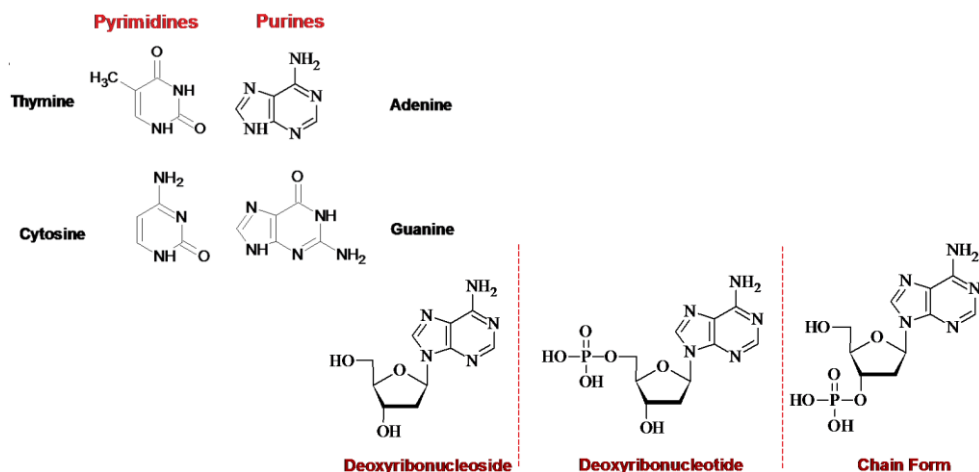


**Figure 2.9.** From left to right: Pyrimidines (thymine and cytosine) and Purines (adenine, guanine) are depicted with their complementary pair. Sequential assembly of a single stranded DNA chain starting with a deoxyribonucleoside, then with the addition of one phosphate group formation of a deoxyribonucleotide and finally reaching to the form of a deoxyribonucleotide within a chain.

### 2.2.1 DNA structure

The canonical Watson-Crick DNA structure (*B-DNA*) is the main relevant structure at physiological conditions. Nevertheless, Watson and Crick noticed that DNA could present structural changes depending on its sequence and

environment [18]. To illustrate this, alternative structures of DNA are listed in **Fig. 2.10** and **Table 2.2**, starting from left to right: *A-DNA*, *B-DNA* and *Z-DNA*.

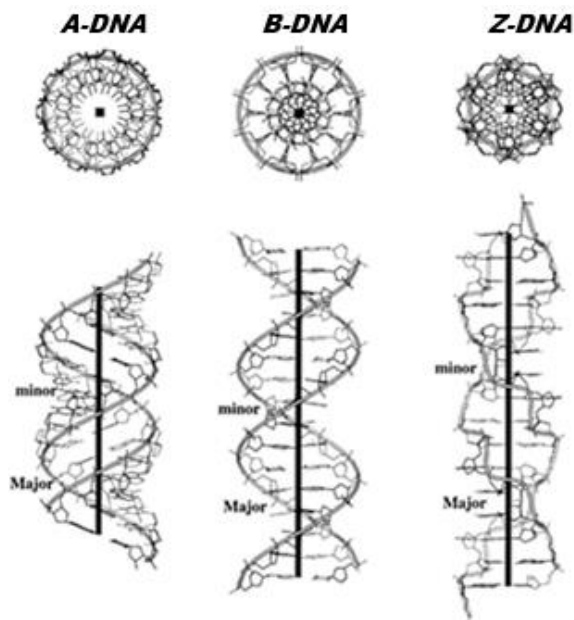


**Figure 2.10.** Top-and-side views of different *DNA* structures. **A-DNA**: right handed type with a tilted compact helical axis and base pairs point towards the minor groove. **B-DNA**: canonical structure (right handed), where the base pairs orient along the helical axis at similar distances. **Z-DNA**: left handed structure, with a zigzag type of backbone [19]

**Table 2.2** X-ray diffraction parameters observed for *A*-, *B*- and *Z-DNA*.

	<b>A-DNA</b>	<b>B-DNA</b>	<b>Z-DNA</b>
<b>Helix sense</b>	RH	RH	LH
<b>Bp per turn</b>	11	10	12
<b>Vertical rise per bp (nm)</b>	0.256	0.34	0.37
<b>Rotation per bp (°)</b>	+33	+36	-30
<b>Helical diameter (nm)</b>	2.3	1.9	1.8

### 2.2.1.1 A-DNA: underwinding for replication

In 1953 *A-DNA* was the first DNA structure to be characterized, produced by dehydration of DNA fibers [20]. Further studies indicate that this form is involved in the mechanism of DNA replication. Here the DNA polymerase gives rise to a complex with DNA, presenting a conformational switch from the *B*- to the underwound *A*-form. This is important because DNA polymerases are not sequence specific, so the enzyme must differentiate a proper Watson-Crick base pair from various mismatches. As a consequence, by inducing the *A*-type, the polymerase exploits the structural features of the highly accessible minor-groove to ensure that the correct base has been added relative to the template sequence [21, 22].

### 2.2.1.2 B-DNA: the standard form

In aqueous solution, native DNA consists on a right-double handed double helix with ten nucleotides per turn, separated by a 3.4 Å translation along the helix axis in each of the two chains, and an average angle of 36-degree between successive base pairs (bp). The two chains are aligned mutually in an antiparallel orientation (**Fig. 2.11**). It encodes the genome sequence in a number of structural polymorphisms of DNA which enables the inheritance and adaptation mechanisms [18, 22–25]. Moreover, DNA molecules were believed to interconvert only between two well defined right handed double-helical structures, *e.g.* *A* and *B*. Nowadays, we are aware of the high adaptability of DNA to its environment by means of twisting, turning and stretching, leading to a wide range of structures, experimentally unveiled by X-ray diffraction, nuclear magnetic resonance (NMR) and other spectroscopic techniques. These changes are a consequence of minor variations in some parameters, such as helical-axis direction, base-pairing scheme, or even the number of interconnecting strands and every different DNA structure is identified with one-alphabet letter name, such as *B*-DNA [22].

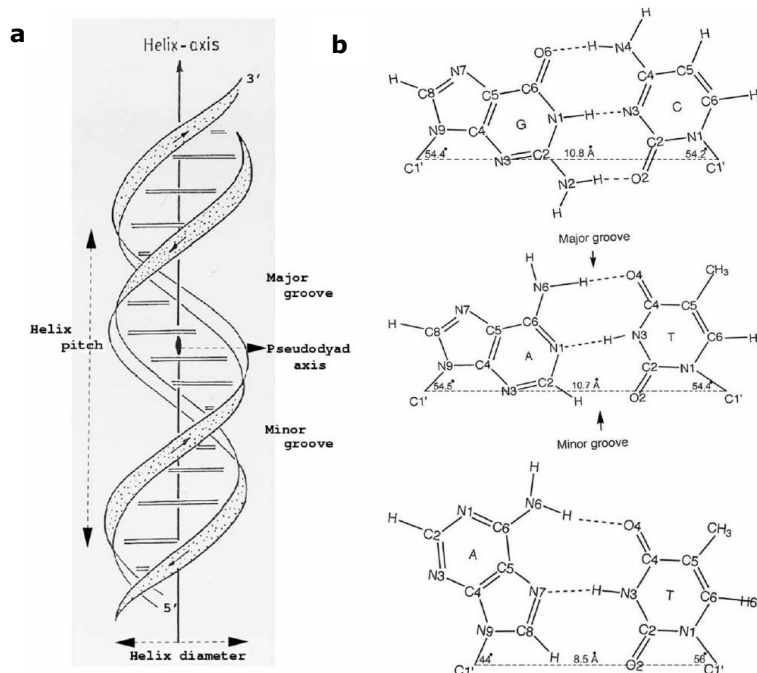


**Figure 2.11. (a)** Diagram of a Watson-Crick double helix (*B-DNA*). The horizontal bars represent the base pairs, the sugar-phosphate backbones are depicted as ribbons, related by a twofold rotation axis perpendicular to the helix running in opposite directions. **(b)** Base pairs: G-C and A-T hydrogen bonds are shown, where the major and minor grooves of DNA can be identified [22].

### 2.2.1.3 Z-DNA: the left-handed structure

The particular *Z-DNA* structure was first investigated at high salt concentrations (3 M NaCl). It serves as a sink to superhelical tension and it seems to have a role in the regulation of eukaryotic genes. This was suggested after Z-form sequences were observed to accumulate near the transcription start site of eukaryotic genes (*e.g.* human chromosome 22 has ~ 80% *Z-DNA* sequences close to their transcription start sites) [21].

### 2.2.2 DNA electronics

In the early 60's, Eley and Spivey [26] observed that the bases in *B-DNA* (**Fig. 2.11**) are planar molecules, placed inwards the helix, arranged along the axis with similar inter-plane spacing ( $\pi$ - $\pi$  orbitals stacking) to one-dimensional aromatic crystals [27]–[29], thus it is expected that DNA shows a  $\pi$ -electron conductivity along this axis. To prove this, they measured dc-conductivity along four types of DNA molecules (calf thymus, wheat-germ, herring sperm and penicillum) and one RNA (yeast) on dry state using a pressure cell, illustrated in **Fig. 2.12** [26]. The sample was pressed between the Pt electrodes under a pressure corresponding to  $70 \text{ kg cm}^{-2}$  and kept under a pressure of  $10^{-6}$  torr to ensure a dry environment. Plots of resistance vs temperature indicated that DNA and RNA samples have a resistivity of  $5 \times 10^{11} \Omega \text{ cm}$  at 400 K, with an energy gap of  $2.42 \pm 0.05 \text{ eV}$ .

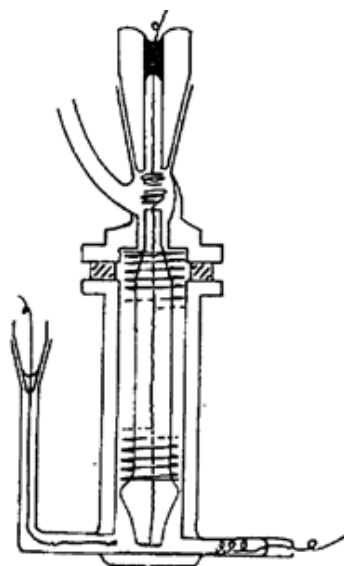


**Fig. 2.12. The pressure cell.** The upper platinum electrode is carried on a silica tube attached to a ground silica stopper. The outer vessel is a pyrex tube (thickness of 0.2 inches) and the flanges are mechanically clamped together by an intervening rubber washer (clamp is not shown). A Pt/Pt-Rh thermocouple is brought into the side of the cell via a B7 cone [30].

Following this idea, different approaches have been followed to study the electronic behaviour of DNA at the single molecule level, where a variety of techniques (indirect and direct measurements) and conditions (*i.e.* sequences, fragment lengths, humidity, salt concentration, etc.) have been studied, resulting in contradictory results. However, we group the main experiments as: *i)* Conducting and Semiconducting behaviour and, *ii)* Insulating behaviour. A summary of experimental results is presented in **Table 2.3**. Finally, some of the applications of DNA as metallized nanowires and DNA self-assembly property to produce supramolecular structures by means of DNA origami.

### 2.2.2.1 Conducting and semiconducting behaviour

Experimental research on DNA's charge transport started in the nineties, with indirect measuring techniques, using an excited donor and electron acceptor to measure rates of charge transfer. These donor and acceptor molecules can be either metals intercalated in the DNA structure [31] or organic molecules [32]–[34]. In general, it was concluded that charge-transfer rates drop off fast as the length of DNA increases (sequential tunneling mechanism), except for the metal intercalators, where these molecules appear to cooperatively bind to DNA, showing a small distance dependence rate of charge transfer (hopping mechanism) [16, 35].

Factors such as base sequence and the way of how charges were injected in the system, played a key role in these experiments. In this respect, if holes were injected into a GC pair and three G's were located in one strand, these last ones behaved as acceptors, thus charges will hop along similar G triplets in a maximum theoretical distance of 300 Å [36–39]. Nevertheless, the rate of charge transfer drops off exponentially when the number of AT pairs is increased in the sequence, where a change of charge transfer seems to be observed, with a transition from tunneling to a multistep hopping mechanism [40].

More experiments were performed using direct measurements on DNA, beginning in 1999 with the experiments of Fink and Schönemberger [41]. They managed to detect holes (positive charges) through  $\lambda$ -DNA ropes, using a Low-



Energy Electron Point Source (LEEPS) Microscope in vacuum, rendering DNA as a conductor. However, LEEPS was found to contaminate DNA and could possibly be responsible for the observed conducting behaviour in this experiment [42].

Further work using homogeneous DNA sequences, containing poly(G)-poly(C) DNA [43] pointed to DNA as a wide-bandgap semiconductor. In this experiment, a 10.4 nm long DNA (30 bp) was trapped electrostatically between two gold electrodes separated by 8 nm. Measurements were done in dry and inert environment. Note that no charges are conducted through the DNA below 1 V at room temperature, leading to a wide-bandgap semiconductor type of DNA (**Fig. 2.12**). In addition, experiments done with Transverse Scanning Tunneling Microscopy (STM) on top of DNA single molecules show that in this condition, tunneling from the DNA base pair to gold is observed, with no conduction at values between 2 V to -2 V at 78 K [44, 45].

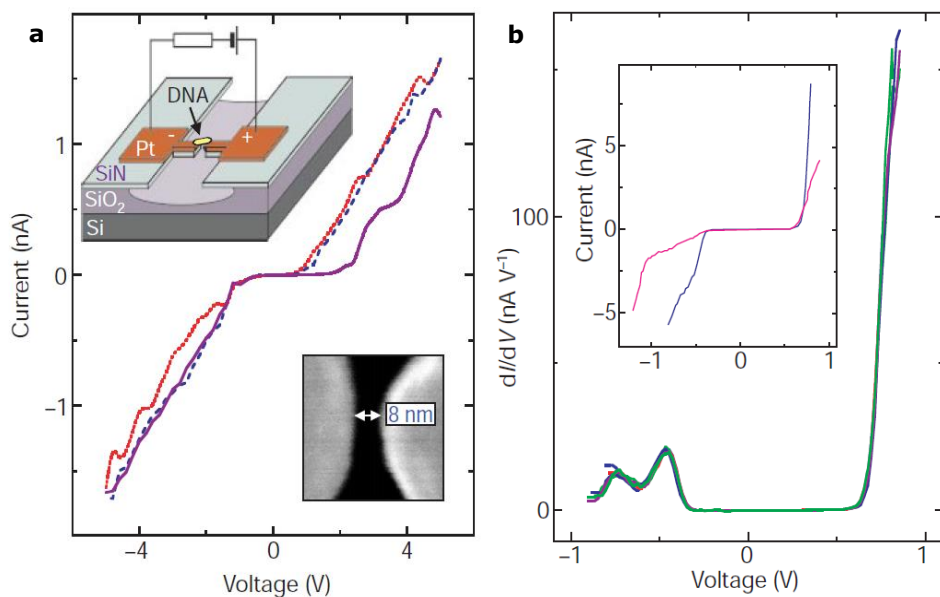


**Figure 2.12 (a)** Current-voltage curves measured at room temperature on a DNA molecule (30 bp) trapped between two metal nanoelectrodes with a separation of 8 nm. **(b)** Differential conductance  $dI/dV$  versus applied voltage  $V$  at 100 K [43].

The group of Watanabe *et al.* designed a more sophisticated experiment to measure charge transfer, using a triple-probe atomic force microscope on top of

a SiO<sub>2</sub>/Si surface (**Fig. 2.13**). This means that single DNA molecules were connected using a carbon nanotube tip and two nanotube wires (nanotweezer). I-V curves indicated that DNA is a semiconductor with a voltage gap of about 2 V [46]. Furthermore, I-V experiments by Yoo *et al.* [47] proved that poly(dA)-poly(dT) DNA displays a *n*-type of conducting behaviour. On the other hand, poly(dG)-poly(dC) DNA presents a *p*-type behaviour. Experiments have confirmed that the environmental conditions (humidity and temperature) have a direct effect on the conduction through poly(dG)-poly(dC) or poly(dA)-poly(dT) specimens [48].

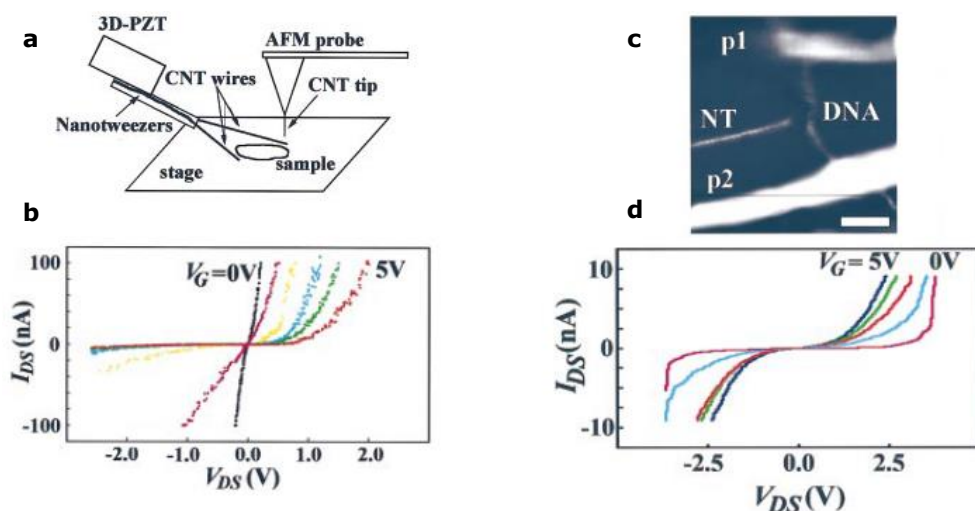


**Figure 2.13** (a) Diagram of the Triple-probe AFM setup. (b) Reference measurements on CNT ring. (c) AFM image of 1 DNA molecule contacted by the nanotweezers and AFM tip. (d) I-V curve indicates a semiconductor type of behavior [46].

Another type of experiments were performed by Cai *et al.* [49] on DNA networks, composed of poly(dG)-poly(dC) DNA, displaying a *p*-type rectifier behaviour compared to poly(dA)-poly(dT) DNA, showing much higher resistances. Lee *et al.* [50] tested the effect of oxygen hole doping on poly(dG)-poly(dC) DNA molecules, increasing its *p*-type of semiconductor behaviour. These changes were also observed for poly(dA)-poly(dT), raising its *n*-type of conductor behaviour.

In addition, Slinker *et al.* [51] measured charge transport on 34 nm DNA monolayers, assembled on top of gold electrodes and measured with an electrochemical setup. A comparison of the signal in presence of fully matched DNA compared to mismatches on the sequence, were taken as evidence on the changes of the  $\pi$ - $\pi$  orbital stack [52, 53]. Therefore a decrease in conductivity is observed for mismatches, proving that DNA can be used as a molecular wire to connect an electrode to a redox probe in this particular case.

From the biological point of view, understanding the type of charge transport through DNA could be of use to investigate base pairs damage [54–56] and repair [57]. **Figure 2.14** illustrates how DNA electron transfer could be involved on the process of repair enzymes. The first section (**Fig. 2.14a**), shows long range redox interactions that are mediated between a redox active protein and DNA  $\pi$ -stack. By means of electron transfer, one is oxidized and the other is reduced. It is known that numerous transcription factors dissociate from the DNA when their enzyme is oxidized. Thus, the enzyme could relocate to another region of the DNA, reduction and reactivation of processive scanning capabilities of this enzyme could then occur, either through diffusional contacts with the new region of DNA or search for a new DNA substrate, which would render a more efficient genome scan than a strict sequence reading. On the other hand, see **Fig 2.14b**, if there are disruptions in the base stacking, oxidation will be prevented and as a consequence, no DNA-mediated electron transfer takes place. Thus, dissociation of the enzyme will be affected. Moreover, understanding the type of DNA electron transfer could provide information on the mechanisms behind carcinogenesis and mutagenesis [58, 59].

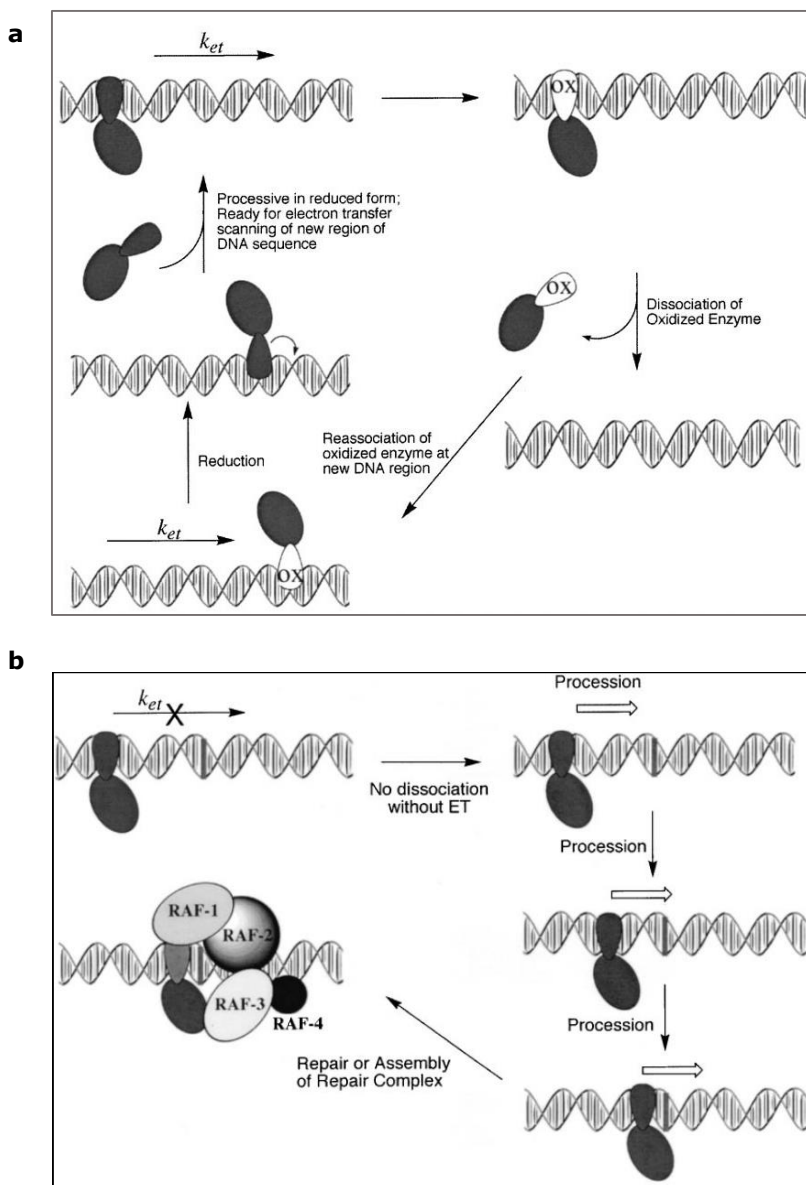


**Figure 2.14** Mechanism of DNA processing coupled with long-range electron-transfer based on sensing disruptions in  $\pi$ -stacking of DNA base pairs: **(a)** Normal base pair stacking and signaling to the redox active protein and, **(b)** Disruption in the  $\pi$ -stacking inducing changes on the signaling and DNA processing [57].

### 2.2.2.2 Insulating behaviour

Indirect measurements without contacting DNA were done, using adsorbed single-walled carbon nanotubes and DNA on different insulating substrates. Afterwards, a gold electrode was evaporated on a segment of the substrate. DNA molecules were imaged near the electrode with a scanning probe microscope tip and, after application of 1.6 V, only the carbon nanotubes were differentiated from the surface. Additional scans indicated that DNA had an insulating character [60].

The insulating characteristics of DNA were also demonstrated directly with Scanning Probe Microscopy on  $\lambda$ -DNA molecules, measured on top of a mica surface next to a gold electrode, obtaining values of  $10^4$  to  $10^6 \Omega \text{ cm}$  for DNA, confirming their previous reports [42, 60].

Moreover, some of the discrepancies and contradictory results on DNA conductivity were figured out by Kasumov *et al.* [61], where they found a correlation between the DNA experimental thickness and conductivity. If the DNA presents a thickness below 2 nm (topography measured with AFM), DNA will adopt a different structure than *B-DNA*, which may have a negative effect on the conductivity, due to changes on the base to base distance and  $\pi$ - $\pi$  orbital stacking [62].

Additional experiments have been done on 1.5  $\mu\text{m}$  long DNA molecules (thickness of 0.5 nm) on top of a  $\text{SiO}_2$  surface, from which about 10 molecules placed in parallel presented a resistance limit of 10 T $\Omega$  [63]. Finally Zhang *et al.* [64] removed all counter-ions from a thiol-modified DNA and measured it with a two-probe type of setup, reaching the conclusion that  $\lambda$ -DNA is an insulator (resistance=  $10^6 \Omega \text{ cm}$ ) (**Fig. 2.15**).

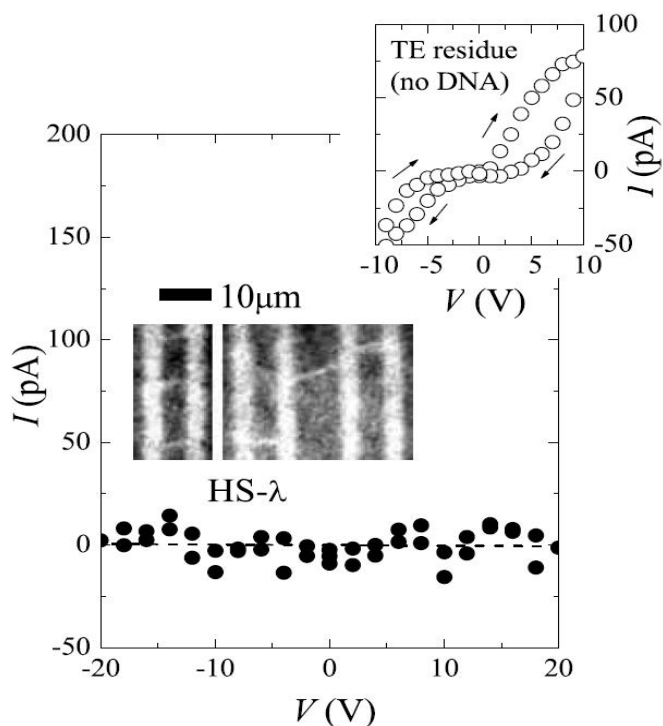


**Figure 2.15** The two-probe current vs voltage (I-V) curve for a sample of  $\lambda$ -DNA bridging 2 parallel gold electrodes separated by 4  $\mu\text{m}$  (the sample comprises  $\sim 1000$  molecules). The DNA was rinsed with ammonium acetate before the measurement to remove the buffer salt residue. The dashed line is a linear fit to the data. The inset shows the two-probe I-V curve for a test chip containing 1 x TE buffer solution (without DNA). Also, the chip was dried in vacuum but not subject to ammonium acetate rinsing. Finally, the observed conductance is entirely from trace TE salt residue. Both measurements were done in vacuum at 295 K. Open-circuit impedance between any two electrodes was always 10 T $\Omega$  [64].

**Table 2.3.** Overview of the different experimental approaches and electrical characterization of DNA.

Experiment	Technique	Nr. Molecules	Behaviour	Reference
15 bp DNA. Metal intercalators: Donor Ru(II), Acceptor Rh(III).	Luminescence Quenching.	Several molecules in solution; 5 $\mu$ M of DNA. Buffer: 50 mM NaCl.	Conductor (distances > 40 Å).	[30] (Murphy).
<i>E. coli</i> bacteriophage (better known as " $\lambda$ -DNA"); length between 600- 900 nm.	Low Energy Electron Point Source (LEEPS) Microscope. Pressure: $10^{-7}$ mbar.	Several ropes of DNA. 0.3 $\mu$ g/ml DNA deposited on sample holder and dried. Buffer: 10 mM Tris HCl, 1 mM EDTA, pH= 8	Conductor ( $\pm$ 20 mV): 2.5 M $\Omega$ for 600 nm 3.3 M $\Omega$ for 900 nm.	[40] (Fink).
$\lambda$ -DNA	Conductive AFM (I-AFM). Platinum electrode. Mica: bare or coated with pentylamine.	1-5 molecules.	Insulator for compressed DNA (height= 1.1 nm). Conductor for B-DNA (h= 2.4 nm).	[60] (Kasumov).
Calix Thymus DNA: 587-831 bp. Intercalators: Ethidium Bromide, Acridine Orange, DAP <sup>2+</sup> .	Fluorescence Quenching. Time Correlated Single Photon Counting Technique. Laser Flash Photolysis. Cyclic Voltammetry.	Several molecules in solution: 1.4 mM DNA in 5 mM phosphate buffer with 5 mM sodium sulfate.	Semiconductor (sequence tunneling $d > 10$ Å).	[31] (Brun).
Pd(II) porphyrins [cation and anion]. Calix Thymus DNA. Synthetic poly(dG-dC) <sub>2</sub> and poly(dA-dT) <sub>2</sub> .	Fluorescence Quenching. Time Correlated Single Photon Counting Technique. Laser Flash Photolysis. Time Resolved Luminescence Spectroscopy.	Several molecules in solution: 1.4 mM DNA in 5 mM phosphate buffer with 5 mM sodium sulfate.	Semiconductor (sequence tunneling $d = 13.6$ Å).	[32] (Brun).

Continue from **Table 2.3**. Overview of the different experimental approaches and electrical characterization of DNA.

Experiment	Technique	Nr. Molecules	Behaviour	Reference
<p>Acceptor: MV<sup>2+</sup>, Donor: DAP<sup>2+</sup>.</p> <p>Poly(dA)-poly(dT) and poly(dG)-poly(dC). Calf Thymus DNA.</p>	<p>Steady State Fluorescence Spectroscopy.</p> <p>Time Correlated Single Photon Counting Technique.</p>	<p>Several molecules in solution: 100 mM in 5 mM phosphate buffer, pH=7 with 5mM sodium sulfate.</p>	<p>Semiconductor (sequence tunneling, fast for intercalators at close range, <math>d \sim 10.2</math> Å).</p>	[33] (Harriman)
<p>Poly(G)-poly(C): 10.4 nm.</p>	<p>FET.</p> <p>Electrostatic Trapping molecules between electrodes.</p>	<p>1 molecule.</p> <p>Sample dried under nitrogen flow. Buffer: 30 mM NaCl, 10 mM sodium citrate and 5 mM EDTA.</p>	<p>Semiconductor (sequence tunneling <math>\pm 4V</math>).</p>	[42] (Porath).
<p>Poly(G)-poly(C): 1.2 <math>\mu\text{m}</math>.</p>	<p>STM @ 78 K. Tungsten tip.</p> <p>Gold substrate.</p> <p>180 mV applied to substrate for <math>\sim 15</math> min to attract electrostatically DNA to surface.</p> <p><math>P: 5 \times 10^{-11}</math> mbar.</p>	<p>1 molecule.</p>	<p>Semiconductor (transverse tunneling).</p>	[43] (Shapir).
<p>Salmon sperm DNA: 30-45 kbp.</p>	<p>Triple Probe AFM:</p> <ul style="list-style-type: none"> <li>- Nanotweezers (MWCNT).</li> <li>- AFM (tip MWCNT).</li> </ul> <p>SiO<sub>2</sub>/Si (100) substrate.</p> <p>Room temperature.</p> <p>Nitrogen environment.</p>	<p>1 molecule.</p> <p>Buffer: 300 mM NaCl, 10 mM sodium citrate and 5 mM EDTA.</p>	<p>Semiconductor</p>	[45] (Watanabe).



Continue from **Table 2.3**. Overview of the different experimental approaches and electrical characterization of DNA.

Experiment	Technique	Nr. Molecules	Behaviour	References
<p>Poly(dA)-poly(dT): 0.5-1.5 <math>\mu\text{m}</math>. Poly(dG)-poly(dC): 1.7-2.9 <math>\mu\text{m}</math>.</p>	<p>FET. Au/Ti electrodes. SiO<sub>2</sub>/Si substrate. Electrostatic trapping.</p>	<p>1 molecule of supercoiled DNA, folded to 100 nm between the electrodes.</p>	<p>Semiconductor (polaron Hopping): Poly(dA)-poly(dT)= N-type. Poly(dG)-poly(dC)= P-type.</p>	<p>[46] (Yoo).</p>
<p>Poly(dA)-poly(dT): 0.5-1.5 <math>\mu\text{m}</math>. Poly(dG)-poly(dC): 1.7-2.9 <math>\mu\text{m}</math>.</p>	<p>Temperature humidity chamber. FET. Au/Ti electrodes. I-V Semiconductor Parameter Analyzer. SiO<sub>2</sub> substrate.</p>	<p>Few molecules. Supercoiled molecules.</p>	<p>Poly(dG)-poly(dC) more sensitive to humidity than poly(dA)-poly(dT). Conductor to semiconductor depending on humidity: 50%= high conductor 20%= semiconductor.</p>	<p>[47] (Ha).</p>
<p>Poly(dA)-poly(dT): height of 0.8 nm. Poly(dG)-poly(dC): height of 2.1 nm.</p>	<p>I-AFM. Au tip. Au electrode. Vacuum: 10<sup>-6</sup> Torr. Mica substrate.</p>	<p>Several DNA networks.</p>	<p>Semiconductor. Better performance of poly(dG)-poly(dC) than Poly(dA)-poly(dT).</p>	<p>[48] (Cai).</p>
<p>Poly(dA)-poly(dT): 0.5-1.5 <math>\mu\text{m}</math> (flat appearance). Poly(dG)-poly(dC): 1.7-2.9 <math>\mu\text{m}</math> (rod like appearance).</p>	<p>FET. Au/Ti electrodes. Doping with oxygen gas.</p>	<p>Several (25-250 <math>\mu\text{g/ml}</math>).</p>	<p>Semiconductor. Poly(dA)-poly(dT)= N-type. Poly(dG)-poly(dC)= P-type.</p>	<p>[49] (Lee).</p>

Continue from **Table 2.3**. Overview of the different experimental approaches and electrical characterization of DNA.

Experiment	Technique	Nr. Molecules	Behaviour	References
100 bp DNA (desalted). Alkane thiol linker (6C). Nile Redox Blue attached to DNA.	Electrochemistry. Chips with Au electrodes.	DNA monolayers. 25 $\mu$ M DNA in PBS with 100 mM $MgCl_2$ .	Semiconductor (hopping mechanism).	[50] (Sinker).
17 bp DNA. Rh(III).	Photoexcitation of Rh(III) @365 nm induce oxidative damage on DNA $\rightarrow$ Analysis with 5'- <sup>32</sup> P-oligonucleotide.	Several molecules in solution. 8 $\mu$ M DNA in 25 mM ammonium acetate, pH= 9.	Semiconductor (multistep hopping mechanism). Stacking relevant for damage protection.	[51] (Hall).
Calf Thymus DNA. Dppz, Ru(II), Os (II).	Time Resolved Resonance Raman Spectroscopy.	Several molecules in solution. Buffer: 5 mM Trizma, pH= 7, 50 mM NaCl.	Semiconductor (hopping).	[52] (Chen).
Poly(dG)-poly(dC): 20 bp. Ru(II).	Flash-Quenching Technique. Laser Spectroscopy.	Several molecules in solution. 30 $\mu$ M DNA in 5mM phosphate buffer with 50 mM NaCl, pH= 8.5	Semiconductor (hopping).	[54] (Stemp).
Calf Thymus DNA. Linearized plasmid: 3430 nm length. Poly(dA)-poly(dT) Poly(dG)-poly(dC) Anthraquinone.	Circular Dichroism. AFM. Laser Spectroscopy. Phosphorescence Quenching.	Several molecules in solution. Addition of anthraquinone produce shrink of DNA to 300 nm.	Semiconductor (hopping).	[55] (Breslin).

Continue from **Table 2.3**. Overview of the different experimental approaches and electrical characterization of DNA.

Experiment	Technique	Nr. Molecules	Behaviour	References
<p><b>HeLa cells: DNA of 1.5 kbp.</b></p> <p><b>Rh(III).</b></p>	<p>Photooxidation.</p> <p>SDS-PAGE.</p>	<p>Several molecules in solution.</p> <p>50 ng/<math>\mu</math>l DNA in 5mM Tris, pH= 8 with 25 mM NaCl.</p>	<p>Semiconductor (hopping mechanism).</p> <p>Higher damage on guanine rich tracts.</p>	<p>[57] (Merino).</p>
<p><b><math>\lambda</math>-DNA= 1-15 <math>\mu</math>m.</b></p>	<p>I-AFM. Au tip.</p> <p>Au electrode.</p> <p>Mica substrate.</p> <p>Additional: LEEPS experiment-contamination.</p>	<p>1000 DNA chains.</p>	<p>Insulator (ranges up to 10 V).</p>	<p>[41] (de Pablo).</p>
<p><b>Poly(dG)-poly(dC): 40-500 nm (height: 0.5 nm).</b></p> <p><b>Thiol linker: (CH<sub>2</sub>)<sub>6</sub>SH.</b></p>	<p>AFM.</p> <p>Electrode: Au or Pt.</p> <p>SiO<sub>2</sub> or mica substrate.</p> <p>Electrostatic doping fields.</p>	<p>1 molecule.</p>	<p>Insulator.</p>	<p>[62] (Storm).</p>
<p><b><math>\lambda</math>-DNA= 1.6 <math>\mu</math>m.</b></p> <p><b>Thiol linker.</b></p>	<p>AFM.</p> <p>Au electrodes.</p> <p>High vacuum (&lt;10<sup>-7</sup> Torr).</p> <p>Quartz chips.</p>	<p>1 molecule (sample ~1000 molecules).</p> <p>Buffer 1: 5 mM ammonium acetate, pH= 6.6.</p> <p>Buffer 2: 10 mM MgSO<sub>4</sub>, 40 mM Tris-HCl, pH= 8.</p> <p>Buffer 3: 1xTE buffer (10 mM Tris, pH= 8, 1mM EDTA).</p>	<p>Insulator (ranges up to 20 V).</p> <p>Buffer 3 = semiconductor.</p> <p>DNA + Buffer 2+1= insulator.</p>	<p>[63] (Zhang).</p>

### 2.2.2.3 Applications

Due to the lack of consensus on DNA's type of electronic behaviour, a current method consists on using DNA as a template for the construction of metallized nanowires, with perspective applications for the construction of nanoelectronic devices. The first type was prepared by Braun *et al.* [65] using two gold electrodes separated by 12-16  $\mu\text{m}$  and a  $\lambda$ -DNA covered by metallic silver aggregates (silver wire) producing a conductive nanowire. Furthermore, Richter *et al.* [66] developed a highly conductive nanowire using palladium aggregates at temperature above 30 K (**Fig. 2.16**). However, the drawback that this technique presents is the production of nanowires with the same thickness and behaviour because of the difficulty to control the metal aggregates (amount) that deposit on the DNA [67]. Further developments on DNA nanowires were based on *M-DNA* structures. They are formed after *B-DNA* molecules are placed in a solution containing  $\text{Zn}^{2+}$ ,  $\text{Co}^{2+}$  or  $\text{Ni}^{2+}$  at a basic pH (pH 8), changing the electronic and physical structure of DNA [16].

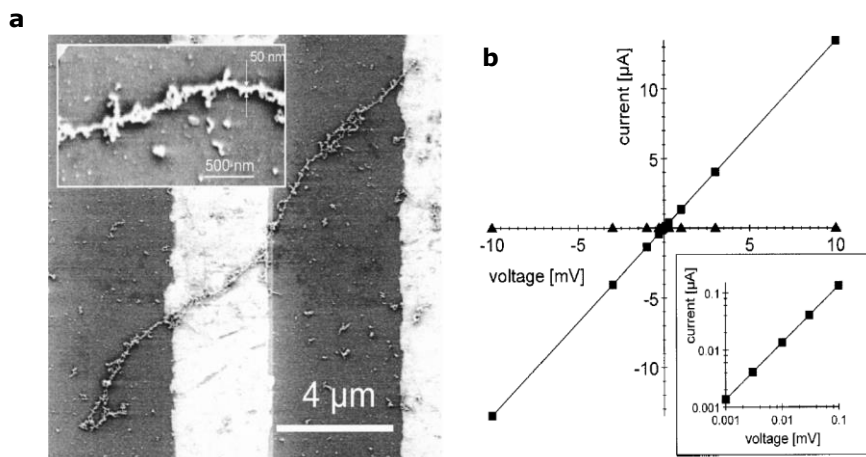


**Figure 2.16** (a) Low voltage scanning electron microscope image (1 kV) of a single palladium metallized DNA strand with a length  $\sim 16 \mu\text{m}$  corresponding to the length of a  $\lambda$ -DNA molecule. The right-hand side of the strand connects two gold electrodes over a  $\text{SiO}_2$  substrate. Inset: Magnification of the middle part with a diameter of 50 nm. (b) Two-terminal I-V curve of the single, pinned nanowire. The wire resistance is  $743 \Omega$  corresponding to a minimum estimated specific conductivity of  $\sigma_1 \approx 2 \times 10^4 \text{ S/cm}$ . Inset: ohmic I-V characteristics of the nanowire down to  $1 \mu\text{V}$ . After cutting, the sample was insulating [66].

Moreover, other applications are based on DNA's inherent property of self-assembly, which make it interesting for various scientific fields, such as molecular computation [68–70] and DNA nanotechnology (e.g. DNA origami, etc.) [71–77].

### 2.3 Conclusions

- Planar aromatic (conjugated) molecules contain  $sp^2$  type of orbitals, consisting of  $\sigma$  bonds (one plane) and  $\pi$ -orbitals that allow delocalization of electrons within the structure.
- Organic molecules with this type of delocalized bonding, have been studied as Molecular Resistors, Rectifiers, Switches and Memories and Molecular Wires.
- The analogy of the structure of DNA (*B-DNA*) with other conducting materials has raised the interest on developing experiments to unravel DNA's type of charge transport. So far, experimental approaches lack of a consensus, between conductor, semiconductor and insulator.
- Understanding DNA electronics could be of use for studies related to DNA damage, occurrence of mutations and repair mechanisms.
- Finally, an overview of the most popular applications of DNA is presented, such as DNA metallized nanowires and DNA origami.

### 2.4 References

- [1] M. B. Smith and J. March, *March's advanced organic chemistry*, 6th ed. New Jersey, U.S.: John Wiley & Sons, Inc., 2007.
- [2] J. McMurry, *Organic Chemistry*, 8th ed. Belmont, California: Brooks/Cole Cengage Learning, 2010.
- [3] R. M. Metzger, "Unimolecular electronics and rectifiers," *J. Mater. Chem.*, vol. 18, pp. 4364–4396, 2008.

- [4] H. Taube and E. S. Gould, "Organic molecules as bridging groups in electron-transfer reactions," *Acc. Chem. Res.*, vol. 2, no. 11, pp. 321–329, 1969.
- [5] L. Venkataraman, J. E. Klare, C. Nuckolls, M. S. Hybertsen, and M. L. Steigerwald, "Dependence of single-molecule junction conductance on molecular conformation," *Nature*, vol. 442, no. 7105, pp. 904–7, 2006.
- [6] B. Xu and N. J. Tao, "Measurement of single-molecule resistance by repeated formation of molecular junctions," *Science*, vol. 301, pp. 1221–3, 2003.
- [7] L. A. Bumm, J. J. Arnold, M. T. Cygan, T. D. Dunbar, T. P. Burgin, L. J. II, D. L. Allara, J. M. Tour, and P. S. Weiss, "Are single molecular wires conducting?," *Science*, vol. 271, pp. 1705–1707, 1996.
- [8] R. Breslow and S. T. Schneebeli, "Structure–property relationships in molecular wires," *Tetrahedron*, vol. 67, no. 52, pp. 10171–10178, 2011.
- [9] T. R. Kuphaldt, *Lessons in electric circuits, volume III- semiconductors*, 5th edit. Design Science License, 2009.
- [10] A. Aviram and M. A. Ratner, "Molecular rectifiers," *Chem. Phys. Lett.*, vol. 29, no. 2, pp. 591– 595, 1974.
- [11] (CSSAC) Center for Student Success and Academic Counseling, "Second substitution," *The Center for student success and academic counseling*. [Online]. Available: <https://cssac.unc.edu/programs/learning-center/Resources/Study/Guides/chemistry-261/second-substitution>. [Accessed: 13-Mar-2015].
- [12] R. M. Metzger, B. Chen, U. Höpfner, M. V. Lakshmikantham, D. Vuillaume, T. Kawai, X. Wu, H. Tachibana, T. V. Hughes, H. Sakurai, J. W. Baldwin, C. Hosch, M. P. Cava, L. Brehmer, and G. J. Ashwell, "Unimolecular electrical rectification in hexadecylquinolinium tricyanoquinodimethanide," *J. Am. Chem. Soc.*, vol. 119, no. 43, pp. 10455–10466, 1997.
- [13] W. J. Zhang, Q. F. Zhang, Y. Chai, X. Shen, and J. L. Wu, "Carbon nanotube intramolecular junctions," *Nanotechnology*, vol. 18, p. 395205, 2007.
- [14] L. D. A. Siebbeles and F. C. Grozema, *Charge and exciton transport through molecular wires*. Weinheim, Germany: Wiley-VCH Verlag and Co. KGaA, 2011.
- [15] C. P. Collier, "Electronically configurable molecular-based logic gates," *Science*, vol. 285, pp. 391–394, 1999.

- [16] M. Di Ventra and M. Zwolak, "DNA electronics," in *Encyclopedia of Nanoscience and Nanotechnology*, vol. 2, H. S. Nalwa, Ed. California, U.S.: American Scientific Publishers, pp. 475–493, 2004.
- [17] E. Chargaff, C. F. Crampton, and R. Lipshitz, "Separation of calf thymus deoxyribonucleic acid into fractions of different composition," *Nature*, vol. 172, no. 4372, pp. 289–292, 1953.
- [18] J. D. Watson and F. H. C. Crick, "Molecular structure of nucleic acids. A structure for deoxyribose nucleic acid," *Nature*, vol. 171, no. 4356, pp. 737–738, 1953.
- [19] X. J. Lu and W. K. Olson, "3DNA: A software package for the analysis, rebuilding and visualization of three-dimensional nucleic acid structures," *Nucleic Acids Res.*, vol. 31, no. 17, pp. 5108–5121, 2003.
- [20] R. E. Franklin and R. G. Gosling, "The structure of sodium thymonucleate fibres. I. The influence of water content," *Acta Crystallogr.*, vol. 6, pp. 673–677, 1953.
- [21] P. S. Ho and M. Carter, "DNA structure: Alphabet soup for the cellular soul," in *DNA Replication-Current Advances*, H. Seligmann, Ed. Intech, 2011, p. 694.
- [22] A. Ghosh and M. Bansal, "A glossary of DNA structures from A to Z," *Acta Crystallogr. - Sect. D Biol. Crystallogr.*, vol. 59, pp. 620–626, 2003.
- [23] O. T. Avery, C. M. MacLeod, and M. McCarty, "Studies on the chemical nature of the substance inducing transformation of pneumococcal types," *J. Exp. Med.*, vol. 79, pp. 137–158, 1943.
- [24] A. D. Hershey and M. Chase, "Independent functions of viral protein and nucleic acid in growth of bacteriophage," *J. Gen. Physiol.*, pp. 39–56, 1952.
- [25] G. Mendel and W. Bateson, "Experiments in plant hybridization (EN transl.)," *J. R. Hort. Soc.*, pp. 1–27, 1865.
- [26] D. D. Eley and D. I. Spivey, "Semiconductivity of organic substances. Part 9. Nucleic acid in the dry state," *Trans. Faraday Soc.*, vol. 58, pp. 411–415, 1961.
- [27] K. S. Novoselov, A. K. Geim, S. V. Morozov, D. Jiang, Y. Zhang, S. V. Dubonos, I. V. Grigorieva, and A. A. Firsov, "Electric field effect in atomically thin carbon films," *Science*, vol. 306, pp. 666–669, 2004.
- [28] A. M. van de Craats, J. M. Warman, M. P. Haas, D. Adam, J. Simmerer, D. Haarer, and P. Schuhmacher, "The mobility of charge carriers in all

- four phases of the columnar discotic material hexakis(hexylthio)triphenylene: Combined TOF and PR-TRMC results," *Adv. Mater.*, vol. 8, no. 10, pp. 823–826, 1996.
- [29] A. M. van de Craats and J. M. Warman, "The core-size effect on the mobility of charge in discotic liquid crystalline materials," *Adv. Mater.*, vol. 13, no. 2, pp. 130–133, 2001.
- [30] M. H. Cardew and D. D. Eley, "The semiconductivity of organic substances. Part 3: Haemoglobin and some amino acids," *Discuss. Faraday Soc.*, vol. 27, pp. 115–128, 1959.
- [31] C. J. Murphy, M. R. Arkin, Y. Jenkins, N. D. Ghatlia, S. H. Bossmann, N. J. Turro, and J. K. Barton, "Long-range photoinduced electron transfer through a DNA helix," *Science*, vol. 262, no. 15, pp. 1025–1029, 1993.
- [32] A. M. Brun and A. Harriman, "Dynamics of electron transfer between intercalated polycyclic molecules: Effect of interspersed bases," *J. Am. Chem. Soc.*, vol. 114, no. 10, pp. 3656–3660, 1992.
- [33] A. M. Brun and A. Harriman, "Energy- and electron-transfer processes involving palladium porphyrins bound to DNA," *J. Am. Chem. Soc.*, vol. 116, no. 9, pp. 10383–10393, 1994.
- [34] A. Harriman, "Electron tunneling in DNA," *Angew. Chemie Int. Ed.*, vol. 38, no. 7, pp. 945–949, 1999.
- [35] P. Lincoln, A. Broo, and B. Nordén, "Diastereomeric DNA-binding geometries of intercalated ruthenium(II) trischelates probed by linear dichroism:  $[\text{Ru}(\text{phen})_2\text{DPPZ}]^{2+}$  and  $[\text{Ru}(\text{phen})_2\text{BDPPZ}]^{2+}$ ," *J. Am. Chem. Soc.*, vol. 118, no. 11, pp. 2644–2653, 1996.
- [36] M. Bixon, B. Giese, S. Wessely, T. Langenbacher, M. E. Michel-Beyerle, and J. Jortner, "Long-range charge hopping in DNA," *Proc. Natl. Acad. Sci. U. S. A.*, vol. 96, no. 21, pp. 11713–11716, 1999.
- [37] M. Bixon and J. Jortner, "Energetic control and kinetics of hole migration in DNA," *J. Phys. Chem. B*, vol. 104, no. 16, pp. 3906–3913, 2000.
- [38] A. A. Voityuk, J. Jortner, M. Bixon, and N. Rösch, "Electronic coupling between Watson–Crick pairs for hole transfer and transport in desoxyribonucleic acid," *J. Chem. Phys.*, vol. 114, no. 13, p. 5614, 2001.
- [39] F. C. Grozema, Y. A. Berlin, and L. D. A. Siebbeles, "Mechanism of charge migration through DNA: Molecular wire behavior, single-step tunneling or hopping?," *J. Am. Chem. Soc.*, vol. 122, no. 44, pp. 10903–10909, 2000.



- [40] Y. A. Berlin, A. L. Burin, and M. A. Ratner, "Elementary steps for charge transport in DNA: Thermal activation vs. tunneling," *Chem. Phys.*, vol. 275, pp. 61–74, 2002.
- [41] H.-W. Fink and C. Schönberger, "Electrical conduction through DNA molecules," *Nature*, vol. 398, pp. 407–410, 1999.
- [42] P. J. De Pablo, F. Moreno-Herrero, J. Colchero, J. Gómez Herrero, P. Herrero, a. M. Baró, P. Ordejón, J. M. Soler, and E. Artacho, "Absence of dc-conductivity in  $\lambda$ -DNA," *Phys. Rev. Lett.*, vol. 85, pp. 4992–4995, 2000.
- [43] D. Porath, A. Bezryadin, S. de Vries, and C. Dekker, "Direct measurement of electrical transport through DNA molecules," *Nature*, vol. 403, pp. 635–638, 2000.
- [44] E. Shafir, H. Cohen, A. Calzolari, C. Cavazzoni, D. a Ryndyk, G. Cuniberti, A. Kotlyar, R. Di Felice, and D. Porath, "Electronic structure of single DNA molecules resolved by transverse scanning tunneling spectroscopy.," *Nat. Mater.*, vol. 7, pp. 68–74, 2008.
- [45] D. A. Ryndyk, E. Shafir, D. Porath, A. Calzolari, R. Di Felice, and G. Cuniberti, "Scanning tunneling spectroscopy of single DNA molecules," *ACS Nano*, vol. 3, no. 7, pp. 1651–6, 2009.
- [46] H. Watanabe, C. Manabe, T. Shigematsu, K. Shimotani, and M. Shimizu, "Single molecule DNA device measured with triple-probe atomic force microscope," *Appl. Phys. Lett.*, vol. 79, no. 15, pp. 2462–2464, 2001.
- [47] K.-H. Yoo, D. Ha, J.-O. Lee, J. Park, J. Kim, J. Kim, H.-Y. Lee, T. Kawai, and H. Choi, "Electrical conduction through poly(dA)-poly(dT) and poly(dG)-poly(dC) DNA Molecules," *Phys. Rev. Lett.*, vol. 87, no. 19, p. 198102, 2001.
- [48] D. H. Ha, H. Nham, K.-H. Yoo, H. So, H.-Y. Lee, and T. Kawai, "Humidity effects on the conductance of the assembly of DNA molecules," *Chem. Phys. Lett.*, vol. 355, pp. 405–409, 2002.
- [49] L. Cai, H. Tabata, and T. Kawai, "Self-assembled DNA networks and their electrical conductivity," *Appl. Phys. Lett.*, vol. 77, no. 19, p. 3105, 2000.
- [50] H.-Y. Lee, H. Tanaka, Y. Otsuka, K.-H. Yoo, J.-O. Lee, and T. Kawai, "Control of electrical conduction in DNA using oxygen hole doping," *Appl. Phys. Lett.*, vol. 80, no. 9, p. 1670, 2002.
- [51] J. D. Slinker, N. B. Muren, S. E. Renfrew, and J. K. Barton, "DNA charge transport over 34 nm.," *Nat. Chem.*, vol. 3, no. 3, pp. 228–33, 2011.

- [52] D. B. Hall and J. K. Barton, "Sensitivity of DNA-mediated electron transfer to the intervening  $\pi$ -stack: A probe for the integrity of the DNA base stack.," *J. Am. Chem. Soc.*, vol. 119, no. 21, pp. 5045–5046, 1997.
- [53] W. Chen, C. Turro, L. A. Friedman, J. K. Barton, and N. J. Turro, "Resonance Raman investigation of Ru(phen)<sub>2</sub>(dppz)<sup>2+</sup> and related complexes in water and in the presence of DNA," *J. Phys. Chem. B*, vol. 101, no. 35, pp. 6995–7000, 1997.
- [54] S. Steenken, "Purine bases, nucleosides, and nucleotides: Aqueous solution redox chemistry and transformation reactions of their radical cations and e<sup>-</sup> and OH adducts," *Chem. Rev.*, vol. 89, pp. 503–520, 1989.
- [55] E. D. A. Stemp, M. R. Arkin, and J. K. Barton, "Oxidation of guanine in DNA by Ru(phen)<sub>2</sub>(dppz)<sup>3+</sup> using the flash-quench technique," *J. Am. Chem. Soc.*, vol. 119, pp. 2921–2925, 1997.
- [56] D. T. Breslin, J. E. Coury, J. R. Anderson, L. McFail-Isom, Y. Kan, L. D. Williams, L. A. Bottomley, and G. B. Schuster, "Anthraquinone photonuclease structure determines its mode of binding to DNA and the cleavage chemistry observed," *J. Am. Chem. Soc.*, vol. 119, no. 21, pp. 5043–5044, 1997.
- [57] S. R. Rajski, B. A. Jackson, and J. K. Barton, "DNA repair: Models for damage and mismatch recognition.," *Mutat. Res.*, vol. 447, no. 1, pp. 49–72, 2000.
- [58] E. J. Merino, M. L. Davis, and J. K. Barton, "Common mitochondrial DNA mutations generated through DNA-mediated charge transport," *Biochemistry*, vol. 48, no. 4, pp. 660–666, 2009.
- [59] P. K. Bhattacharya and J. K. Barton, "Influence of intervening mismatches on long-range guanine oxidation in DNA duplexes," *J. Am. Chem. Soc.*, vol. 123, no. 36, pp. 8649–8656, 2001.
- [60] C. Gómez-Navarro, A. Gil, M. Álvarez, P. J. De Pablo, F. Moreno-Herrero, I. Horcas, R. Fernandez-Sanchez, J. Colchero, J. Gómez-Herrero, and M. A. Baró, "Scanning force microscopy three-dimensional modes applied to the study of the dielectric response of adsorbed DNA molecules," *Nanotechnology*, vol. 13, p. 314, 2002.
- [61] A. Y. Kasumov, D. V. Klinov, P.-E. Roche, S. Guéron, and H. Bouchiat, "Thickness and low-temperature conductivity of DNA molecules," *Appl. Phys. Lett.*, vol. 84, no. 6, pp. 1007–1009, 2004.
- [62] B. Song, M. Elstner, and G. Cuniberti, "Anomalous conductance response of DNA wires under stretching.," *Nano Lett.*, vol. 8, no. 10, pp. 3217–20, 2008.

- [63] A. J. Storm, J. Van Noort, S. De Vries, and C. Dekker, "Insulating behavior for DNA molecules between nanoelectrodes at the 100 nm length scale," *Appl. Phys. Lett.*, vol. 79, no. 2001, pp. 3881–3883, 2001.
- [64] Y. Zhang, R. H. Austin, J. Kraeft, E. C. Cox, and N. P. Ong, "Insulating behavior of lambda-DNA on the micron scale," *Phys. Rev. Lett.*, vol. 89, p. 198102, 2002.
- [65] E. Braun, Y. Eichen, U. Sivan, and G. Ben-Yoseph, "DNA-templated assembly and electrode attachment of a conducting silver wire," *Nature*, vol. 391, pp. 775–778, 1998.
- [66] J. Richter, M. Mertig, W. Pompe, I. Mönch, and H. K. Schackert, "Construction of highly conductive nanowires on a DNA template," *Appl. Phys. Lett.*, vol. 78, no. 4, pp. 536–538, 2001.
- [67] C. Erler, K. Günther, and M. Mertig, "Photo-induced synthesis of DNA-templated metallic nanowires and their integration into micro-fabricated contact arrays," *Appl. Surf. Sci.*, vol. 255, pp. 9647–9651, 2009.
- [68] L. M. Adleman, "Molecular computation of solutions to combinatorial problems," *Science*, vol. 266, no. 5187, pp. 1021–1024, 1994.
- [69] M. Ogihara and A. Ray, "Simulating boolean circuits on a DNA computer," *Algorithmica*, vol. 25, pp. 239–250, 1999.
- [70] Y. Benenson, B. Gil, U. Ben-Dor, R. Adar, and E. Shapiro, "An autonomous molecular computer for logical control of gene expression," *Nature*, vol. 429, no. 6990, pp. 423–429, 2004.
- [71] N. C. Seeman, "Nucleic acid junctions and lattices," *J. Theor. Biol.*, vol. 99, pp. 237–247, 1982.
- [72] P. W. K. Rothemund, "Folding DNA to create nanoscale shapes and patterns," *Nature*, vol. 440, pp. 297–302, 2006.
- [73] N. C. Seeman, "Biochemistry and structural DNA nanotechnology: An evolving symbiotic relationship," *Biochemistry*, vol. 42, no. 24, pp. 7259–7269, 2003.
- [74] W. B. Sherman and N. C. Seeman, "A precisely controlled DNA biped walking device," *Nano Lett.*, vol. 4, no. 9, pp. 1801–1801, 2004.
- [75] H. Zhong and N. C. Seeman, "RNA used to control a DNA rotatory nanomachine," *Nano Lett.*, vol. 6, no. 12, pp. 2899–2903, 2006.

- 
- [76] L. A. Yatsunyk, O. Mendoza, and J. L. Mergny, "Nano-oddities': Unusual nucleic acid assemblies for DNA-based nanostructures and nanodevices," *Acc. Chem. Res.*, vol. 47, pp. 1836–1844, 2014.
- [77] B. Albinsson, J. K. Hannestad, and K. Börjesson, "Functionalized DNA nanostructures for light harvesting and charge separation," *Coord. Chem. Rev.*, vol. 256, no. 21–22, pp. 2399–2413, 2012.

## Chapter 3

### Charge Transport in DNA

Experimental information on DNA charge migration, separation, shift and recombination are focused on hole (positive ion) transfer and /or transport in solution [1]–[22], models that will be presented in on section 3.1. Mainly, the process of charge transport consists of charge transfer from the hole acceptor to the electronically excited (or positively charged) hole donor. Furthermore, there are two conventional mechanisms where charges can be transferred in DNA: *i*) sequential tunneling and *ii*) multistep hopping.

#### 3.1 Theoretical framework

Few years after the structural elucidation of DNA in 1959, Pullman and Pullman [1] used a quantum chemistry model to calculate the energy corresponding to the molecular orbitals on either G-C pairs or A-T pairs. Some of the parameters taken into account were the resonance energy and complementary stabilization (hydrogen bond). From these data, G-C pairs had better electron donor and acceptor characteristics than A-T pairs.

This was confirmed by Steenken [2] with his experiments using redox chemistry on DNA nucleotides, where he concluded that radical cations are trapped by the purines, particularly the guanine moiety. In addition, he observed that when DNA is subject of irradiation there is not an equal distribution for C, G, A, T radicals, due to the fast electron transfer taking place from base to base along the helix, even faster than the proton transfer (**Fig. 3.1**).

With the increase of experimental data on DNA charge transfer, researchers were able to formulate an empirical relation between the rate of electron transfer ( $k_{ET}$ ) and distance (which has an exponential dependence on the electronic coupling), defined in **Eq. 3.1** [24]:

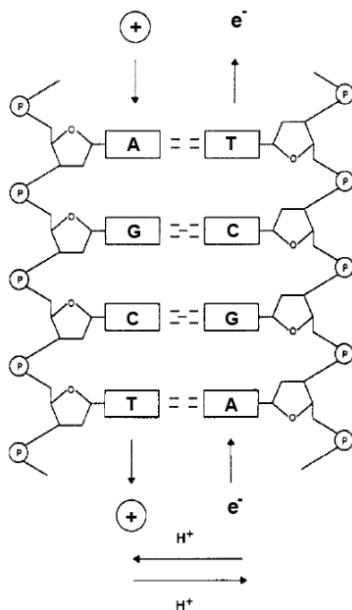


**Fig. 3.1.** Competition between electron transfer and proton transfer. Quantum chemical methods estimate that the electron transfer in DNA is of the order of  $10^{14} \text{ s}^{-1}$  [23]. (Image taken from [2]).

$$k_{\text{ET}} \propto \exp[-\beta(R-R_0)] \quad (\text{Equation 3.1})$$

Where  $R_0$  is the donor-acceptor distance by  $\beta$  is the fall-off parameter. However, discrepancies on values obtained between different groups indicated that **Eq. 3.1** was unable to cope with more realistic parameters. As a matter of fact, some of the drawbacks that prevent the use of Marcus theory to study Electron Transfer in DNA are [22]:

- i) It assumes that charges are localized in one fragment.
- ii) Prior knowledge if a process is adiabatic or non-adiabatic is required.
- iii) Difficulty to obtain accurate reorganization energies.

Therefore, Priyadarshy *et al.* [3] developed a model based on donor-bridge-acceptor to account for long range electron transfer in DNA (bridge= DNA). First, a weak donor-acceptor interaction is established in:

$$k_{ET} = \frac{2\pi}{\hbar} |T_{DA}|^2 (FWCDS)$$

Where  $T_{DA}$  is the electronic coupling matrix element, FWCDS is the Franck-Condon weighted density of states (FWCDS) and,  $\hbar$  is the Planck's constant divided by  $2\pi$ . Moreover, FWCDS depends on the reaction driving force ( $-\Delta G^0$ ), nuclear reorganization energy ( $\lambda$ ) and on the temperature.

$$T_{DA}(E_{Tun}) = \sum_{d,i,j,a} c_d^* v_{d,i} G_{ij}(E_{Tun}) v_{j,a} c_a$$

$$G_{ij}(E_{Tun}) = \sum_n \frac{c_i^n c_j^*}{E_n - E_{Tun}}$$

Here,  $d$  and  $a$  are the sum of the atomic orbitals of donor and acceptor respectively,  $i$  and  $j$  sum over the atomic orbitals of the bridge and,  $n$  sums over the bridge molecular orbitals. Particularly,  $c_i^n$  is the bridge wave function amplitude for atomic orbital  $i$  in the molecular orbital  $n$ . In addition,  $v_{d,i}$  is the interaction element between atomic orbital  $d$  on the donor and  $i$  of the bridge,  $c_d(c_a)$  is the donor (acceptor) wave function amplitude on atomic orbital  $d$  ( $a$ ). Finally  $G_{ij}(E_{Tun})$  is an intrinsic conductivity property of the bridge. Furthermore, Priyadarshy and coworkers concluded on two factors that influence ET rates in this system are:

- i) The strength of donor-acceptor coupling ( $T_{DA}$ ), which depends on orbital energetics, orbital symmetry and separation distance.
- ii) Activation energy of the reaction, that depends on the reaction free energy and reorganization energy.

The fact that different  $\beta$  values were experimentally obtained for DNA, forced researchers to evaluate their experiments with the two most widely accepted charge transfer mechanisms in DNA [5]:

- i) Unistep charge transfer between donor-acceptor sites, involving DNA nucleobases as superexchange-mediators ( $\beta = 0.5-1.5 \text{ \AA}^{-1}$ ).

- ii) Multistep hopping-type of charge transport between the redox centers along the nucleobases forming the bridge ( $\beta = 0.01-0.1 \text{ \AA}^{-1}$ ).

In this context, Meggers *et al.* [4] reported a multistep hopping process between G bases along a mixed strand of DNA (heterogeneous sequences). **Fig. 3.2** illustrates the construction of the sequence, where a guanine radical cation ( $G^{+\bullet}$ ) is at one side and a guanine triplet (GGG) at the other side. Thus, the individual "steps" contribute to the overall rate. Also, the content of AT pairs in between the "steps" renders a decrease on the rates. Finally, the calculated  $\beta$  value was  $0.7 \text{ \AA}^{-1}$  for a maximum  $G^{+\bullet}$  distance of  $17 \text{ \AA}$ .

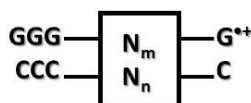


**Fig. 3.2.** Representation of the sequence, where "N" are the AT pair and subindex "m" ranges from 1 to 4.  $N_n$  represents the AT complementary pair [4].

Furthermore, Bixon and coworkers [5, 6] modelled DNA duplexes with a similar sequence as above, using a kinetic scheme (**Fig. 3.3**), where both types of charge transfer were evaluated (unistep charge transfer and multistep charge hopping).

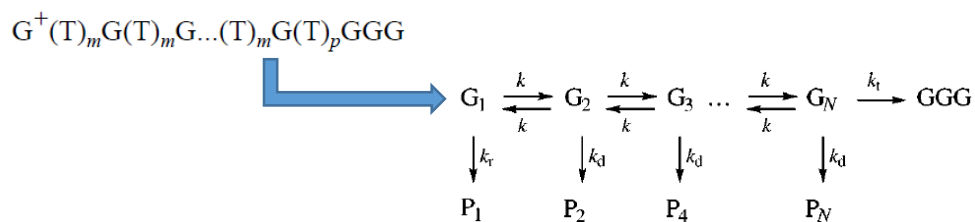


**Fig. 3.3. Sequence and kinetic scheme.** Initial formation of  $G_1^+$  followed by the reversible hole hopping with a rate  $k$  between nearest-neighbour G bases, separated by  $m$  T or A bases ( $m= 1-3$  and  $p= 1-4$ ). The process is terminated by hole trapping from  $G^+$  at GGG with a rate  $k_t$  [5].

As a result, Bixon *et al.* [6] formulated the features that influence the implementation of one or another model, based on experimental data:



- i) Donor-bridge energetic separation. Distinct donors generate different energetics, thus for unistep charge transfer we expect a positive energy gap between the donor and the bridge ( $\Delta E > 0$  and off-resonance coupling), and for multistep hopping a negative gap ( $\Delta E < 0$  and resonance coupling).
- ii) Intrabridge energetics involving the relative energies of the bases within the bridge. For example, **Fig. 3.4** illustrate how T bases are off-resonance relative to the G bases, with a large  $G^+T = GT^+$  energy gap ( $\delta E = 0.6$  eV).

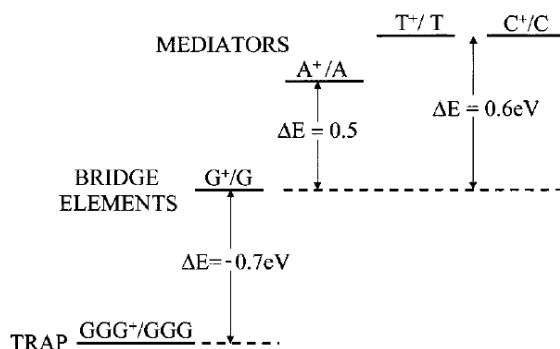


**Fig. 3.4.** Energetics of the guanine bridge elements, the superexchange mediators (T, A, C) and the trap of a triple GGG unit. The energetic data for the nucleobases rest on the redox potential data in solution, assuming that the energy differences are maintained in DNA. The energy of the triple GGG is based on theoretical calculations of ionizations potentials [6].

An improvement to the earlier theoretical work was the use of a tight-binding Hamiltonian, where additional terms can be adjusted, such as dynamic disorder or a dissipative environment (*e.g.* conductance measurements of DNA in aqueous solution). Dynamic disorder takes into account fluctuations that cause dephasing on the tight-binding Hamiltonian. If the system would be perfectly ordered without these fluctuations, we would expect to observe a unistep charge transfer (or sequential tunneling) [8, 9, 17–20]. In particular Grozema *et al.* [8, 9] analysed donor-DNA-acceptor systems with similar sequences as **Figs. 3.2-3**, implementing the tight binding approximation adjusted with dynamic disorder.

They concluded that charge migration in sequences containing only AT base pairs is determined by the difference in ionization potential (*e.g.* injection barrier) between the donor and the AT pairs. As a consequence, if the injection barrier is 0.55 eV, a sequential tunneling process will take place but at lower injection barriers, more charge density will be expected on the bridge (thus a multistep hopping mechanism will be favored). Besides, at injection barriers of 0.55 eV, sequences with a majority of GC pairs will display a multistep hopping mechanism opposite to sequences containing higher amount of AT pairs, where a sequential tunneling mechanism is foreseen. Finally, calculations on poly(G)-poly(C) duplexes taking into account dynamic and static fluctuations indicated that hole mobilities in DNA will be  $0.1 \text{ cm}^2\text{V}^{-1}\text{s}^{-1}$  [9]. This model has also been tested as well for stilbene-DNA hairpins [10, 11], 25].

Additional studies on the radical cation reactivities [12] and type of charge migration through short and long range distances [14, 17, 18, 20–22, 26–29] have reach an agreement:

- i) For heterogeneous DNA sequences, the main charge involved in charge migration will be holes. In particular, oxidation of guanines (radical cations) will favour multistep charge hopping over long distances.
- ii) Local measurements on DNA are dependent on the base pairs orientation with respect to the substrate (symmetric or asymmetric I-V curves). If the Fermi level of the substrate falls in between the energy levels of the DNA (*e.g.* HOMO and HOMO-1 level of guanine), then changes on the shape of DNA conductance can be expected.
- iii) Structural fluctuations and overstretching may interfere with the  $\pi$ -stack and base-base distances, thus disturbing charge migration. Direct measurements on DNA may also induce structural rearrangements.

### 3.2 Sequential tunneling (unistep charge transfer or coherent tunneling)

The general concept of single step tunneling or coherent tunneling implies that all interactions with the environment are omitted. In this case, the Hamiltonian alone governs the system dynamics, where the motion of a particle is described on the basis of a low-dimensional Hilbert space [30].

It is important to mention that treating DNA as a molecular wire differs from a metal wire in the sense that metals have partially empty valence bands, while DNA has a filled valence band and a large gap separating the filled valence and empty conduction band of the system. This would be the case if we model DNA as an insulator or poor semiconductor.

Generally, this type of mechanism implies that charge can tunnel through a whole length of DNA. Thus, the charge wavefunction does not lose phase coherence and has strong distance dependence. In DNA, it can be assumed that charge can coherently tunnel through the entire length of DNA, with a rate of charge transfer,  $k_{ET}$ , given in **Eq. 3.2** [24]:

$$k_{ET} = k_0 \exp^{-\beta R} \quad (\text{Equation 3.2})$$

Here  $R$  is the length of the DNA molecule and  $\beta$  is the tunneling decay length. A large value of  $\beta$  means that the rate of tunneling will decrease rapidly with increasing distance. From theoretical studies, coherent tunneling is expected to drop off dramatically with distance for DNA. Therefore, a large  $\beta$  value ( $\approx 1 \text{ \AA}^{-1}$ ) represents a single step tunneling process, while a small value for  $\beta$  ( $\approx 0.1 \text{ \AA}^{-1}$ ) indicates that the electron transfer rate depends weakly on the distance between the donor and the acceptor (hopping mechanism) [10, 31].

More in detail, sequential tunneling is mainly used to study charge transfer in donor-DNA-acceptor systems, using a semiclassical electron transfer (ET) theory. **Eq. 3.3** gives the rate of ET ( $k_{ET}$ ) in terms of three key parameters: i)  $H_{AB}$ , the electronic coupling between the donor and acceptor groups, ii)  $\lambda$ , the

reorganization energy needed to reposition the nuclei of the ET products and of the DNA and solvent surrounding them after the ET event and, iii)  $\Delta E$ , the energy of the ET reaction [32].

$$k_{ET} = \frac{2\pi^{3/2}H_{AB}^2}{h} \left(\frac{1}{\lambda kT}\right)^2 \exp\left[-\frac{(\Delta E + \lambda)^2}{4\lambda kT}\right] \quad (\text{Equation 3.3})$$

Within **Eq. 3.3**,  $h$  is the Planck constant,  $k$  is the Boltzmann constant and  $T$  is the absolute temperature. When the donor-to-acceptor distance increases,  $\lambda$  should increase as well. The focus on this approximation will be the  $H_{AB}$  term, which is expected to decay exponentially with increase of the donor-to-acceptor separation. It can be understood simply by analogy to the decay of electron tunneling probability through a one dimensional square barrier as the barrier thickness is increased. In a molecular donor-acceptor ET problem, the increase in barrier thickness arises from a decrease in donor-acceptor orbital overlap as the separation distance increases. The exponential decay of electronic coupling as a function of the edge-to-edge donor-acceptor separation  $r$  is then defined in **Eq. 3.4**.

$$H_{AB}(r) = H_{AB}^0 \exp\left[-r\frac{\beta}{2}\right] \quad (\text{Equation 3.4})$$

with  $H_{AB}^0$  as the electronic coupling when the donor and acceptor are in contact ( $r = 0$ ). The key question in ET studies on DNA is about the value of electronic coupling decay parameter,  $\beta$  [32].

Experimental data on this coupling decay parameters have been obtained, with  $\beta$  values of  $< 0.2$  [33],  $0.65$  [34] and  $1 \text{ \AA}^{-1}$  [35]. If we postulate an electron transfer time of  $0.1 \text{ ps}$  for a given donor-acceptor brought in contact, then for a  $40 \text{ \AA}$  donor-acceptor separation the respective transfer times with the given  $\beta$ , would be of  $< 300 \text{ ps}$ ,  $13 \text{ ms}$  and  $6.5 \text{ h}$ . Closer evaluation of the data indicates that the value of  $0.64 \text{ \AA}^{-1}$  is the most reliable for a donor-DNA-spacer system, obtained on five different hairpin duplexes coupled to stilbene moieties [8, 10, 36, 37].

Note that in **Eq. 3.3**,  $k_{ET}$  depends on the square of  $H_{AB}$  and it depends on the overlap of the donor and acceptor wave functions. For calculations on long-range electron transfer between a donor-DNA-acceptor,  $H_{AB}$  can be seen as the interaction of donor and acceptor orbitals, with the intervening bridge orbitals summed over all occupied and unoccupied molecular orbitals of the bridge. Also, the interaction of the bridge orbitals is relevant because they can also provide information on the virtual ionic states of the DNA bridges and of the reaction tunneling energies ( $E_{tun}$ ). Consequently, when kinetic studies of ET in DNA duplexes make use of donors and acceptors that are chemically different from the DNA bases,  $\beta$  values will be  $\sim 1 \text{ \AA}^{-1}$ .

In addition, Steenken *et al.* [2] determined the nucleoside oxidation potentials, where  $dG(-H)^{\bullet}$  and  $dA(-H)^{\bullet}$  were reduced in water at pH 7 with the addition of a proton at 1.29 and 1.42 V, respectively (versus Standard Calome Electrode, SCE), yielding a 130 mV separation of the oxidation potentials corresponding to dG and dA. When these oxidation potentials are combined with the reduction potential of stilbene and its excited state energy, it yields free energies ( $\Delta G$ , replacing  $\Delta E$  in **Eq. 3.3**) of ET with values of -0.21 and -0.08 eV respectively. Therefore, the reaction for hairpins coupled with stilbene is thermodynamically favorable at pH 7 (**Fig. 3.5**), where the tunneling-gap energy of ET transfer reactions is smaller compared to other experiments [33, 38, 39].

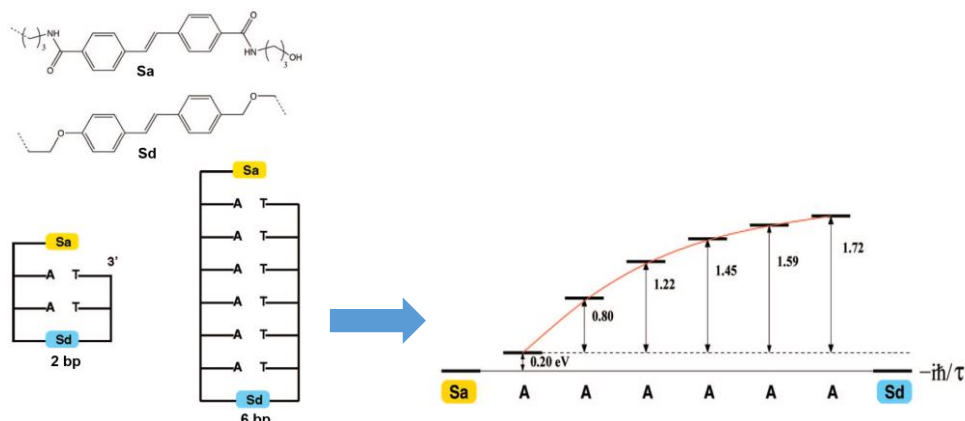


**Fig. 3.5.** Representation of the stilbene acceptor and donor moieties (Sa and Sd), and how they are linked to DNA hairpins. The graph represents the energetics associated to DNA hairpins. The red line indicates the Coulomb well from which the charge has to escape in order to move away from the hole donor [10].

To summarize, from **Eq. 3.3**, the rate of long-distance ET reaction ( $k_{ET}$ ) depends on three key parameters: *i*) the electronic coupling,  $H_{AB}$ , *ii*) the free energy of the reaction  $\Delta G \approx \Delta E$ , and *iii*) the nuclear reorganization energy,  $\lambda$ . In order to study ET rates,  $\lambda$  is minimized if the initially reduced or oxidized DNA base is allowed to transfer its excess electron or hole to a distant trap. The use of photoreductants or photooxidants covalently attached to DNA bases, allow this type of studies to be sufficiently long-lived [32].

### 3.2.1 Steady states for sequential tunneling

Another approach to study sequential tunneling is offered in this section, with a possible application to our experimental system described in detail in Chapter 7. This approach is using a steady state formulation of the electron-transfer rate problem, and under certain conditions the rate of steady state phases ( $k_{ss}$ ) provides a good estimate of the rate associated with the long-time tail of the electron transfer process following an excitation. On the other hand, steady-state experiments can be performed using current vs imposed electrostatic voltage data. Next, a relationship between  $k_{ss}$  related to a given molecular bridge and the conductance of a junction based on the same molecule can be established. For this case, the "donor" and "acceptor" levels should be thought of as the Fermi energies for the metal junctions on the two sides of the molecular bridge. With the use of the Landauer formula (**Eq. 3.5**) [40], a relation between the transmission coefficients  $T$  for a free particle that enter the junction from the left, say, to emerge on the right and the junction conductance  $g$  is shown [41].

$$g = \frac{e^2}{\pi h} T(E_F) \quad (\text{Equation 3.5})$$

Here  $E_F$  is the Fermi energy of the metal junction at zero bias. In order to compute this coefficient, the non-equilibrium Green function (NEGF) approach can be used [42]. Taking into account that DNA contains a large number of atoms, it is more appropriate to use a tight-binding Hamiltonian model to calculate the transmission coefficient. Assuming that DNA is a HOMO type of conductor, each HOMO base pair is included. These levels can be considered

isoenergetic, with an energy of  $\sim E_{bp} = -2$  eV. This energy roughly corresponds to the difference between the ionization potential (IP) of the adenine (IP = 7.62 eV) or guanine (6.84 eV) and the Fermi energy of gold at about  $E_F = 5$  eV [12, 42].

Moreover, **Fig. 3.6** illustrates the parameters that must be defined in the model to compute the transmission coefficient: *i*) the electronic coupling between neighbouring base pairs, (e.g.  $V_{bp} = 50$  meV) in agreement with electronic structure calculations [10]; *ii*) the energy of the acceptor (e.g.  $E_f$ ); *iii*) the coupling between the terminal base pair and the neighbouring acceptor ( $V_f = 5$  meV) and, *iv*) a self energy  $\Gamma$  to simulate the tip contact with the base pair in a similar way as a coupling with the electrodes, **Eq. 3.5**.

$$T(E) = Tr[\Gamma_S g(E) \Gamma_T G^\dagger(E)] \quad (\text{Equation 3.6})$$

$\Gamma_{S/T}$  represents the coupling between the DNA and the surface/tip and  $g(E) = (E - H + i0^+)^{-1}$  is the Green function of the DNA with  $H$  its model Hamiltonian.

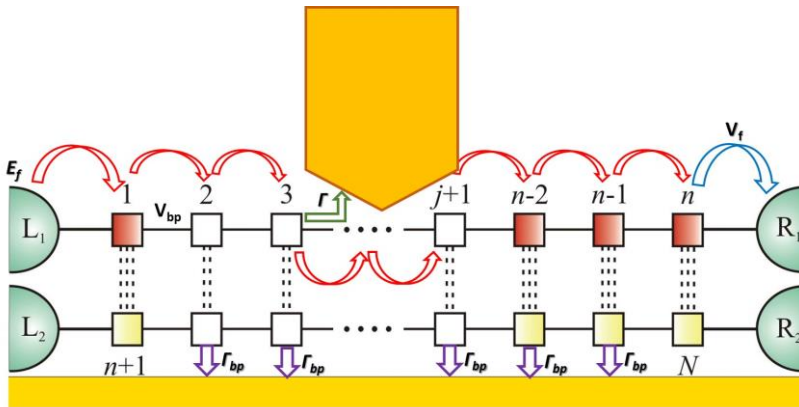


**Figure 3.6.** Scheme representing the parameters involved in sequential tunneling charge migration through a DNA bridge, where L1 and R1 represent the donor or acceptor moieties and an electrode tip is incorporated in the model as an acceptor or donor group, for comparison with experimental calculations [43].

### 3.3 Multistep Hopping

Different from sequential tunneling, this mechanism has a weak distance dependence of charge migration. It also involves the relative energies of the nucleobases in the bridge. For hole hopping, the positive charge will be mainly located on the guanines, which is the nucleobase with the lowest oxidation potential compared to adenine ( $\sim 0.4$  eV) and values are already experimentally confirmed [4].

Multistep charge transport between the nucleobases of the bridge is performed under the conditions of resonant donor-bridge-coupling. The lowest vibronic state of the donor is in resonance with the vibronic manifolds of some nucleobases of the DNA bridge. These charged nucleobases constitute genuine chemical intermediates, which can be observed by time-resolved spectroscopy, or participate in chemical reactions with the solvent. The hopping mechanism can be specified in terms of a random walk model, which results in a weak algebraic distance dependence of the lifetime for charge transport [5], shown in **Eq. 3.6**.

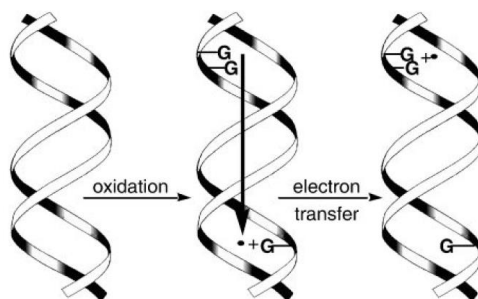
$$\tau_{CT} \approx k_{hop}^{-1} N^\eta \quad (\text{Equation 3.6})$$

Here  $k_{hop}$  is the hopping rate,  $N$  is the number of specific bases participating in the charge transport, and  $\eta = 1-2$  (for acceptor-direction biased random walk process [44]). These features of hopping permit long-range charge transport. Moreover for practical reasons, the nucleic bases will be denoted G, guanine; A, adenine; T, thymine and; C, cytosine. The multistep hole hopping mechanism for donor-bridge coupling was studied by Giese *et al.* [4] confirmed that hole hopping occurs via the guanines within a single GTTGTTG...TTGGG strand, which is trapped by a triple GGG (**Fig. 3.7**).

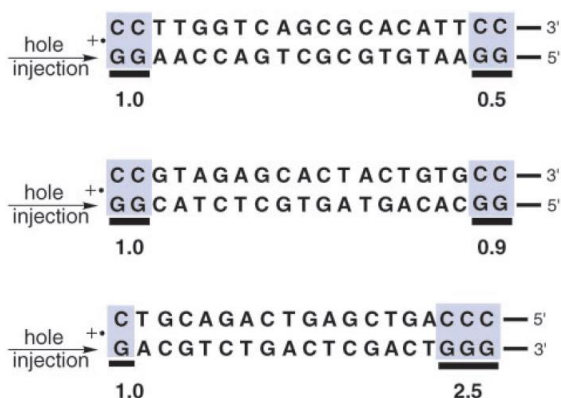
This hole hopping has also been observed via GG groups in both strands [45]. An additional element of energetic control to the charge hopping mechanism is the intrabridge energetic control that involves the relative energies of the nucleobases within the bridge. In strands containing G, hole hopping is



expected, where the intrabridge energetic control of the positive charge will be located exclusively on the G (lower oxidation potential) (**Fig. 3.8**).



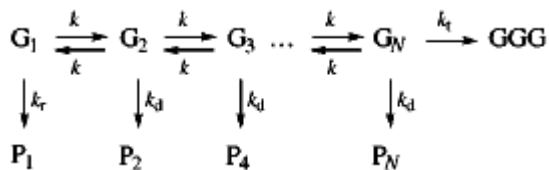
**Figure 3.7.** Oxidation of a guanine G in double-stranded DNA and electron migration from a GG unit [14].



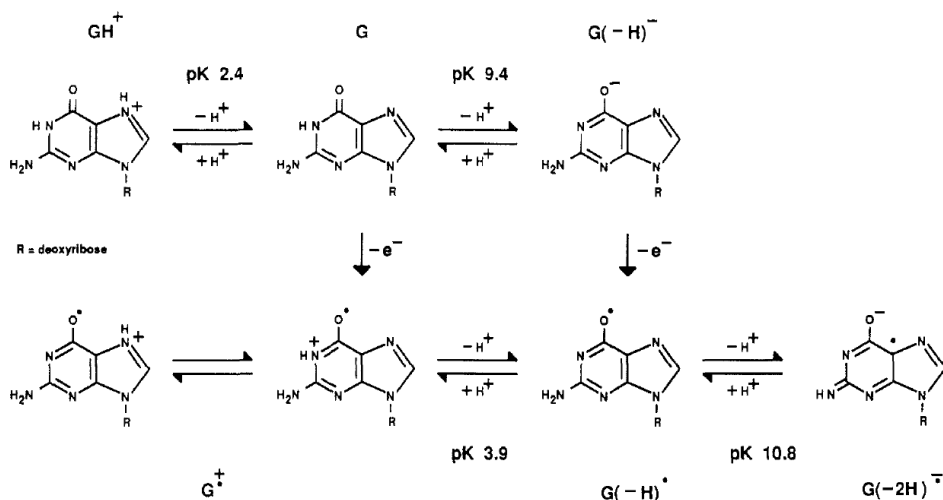
**Figure 3.8.** Long-distance hole transport between guanines (shaded in gray). The numbers below these sites are the relative amounts of the positive charges detected by water-trapping reactions. The larger the number at the last guanines at the right end, the more efficient is the charge transport [14].

### 3.2.1 Kinetics of hole transport

Giese *et al.* [4] studied hole hopping in a  $G(T)_mG(T)_mG...(T)_pGGG$  strand, that contains  $N$  guanine bases (**Scheme I** extracted from **Fig. 3.3**).

**Scheme I**

This kinetic scheme corresponds to the initial formation of  $G_1^+$  followed by the reversible hole hopping with a rate  $k$  between nearest-neighbour G bases, which are separated by different  $m$  number of T bases. The process is terminated by hole trapping from  $G^+$  at GGG with a rate  $k_t$ . According to quantum mechanical theory of charge transfer, the rates  $k$  and  $k_t$  correspond to the superexchange rates in the  $G_j^+(T)_m G_{j\pm 1}$  (for  $k$ ) and in the  $G_N^+(T)_p GGG$  (for  $k_t$ ) subsystems, which are mediated by off-resonance coupling of  $G^+$  with the T bases. Therefore, the kinetic **Scheme I** represents a hopping mechanism with the individual rates  $k$  and  $k_t$  being determined by superexchange interactions. Moreover, the charge hopping across the G groups in the DNA strand competes with the chemical side reactions of the guanine adducts. Similar to the experiments, for the case  $m = 2$ , the initially formed cation  $G_1^{+\bullet}$  can undergo several side reactions (**Fig. 3.9**), with a rate constant  $k_r$  [2].

**Figure 3.9.** Deprotonation reaction of the radical cation  $G^{+\bullet}$  to give the neutral radical  $G(-H)^{\bullet}$  [2].

The yield for the reaction  $G_1^{+\bullet}$  with water is proportional to the product yield  $P_1$  of all the side reactions at this cation base. Other side reactions can take place at the  $G_j^+$  ( $j = 2-N$ ) sites with the global rate  $k_d$  leading to the products  $P_j$  ( $j = 2, \dots, N$ ), with  $k_d$  being taken to be independent of  $j$ . The formation of the chemical products compete with hole hopping and trapping. Then the kinetic equation for **Scheme I** is described in **Eq. 3.7**:

$$\frac{da(t)}{dt} = Aa(t) \quad \text{(Equation 3.7)}$$

The formal solution for the earlier differential equation is:

$$A(t) = \exp(At)(0) \quad \text{(Equation 3.8)}$$

Where the kinetic matrix is

$$A = \begin{bmatrix} -k-k_r & k & 0 & 0 & \dots & 0 \\ k & -2k-k_d & k & 0 & \dots & 0 \\ 0 & k & -2k-k_d & k & 0 & 0 \\ 0 & 0 & k & \ddots & \ddots & 0 \\ \vdots & \vdots & 0 & \ddots & -2k-k_d & k \\ 0 & 0 & 0 & 0 & k & -k-k_t-k_d \end{bmatrix}$$

and  $a(t)$  is the vector of the relative concentrations  $a_j(t)$  of  $G_j^+(t)$  ( $j = 1, \dots, N$ ) at time  $t$ . The initial conditions are [5]:

$$a_1(t=0) = 1, \quad a_{j \neq 1}(t=0) = 0 \quad \text{(Equation 3.9)}$$

For our experiments, we must consider a heteroatomic type of sequence in a semidry environment, with variable range of trapping holes through the sequence. Therefore, we decided to use a more suitable charge hopping mechanism, based on steady-states.

### 3.2.2 Steady states for multistep charge hopping

This approach can be used for either sequential tunneling or for multistep hopping, and differences on the charge transfer can be observed depending on the energetics, the temperature, the bridge length and the existence of competing channels.

First, we consider the classical model where the transfer proceeds by a hopping between levels according to **Eq. 3.9**:

$$\frac{dP_n}{dt} = -(k_{n-1 \leftarrow n} + k_{n+1 \leftarrow n})P_n + k_{n \leftarrow n-1}P_{n-1} + k_{n \leftarrow n+1}P_{n+1} \quad (\text{Equation 3.10})$$

where  $P_n$  is the population at site  $n$  and where  $E_n > E_m$ , shown in **Eq. 3.11**.

$$k_{n \leftarrow m} = \begin{cases} k_0 \exp\left(-\frac{E_n - E_m}{k_B T}\right) \\ k_0 \end{cases} \quad (\text{Equation 3.11})$$

Using this kinetic scheme, the rates associated with the energy levels are defined by: *i*) charge localization on a given base pair which can hop to a neighbouring base pair at a rate ( $k_{bp} = \tau_{bp}^{-1}$ , for DNA  $\sim 10$ -100 ps [46]); *ii*) the injection rate ( $\Gamma$ ) and; *iii*) a possible direct charge injection from each base pair directly to the surface ( $\Gamma_{bp}$ ), as represented in **Fig. 3.10**.

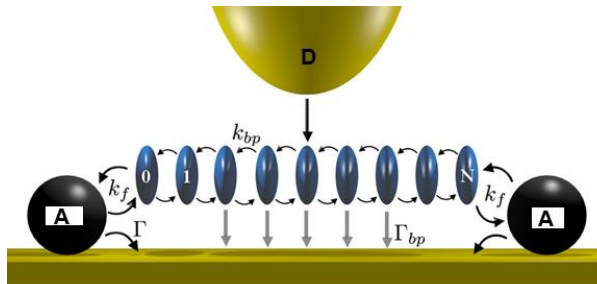


**Figure 3.10.** Scheme representing the parameters involved in multistep charge hopping through a DNA bridge, where A represent the acceptor groups and an electrode tip acts as a donor in this particular case.

In the steady state limit, *i.e.* when a steady state current has been established between the junction and the surface, this population must have reached equilibrium. Thus, we impose  $\frac{dP_x}{dt} = 0$  and we suppose that the current flows from the junction to the surface and that the center of the junction is located above the  $i$ -th base pair of the sequence with  $i = 1 - N$ . We hence impose  $P_i = 1$ . This condition simulates the constant injection of charge from the junction to the initial base pair. The system of linear equations can then be solved using usual techniques to obtain the steady state population of the different base pairs. The steady state injection rate is then calculated as **Eq. 3.12**:

$$k_{SS} = \Gamma(P_{fL} + P_{fR}) + \sum_{n=1}^N \Gamma_{bp} P_n \quad (\text{Equation 3.12})$$

This rate captures the time required for a charge to transfer from the DNA to the surface (substrate) once the steady state has been reached. The product of this rate with the total electronic charge that is transferred consequently gives the final current (**Eq. 3.13**):

$$I(V) = (-e)N_e k_{SS} \quad (\text{Equation 3.13})$$

Where  $N_e$  is the total number of charge that are available for transfer at a given bias voltage. The conductance is hence given by (**Eq. 3.14**):

$$g = \frac{dI}{dV} = (-e) \frac{dN_e}{dV} k_{SS} = (-e) \rho(E_F) k_{SS} \quad (\text{Equation 3.14})$$

Here,  $\rho(E_F)$  is the density of states of the junction expressed here in number of states/eV. Thus, the density of states has to be established, depending on the type of junction and experimental bias voltage.

Finally, to calculate **Equation 3.14**, it is necessary to combine the solutions of **Equations 3.10-3.13**, which is useful to experimentally determine the type of charge transport at different positions on a given DNA sample, as demonstrated in Chapter 6.

### 3.4 Conclusions

- There are two most accepted mechanisms for charge transport in DNA: sequential tunneling and multistep hopping.
  
- Sequential Tunneling (coherent tunneling).
  - Assumes no interaction with the environment, thus the Hamiltonian governs the system dynamics.
  - The rate of long charge distance of electron transfer reaction depends on three parameters: *i*) the electronic coupling, *ii*) the free energy of the reaction and, *iii*) the nuclear reorganization energy. Consequently, it depends strongly on the distance.
  - It can be also calculated with the steady states approach. This is based on the tight binding Hamiltonian and incorporates the conductance from the Landauer formalism.
  
- Multistep Charge Hopping (incoherent tunneling):
  - Presents a weak distance dependence.
  - Guanines are the preferred relays for charge hopping due to their low ionization energies.
  - Hole transport kinetics is mainly used for poly(G)-poly(C) sequences.
  - The steady states approach can also be used here to obtain the conductance in the system, based on the density of states on the junction (metal-molecule-metal).

### 3.4 References

- [1] B. Pullman and A. Pullman, "The electronic structure of the purine-pyrimidine pairs of DNA," *Biochim. Biophys. Acta*, vol. 36, pp. 343–350, 1959.
- [2] S. Steenken, "Purine bases, nucleosides, and nucleotides: Aqueous solution redox chemistry and transformation reactions of their radical cations and  $e^-$  and OH adducts," *Chem. Rev.*, vol. 89, pp. 503–520, 1989.

- [3] S. Priyadarshy, S. M. Risser, and D. N. Beratan, "DNA-mediated electron transfer," *J. Biol. Inorg. Chem.*, vol. 3, pp. 196–200, 1998.
- [4] E. Meggers, M. E. Michel-Beyerle, and B. Giese, "Sequence dependent long range hole transport in DNA," *J. Am. Chem. Soc.*, vol. 120, no. 5, pp. 12950–12955, 1998.
- [5] M. Bixon, B. Giese, S. Wessely, T. Langenbacher, M. E. Michel-Beyerle, and J. Jortner, "Long-range charge hopping in DNA.," *Proc. Natl. Acad. Sci. U. S. A.*, vol. 96, no. 21, pp. 11713–11716, 1999.
- [6] M. Bixon and J. Jortner, "Energetic control and kinetics of hole migration in DNA," *J. Phys. Chem. B*, vol. 104, no. 16, pp. 3906–3913, 2000.
- [7] A. A. Voityuk, J. Jortner, M. Bixon, and N. Rösch, "Electronic coupling between Watson–Crick pairs for hole transfer and transport in desoxyribonucleic acid," *J. Chem. Phys.*, vol. 114, no. 13, p. 5614, 2001.
- [8] F. C. Grozema, Y. A. Berlin, and L. D. A. Siebbeles, "Mechanism of charge migration through DNA: Molecular wire behavior, single-step tunneling or hopping?," *J. Am. Chem. Soc.*, vol. 122, no. 44, pp. 10903–10909, 2000.
- [9] F. C. Grozema, L. D. A. Siebbeles, Y. A. Berlin, and M. A. Ratner, "Hole mobility in DNA: Effects of static and dynamic structural fluctuations.," *Chemphyschem*, vol. 3, no. 6, pp. 536–9, 2002.
- [10] F. C. Grozema, S. Tonzani, Y. A. Berlin, G. C. Schatz, L. D. A. Siebbeles, and M. A. Ratner, "Effect of structural dynamics on charge transfer in DNA hairpins," *J. Am. Chem. Soc.*, vol. 130, no. 15, pp. 5157–5166, 2008.
- [11] L. D. A. Siebbeles and F. C. Grozema, *Charge and Exciton Transport through Molecular Wires*. Weinheim, Germany: Wiley-VCH Verlag and Co. KGaA, 2011.
- [12] D. Mishra and S. Pal, "Ionization potential and structure relaxation of adenine, thymine, guanine and cytosine bases and their base pairs: A quantification of reactive sites," *J. Mol. Struct. Theochem*, vol. 902, pp. 96–102, 2009.
- [13] Y. A. Berlin, A. L. Burin, and M. A. Ratner, "Elementary steps for charge transport in DNA: Thermal activation vs. tunneling," *Chem. Phys.*, vol. 275, pp. 61–74, 2002.
- [14] B. Giese, "Long-distance electron transfer through DNA," *Annu. Rev. Biochem.*, vol. 71, pp. 51–70, 2002.

- [15] B. Giese, B. Carl, T. Carl, T. Carell, C. Behrens, U. Hennecke, O. Schiemann, and E. Feresin, "Excess electron transport through DNA: A single electron repairs more than one UV-induced lesion," *Angew. Chemie*, vol. 116, no. 14, pp. 1884–1887, 2004.
- [16] B. Giese, "Electron transfer through DNA and peptides.," *Bioorg. Med. Chem.*, vol. 14, no. 18, pp. 6139–43, 2006.
- [17] G. Cuniberti, L. Craco, D. Porath, and C. Dekker, "Backbone-induced semiconducting behavior in short DNA wires," *Phys. Rev. B*, vol. 65, no. 24, p. 241314, 2002.
- [18] S. Mandal and G. Cuniberti, "Quantum transport through a DNA wire in a dissipative environment," *Nano Lett.*, vol. 5, no. 6, pp. 1039–1097, 2005.
- [19] E. Shafir, H. Cohen, A. Calzolari, C. Cavazzoni, D. A. Ryndyk, G. Cuniberti, A. Kotlyar, R. Di Felice, and D. Porath, "Electronic structure of single DNA molecules resolved by transverse scanning tunneling spectroscopy," *Nat. Mater.*, vol. 7, pp. 68–74, 2008.
- [20] D. A. Ryndyk, E. Shafir, D. Porath, A. Calzolari, R. Di Felice, and G. Cuniberti, "Scanning tunneling spectroscopy of single DNA molecules," *ACS Nano*, vol. 3, no. 7, pp. 1651–6, 2009.
- [21] B. Song, M. Elstner, and G. Cuniberti, "Anomalous conductance response of DNA wires under stretching.," *Nano Lett.*, vol. 8, no. 10, pp. 3217–20, 2008.
- [22] T. Kubař, R. Gutiérrez, U. Kleinekathöfer, G. Cuniberti, and M. Elstner, "Modeling charge transport in DNA using multi-scale methods," *Phys. Status Solidi*, vol. 250, no. 11, pp. 2277–2287, 2013.
- [23] D. Dee and M. E. Baur, "Charge and excitation migration in DNA chains," *J. Chem. Phys.*, vol. 60, no. 2, pp. 541–560, 1974.
- [24] R. A. Marcus, "Electron transfer reactions in chemistry: Theory and experiment," *Rev. Mod. Phys.*, no. 2, pp. 69–92, 1992.
- [25] F. D. Lewis, H. Zhu, P. Daublain, B. Cohen, and M. R. Wasielewski, "Hole mobility in DNA A tracts," *Angew. Chemie - Int. Ed.*, vol. 45, pp. 7982–7985, 2006.
- [26] G. I. Livshits, A. Stern, D. Rotem, N. Borovok, G. Eidelstein, A. Migliore, E. Penzo, S. J. Wind, R. Di Felice, S. S. Skourtis, J. C. Cuevas, L. Gurevich, A. B. Kotlyar, and D. Porath, "Long-range charge transport in single G-quadruplex DNA molecules," *Nat. Nanotechnol.*, vol. 9, pp. 1040–1046, 2014.



- [27] J. D. Slinker, N. B. Muren, S. E. Renfrew, and J. K. Barton, "DNA charge transport over 34 nm," *Nat. Chem.*, vol. 3, no. 3, pp. 228–33, 2011.
- [28] A. Messer, K. Carpenter, K. Forzley, J. Buchanan, S. Yang, Y. Razskazovskii, Z. Cai, and M. D. Sevilla, "Electron spin resonance study of electron transfer rates in DNA: Determination of the tunneling constant  $\beta$  for single-step excess electron transfer," *J. Phys. Chem. B*, vol. 104, pp. 1128–1136, 2000.
- [29] J. S. Hwang, K. J. Kong, D. Ahn, G. S. Lee, D. J. Ahn, and S. W. Hwang, "Electrical transport through 60 base pairs of poly(dG)-poly(dC) DNA molecules," *Appl. Phys. Lett.*, vol. 81, no. 6, p. 1134, 2002.
- [30] T. Meier, P. Thomas and W. S. Koch, *Coherent semiconductor optics. From basic concepts to nanostructure applications. Chapter: Coherent tunneling*. Springer Berlin Heidelberg, 2007.
- [31] M. Zwolak and M. Di Ventra, "Molecular electronics," in *Introduction to Nanoscale Science and Technology*, 1st ed., M. Di Ventra, S. Evoy, and J. R. Heflin Jr., Eds. New York, USA.: Springer US, pp. 261–282, 2004.
- [32] T. L. Netzel, "Present status and future directions of research in electron-transfer mediated by DNA," *J. Biol. Inorg. Chem.*, vol. 10, pp. 210–214, 1998.
- [33] C. J. Murphy, M. R. Arkin, Y. Jenkins, N. D. Ghatlia, S. H. Bossmann, N. J. Turro, and J. K. Barton, "Long-range photoinduced electron transfer through a DNA helix," vol. 262, no. 15, pp. 1025–1029, 1993.
- [34] F. D. Lewis, T. Wu, Y. Zhang, R. L. Letsinger, S. R. Greenfield, and M. R. Wasielewski, "Distance-dependent electron transfer in DNA hairpins," *Science*, vol. 277, pp. 673–676, 1997.
- [35] A. M. Brun and A. Harriman, "Dynamics of electron transfer between intercalated polycyclic molecules: Effect of interspersed bases," *J. Am. Chem. Soc.*, vol. 114, no. 10, pp. 3656–3660, 1992.
- [36] F. D. Lewis and R. L. Letsinger, "Distance-dependent photoinduced electron transfer in synthetic single-strand and hairpin DNA," *J. Biol. Inorg. Chem.*, vol. 3, no. 2, pp. 215–221, 1998.
- [37] F. D. Lewis, H. Zhu, P. Daublain, T. Fiebig, M. Raytchev, Q. Wang, and V. Shafirovich, "Crossover from superexchange to hopping as the mechanism for photoinduced charge transfer in DNA hairpin conjugates," *J. Am. Chem. Soc.*, vol. 128, no. c, pp. 791–800, 2006.
- [38] W. Chen, C. Turro, L. A. Friedman, J. K. Barton, and N. J. Turro, "Resonance Raman investigation of  $\text{Ru}(\text{phen})_2(\text{dppz})^{2+}$  and related

- complexes in water and in the presence of DNA," *J. Phys. Chem. B*, vol. 101, no. 35, pp. 6995–7000, 1997.
- [39] E. D. A. Stemp, M. R. Arkin, and J. K. Barton, "Oxidation of guanine in DNA by  $\text{Ru}(\text{phen})_2(\text{dppz})^{3+}$  using the flash-quench technique," *J. Am. Chem. Soc.*, vol. 119, pp. 2921–2925, 1997.
- [40] R. Landauer, "Spatial variation of currents and fields due to localized scatterers in metallic conduction," *IBM J.*, pp. 223–231, 1957.
- [41] D. Segal, A. Nitzan, W. B. Davis, M. R. Wasielewski, and M. A. Ratner, "Electron transfer rates in bridged molecular systems 2. A steady-state analysis of coherent tunneling and thermal transitions," *J. Phys. Chem. B*, vol. 104, no. 16, pp. 3817–3829, 2000.
- [42] S. Datta, *Electronic transport in mesoscopic systems. Cambridge studies in semiconductor physics and microelectronic engineering*. Cambridge University Press, 1995.
- [43] N. V. Grib, D. A. Ryndyk, R. Gutierrez, and G. Cuniberti, "Distance-dependent coherent charge transport in DNA: Crossover from tunneling to free propagation," *J. Biophys. Chem.*, vol. 01, no. 02, pp. 77–85, 2010.
- [44] J. Jortner, M. Bixon, T. Langenbacher, and M. E. Michel-Beyerle, "Charge transfer and transport in DNA," *Proc. Natl. Acad. Sci. U. S. A.*, vol. 95, pp. 12759–12765, 1998.
- [45] D. T. Breslin, J. E. Coury, J. R. Anderson, L. McFail-Isom, Y. Kan, L. D. Williams, L. A. Bottomley, and G. B. Schuster, "Anthraquinone phototonuclease structure determines its mode of binding to DNA and the cleavage chemistry observed," *J. Am. Chem. Soc.*, vol. 119, no. 21, pp. 5043–5044, 1997.
- [46] C. Wan, T. Fiebig, O. Schiemann, J. K. Barton, and A. H. Zewail, "Femtosecond direct observation of charge transfer between bases in DNA," *Proc. Natl. Acad. Sci. U. S. A.*, vol. 97, pp. 14052–14055, 2000.

## Chapter 4

### Experimental Techniques

The goal of this chapter is to introduce the reader with the basic concepts underneath the experimental techniques used in **Chapters 5 to 7**. First the synthesized molecular wires (Fullerene-DNA molecules) were characterized by optical spectroscopic techniques, indicating: *i*) the absence of clusters and concentration of DNA in the sample (UV-vis), *ii*) identification of corresponding functional groups related to the synthesis (FTIR) and, *iii*) demonstration of the covalent attachment of a fullerene to DNA (Raman).

In order to evaluate the integrity of the sample after hybridization, the fullerene-DNA molecules, the samples were introduced into an agarose gel (electrophoresis), confirming the absence of secondary structures and thus the presence of only one band (one type of fullerene-DNA wire).

Finally, the electrical characterization of the samples was performed in a “dry” environment on top of gold substrates by means of Conductive-AFM (I-AFM) and Scanning Tunneling Microscopy (STM). The working principle and differences between I-AFM and STM become a key factor in the discussion between our results (**Chapter 7**) and literature reports on DNA (**Chapters 2-3**).

#### 4.1 Physico-chemical techniques

##### 4.1.1 Electromagnetic Radiation

Light is described in classical physic, in terms of the electromagnetic field. This is an oscillating electric and magnetic disturbance that spreads as a harmonic wave through empty space (vacuum). Such waves are generated by the acceleration of electric charge, then the wave travels at a constant speed (speed of light,  $c = 2.997925 \times 10^8 \text{ m s}^{-1}$ ). An electromagnetic field is composed of an electric field that acts on charged particles (stationary or moving) and a magnetic field that only acts on moving charged particles (Fig. 4.1) [1].

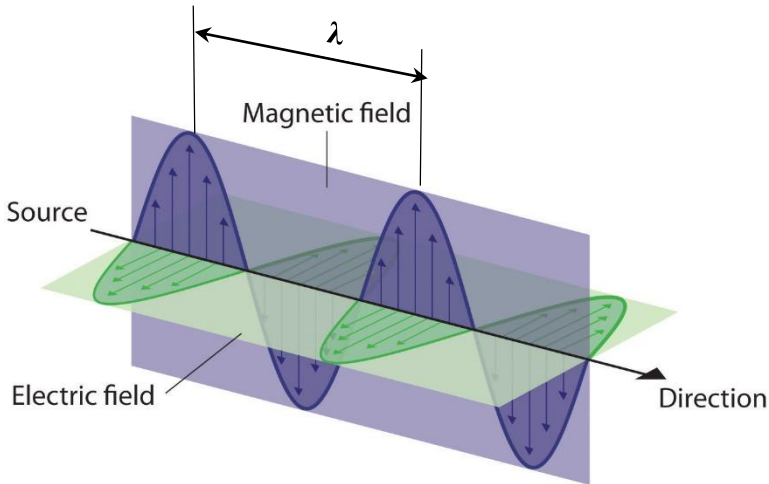


**Figure 4.1.** Scheme that represents the perpendicular oscillating electric and magnetic fields of an electromagnetic wave [2].

In this context, the Lorentz force describes the combination between electric and magnetic forces on a point charge due to electromagnetic fields. If a particle of charge  $q$  moves with velocity  $v$  in the presence of an Electric field  $E$  and a magnetic field  $B$ , then it will experience a force depicted in **Eq. 4.1**:

$$F = q[E + (v \times B)] \quad (\text{Equation 4.1})$$

The characteristics of an electromagnetic field are the wavelength  $\lambda$ , or the distance between two adjacent peaks of the wave and its frequency,  $\nu$ , the number of cycles per second at which its displacement at a fixed position returns to its original value. Frequency is measured in *Hertz* ( $1 \text{ Hz} = 1 \text{ s}^{-1}$ ) [1, 3]. Maxwell's equations allow us to describe this relation (**Eq. 4.2**):

$$c = \lambda\nu \quad (\text{Equation 4.2})$$

As a consequence, the longer the wavelength the lower the frequency will be. On the other hand, the wavenumber ( $\bar{\nu}$  in  $\text{cm}^{-1}$ ) is the number of waves in a length of one centimeter and has the advantage of being linear with energy. It is given by the following relationship (**Eq. 4.3**):

$$\bar{\nu} = \frac{1}{\lambda} = \frac{\nu}{c} ; E = h\nu \rightarrow E = hc\bar{\nu} \quad (\text{Equation 4.3})$$

Furthermore, a summary of the electromagnetic spectrum is shown in Fig. 4.2, grouping its subtypes depending on its frequency and wavelength. The area of interest for our measurements will be in the wavelength range between 0.2-100  $\mu\text{m}$ .

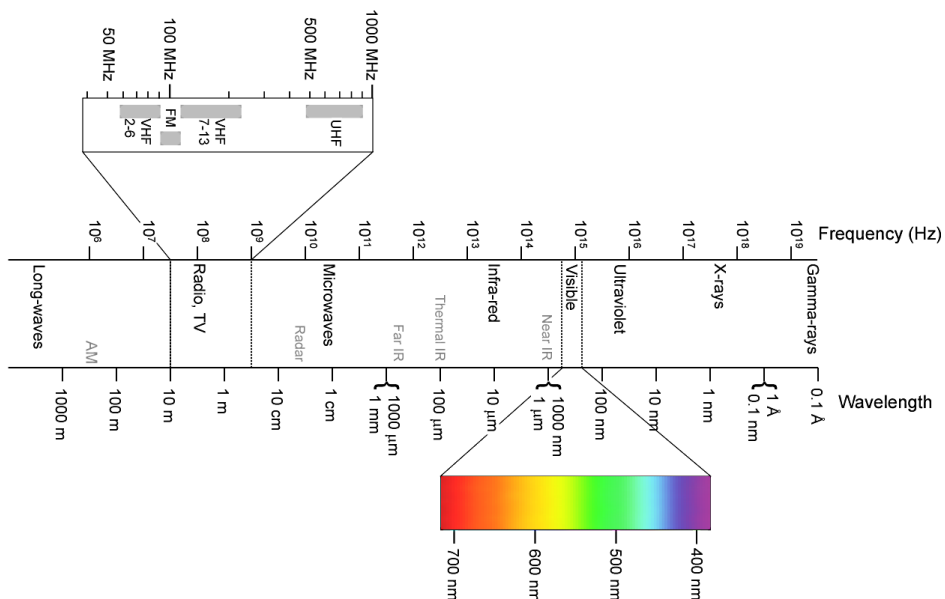


**Figure 4.2.** Illustration of the electromagnetic spectra, including ranges of frequency and wavelength for the most representative spectral regions.

#### 4.1.1.1 Optical Spectroscopy

When energy changes on a molecule, a photon experiences absorption, emission or scattering producing as a consequence spectral lines. It differs from atomic spectroscopy where the energy of a molecule can change with the electronic transitions as well as with changes of rotational and vibrational state. On the other hand, molecular spectra contain more complex information as the sample properties (*e.g.* bond strengths, lengths and angles) and composition.

Emission spectroscopy is applied when a molecule undergoes a transition from a state of high energy  $E_1$  to a state of lower energy  $E_2$  and emits the excess energy as a photon. On the other hand, in absorption spectroscopy the net absorption of nearly monochromatic (single frequency) incident radiation is monitored as the radiation wavelength is scanned over a range of frequencies.

Net absorption means that, when a sample is irradiated, both absorption and emission at a given frequency are stimulated, and the detector measures the difference. Moreover, the energy of the photo emitted or absorbed  $h\nu$ , is given by the Bohr frequency condition (**Eq. 4.4**),

$$h\nu = |E_1 - E_2| \quad (\text{Equation 4.4})$$

Here  $\nu$  is the frequency of the emitted or absorbed radiation and  $h$  is the Planck constant ( $h = 6.626 \times 10^{-34}$  J s).

Absorption spectroscopy is widely used for studies on electronic transitions, molecular rotations, and molecular vibrations. A spectrometer is an instrument that detects the characteristics of light scattered, emitted or absorbed by atoms and molecules. Radiation from an appropriate source is directed toward a sample. For most spectrometers, the light that is transmitted, emitted or scattered by the sample is collected by mirrors or lenses and strikes a dispersing element that separates radiation into different frequencies. The light intensity at each frequency is analysed by a suitable detector. Modern spectrometers tend to use the Fourier transform techniques of spectral detection and analysis. This is because a Fourier transform is based on a Michelson interferometer, a device for analyzing the frequencies present in a composite signal, stretching the signal into a spectrum [1]. Thus, a spectrum plots the response of interest as a function of wavelength or frequency [4].

Note that vibrations in polyatomic molecules are more complex than for diatomic molecules, where only one mode of vibration is observed (the bond stretch). Polyatomic molecules, on the other hand, show several modes of vibration due to their different bond lengths and angles. In order to calculate the total number of vibrational modes of a polyatomic molecule, a combination of these atomic displacements could give a description of the resulting vibrations. Then, a linear molecule with  $N$  atoms will show  $3N-5$  independent vibrational modes and a non-linear molecule, will have  $3N-6$  modes of vibration [1]. Typically, vibrational absorption is associated with the infrared region while the differences between energy levels related to molecular rotation are so small that far infrared or even microwave lengths are effective (**Fig. 4.3**).

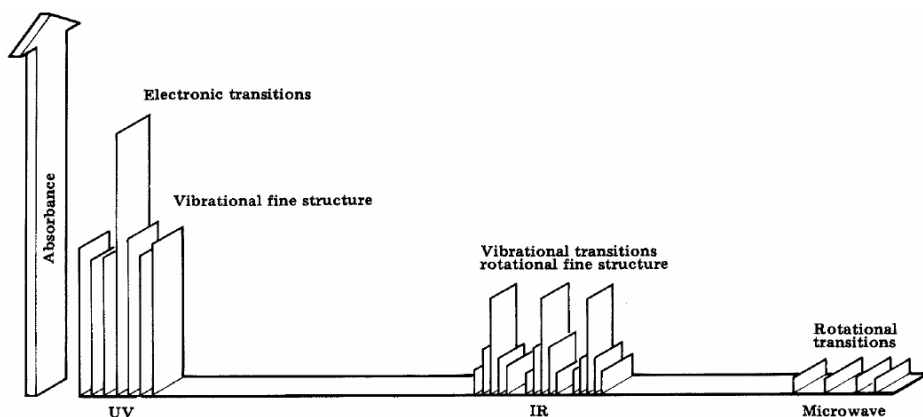


**Figure 4.3.** Relationship of wavelength and energy-induced transitions [9].

#### 4.1.1.1.1 Ultraviolet-visible spectroscopy (UV-vis)

Ultraviolet spectroscopy is a type of absorption spectroscopy in the ultraviolet-visible spectral region. It is less commonly used than IR or Raman because it gives specialized information, such as the nature of conjugated  $\pi$  electron systems. The UV range in the electromagnetic spectrum corresponds to the area between 200-400 nm. With UV radiation, the absorbed energy corresponds to the amount necessary to promote an electron from one orbital to another. When a conjugated molecule is irradiated with ultraviolet light, energy absorption occurs and a  $\pi$  electron is promoted from the highest occupied molecular orbital (HOMO) to the lowest unoccupied molecular orbital (LUMO) [5].

In practice, an ultraviolet spectrum is recorded by irradiating the sample with UV light of continuously changing wavelength. The ratio of the transmitted intensity,  $I$ , to the incident intensity,  $I_0$  at a given frequency is called the transmittance,  $T$ , of the sample at that frequency (**Eq. 4.5**).

$$T = \frac{I}{I_0} \quad \text{or} \quad \%T = \frac{I}{I_0} \times 100 \quad (\text{Equation 4.5})$$

Empirically, the Beer-Lambert law describes how the transmitted intensity varies with the length  $l$  of the sample (thickness of the medium in the light path) and the molar concentration  $C$  of the absorbing molecules.

$$I = I_0 10^{-\epsilon Cl} \quad (\text{Equation 4.6})$$

The term  $\epsilon$  is called the molar absorption coefficient (or "extinction coefficient"). It depends on the frequency of the incident radiation and is greatest where the absorption is most intense, with dimensions of  $[\text{concentration} \times \text{length}]^{-1}$ , and it is usually expressed in  $(\text{cm}^2 \text{ mol}^{-1})$ .

When the wavelength corresponds to the energy level required to excite an electron to a higher level, energy is absorbed. This absorption is detected and displayed on a chart that plots absorbance ( $A$ ) versus wavelength, defined as [1]:

$$A = \log \frac{I_0}{I} \quad \text{or} \quad A = -\log T \quad (\text{Equation 4.7})$$

Then the Beer-Lambert law can be rewritten into the **Eq. 4.8**:

$$A = \epsilon Cl \quad (\text{Equation 4.8})$$

Molar absorptivity is a physical constant, characteristic of the particular substance being observed and thus characteristic of the particular  $\pi$  electron system in the molecule. Typical values for conjugated dienes are in the range of  $\epsilon = 10,000$  to  $25,000 \text{ M}^{-1} \text{ cm}$  [5].

The basic components of a UV-vis spectrometer are [6]:

- i)* A source that generates a broad band of electromagnetic radiation.
- ii)* A dispersion device that selects from the broadband radiation of the source at a particular wavelength (monochromators, **Fig 4.4**). At the same time a monochromator consists: *a)* entrance slit, *b)*



collimating device (producing parallel light), *c*) a wavelength selection (*e.g.* prism or diffraction grating), *d*) a focusing lens or mirror and, *e*) an exit slit.

- iii*) A sample area and
- iv*) One or more detectors to measure the intensity of radiation (*e.g.* a photomultiplier tube, a photodiode or a charge-coupled device, CCD). Other optical components, such as lenses or mirrors, relay light through the instrument.

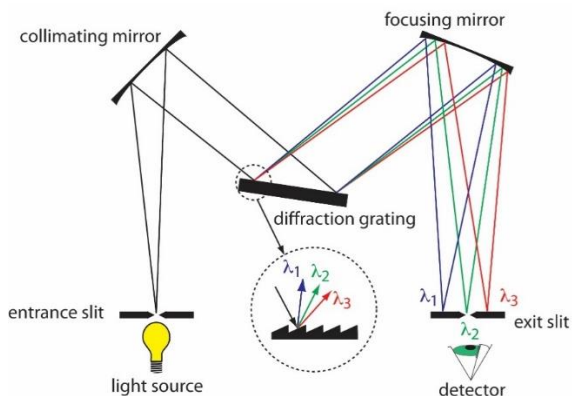


**Figure 4.4.** Schematic diagram of a monochromator. Radiation enters to the monochromator via the entrance slit. A collimating mirror collects then the light and reflect it to a diffraction grating, which disperses the radiation. Finally, a second mirror focus the radiation onto a planar surface (exit slit) where only the selected wavelength exits the monochromator [7].

For example, in **Fig. 4.5** the sources of radiation are a tungsten filament (range between 300 and 2500 nm) and a deuterium arc lamp (wavelength range from 190 to 400 nm). Radiation passes through the monochromator, which selects a wavelength by means of a filter (prism). Then the selected wavelength is directed from the sample area (*i.e.* for quartz cuvette, a pathlength is 10 mm) to the detector, based on photodiodes. A reference sample is taken into account to discard absorption bands that depend on the medium (*e.g.* for a sample dissolved in water, water will serve as a reference). After computing the sample and reference data, the device generates an absorption spectrum.

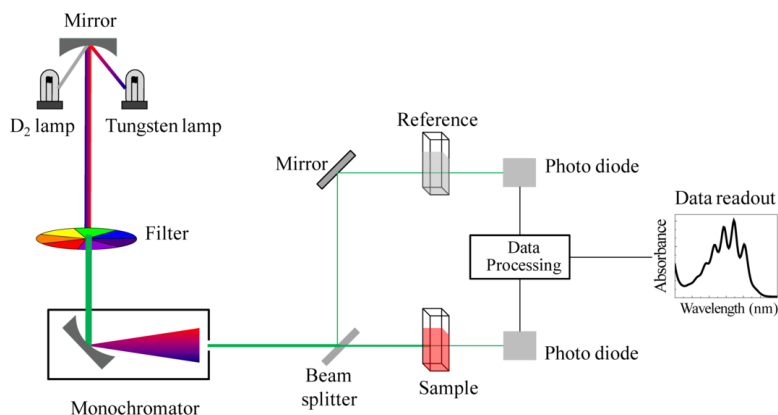


**Figure 4.5.** Representation of the components inside an UV-vis spectrometer [8].

In our experiments, we used the NanoDrop 2000/ 2000c UV-vis spectrophotometer (Thermo Fisher Scientific Inc., **Fig. 4.6**). Here the light source was a Xenon flash lamp with wavelength range between 190 to 840 nm and a detector based on a silicon CCD array. Sample volumes can vary between 0.5-2  $\mu\text{l}$  for the sample area (pathlength) of 1 mm.



**Figure 4.6:** Photograph of the actual UV-vis spectrophotometer used in this thesis.

## 4.1.1.1.2 Infrared spectroscopy (IR)

Infrared photons have less energy than photons in the visible range, so upon absorption by a molecule the energy is not sufficient to reach an excited electronic level. We focus in this section on diatomic molecules (**Fig. 4.7**).

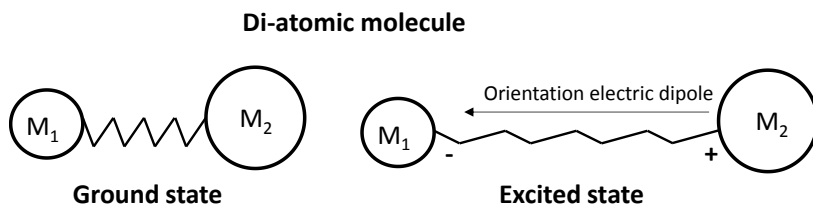


**Figure 4.7.** Classical view for IR absorption by a diatomic molecule.

The selection rule for IR absorptions is that the molecule should present an electric dipole moment that changes during the vibration. An understanding of molecular symmetry and group theory is important when infrared bands are assigned. Additionally, IR absorptions are not infinitely narrow and there are several factors that can contribute to the broadening (e.g. Doppler effect in gases and collision of molecules) [3]. Moreover, two concepts are also used to explain changes in frequency and vibrational modes. One is the stiffness of the bond,  $k$  or force constant (from Hooke's law) and the other one takes into account the individual atomic masses or the reduced mass,  $\mu$  (**Eq. 4.9**):

$$\frac{1}{\mu} = \frac{1}{m_1} + \frac{1}{m_2} \quad \text{and} \quad \mu = \frac{m_1 m_2}{(m_1 + m_2)} \quad (\text{Equation 4.9})$$

Where  $m_1$  and  $m_2$  are the masses of the atoms at the ends of the bond. Then, a relationship between force constant, reduced mass and frequency of absorption can be established (**Eq. 4.10**).

$$\nu = \frac{1}{2\pi} \sqrt{\frac{k}{\mu}} \quad (\text{Equation 4.10})$$

A molecule can only absorb radiation when the incoming infrared radiation has the same frequency as one of the fundamental vibration modes of the molecule. Therefore, the vibrational motion of a small part of the molecule is increased

while the rest of the molecule is left unaffected. Vibrational changes are observed in either bond length (stretching) or bond angle (bending) (**Fig. 4.8a**). In addition, stretching can be in-phase (symmetrical) or out-of-phase (asymmetric) (**Fig. 4.8b**).

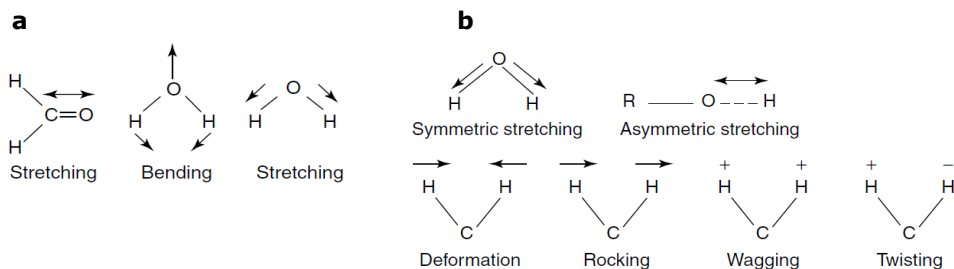


**Figure 4.8.** (a) Vibrational modes, stretching and bending for methanol (CH<sub>3</sub>O) and water. (b) Above: types of stretching modes and, below: variations of bending modes, where the arrows indicate in-plane bending and signs "+" or "-" indicate out-of-plane bending, while the carbon is left unaffected [3].

The most effective way to obtain an IR spectrum is using the Fourier transform, where all wavelengths pass simultaneously and afterwards the spectral information is extracted by a fast Fourier transformation. When waves overlap in space, they can enhance or quench each other (constructive- or destructive-interference). Some frequencies will pass unhindered, while others will be partially or completely absorbed because they excite vibronic modes in the sample molecules. The interference pattern of the transmitted beams is recorded, resulting in a so-called interferogram which is sent digitalized to the measurement computer. Based on the equivalence of data in the temporal and frequency domain, a "fast Fourier transformation" (FFT) is applied. This is a computer algorithm that performs a Fourier transformation to convert the interferogram into a graph in the frequency (or wavenumber) domain.

An interferogram is a signal produced as a function of the change of pathlength between the two beams (Michelson-interferometer illustrated in **Fig. 4.9**). Then, the two domains of distance and frequency are interconvertible by the mathematical method of Fourier-transformation. Normally, the mathematical process of Fourier transformation assumes infinite time boundaries, which

produces negative and positive side lobes with diminishing amplitudes. For practical reasons these lobes ( $-\infty$  to  $+\infty$ ) have to be mathematically corrected to remove them. This process is called apodisation, where the interferogram is multiplied with a suitable function ("boxcar" or step function) before the Fourier-transformation is carried out [2, 3].

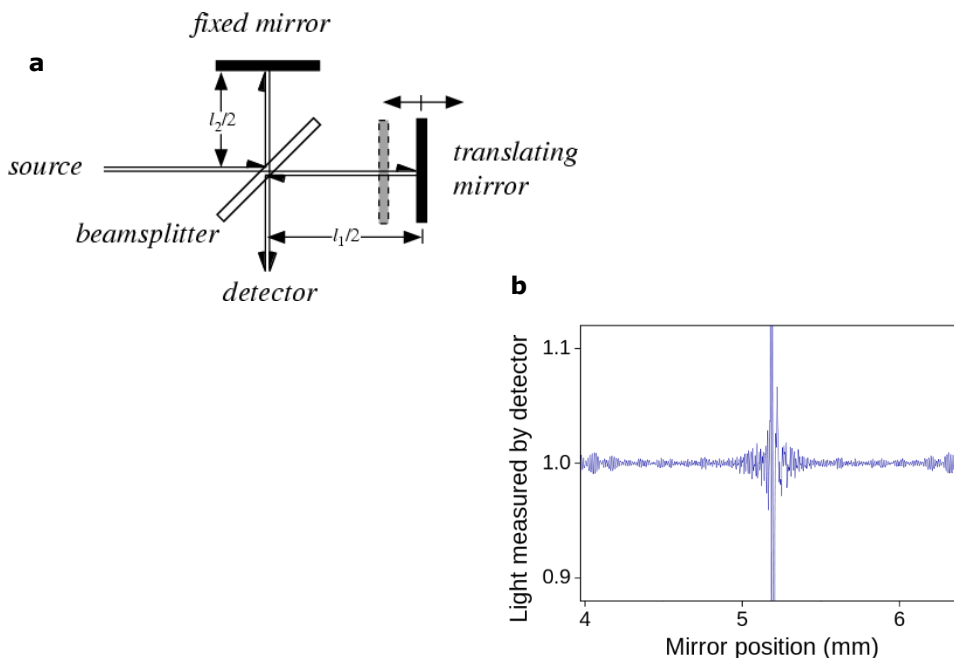


**Figure 4.9.** (a) Scheme of a typical Michelson-interferometer. By scanning the translating mirror over some distance, an interference pattern is produced, encoding the spectrum of the source. A beamsplitter is generally placed at the vertex of the right angle and oriented at a  $45^\circ$  angle relative to the two mirrors. Radiation is divided at the beamsplitter into two parts. Then radiation propagates and when the two beams recombine ( $l_1/2$  and  $l_2/2$ ), they are transmitted out of the port. (b) Example of an interferogram.

Moreover, the FTIR components are depicted in **Figure 4.10**. To obtain a FTIR spectra, a white light source is used. It hits a beam splitter (dichroic mirror), which splits the beam into a transmitted and a reflected beam. One of the beams will hit a fixed mirror, while the other reflects at a scanning mirror, constantly moving back and forth over a few millimeters. Then both reflected beams are recombined. When the waves spatially overlap, they interfere. The

combination of a beam splitter with one fixed and one moving mirror is called an (Michelson) interferometer. This interfering beam then hits the sample and, depending on the molecules present, some frequencies will be partially or completely absorbed. Consequently, the interference pattern of the transmitted beams is recorded resulting in an “interferogram”, which will be digitalized to the measuring computer. Finally, a fast Fourier transform will be applied, converting the interferogram into a graph in the frequency (or wavenumber) domain [3].

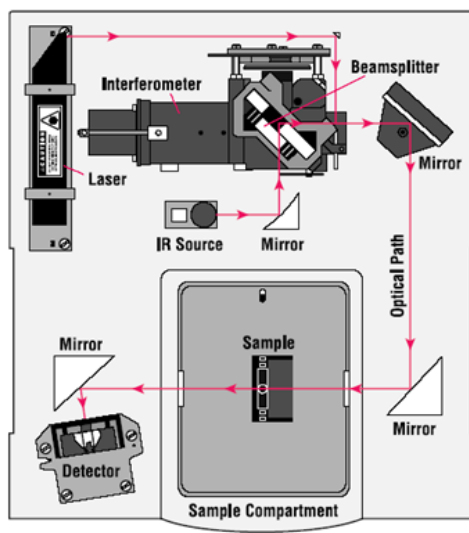


**Figure 4.10.** General representation of a FTIR spectrometer layout. Since the production of an accurate interferometer is expensive, a laser (HeNe) is used as internal reference source to solve this.

Moreover, the IR region of the spectrum is usually divided into three regions.

- Near-IR, between  $14,000\text{-}4000\text{ cm}^{-1}$ , which can excite overtone of harmonic vibrations
- Mid-IR, between  $4000\text{-}400\text{ cm}^{-1}$ , range where molecular structural vibrations can be studied.
- Far-IR, between  $400\text{-}100\text{ cm}^{-1}$ , close to the microwave region and of very low energy. Useful for rotational spectroscopy [2]–[4].

Therefore, the infrared region that provides information about functional groups in a molecule (structural vibrations) is the Mid-IR. We used the Bruker instrument

Tensor 37 (**Fig. 4.11**) with a Pike MIRacle ATR "cell" for loading small volumes ( $\mu\text{l}$ ). A potassium bromide (KBr) crystal was used as beamsplitter and deuterated triglycine sulfate (DTGS) as the detector.



**Figure 4.11.** Photograph of the FTIR spectrometer device used for identification of functional groups.

#### 4.1.1.1.3 Raman Spectroscopy

Raman spectroscopy is interesting for our experiments because it shows symmetry bands related to C60 that are normally not visible by means of infrared spectroscopy. It differs from IR spectroscopy because it is based on the inelastic scattering of photons by molecules rather than on the absorption of photons [9].

There are three types of scattering: i) Rayleigh, where photons are elastically scattered at same frequency and wavelength as the incident photons, ii) Stokes scattering, where the material absorbs energy and the emitted photon has a lower energy than the absorbed photon and, iii) Anti-Stokes Raman scattering, where the material loses energy and the emitted photon has a higher energy than the absorbed photon (**Fig. 4.12**).

In an electric field, the distortion of a molecule is determined by its polarizability  $\alpha$ . More precisely, if the strength of the field is  $E$ , then the molecule acquires an induced dipole moment (**Eq. 4.11**):

$$\mu = \alpha E \quad (\text{Equation 4.11})$$

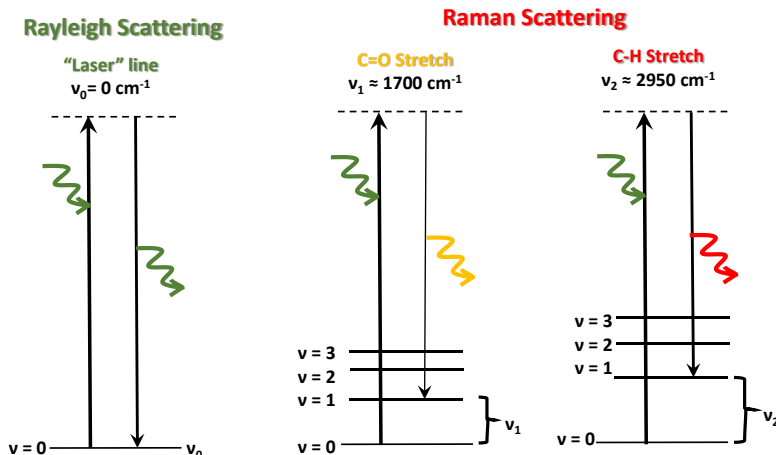


**Figure 4.12:** Energy level diagram, showing the states involved in scattering. The thickness of the line (up to down, going from the excited state and scattering towards ground state) is a rough approximate on the signal strength for different transitions [10].

Atoms are isotropically polarizable; this means that the same distortion is induced whatever the direction of the applied field is. The polarizability of a spherical rotor (*e.g.* molecule) is also isotropic. Nevertheless, non-spherical rotors have polarizabilities that do depend on the direction of the field relative to the molecule, so these molecules are anisotropically polarizable. Linear molecules are described by a single moment of inertia,  $J$ , which defines the magnitude of the rotational angular momentum. Nonlinear molecules (whether homo- or hetero-nuclear) present two moments of inertia and energy depends on a second rotational quantum number,  $K$ , which defines the vector component of rotational angular momentum along the principal symmetry axis. Both, linear and nonlinear molecules have anisotropic polarizabilities, and therefore are rotationally Raman active. Thus, the specific rotational Raman selection rules are:

$$\text{Linear rotors: } \Delta J = 0, \pm 2$$

$$\text{Symmetric rotors: } \Delta J = 0, \pm 1, \pm 2; \quad \Delta K = 0$$



Moreover, the  $\Delta J = 0$  transitions do not lead to a shift of the scattered photon's frequency in pure rotational Raman spectroscopy, and contribute to the unshifted Rayleigh radiation.

We can predict the form of the Raman spectrum of a linear rotor by applying the selection rule  $\Delta J = +2$ , the scattered radiation leaves the molecule in a higher rotational state, so the wavenumber of the incident radiation, initially  $\bar{\nu}_i$ , is decreased. These transitions account for the Stokes lines in the spectrum:

$$\bar{\nu}(J \rightarrow J + 2) = \bar{\nu}_i - \{F(J + 2) - F(J)\} = \bar{\nu}_i - 2B(2J + 3)$$

**(Equation 4.12)**

The Stokes lines appear to low frequency of the incident radiation and at displacements,  $6B, 10B, 14B, \dots$  from  $\bar{\nu}_i$  for  $J = 0, 1, 2, \dots$ . When the molecule makes a transition with  $\Delta J = -2$ , the scattered photon emerges with increased energy. These transitions count for the anti-Stokes lines of the spectrum [1, 9]:

$$\bar{\nu}(J \rightarrow J - 2) = \bar{\nu}_i + \{F(J) - F(J - 2)\} = \bar{\nu}_i + 2B(2J - 1)$$

**(Equation 4.13)**

Finally, the anti-Stokes lines occur at displacements of  $6B, 10B, 14B, \dots$  (for  $J = 2, 3, 4, \dots$ ;  $J = 2$  it is the lowest state that can contribute under the selection rule  $\Delta J = -2$ ) to high frequency of the incident radiation. In general, the Raman technique involves shining a monochromatic light source (e.g. Laser) on a sample and detecting the scattered light. The majority of the scattered light is of the same frequency as the excitation source, known as Rayleigh or elastic scattering. A very small amount of the scattered light ( $\sim 10^{-6}$  times the incident light intensity) is shifted in energy from the laser frequency due to interactions between the incident electromagnetic waves and the vibrational energy levels of the molecules in the sample. A plot of this "shifted" light vs frequency results in a Raman spectrum of the sample [10].

### 4.1.2 Electrophoresis

Besides an optical characterization, a structural characterization was necessary to determine whether functionalized DNA is linear or it adopts a secondary structure during the synthesis, which could affect the reproducibility of the electrical measurements. For this purpose, electrophoresis experiments were performed to analyse if the presence of one type of structure (one band at the expected molecular weight), degradation (a group of bands in a well) or secondary structures (a band at higher molecular weight) are in the synthetic solution.

When an electrical field is applied to a solution, the positive charged molecules will move towards the cathode while the negative charged molecules will move towards the anode. This displacement is called electrophoresis. Additionally, the speed of the molecules depends on two factors: i) the force that drives the movement,  $qE$ , applied by the electrical field over the particle, where  $q$  is the molecule charge [Coulombs], and the electrical field force,  $E$  [Volts/meter] and; ii) the force that resists the movement or the friction force,  $fv$ , produced by the particle's surroundings, while  $v$  is the speed of the particle and  $f$  is its friction coefficient. Such coefficient depends on the size and shape of the molecules. Therefore, large or asymmetrical molecules will present higher friction resistance than small or compact molecules.

With the activation of an electrical field, the molecule accelerates fast until it reaches a speed in which these forces are equilibrated, and then it will move constantly at that speed. A constant speed is determined by **Eq. 4.14**:

$$fv = qE \quad \text{(Equation 4.14)}$$

If we rewrite Eq. 4.14 as:  $v/E = q/f$ , we can then express the movement speed per force field unit,  $v/E$ . This coefficient is named the molecule electrophoretic mobility ( $\mu$ ).

$$\mu = \frac{v}{E} = \frac{q}{f} = \frac{Ze}{f} \quad \text{(Equation 4.15)}$$

The last term on **Eq. 4.15** refers to the charge over the molecule as a product of the electron (or proton) charge unit,  $e$ , by the number of charge units,  $Z$  (a positive or negative integer). From **Eq. 4.14**, it can be seen that the mobility of molecules depend on its charge and dimensions.

Agarose gel electrophoresis is the most common technique to separate nucleic acids in molecular biology where the gel works as a polymeric grid of controllable "pore size" and the nucleic acids migrate through it by means of an applied electrical field. In general, an agarose gel is mixed with a dye (gel red) and poured first within a template and after it solidifies, the gel is placed at a buffering solution. The samples (nucleic acid + dye + glycerol) are loaded carefully into the gel and finally, the gel is placed between the electrodes.

The purpose of the dye on the samples is to visually indicate the progress of the molecules migration during the electrophoresis while the glycerol allows to produce more dense samples that prevent mixing with the buffer solution. Finally, the current is maintained until the sample dye reaches the lowest part of the gel, and when the gel is illuminated with UV light, the gel red dye allows visualization of the nucleic acid migrated "bands" [11]. A descriptive scheme containing the steps to prepare an agarose gel is shown in **Fig. 4.13**.

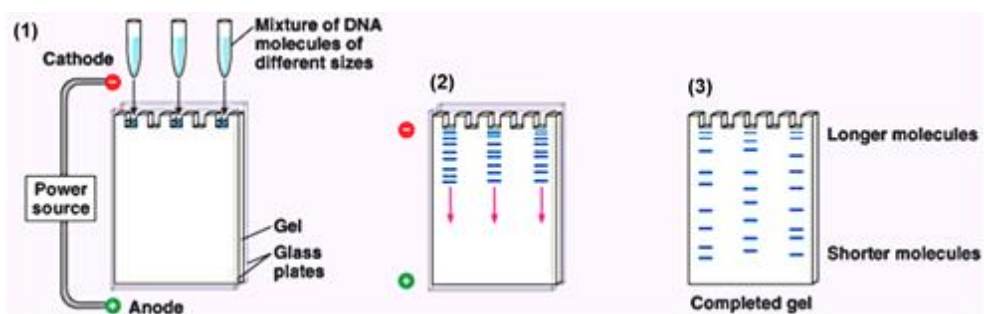


**Figure 4.13:** Representation of the procedure to prepare and load samples for performing a typical gel electrophoresis [12].

## 4.2 Scanning Probe Microscopy (SPM)

Scanning Probe Microscopy involves a collection of techniques in microscopy that can be used to visualize and manipulate objects as small as atoms on surfaces. Thus, SPM has much better resolution than electron microscopy. The way that the SPM interacts with the surface to obtain an image is called a mode [1]. In this thesis, the modes that were used were Scanning Tunneling Microscopy and Atomic Force Microscopy.

### 4.2.1 Scanning Tunneling Microscopy (STM)

In 1982, Binnig and Rohrer developed the first STM, at the IBM facilities in Zürich. The essential components on a STM are: *i*) a probe tip, of tungsten or Platinum-Iridium alloy, which is attached to *ii*) a piezodrive, which consists of three mutually perpendicular piezoelectric transducers (*x*-, *y*- and *z*-piezo). Upon applying a voltage, a piezoelectric transducer expands or contracts. By applying a sawtooth voltage on the *x*-piezo and a voltage ramp on the *y*-piezo, the tip scans on the *xy* plane (**Fig. 4.14**). Using the coarse positioner and the *z*-piezo, the tip and the sample are brought to each other within a fraction of a nanometer each other ( $\sim 0.4$ - $0.7$  nm distance between tip and sample, where the attractive and repulsive interactions are in equilibrium **Fig. 4.15**). The electron wavefunctions in the tip overlap with electron wavefunctions in the sample surface and a finite tunneling conductance is generated. Through applying a bias voltage between the tip and the sample a tunneling current is generated. The most common convention about the polarity of bias voltage is that the tip is virtually grounded. This means that the bias voltage  $V$  is the sample voltage. If  $V > 0$ , then the electrons are tunneling from the occupied states of the tip into the empty states of the sample. If  $V < 0$ , then the electrons are tunneling from the occupied states of the sample into the empty states of the tip.

Moreover, the tunneling current is converted to a voltage by the current amplifier, which is then compared with a reference value and the difference is amplified to drive the *z*-piezo. The phase of the amplifier is chosen to provide a negative feedback: if the absolute value of the tunneling current is larger than

the reference value, then the voltage applied to the z-piezo tends to withdraw the tip from the sample surface, and vice versa. This way, an equilibrium z position is established. As the tip scans over the xy plane, a two-dimensional array of equilibrium z positions, representing a contour plot of the equal tunneling-current surface, is obtained, displayed, and stored in the computer memory.

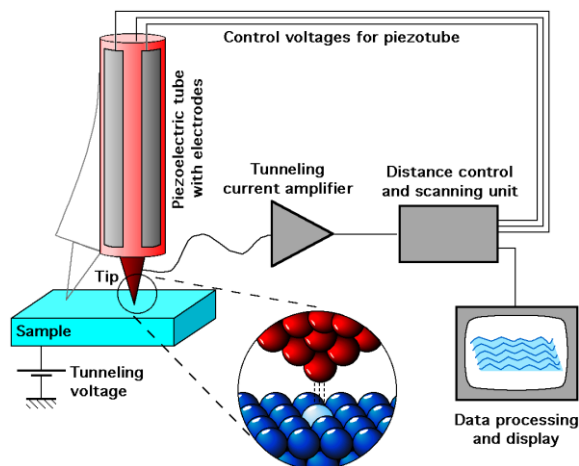


**Figure 4.14:** Representation of the components on a STM device [13].

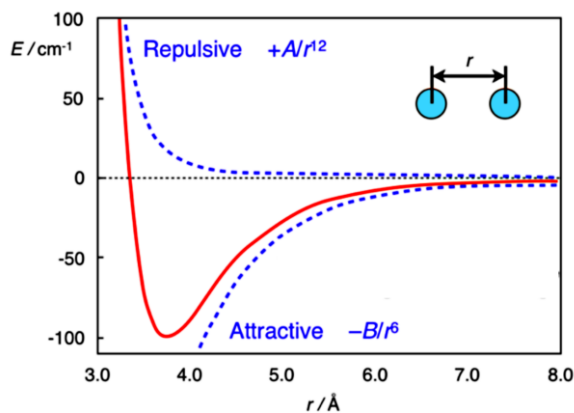


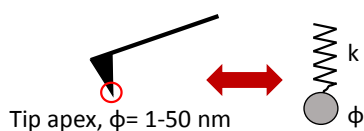
**Figure 4.15:** Plot of potential vs distance, representing the repulsive and attractive forces (according to a Lennard-Jones potential) [14].

The topography of the surface is displayed on a computer screen, e.g. a grey-scale image, where the bright spots represent the high z values (protrusions),

and the dark spots represent low  $z$  values (depressions). The  $z$  values corresponding to the gray levels will be indicated by a scale bar. The most convenient unit for  $x$  and  $y$  is nanometer (nm,  $1 \times 10^{-9}$  m), and the most convenient unit for  $z$  is picometer (pm,  $1 \times 10^{-12}$  m). In order to achieve an atomic resolution, vibration isolation is essential. This is achieved by making the STM unit as rigid as possible and by reducing the influence of environmental vibrations to the STM unit [1, 15–17]. An example of an STM application is the quantization of band structure for ZnO clusters by Schouteden *et al.* [18].

#### 4.2.2 Atomic Force Microscopy (AFM)

Despite the high resolution of the STM, its application was restricted for conductive samples. To overcome this limitation, Binnig *et al.* [19] developed the Atomic Force Microscope, originally conceived as a very sensitive profilometer that operates using a sharp tip in a close proximity to a sample surface, so that their interaction can be measured in either conducting or insulating areas [20]. Some modifications have been done from the first AFM to the current devices. In general, an AFM involves a flexible cantilever positioner that can be controlled by a vertical piezoelectric ( $z$ -scanner). The piezoelectric is at the same time modulated with a potential voltage, thus if it expands it will exert a force on the cantilever. This force will be in balance between the probe interaction with the surface (**Fig. 4.7**) and the load on the cantilever [15, 19–21]. The flexible cantilever will bend proportionally to the force acting upon it, in accordance to Hooke's law, where forces can be converted into deflections of a spring (**Eq. 4.11**):



$$\Delta z = \frac{\Delta F}{k} \quad (\text{Equation 4.16})$$

Then the deflection,  $\Delta z$ , is determined by the acting force,  $\Delta F$ , and the spring constant  $k$ . The resonant frequency of a spring with  $k$  and an effective mass  $m$  is given by:

$$\omega_0 = \sqrt{\frac{k}{m}} \quad (\text{Equation 4.17})$$

Generally, to measure vertical and horizontal deflection of the cantilever, most AFMs use the optical lever, a device that achieves resolution comparable to an interferometer while remaining inexpensive and easy to use (**Fig. 16a**). The optical lever operates by reflecting a laser beam off the back of the cantilever (**Fig. 4.16b**). Angular deflection of the cantilever causes a twofold larger angular deflection of the laser beam. Then, the reflected laser beam strikes a photodetector (position-sensitive) consisting of four side-by-side photodiodes. The difference between the four photodiode signals indicates the position of the laser spot on the detector, thus the angular deflection of the cantilever. If the tip is scanned over the sample surface then the deflection of the cantilever can be recorded as an image of the sample surface (deflection image) (**Fig. 4.16c-d**). In addition, an AFM not only measures the force on the sample but also regulates it, allowing acquisition of images at very low forces [19, 20].

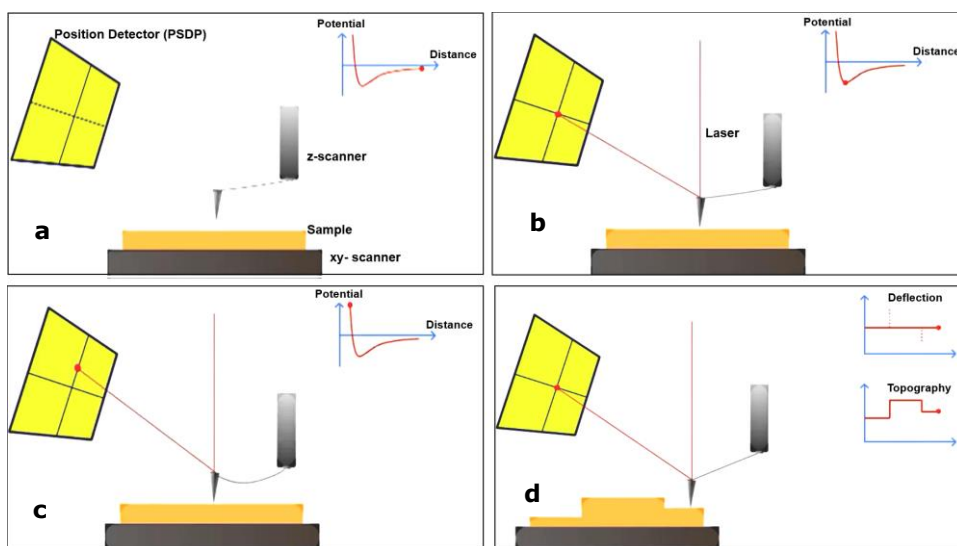


**Figure 4.16:** Schematic diagram of an AFM setup and operation. **(a)** Components of an AFM are: *i*) the vertical piezoelectric (z-scanner), *ii*) a horizontal piezoelectric (xy-scanner) to support the sample and *iii*) PSPD detector. **(b)** When a laser beam is illuminated on the cantilever, changes from the stationary position (equilibrium between repulsive and attractive forces) can be observed on the PSPD. **(c)** Angular deflection of the beam in the range of the repulsive interactions. **(d)** After surface analysis, changes on the deflection are directly correlated with the surface topography [22].

Along the years, it has been demonstrated that AFM is also powerful a tool for biochemical and biological research due to the combination of high resolution and the ability to work under physiological conditions avoiding complex sample preparation procedures and artifacts connected to them when comparing to other techniques such as Scanning Electron Microscopy and Transmission Electron Microscopy. It is currently the only technique allowing obtaining subnanometric resolutions in a physiological environment.

Additionally, it can evaluate intermolecular interaction forces using the force spectroscopy, or characterize single molecules under tensile or torsional load, interaction of surfaces with molecules [23], and cell-cell interactions [24], etc. The most studied biological samples by AFM range from biomolecules (phospholipids [25], proteins, DNA [26], chromosomes, etc.) to subcellular structures (native membranes), all the way up to living cells and tissues [15, 20]. The applications of AFM depend on the scan modes, determined by the type of interaction on the surface, thus the main modes are: Contact (potential range of repulsive forces), Non-contact (potential range of attraction forces) and intermittent-contact (between contact and non-contact modes).

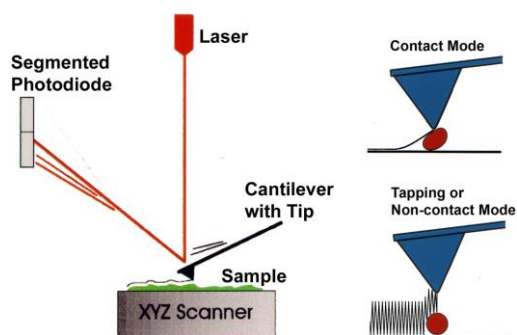


**Figure 4.17:** Representation of an AFM scanning a surface with either contact or non-contact mode [27].

#### 4.2.2.1 Contact Probe Atomic Force Microscopy (C-AFM)

Contact mode or static mode, occurs when an AFM tip makes a soft “physical contact” with the surface. The tip is attached to the end of a cantilever with a



low spring constant, lower than the effective spring constant holding the atoms of the sample together. While the tip scans across the sample, it measures the static deflection of the cantilever in accordance to the surface topography.

At the right side of the curve from **Fig. 4.17**, the atoms are separated by a large distance and the potential is negative. Next, the atoms are gradually brought together, attracting weakly each other (van der Waals forces). This attraction increases until the atoms are so close together that their electronic orbitals begin to repel each other electrostatically until the potential reaches its minimum value (distance between atoms  $\sim$ length of a chemical bond). When the potential values are positive (repulsive forces), the atoms are in contact and the slope of the curve becomes very steep. This means that the interacting forces compensate for almost any force that attempts to push the atoms close together. Moreover, in AFM it is understood as when the cantilever pushes the tip against the sample, the cantilever bends rather than forcing the tip atoms closer to the sample atoms. Other forces that are also present in contact mode are: a capillary force related to the thin water layer (environment) and the force applied by the cantilever itself [21].

In contact mode, when imaging a sample surface, the applied force is kept constant by the feedback system (the set point is fixed at a given value) and the images are obtained by recording the vertical position of the piezoactuator required to maintain the force constant, the corresponding image is called "Height image". In constant height mode, the z-piezo movement is kept constant and an image is generated from the cantilever deflection. To avoid artifacts, the error mode based on the error signal can be used, where the cantilever deflection signal is recorded keeping the feedback response time as fast as possible.

The error signal gives a measure of how the feedback system is maintaining the desired deflection set point constant. Due to several parameters, such as issues related to changes of the scan frequency or feedback loop parameters, etc., the cantilever will not be always at the same deflection value (constant force) generating an error signal, which can be exploited to obtain an image rich in

information, the corresponding image is called “deflection image”. For example, such image is used if one wants to observe small features while recording voluminous object such as living cells [20].

To evaluate the applied force, one can exploit this laser beam in the following ways. In static mode, one measures the arrow at the loose lead of the beam corresponding to the inflection of this one. For weak deflections, the force is simply obtained by multiplying cantilever stiffness and its deflection. In order to reach the mechanical properties of the analysed materials, basic models are built starting from more or less complex combinations of springs (sample and probe). These models can lead to qualitative evaluations of local elastic modulus and to friction coefficient measurements. In the majority of cases, one cannot avoid the wear of surface nor that of the tip what leads to plastic deformations and/or permanent deformations. Thus, it is extremely difficult to be able to image soft materials in air with this mode.

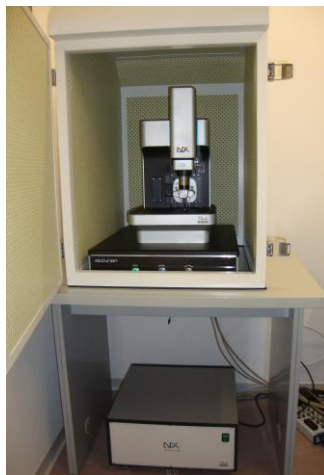


**Figure 4.18:** Photograph of the NX10 AFM device used for C-AFM and NC-AFM measurements.

#### 4.2.2.1.1 Conductive Probe Atomic Force Microscopy (I-AFM)

For a macroscopic sample, the resistance can be measured by using a multimeter with probes or alligator clips to contact the sample. The simplest

configuration is when the multimeter applies a small voltage between the two probes. As a result, a current through the sample will be measured and converted to a resistance via Ohm's law,  $R = V/I$ . I-AFM represents an extension of this basic concept, where a sharp conductive probe with a contact area of about  $15 \text{ nm}^2$  is used to electrically connect to nanostructures on a sample surface. The counter-electrode is normally a microfabricated wire on the sample surface or a conducting substrate. A voltage is then applied between the electrodes, and the current is measured. This approach allows combining AFM imaging of the surface topography with a nanometer-scale precision to position a probe on the sample. Consequently, small groups of molecules and even individual molecules can be studied through I-AFM. The advantage of I-AFM over STM is that insulating, semiconductor and conductor molecules can be measured without a prior knowledge on their electrical behaviour and it does not require an ultra-high vacuum chamber, thus measurements can be performed in inert environment at room temperature. Another abbreviation of I-AFM is C-AFM but for the sake of clarity, we will only use the I-AFM acronym for conductive-AFM mode in the following chapters.

Furthermore, the force applied by the probe is an important factor during the measurement. The force should be strong enough that results in an electrical contact, but soft enough to prevent damage in the sample. Therefore, an I-AFM contains force-feedback electronics to keep a constant force during the AFM imaging. On the other hand, contacts play a critical role in determining transport behaviour. This is the alignment of the electrode's Fermi level with the HOMO-LUMO levels of the molecules and the nature of the bond between molecules and electrodes largely determine the magnitude of the energetic barriers which exist at the molecule-electrode interfaces. In addition, I-AFM can be used to compare between molecules with different molecule-electrode couplings [28].

First experiments performed in this mode were performed in 1992 for investigating the dielectric strength of  $\text{SiO}_2$  gate oxide films [29]. Basically, I-AFM operates in C-AFM mode by using an AFM tip, coated with an electrical conductor material, as a movable electrode. The contact tip is approached in contact with the sample surface with a user-specified applied force. Next, the z-

feedback maintains a constant force to scan the surface. Then, the current-voltage ( $I$ - $V$ ) characteristics are acquired at fixed points on the surface by applying a voltage between the AFM tip and a fixed counter electrode, and measuring the resulting current between the electrodes. Current values can vary from pico- to hundreds of nano-Amperes. Normally, the resistance of the tip-sample junction is calculated from the inverse slope of the  $I$ - $V$  trace, according to Ohm's law, at small voltages where the  $I$ - $V$  behaviour is usually linear. The built-in preamplified scanner head measures the current passing through the tip and sample [28, 29]. Typically, there are two configurations to perform I-AFM measurements:

- Vertical configuration (**Fig. 4. 19a**): a conducting substrate is used as counter-electrode. Normally used for SAMs. Mainly used for comparison between molecules in search for structural variations and thus, changes in the charge transport.
- Horizontal configuration (**Fig. 4.19b**): currents are measured between the AFM tip and a metallic contact pad on top of an insulating substrate surface. The nanostructure of interest bridges the electrode gap between the movable AFM tip and the contact on the surface. Normally implemented to study nanostructures.

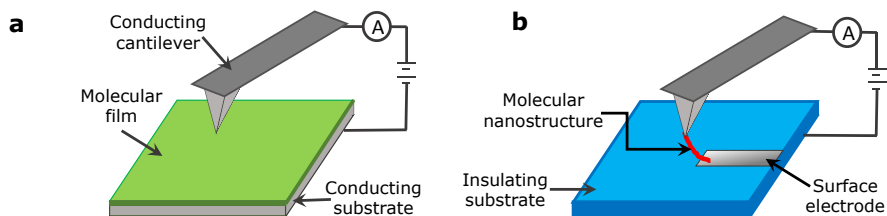


**Figure 4.19. I-AFM configurations (a)** Vertical type, where a molecular film is placed on top of a conducting substrate (electrode, green) to be locally probed with a conducting cantilever and, **(b)** Horizontal type, where an electrode is placed on top of an insulating substrate (blue) and the conducting cantilever locally approaches the molecular nanostructure of interest [28].

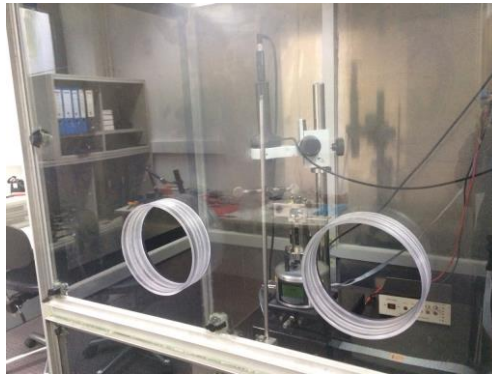


**Figure 4.20:** Photograph of the actual Bruker Multimode 8 device used for I-AFM measurements.

### 4.3 Conclusions

- The most common experimental techniques in biochemistry and biophysics are based on optical spectroscopy, electrophoresis and scanning probe microscopy.
- In spectroscopy a photon can experience absorption (UV-vis, IR), emission or scattering (Raman effect).
- Electrophoresis is based on electrical fields, where positive charged molecules migrate to the cathode and negative charged molecules migrate to the anode.
- Scanning Probe Microscopy, composes a group of techniques to visualize and manipulate objects as small as atoms on surfaces.
  - Scanning Tunneling Microscopy (STM) is restricted to conducting surfaces.
  - Atomic Force Microscopy (AFM) is useful for surfaces ranging from insulator to conductor and it is also adaptable for liquid or dry conditions. It relies on attraction and repulsion forces interacting on a surface. Consequently, different modes have been developed exploiting the interactions and type of approach to the surface (e.g. Contact mode

and Conductive AFM). I-AFM works according to the AFM principle with the additional option to measure the electrical conductivity between tip and sample.

#### 4.4 References

- [1] P. Atkins and J. de Paula, *Atkin's Physical Chemistry*, 8th ed. New York, USA.: Oxford University Press, 2006.
- [2] B. Averill and P. Eldredge, *General Chemistry: Principles, Patterns and Applications*, V.1.0 (2 v). Flat World Education, Inc, 2015.
- [3] B. Stuart, *Infrared Spectroscopy: Fundamentals and Applications*. Wiley-VCH Verlag and Co. KGaA, 2004.
- [4] D. A. Skoog, F. J. Holler, and T. A. Nieman, *Principles of Instrumental Analysis*, 5th ed. New York, USA.: Saunders College Publishing, 1997.
- [5] J. McMurry, *Organic Chemistry*, International USA: Brooks/Cole (Thomson Learning), 2004.
- [6] T. Owen, "Fundamentals of UV-visible spectroscopy," *Agilent Technologies*, 2000. [Online]. Available: [http://www.chem.agilent.com/Library/primers/Public/59801397\\_020660.pdf](http://www.chem.agilent.com/Library/primers/Public/59801397_020660.pdf). [Accessed: 22-Mar-2015].
- [7] D. Harvey, "10.A: Overview of Spectroscopy," *National Science Foundation: Advancing Undergraduate Chemistry Education with Dynamic Open-Access ChemWiki HyperTextbooks.*, 2013. [Online]. Available: [http://chemwiki.ucdavis.edu/Analytical\\_Chemistry/Analytical\\_Chemistry\\_2.0/10\\_Spectroscopic\\_Methods/10A%3A\\_Overview\\_of\\_Spectroscopy](http://chemwiki.ucdavis.edu/Analytical_Chemistry/Analytical_Chemistry_2.0/10_Spectroscopic_Methods/10A%3A_Overview_of_Spectroscopy). [Accessed: 08-May-2015].
- [8] Sobarwiki, "Schematic of UV-visible spectrophotometer," [http://en.wikipedia.org/wiki/Ultraviolet%E2%80%93visible\\_spectroscopy](http://en.wikipedia.org/wiki/Ultraviolet%E2%80%93visible_spectroscopy), 2014. [Online]. Available: "<ahref='http://commons.wikimedia.org/wiki/File:Schematic\_of\_UV-visible\_spectrophotometer.png#/media/File:Schematic\_of\_UV-visible\_spectrophotometer.png'>Schematic of UV-visible spectrophotometer</a>" by <a href="//commons.wikimedia.org/wiki/User:Sobar">Sobar. [Accessed: 22-Mar-2015].
- [9] F. Siebert and P. Hildebrandt, "Theory of Infrared Absorption and Raman Spectroscopy," in *Vibrational Spectroscopy in Life Science*, Weinheim, Germany: Wiley-VCH Verlag GmbH & Co. KGaA, pp. 11–61, 2007.

- [10] "An Introduction to Raman for the Infrared Spectroscopist," *InPhotonics*, 1999. [Online]. Available: <http://www.inphotonics.com/technote11.pdf>. [Accessed: 21-Mar-2015].
- [11] K. C. Mathews, K. E. van Holde, and K. G. Ahern, *Bioquímica*, 3rd ed. Madrid, España: Pearson Educacion, S. A., 2002.
- [12] B. Guess, "Gel Electrophoresis," *Cellular Physiology*, 2015. [Online]. Available: <https://cellularphysiology.wikispaces.com/Gel+Electrophoresis>.
- [13] M. Schmid, "Schematic view of an STM," *Creative Commons Attribution ShareAlike 2.0 Austria License.*, 2005. [Online]. Available: "<a href='\"http://commons.wikimedia.org/wiki/File:ScanningTunnelingMicroscope\_schematic.png#/media/File:ScanningTunnelingMicroscope\_schematic.png\"'>ScanningTunnelingMicroscope\_schematic</a>" by <a href='\"//commons.wikimedia.org/wiki/User:Schmid\"' title='\"User:'
- [14] "Molecular Interactions," *Cambridge MedChem Consulting*. [Online]. Available: [http://www.cambridgemedchemconsulting.com/resources/molecular\\_interactions.html](http://www.cambridgemedchemconsulting.com/resources/molecular_interactions.html). [Accessed: 23-Mar-2015]
- [15] C. J. Chen, *Introduction to Scanning Tunneling Microscopy Second Edition*, 2nd ed. New York, USA.: Oxford University Press, 2008.
- [16] G. Binnig, H. Rohrer, C. Gerber, and E. Weibel, "Tunneling through a controllable vacuum gap," *Appl. Phys. Lett.*, vol. 40, no. 2, pp. 178–180, 1982.
- [17] G. Binnig, H. Rohrer, C. Gerber, and E. Weibel, "Surface studies by scanning tunneling microscopy," *Am. Phys. Soc.*, vol. 49, no. 1, pp. 57–61, 1982.
- [18] K. Schouteden, Y.-J. Zeng, K. Lauwaet, C. P. Romero, B. Goris, S. Bals, G. Van Tendeloo, P. Lievens, and C. Van Haesendonck, "Band structure quantization in nanometer sized ZnO clusters.," *Nanoscale*, vol. 5, no. 9, pp. 3757–63, 2013.
- [19] G. Binnig and C. F. Quate, "Atomic force microscope," *Phys. Rev. Lett.*, vol. 56, no. 9, pp. 930–933, 1986.
- [20] T. Cohen-Bouhacina and A. Maali, "AFM imaging in physiological environment from biomolecules to living cells," *Chapter 28 in Soft Matter Characterization*. 1<sup>st</sup> ed., R. Borsali and A. MaAli, Eds., Springer Netherlands, pp. 1379–1438, 2008.
- [21] "The principles of Atomic Force Microscopy ( AFM )," *Noppa Aalto Finland*, 2012. [Online]. Available: [https://noppa.aalto.fi/noppa/kurssi/tfy-125.4314/lisatty12701/Tfy-125\\_4314\\_principles\\_of\\_afm.pdf](https://noppa.aalto.fi/noppa/kurssi/tfy-125.4314/lisatty12701/Tfy-125_4314_principles_of_afm.pdf).

- [22] "AFM Principle-Basic Training," 2014. [Online]. Available: <https://www.youtube.com/watch?v=s6KqJS1GZNE>. [Accessed: 23-Mar-2015].
- [23] M. Peeters, S. Kobben, K. L. Jiménez-Monroy, L. Modesto, M. Kraus, T. Vandenryt, A. Gaulke, B. van Grinsven, S. Ingebrandt, T. Junkers, and P. Wagner, "Thermal detection of histamine with a graphene oxide based molecularly imprinted polymer platform prepared by reversible addition-fragmentation chain transfer polymerization," *Sensors and Actuators B Chem.*, vol. 203, pp. 527–535, 2014.
- [24] K. Eersels, B. van Grinsven, A. Ethirajan, S. Timmermans, K. L. Jiménez-Monroy, J. F. J. Bogie, S. Punniyakoti, T. Vandenryt, J. J. A. Hendriks, T. J. Cleij, M. J. A. P. Daemen, V. Somers, W. De Ceuninck, and P. Wagner, "Selective identification of macrophages and cancer cells based on thermal transport through surface-imprinted polymer layers," *ACS Appl. Mater. Interfaces*, vol. 5, no. 15, pp. 7258–7267, 2013.
- [25] P. Losada-Pérez, K. L. Jiménez-Monroy, B. van Grinsven, J. Leys, S. D. Janssens, M. Peeters, C. Glorieux, J. Thoen, K. Haenen, W. De Ceuninck, and P. Wagner, "Phase transitions in lipid vesicles detected by a complementary set of methods: heat-transfer measurements, adiabatic scanning calorimetry, and dissipation-mode quartz crystal microbalance," *Phys. Status Solidi Appl. Mater. Sci.*, vol. 211, no. 6, pp. 1377–1388, 2014.
- [26] B. van Grinsven, N. Vanden Bon, H. Strauven, L. Grieten, M. Murib, K. L. Jiménez-Monroy, S. D. Janssens, K. Haenen, M. J. Schöning, V. Vermeeren, M. Ameloot, L. Michiels, R. Thoelen, W. De Ceuninck, and P. Wagner, "Heat-transfer resistance at solid-liquid interfaces: A tool for the detection of single-nucleotide polymorphisms in DNA," *ACS Nano*, vol. 6, no. 3, pp. 2712–2721, 2012.
- [27] H. Greenwood Hansma, "Research on biological atomic force microscopy." [Online]. Available: <http://web.physics.ucsb.edu/~hhansma/biomolecules.htm>. [Accessed: 25-Mar-2015].
- [28] J. M. Mativetsky, M. Palma, and P. Samorì, "Exploring electronic transport in molecular junctions by conducting atomic force microscopy," *Top Curr. Chem.*, vol. 285, pp. 157–202, 2008.
- [29] M. P. Murrell, M. E. Welland, S. J. O. Shea, T. M. H. Wong, J. R. Barnes, A. W. Mckinnon, M. Heyns, and S. Verhaverbeke, "Spatially resolved electrical measurements of SiO<sub>2</sub> gate oxides using atomic force microscopy," *Appl. Phys. Lett.*, vol. 62, no. 7, pp. 786–788, 1993.



## Chapter 5

# Synthesis and characterization of DNA-fullerene complexes

The importance of the composition of molecular wires was briefly mentioned in **Chapter 2**. This chapter focuses on the experimental design and parameters. In order to study the electrical characteristics in single DNA molecules, it is necessary to identify the most suitable moiety that can produce: *i*) single DNA molecules with a strong interaction with metallic electrodes, *ii*) serve as an electron donor-acceptor to the DNA, and *iii*) allows the DNA molecule to maintain its native structure, even in semi-dry environment. For this purpose, the moiety should have a covalent bond with the DNA to permit a suitable alignment of molecular orbitals between the functional group, the DNA and the conducting surface. A material that fulfils these requirements are fullerenes, which have been already studied in systems containing organic molecules for photovoltaic applications [1, 2]. Additionally, it was one of the first single molecules to be electronically characterized [3, 4] and categorized as an electromechanical amplifier [5]. Moreover, factors such as the DNA sequence and salt concentration also play a critical role on the construction of molecular wires, as well as the environment (*i.e.* temperature, air or inert atmosphere) and humidity conditions.

### 5.1 Why Fullerene to prepare single DNA molecules?

Since the discovery of fullerenes [6], their electronic properties and possible applications have been found to range from pure physics to medical applications, emerging in the new field of "fullerene chemistry". The criteria to choose fullerenes above other functionalities (*e.g.* thiols, amines and carbon nanotubes), are listed below.

### 5.1.1. Single molecules and contact with metallic surfaces

Fullerene derivatives generally retain the main features of C<sub>60</sub>, such as: *i*) well-defined three dimensional architecture, *ii*) large hydrophobic mass and, *iii*) unique electronic properties [7, 8].

These derivatives offer the possibility of incorporating useful functionalities for further chemical manipulation of groups, and modify the physical characteristics of C<sub>60</sub> (*e.g.* improved solubility in polar solvents [9]). In addition, fullerene derivatives exhibit a range of interesting biological functionalities, including inhibition of HIV enzymes [10, 11], photoinduced cytotoxicity [10–21], DNA cleavage [22–24], and antibacterial and antitumoral activity [25] among others.

Our first interest to prepare single DNA molecules with terminal fullerene groups rose from the elegant approach by Leary *et al.* [26]. In this experiment, the conductance of single, small organic molecules was measured with a Scanning Tunneling Microscope (STM) at room temperature, on top of a gold substrate. Interaction between the gold STM tip and one terminal fullerene was clearly observed as a highly reproducible break junction type of experiment (attachment, elongation and final detachment = changes in conductance).

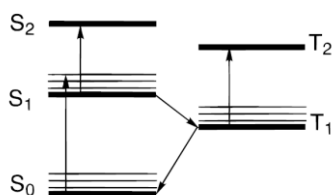
In addition, Martin and co-workers [27] demonstrated that for break junction experiments, the use of C<sub>60</sub> provides better junction stabilities and less fluctuations at the anchoring sites. Thus, leading to lower charge spread in low bias conductance compared to thiol [28] and amine functionalities [29]. Furthermore Rogero *et al.* [30] demonstrated that C<sub>60</sub> and Au (111) have a strong interaction, showing that at in presence of gold, C<sub>60</sub> shows a differential spectra value of 2.3 eV between HOMO-LUMO gap, with the LUMO level located at 0.6 eV above the Fermi level of gold. This was a consequence of the electronic charge transfer between the substrate and C<sub>60</sub>. An experiment that exploits this interaction was published in 2005 [31], where the movement of single-molecule nanocars was controlled on a gold surface using changes of temperature.

Moreover, the specific functionalization of the C<sub>60</sub> to generate a [6-6]-closed derivative (retaining its original 60 $\pi$  electronic system) with one carboxylic acid functionality, is of great advantage for biological applications [32]. A standard EDC-NHS reaction is sufficient to produce a covalent amide bond between an amine-terminated biomolecule (DNA) and the C<sub>60</sub> carboxylic acid in water based solvents. Note that this type of chemical reaction does not lead to additional side products or unwanted ramifications.

### 5.1.2. Electron donor-acceptor behaviour

One of the interesting features in fullerenes is their electron-acceptor capability in both, solid state and in solution. For example, C<sub>60</sub> shows strong absorption in the UV region and weaker but significant bands in the visible region. If C<sub>60</sub> is functionalized, it retains the same characteristics but the absorption of its derivatives will extend into the near-IR region. This means that C<sub>60</sub> and its derivatives are easily excited by low-energy light, rendering them as appealing partners in photoinduced electron transfer and in medicinal chemistry [7].

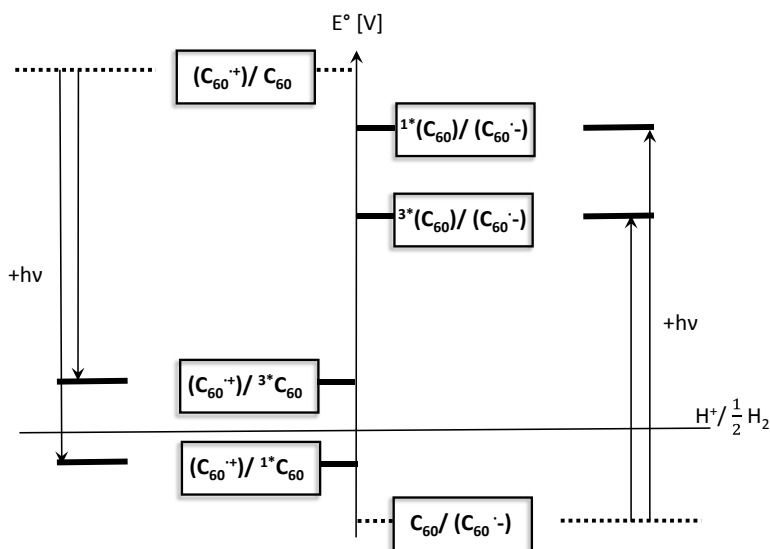
When excited with UV or visible light, the C<sub>60</sub> ground state ( $S_0$ ) population is pumped to the singlet excited state ( $S_1$ , **Scheme I**). Its intermediate state ( $S_2$ , lifetime in the order of nanoseconds) converts rapidly to the triplet excited state ( $T_1$ , lifetime of tens to hundreds of microseconds) with nearly unit yield. In the case of a C<sub>60</sub> functionalization, a perturbation in the fullerene  $\pi$ -system will produce shifts of the excited-state absorptions to lower energies (blue spectral region) compared to C<sub>60</sub> [7]:



**Scheme I.** Ground state and excited states of fullerenes [7].

Moreover, C<sub>60</sub> is an excellent electron acceptor in the ground state and can accept, reversibly, up to six electrons [7]. In particular, the HOMO-LUMO energy

gap is about 1.8 eV, separating a maximal degenerated and fully occupied HOMO from a degenerate LUMO. In contrast, oxidation is more difficult. It is usually limited to two one-electron steps, yielding the di-cation as the highest oxidation state. The redox features of the excited states are of great importance for photoinduced electron- and energy-transfer reactions (**Scheme II**). Population of the excited states (singlet,  $\sim 1.9$  eV, or triplet, 1.5 eV) indicates that an excited fullerene molecule is a better electron acceptor and electron donor compared to the ground-state species. Thus, C<sub>60</sub> displays features of a three-dimensional electron acceptor, which can be used as electron relay or accumulator. Additionally, as observed by Guldi and Prato, materials involving  $\pi$ -conjugated polymers with C<sub>60</sub> results in very fast photoinduced electron-transfer processes, which could be of interest to develop fullerenes as multifunctional electron storage moieties in well-ordered composites [7].



**Scheme II.** Diagram showing the difference in the redox properties between the ground-state  $C_{60}\{E_0[(C_{60})/(C_{60}^{\cdot-})]/E_0[(C_{60}^{\cdot+})/(C_{60})]\}$  and the excited  $1^*C_{60}$  and  $3^*C_{60}$  States [7].

### 5.1.3. Absence of interference with DNA structure

Earlier experiments to study charge transfer in DNA involved metal compounds that intercalated themselves within the DNA structure, affecting the typical  $\pi$ - $\pi$  orbital stacking [33–35]. To overcome this problem, we chose fullerene groups

linked to the terminal sides of the DNA in order to study the main mechanism of charge transport through DNA.

In this context, Shin *et al.* performed a set of experiments, testing the effect of fullerene groups covalently attached to the terminal ends of DNA in aqueous solutions. They observed that besides of the fact that fullerenes do not interfere with the DNA stacking, in acidic or basic media the DNA structure will compact or stretch respectively, rendering "DNA nanomachines" [36, 37].

## 5.2 Optimization of chemical functionalization

The compounds: C60-CHCOOH (C61), N-Hydroxysuccinimide (NHS), and 1-Ethyl-3-(3-dimethyl-aminopropyl)-carbodiimide (EDC), 2-N-morpholino-ethane sulfonic acid (MES) and Phosphate buffered saline (PBS) buffers were purchased from Sigma-Aldrich Co (Sigma-Aldrich BVBA Diegem, Belgium). Two types of DNA sequences (ssDNA) were purchased from Eurogentec (Liège, Science Park; Belgium). The single stranded DNA sequences that we used for this experiment are:

- **Type 1.** Standard length size of a DNA hybridized structure~ 12 nm.

- Hairpin A, 27 bp (**HpA**)

5'-GTC AGC AAG TTC CTG TGC TGA CCT TCC-3'-C<sub>6</sub>H<sub>13</sub>(CH<sub>2</sub>OH)NH<sub>2</sub>

- Hairpin B, 27 bp (**HpB**)

5'-TTT GGG ACA GCA CAG GAA CTT GCT GAC-3'-C<sub>6</sub>H<sub>13</sub>(CH<sub>2</sub>OH)NH<sub>2</sub>

- **Type 2.** Standard length size of a DNA hybridized structure~ 39 nm.

- Forward 102 bp (**Fwd**):

5'-GGG GAC TCG CCA TTC ACC ATC CGC ACA GAA GTG ATG GGG GGC CCC GAG  
TCC CGC GGC GTC CTG CGC AAG ATG AGC GAC CTG CTG GAG CTG ATG GTG  
AAG CGC-3'-C<sub>6</sub>H<sub>13</sub>(CH<sub>2</sub>OH)NH<sub>2</sub>

- Backward 102 bp (**Bwd**):

5'-GCG CTT CAC CAT CAG CTC CAG CAG GTC GCT CAT CTT GCG CAG GAC GCC  
GCG GGA CTC GGG GCC CCC CAT CAC TTC TGT GCG GAT GGT GAA TGG CGA  
GTC CCC-3'-C<sub>6</sub>H<sub>13</sub>(CH<sub>2</sub>OH)NH<sub>2</sub>

Note that the spacer groups, such as  $C_6H_{13}(CH_2OH)NH_2$  are necessary in order to introduce only one amine terminal group to this type of DNA. Also, it is important to mention that type 1 of DNA hairpins is not fully complementary while type 2 sequences are fully complementary.

The original idea behind using DNA hairpins, was to exploit the structural changes from the single stranded form (compact and ball type of shape) to the more linear structure in presence of a complementary strand (wire type of shape for double stranded DNA) in liquid. In presence of their fully complementary sequences, hybridization occurs spontaneously while with mismatched sequences, hairpins will prefer to keep their conformation or hybridize in slower rates rendering different shapes on the surface. These changes should be able to be tracked with very sensitive AFM devices on isolated chambers with controlled temperatures. However, after several attempts the Park AFM NX10 was not suitable for performing this type of experiments on liquid or conductivity measurements, as will be described in detail in **Chapter 7**. To overcome this problem, "linear" DNA sequences with longer sizes (**Type 2**) were designed and successfully tested as molecular wires in a Bruker Multimode 8 AFM.

### 5.2.1 Protocol 1: Functionalization of fullerenes with DNA.

C61 was sonicated in milliQ-water and the well solubilized fraction (0.8 mg/ml) was transferred to another tube. Next, type 1 of DNA (HpA) was mixed with EDC in MES buffer to a final concentration of 5 pmol/ $\mu$ l (pH= 6.5). Then C61 fraction was added, allowing the reaction to take place for one hour. The same procedure was repeated for HpB and afterwards, HpA and HpB were hybridized for 2 h at 4°C.

The immobilization step consisted on drop-casting the mixture to the surface for 2 hours at 4°C. After repeated washing steps with milliQ-water, the sample was dried with a nitrogen flow and later analysed under the AFM (section 5.3.2.3 and 5.3.3.1). The motivation to perform this procedure in bulk was based on the strong adsorption of fullerenes to the surface, thus non-specific molecules present on the surface (*e.g.* EDC and MES salts) were expected to be washed

away, leaving only the molecules of interest. Unfortunately this was not the case and several particles (of different dimensions) were observed to remain on the substrate, thus a new protocol was required.

### 5.2.2 Protocol 2: Selective functionalization of fullerenes with DNA.

This protocol is based on experiments of Shin *et al.* [36]. First, the C61 was sonicated for 30 min in milliQ water and then centrifuged for 20 min at 4400 rpm. Then, the well dispersed supernatant solution ( $0.3 \text{ mg mL}^{-1}$ ) was sonicated for 30 min in the presence of EDC and NHS to form a labile intermediate. The pH was raised to 7.2 and aminoalkyl-modified DNAs in the presence of 0.15 M PBS were added to a final concentration of  $0.5 \text{ mg mL}^{-1}$ . After the reaction at room temperature for 24 h, the reaction mixture was centrifuged for 20 min at 5400 rpm to remove any type of aggregation cluster.

The supernatant fraction from the last centrifugation was purified for the unreacted compounds, namely unreacted fullerene, DNA and salts, using a dialysis method for 7 days at room temperature, (molecular weight cut off (MWCO) = 12000-14000). This protocol produced the best results on single molecules of fullerene-double stranded DNA for all the experiments from **Chapter 6**, section 6.7.

### 5.2.3 Characterization of DNA-fullerene complexes

Samples of protocol 1 were only analysed through UV-vis spectroscopy where broad bands were obtained. Therefore, samples synthesized with protocol 1 were discarded. On the other hand, samples from protocol 2 were investigated by the techniques described in Chapter 4, including UV-vis, FTIR, electrophoresis and Raman spectroscopy.

#### 5.2.3.1 UV-vis spectroscopy

A commercial nanodrop UV-vis device (Nanodrop 2000 UV-vis Spectrophotometer, Thermo Fisher Scientific Inc.) was used to measure the DNA concentration and final spectra from the functionalized structures. The data from

this technique confirmed that no aggregation clusters remained from the functionalization step.

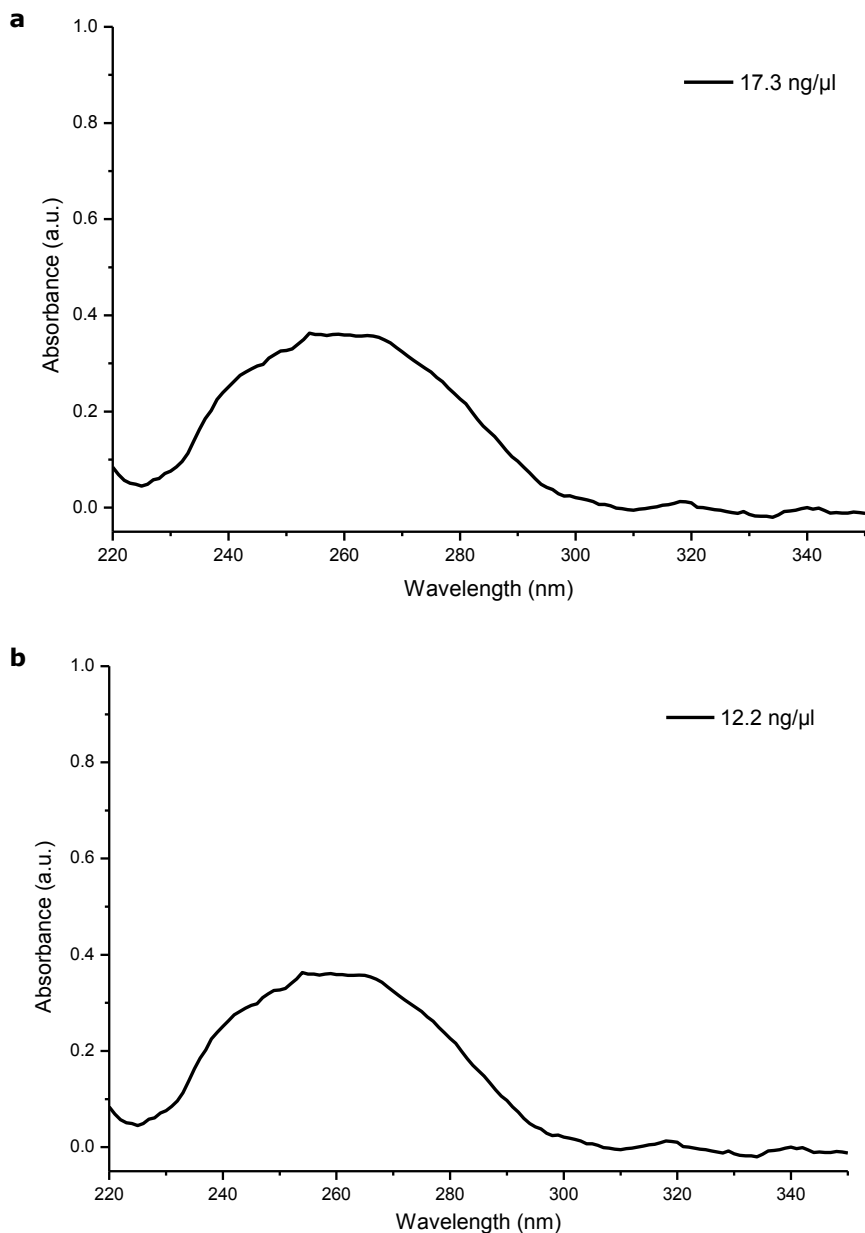


**Figure 5.1. UV-vis spectra from 220-350 nm. (a)** Fullerene-Forward ssDNA (Fwd-C61) and **(b)** Fullerene-Backward ssDNA (Bwd-C61). In both samples, a peak is observed at 260 nm, which is related to DNA aromatic bases. The absorption ratio  $A_{260}/A_{280}$  provides information about the DNA quantity and purity on a sample.



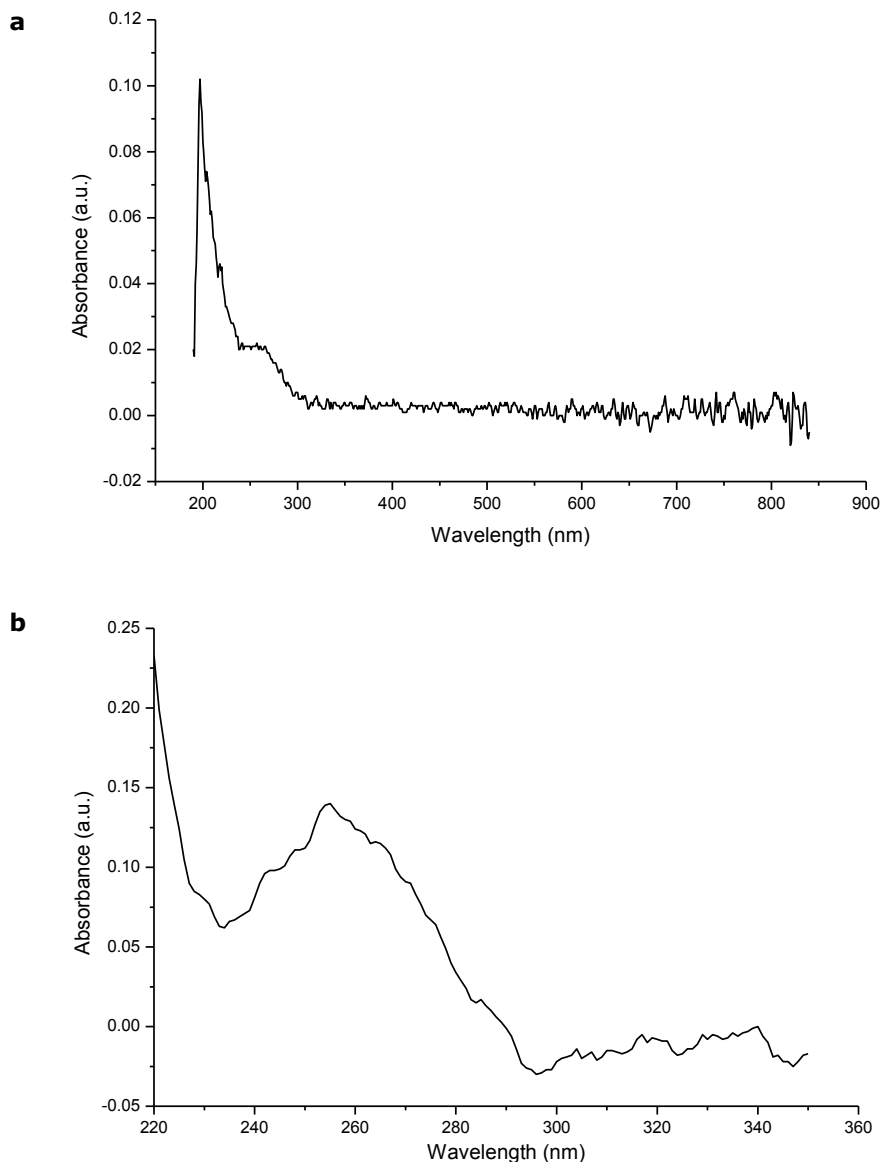


**Figure 5.2. UV-vis spectra from hybridized fullerene-DNA sample type 2, following protocol 2. (a)** Scan from 190 to 850 nm. The graph shows only one main peak at 200 nm related to C61 absorption, indicating that no clusters are present in the solution. In the case of aggregation of clusters, no peak but a broad band would be expected. Also, a shoulder is observed around 250-280 nm, related to the DNA attached to the fullerene. **(b)** Scan from 220-350 nm shows a zoom in on the DNA attached to the fullerene to quantify the DNA present in the solution (here was 6.2 ng/ $\mu$ l).

### 5.2.3.2 FT-IR

We used a Bruker Tensor 27, Pike Miracle ATR cell (FT-IR) in order to check that an amide group was formed between the fullerene and the DNA. The spectra for the functionalized type 2 (**Fig 5.3**) show several peaks due to a larger amount of aromatic bases (102 bp). Here, the transmission signal from the original non modified strands (red line, 150 mM PBS) are compared against C61 (black line, milliQ-water) and the modified DNA-C61 strands (blue line, 0.150 mM PBS).

The main bands that we observe for "C61" correspond to the carboxylic group: C-OH and O=C-OH stretch at 3795.8 and 3325.1  $\text{cm}^{-1}$  and, O-H stretch at 2322.3, 2129.4 and 2013.6  $\text{cm}^{-1}$  from the strong hydrogen bond -COOH. The peak at 1612.5  $\text{cm}^{-1}$  is attributed to the carboxylate anion stretch mode.

On the other hand, double stranded DNA present several peaks related to the aromatic and phosphate groups in the sample. Both modified ssDNA-C61 have the bands at 3179 and 1713  $\text{cm}^{-1}$  corresponding to an amide group. Also, a shift from the original C61 bands at 2322.3, 2129.4 and 2013.6  $\text{cm}^{-1}$  was observed only in the modified DNA-strands: *i*) Fwd-C61 at 2368.5, 2191.1 and 2044.5  $\text{cm}^{-1}$  and, *ii*) Bwd-C61 at 2175.7 and 1975.1  $\text{cm}^{-1}$ .

In **Figure 5.3**, the yellow squares correspond to the fullerene containing a carboxylic group while the red squares correspond to the covalent attachment of DNA via an amide group, where the original bands shifted to a higher wavenumber range.

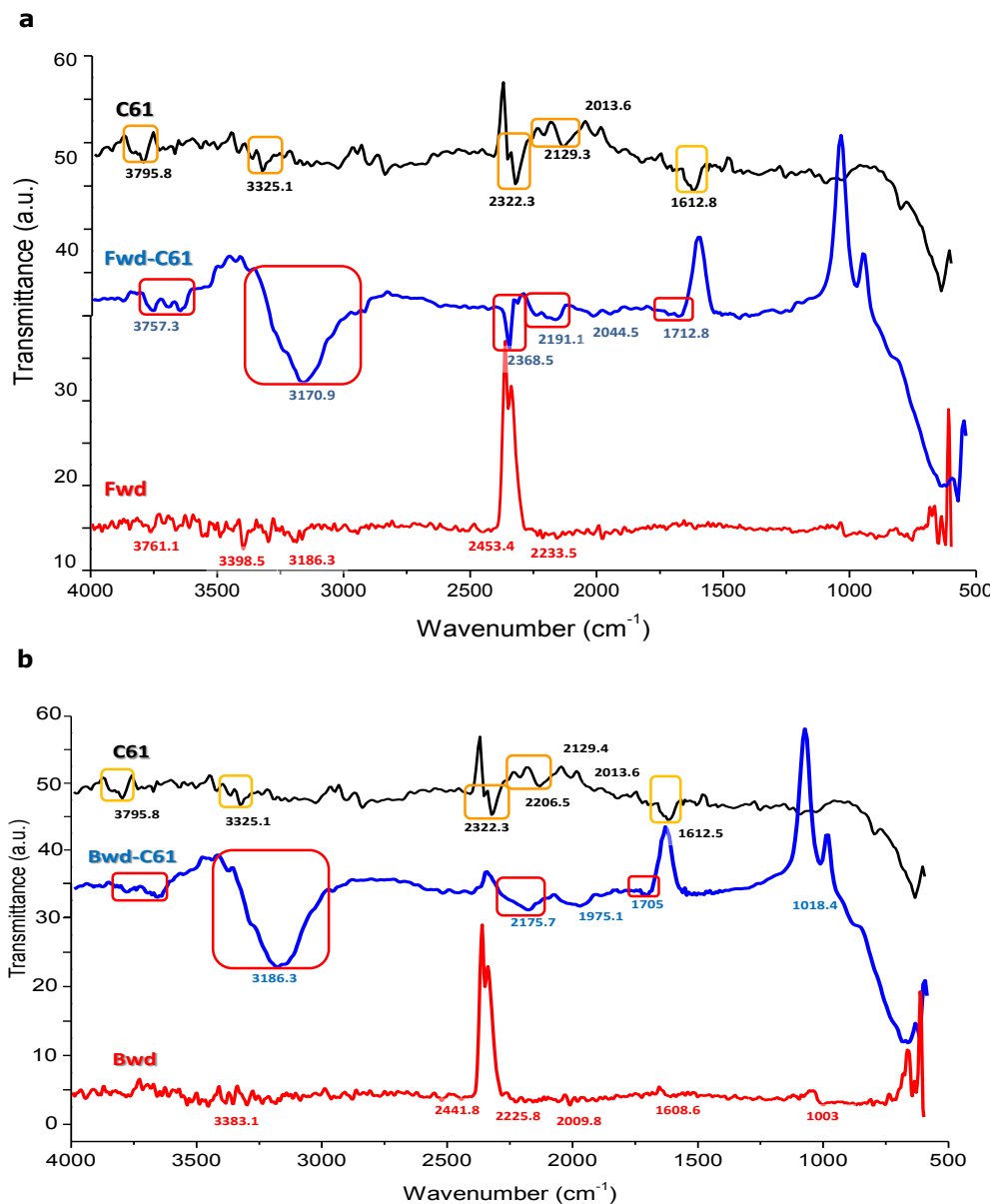


**Figure 5.3. Transmittance vs wavenumber FTIR spectra: (a)** C61 (black), modified Fwd-C61 (blue) and non-modified Fwd single strand (red) are compared in the range between 4000-550  $\text{cm}^{-1}$ ; **(b)** C61 (black), modified Bwd-C61 (blue) and non-modified Bwd single strand (red) are compared in the range between 4000-550  $\text{cm}^{-1}$ .

### 5.2.3.3 Hybridization and electrophoresis

After confirmation of the DNA-fullerene modification, "annealing" and hybridization of both DNA strands was performed in collaboration with drs. David Cortens at the BDG laboratory (IMO-IMOMEC, Hasselt University Campus Diepenbeek). The DNA annealing process consists of mixing ssDNA strands in equimolar concentrations, placing then in a thermocycler and heating at 95°C for 2 minutes. Next, they were gradually cooled to 25°C on a time span of 45 minutes. In order to verify the occurrence of only a single band of modified double-stranded DNA-C61, and no impurities in the steps before, we loaded the samples to a 2% agarose gel with a reference DNA ladder either the "100 bp DNA ladder" or the "Gene Ruler 100bp DNA ladder" (both from Thermo Fisher Scientific Inc.). (**Fig. 5.4**)

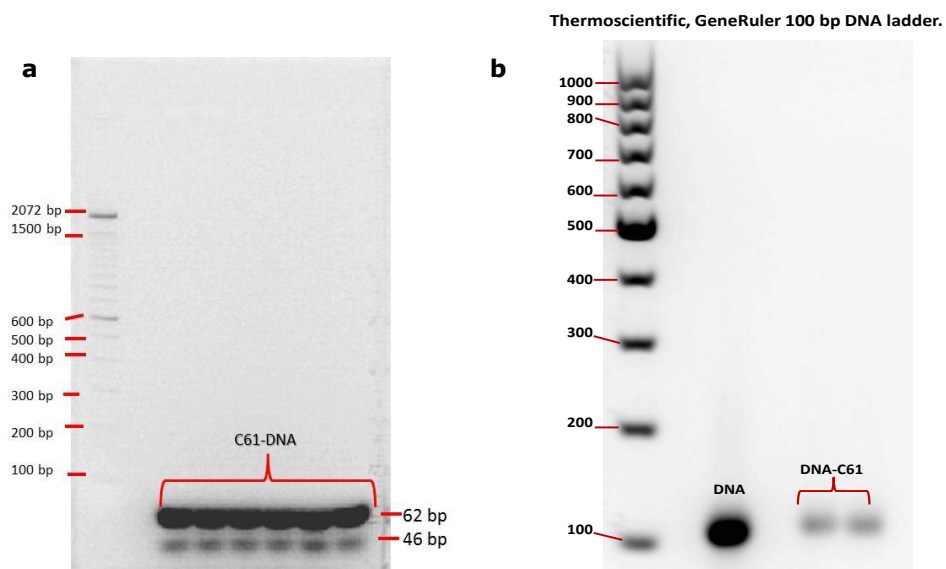


**Figure 5.4. Electrophoresis experiment in 2% agarose gel:** (a) Type 1, protocol 1. The expected size was about 27-30 bp, due to the fullerene friction but here 2 bands of higher size were observed, indicating that more than 1 type of molecules was produced (secondary, tertiary or dimerization). Left lane: DNA ladder 100 bp (Thermo Scientific). (b) Type 2. The DNA-C61 has a slightly higher molecular mass, compared to unmodified DNA, as a result of the attached fullerenes. The fact that only a single band is visible points out that only modified DNA-C61 is present in the sample. Left lane: Gene Ruler 100 bp (Thermo Scientific).

From **Figure 5.4a** a mixture of products was obtained because the hairpin structures were not fully complementary, thus instead of formation of a single fullerene-double stranded DNA molecule of 27-30 bp we obtain secondary type of molecules that appear at 46-62 bp. The possibility of dimerization through the fullerene group (2 +2 cycloaddition) is also an option, however literature reports this event only for very specific conditions (110 °C with light irradiation for 62 h [38, 39]), while our experiments were performed at standard biological conditions. In addition, **Figure 5.4b** shows only one type of fullerene-DNA molecule at the expected range ( $\sim 100$  bp).

#### 5.2.3.4 Raman spectroscopy

An additional characterization was performed with Raman spectroscopy in order to confirm the FTIR data related to a covalent attachment of DNA to the fullerene by means of an amide bond. The measurements on the Raman instrument (Horiba Jobin-Yvon T64000 spectrometer equipped with confocal microscope and monochromator working in subtractive mode, LN<sub>2</sub> cooled CCD detector) were performed in collaboration with Dr. Giedrius Degutis (Group of Organic and Bio-polymeric Chemistry, IMO-IMOMEC) on top of either Si/SiO<sub>2</sub> substrates (thickness  $\sim 300$ nm) or ultra-flat gold. Stock solutions were drop casted on top of the substrates and Raman spectra were obtained, using a sample excitation of 488 nm with the Ar<sup>+</sup> ion laser level SHG-95. Before measurements, the machine was calibrated using the Si (520.7 cm<sup>-1</sup>) mode. The laser was attenuated with a ND filter in order to avoid sample heating.

From **Fig. 5.5** a characteristic peak between 950-1000 cm<sup>-1</sup> is distinguished in all the substrates, corresponding to a two phonon scattering signal of silicon (reference substrate: Si/SiO<sub>2</sub>, green curve). Furthermore, the spectrum for C61 (black curve) displays two small peaks corresponding to the G-band and the D-band, at  $\sim 1790$  cm<sup>-1</sup> (sp<sup>2</sup> bonds of high energy) and  $\sim 1450$  cm<sup>-1</sup> (small shoulders indicate that different bonds than sp<sup>2</sup> are connected to the fullerene) respectively. The sample containing only DNA, shows small bands between 1450 cm<sup>-1</sup> and 1100 cm<sup>-1</sup>, related to the homogeneous content of sp<sup>3</sup> bonded carbons in the structure. Finally, the DNA-C61 molecules show an increase of signal for the G-band at a lower energy shift ( $\sim 1600$  cm<sup>-1</sup>), due to the increase of sp<sup>3</sup>

bonds covalently attached to the original C61 and as a consequence, an increase of disorder is also observed on the corresponding D-band (wider shoulder  $\sim$  between 1300-1400  $\text{cm}^{-1}$ ).

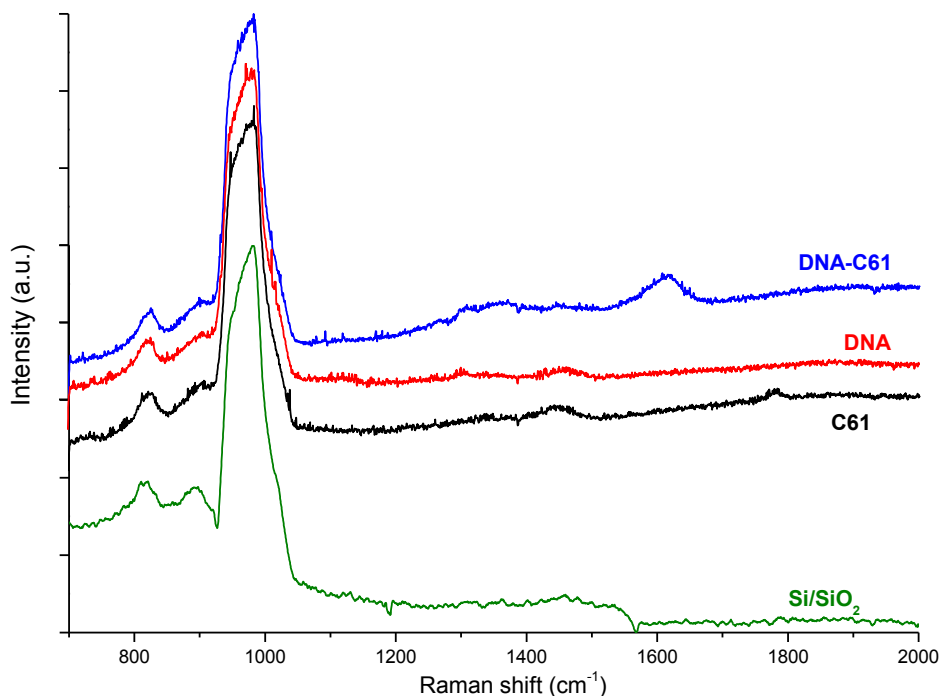


**Figure 5.5. Raman spectroscopy.** The Raman shift for the G-band peak of C61 (black curve at  $\sim 1790 \text{ cm}^{-1}$ ), decreases in energy when a DNA molecule is covalently attached to C61 (DNA-C61) at  $1600 \text{ cm}^{-1}$ , increasing the amount of  $\text{sp}^3$  type of carbons and of disorder in the molecule (D-band shift from  $1450 \text{ cm}^{-1}$  for C61 to a wide shoulder between  $1300$  and  $1400 \text{ cm}^{-1}$  for DNA-C61).

### 5.3 References

- [1] Z. Li, H. C. Wong, Z. Huang, H. Zhong, C. H. Tan, W. C. Tsoi, J. S. Kim, J. R. Durrant, and J. T. Cabral, "Performance enhancement of fullerene-based solar cells by light processing," *Nat. Commun.*, vol. 4, p. 2227, 2013.
- [2] F. Piersimoni, S. Chambon, K. Vandewal, R. Mens, T. Boonen, A. Gadisa, M. Izquierdo, S. Filippone, B. Ruttens, J. D'Haen, N. Martin, L. Lutsen, D.

- Vanderzande, P. Adriaensens, and J. V. Manca, "Influence of fullerene ordering on the energy of the charge-transfer state and open-circuit voltage in polymer: fullerene solar cells," *J. Phys. Chem. C*, vol. 115, no. 21, pp. 10873–10880, 2011.
- [3] C. Joachim, J. Gimzewski, R. Schlittler, and C. Chavy, "Electronic transparency of a single C60 molecule," *Phys. Rev. Lett.*, vol. 74, no. 11, pp. 2102–2105, 1995.
- [4] D. L. Lichtenberger, K. W. Nebesny, C. D. Ray, D. R. Huffman, and L. D. Lamb, "Valence and core photoelectron spectroscopy of C60, buckminsterfullerene," *Chem. Phys. Lett.*, vol. 176, no. 2, pp. 203–208, 1991.
- [5] C. Joachim and J. K. Gimzewski, "An electromechanical amplifier using a single molecule," *Chem. Phys. Lett.*, vol. 265, pp. 353–357, 1997.
- [6] H. W. Kroto, J. R. Heath, S. C. O'Brien, R. F. Curl, and R. E. Smalley, "C60: Buckminsterfullerene," *Nature*, vol. 318, no. 14, pp. 162–163, 1985.
- [7] D. M. Guldi and M. Prato, "Excited state properties of C60 fullerene derivatives," *Acc. Chem. Res.*, vol. 33, pp. 695–703, 2000.
- [8] M. Prato, M. Maggini, and C. Meccanisms, "Fulleropyrrolidines: A family of full-fledged fullerene derivatives," *Acc. Chem. Res.*, vol. 31, no. 9, pp. 519–526, 1998.
- [9] V. K. Periya, I. Koike, Y. Kitamura, S. Iwamatsu, and S. Murata, "Hydrophilic [60]fullerene carboxylic acid derivatives retaining the original 60 $\pi$  electronic system," *Tetrahedron Lett.*, vol. 45, no. 45, pp. 8311–8313, 2004.
- [10] T. Da Ros and M. Prato, "Medicinal chemistry with fullerenes and fullerene derivatives," *Chem. Commun.*, pp. 663–669, 1999.
- [11] R. Bakry, R. M. Vallant, M. Najam-ul-Haq, M. Rainer, Z. Szabo, C. W. Huck, and G. K. Bonn, "Medicinal applications of fullerenes," *Int. J. Nanomedicine*, vol. 2, no. 4, pp. 639–49, 2007.
- [12] Y. Tabata, Y. Murakami, and Y. Ikada, "Photodynamic effect of polyethylene glycol-modified fullerene on tumor," *Japanese J. Cancer Res.*, 1997.
- [13] M. Bergamin, T. Da Ros, G. Spalluto, M. Prato, and A. Bourtine, "Synthesis of a hybrid fullerene–trimethoxyindole–oligonucleotide conjugate," *Chem. Commun.*, no. 1, pp. 17–18, 2001.

- [14] P. Scharff, U. Ritter, O. P. Matyshevska, S. V. Prylutska, I. I. Grynyuk, A. A. Golub, Y. I. Prylutsky, and A. P. Burlaka, "Therapeutic reactive oxygen generation.," *Tumori*, vol. 94, no. 2, pp. 278–83, 2008.
- [15] A. Ikeda, M. Matsumoto, M. Akiyama, J. Kikuchi, T. Ogawa, and T. Takeya, "Direct and short-time uptake of [70]fullerene into the cell membrane using an exchange reaction from a [70]fullerene-gamma-cyclodextrin complex and the resulting photodynamic activity.," *Chem. Commun.*, pp. 1547–1549, 2009.
- [16] E. Otake, S. Sakuma, K. Torii, A. Maeda, H. Ohi, S. Yano, and A. Morita, "Effect and mechanism of a new photodynamic therapy with glycoconjugated fullerene.," *Photochem. Photobiol.*, vol. 86, pp. 1356–1363, 2010.
- [17] S. Yano, S. Hirohara, M. Obata, Y. Hagiya, S. I. Ogura, A. Ikeda, H. Kataoka, M. Tanaka, and T. Joh, "Current states and future views in photodynamic therapy," *J. Photochem. Photobiol. C Photochem. Rev.*, vol. 12, pp. 46–67, 2011.
- [18] A. L. Dellinger, Z. Zhou, D. MacFarland, M. G. Sandros, A. Sawafta, and C. L. Kepley, "Molecular interactions of fullerene derivatives in human serum and inflammatory cells," *Insciences J.*, vol. 1, no. 3, pp. 102–114, 2011.
- [19] E. M. Eropkina, E. V. Ilyinskaya, E. V. Litasova, M. Y. Eropkin, L. B. Piotrovsky, M. a. Dumpis, and O. I. Kiselev, "Effect of different water-soluble forms of fullerene C60 on the metabolic activity and ultrastructure of cells in culture," *Biophysics*, vol. 57, no. 3, pp. 343–349, 2012.
- [20] S. K. Sharma, L. Y. Chiang, and M. R. Hamblin, "Photodynamic therapy with fullerenes in vivo: reality or a dream?," *Nanomedicine*, vol. 6, no. 10, pp. 1813–25, 2011.
- [21] M. A. Orlova, T. P. Trofimova, A. P. Orlov, and O. A. Shatalov, "Perspectives of fullerene derivatives in PDT and radiotherapy of cancers," *Br. J. Med. Med. Res.*, vol. 3, no. 4, pp. 1731–1756, 2013.
- [22] A. S. Boutorine, M. Takasugi, C. Hélène, H. Tokuyama, H. Isobe, and E. Nakamura, "Fullerene-oligonucleotide conjugates: Photoinduced sequence-specific DNA cleavage," *Angew. Chemie Int. Ed. English*, vol. 33, pp. 2462–2465, 1995.
- [23] X. Yang, X. Meng, B. Li, Z. Chen, D. Zhao, X. Tan, and Q. Yu, "Inhibition of in vitro amplification of targeted DNA fragment and activity of exonuclease I by a fullerene-oligonucleotide conjugate," *Biologicals*, vol. 36, pp. 223–226, 2008.



- [24] M. B. Patel, U. Harikrishnan, N. N. Valand, D. S. Mehta, K. V. Joshi, S. P. Kumar, K. H. Chikhalia, L. B. George, Y. T. Jasrai, and S. K. Menon, "Novel cationic fullerene derivatized s-triazine scaffolds as photoinduced DNA cleavage agents: Design, synthesis, biological evaluation and computational investigation," *RSC Adv.*, vol. 3, no. 23, p. 8734, 2013.
- [25] T. Mashino, D. Nishikawa, K. Takahashi, N. Usui, T. Yamori, M. Seki, T. Endo, and M. Mochizuki, "Antibacterial and antiproliferative activity of cationic fullerene derivatives," *Bioorganic Med. Chem. Lett.*, vol. 13, pp. 4395–4397, 2003.
- [26] E. Leary, M. T. González, C. van der Pol, M. R. Bryce, S. Filippone, N. Martín, G. Rubio-Bollinger, and N. Agraït, "Unambiguous one-molecule conductance measurements under ambient conditions.," *Nano Lett.*, vol. 11, pp. 2236–2241, 2011.
- [27] C. A. Martin, D. Ding, J. K. Sørensen, T. Bjørnholm, J. M. van Ruitenbeek, and H. S. J. van der Zant, "Fullerene-based anchoring groups for molecular electronics.," *J. Am. Chem. Soc.*, vol. 130, no. 40, pp. 13198–13199, 2008.
- [28] R. Breslow and S. T. Schneebeli, "Structure–property relationships in molecular wires," *Tetrahedron*, vol. 67, pp. 10171–10178, 2011.
- [29] L. Venkataraman, J. E. Klare, C. Nuckolls, M. S. Hybertsen, and M. L. Steigerwald, "Dependence of single-molecule junction conductance on molecular conformation.," *Nature*, vol. 442, no. 7105, pp. 904–907, 2006.
- [30] C. Rogero, J. I. Pascual, J. Gómez-Herrero, and A. M. Baró, "Resolution of site-specific bonding properties of C<sub>60</sub> adsorbed on Au(111)," *J. Chem. Phys.*, vol. 116, no. 2, p. 832, 2002.
- [31] Y. Shirai, A. J. Osgood, Y. Zhao, K. F. Kelly, and J. M. Tour, "Directional control in thermally driven single-molecule nanocars," *Nano Lett.*, vol. 5, no. 111, pp. 2330–2334, 2005.
- [32] F. Diederich, L. Isaacs, and D. Philp, "Syntheses, structure and properties of methanofullerenes," *Chem. Soc. Rev.*, pp. 243–255, 1994.
- [33] C. J. Murphy, M. R. Arkin, Y. Jenkins, N. D. Ghatlia, S. H. Bossmann, N. J. Turro, and J. K. Barton, "Long-range photoinduced electron transfer through a DNA helix," *Science*, vol. 262, pp. 1025–1029, 1993.
- [34] W. Chen, C. Turro, L. A. Friedman, J. K. Barton, and N. J. Turro, "Resonance Raman investigation of Ru(phen)<sub>2</sub> (dppz)<sup>2+</sup> and related complexes in water and in the presence of DNA," *J. Phys. Chem. B*, vol. 101, no. 35, pp. 6995–7000, 1997.

- [35] E. D. A. Stemp, M. R. Arkin, and J. K. Barton, "Oxidation of guanine in DNA by  $\text{Ru}(\text{phen})_2(\text{dppz})^{3+}$  using the flash-quench technique," *J. Am. Chem. Soc.*, vol. 119, pp. 2921–2925, 1997.
- [36] S. R. Shin, K. S. Jin, C. K. Lee, S. I. Kim, G. M. Spinks, I. So, J. H. Jeon, T. M. Kang, J. Y. Mun, S. S. Han, M. Ree, and S. J. Kim, "Fullerene attachment enhances performance of a DNA nanomachine," *Adv. Mater.*, vol. 21, pp. 1907–1910, 2009.
- [37] K. S. Jin, S. R. Shin, B. Ahn, S. Jin, Y. Rho, H. Kim, S. J. Kim, and M. Ree, "Effect of C60 fullerene on the duplex formation of *i*-Motif DNA with complementary DNA in solution," *J. Phys. Chem. B*, vol. 114, no. 14, pp. 4783–4788, 2010.
- [38] F. Piersimoni, G. Degutis, S. Bertho, K. Vandewal, D. Spoltore, T. Vangerven, J. Drijkoningen, M. K. Van Bael, A. Hardy, J. D'Haen, W. Maes, D. Vanderzande, M. Nesladek, and J. Manca, "Influence of fullerene photodimerization on the PCBM crystallization in polymer: Fullerene bulk heterojunctions under thermal stress," *J. Polym. Sci. Part B Polym. Phys.*, vol. 51, no. 16, pp. 1209–1214, 2013.
- [39] A. Distler, T. Sauermann, H.-J. Egelhaaf, S. Rodman, D. Waller, K.-S. Cheon, M. Lee, and D. M. Guldi, "The effect of PCBM dimerization on the performance of bulk heterojunction solar cells," *Adv. Energy Mater.*, vol. 4, no. 4, p. 1300693, 2014.

## Chapter 6

# Preparation for electronic transport studies on DNA-fullerene complexes

### 6.1 Substrate selection

The first series of experiments was performed using the NX10 Park Systems AFM (Suwon, Korea) in order to determine the most suitable substrate to observe single molecules of DNA.

#### 6.1.1 Nanocrystalline diamond

Due to the expertise of the BIOS group in DNA functionalization, this could be the most obvious approach. Basically, a hydrogen-terminated diamond surface is functionalized via photoactivation (UV wavelength 254 nm) with a fatty acid (10-undecenoic acid). Next, activation of the terminal carboxylic acid group with an EDC linker allows a cross-linking reaction between the fatty acid and an amine-terminated biomolecule, in this case DNA [1–3]. As a consequence, a high density of DNA brushes ( $\sim 10^{12} \text{ cm}^{-2}$ ) is covalently attached to the diamond bio-sensor, where DNA hybridization and denaturation can be detected by impedance spectroscopy or through the novel Heat Transfer Method [3], shown in detail in **Chapter 10**.

Unfortunately, this very dense array of DNA molecules makes it impossible to differentiate the amount of molecules making contact between the AFM tip and the surface. For the case of ssDNA molecules forming an array on the diamond layer and the complementary ssDNA molecules being functionalized on the AFM tip, measurements require an AFM device that is fully functional for measurements in liquid. Then, the arrangement (random coil) and quantity of functionalized ssDNA molecules on the AFM tip presents another issue.

Moreover, a typical hydrogenated-diamond surface is in general very rough (area of  $1 \times 1 \mu\text{m}^2$  shows  $\text{RMS} > 10 \text{ nm}$ ) and force-distance measurements would be highly unreliable. An example of a nanocrystalline diamond (NCD) is shown in **Fig. 6.1**. Therefore, this material and technique were finally not selected.

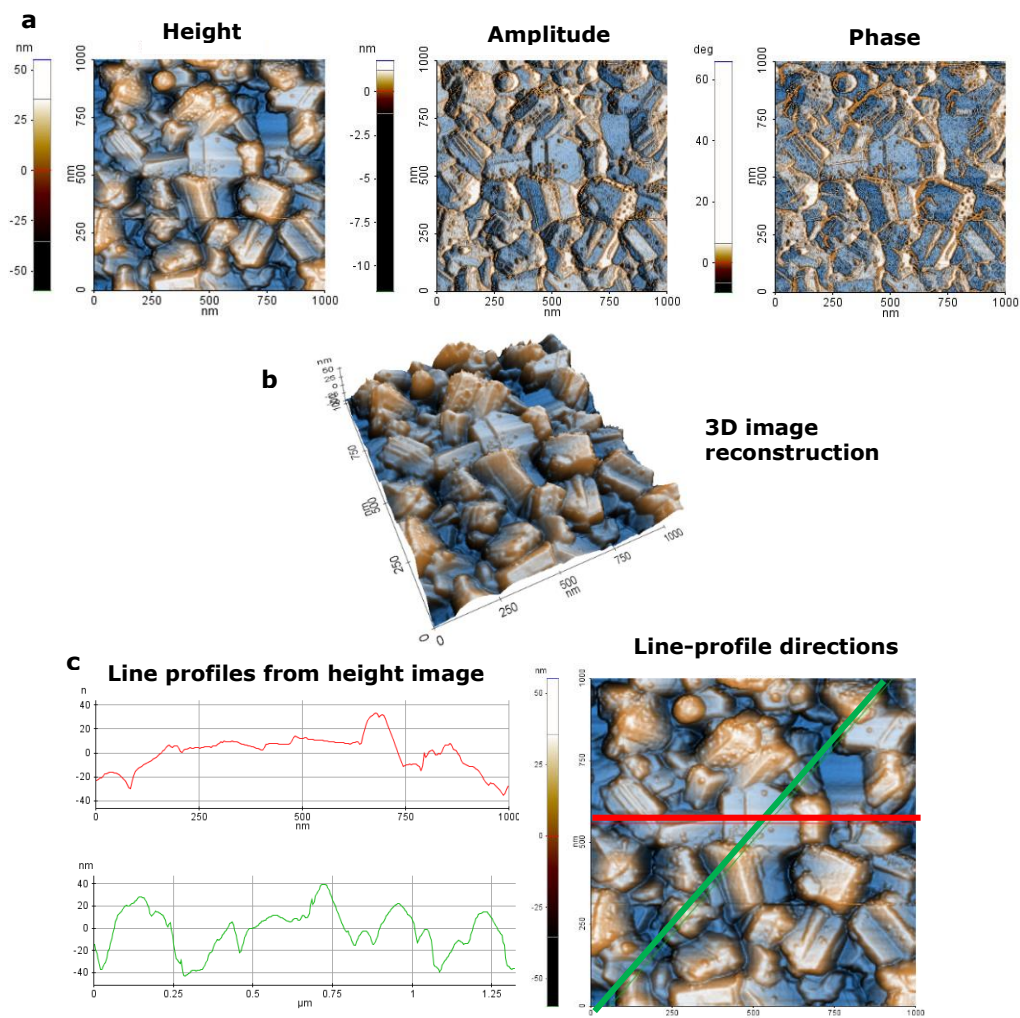


**Fig. 6.1. Non-contact AFM measurement on NCD.** Nominal spring constant of cantilever 40 N/m. Scan size:  $1 \times 1 \mu\text{m}^2$ , RMS: 18.13 nm. **(a)** Height, amplitude and phase images; **(b)** Three dimensional representation and; **(c)** Line profiles, RMS values red line: 14.13 nm and green line: 19.13 nm.

### 6.1.2 Home made gold flame annealed samples.

The next best option in terms of roughness were flame annealed gold samples. Generally, the substrates are composed of silicon dioxide covered with an adhesion layer (chromium  $\sim 10$ -20 nm thick) and then a film  $\sim 200$  nm of Au (111) is evaporated on top of them (chemical vapour deposition) in an inert environment chamber. Samples from the Nanostructures Physics group (NSP) were kindly provided by Prof. Dr. Hans-Gerhard Boyen.

#### 6.1.2.1 AFM characterization before annealing

Non-contact AFM images, were taken before the flame-annealing procedure (**Fig. 6.2**). On a clean substrate, small areas ( $0.5 \times 0.5 \mu\text{m}^2$ ) show peaks ranging between 4-6 nm in height. This could present an adverse issue to visualize single DNA molecules deposited on the surface.

#### 6.1.2.2 AFM characterization after flame annealing of gold surfaces

Flame annealing is a standard procedure to obtain contaminant free areas with flat Au (111) terraces [4]. This procedure is done by placing the gold samples on a clean quartz plate and wearing protective glasses. When the flame is ignited, the hydrogen flow was regulated to obtain a flame of about 4 cm long. Then the quartz plate was heated around the substrate in order to assure even heating. Next, the flame tip was brought to the film at  $\sim 30^\circ$  angle and it was swept back and forth for 30-60 seconds, keeping the small flame spot on the film (surface colour shifts from yellow to light orange glow). In order to avoid a sample overheating or burn, is recommended to turn off the lights and watch carefully the change of colouration which was not performed in these experiments. Finally, the flame regulator was turned off and the film was allowed to cool down for a minute.

Apparently, the flame annealed substrates show an increased roughness after the procedure (**Fig 6.3**). This could be due to sample overheating (burned) or a consequence of the environmental humidity while the samples were cooled down (peaks  $\sim 10$ -25 nm). Additionally, this procedure was repeated on two other

substrates with the similar results of increased roughness after treatment (RMS ranged between 11-18 nm).

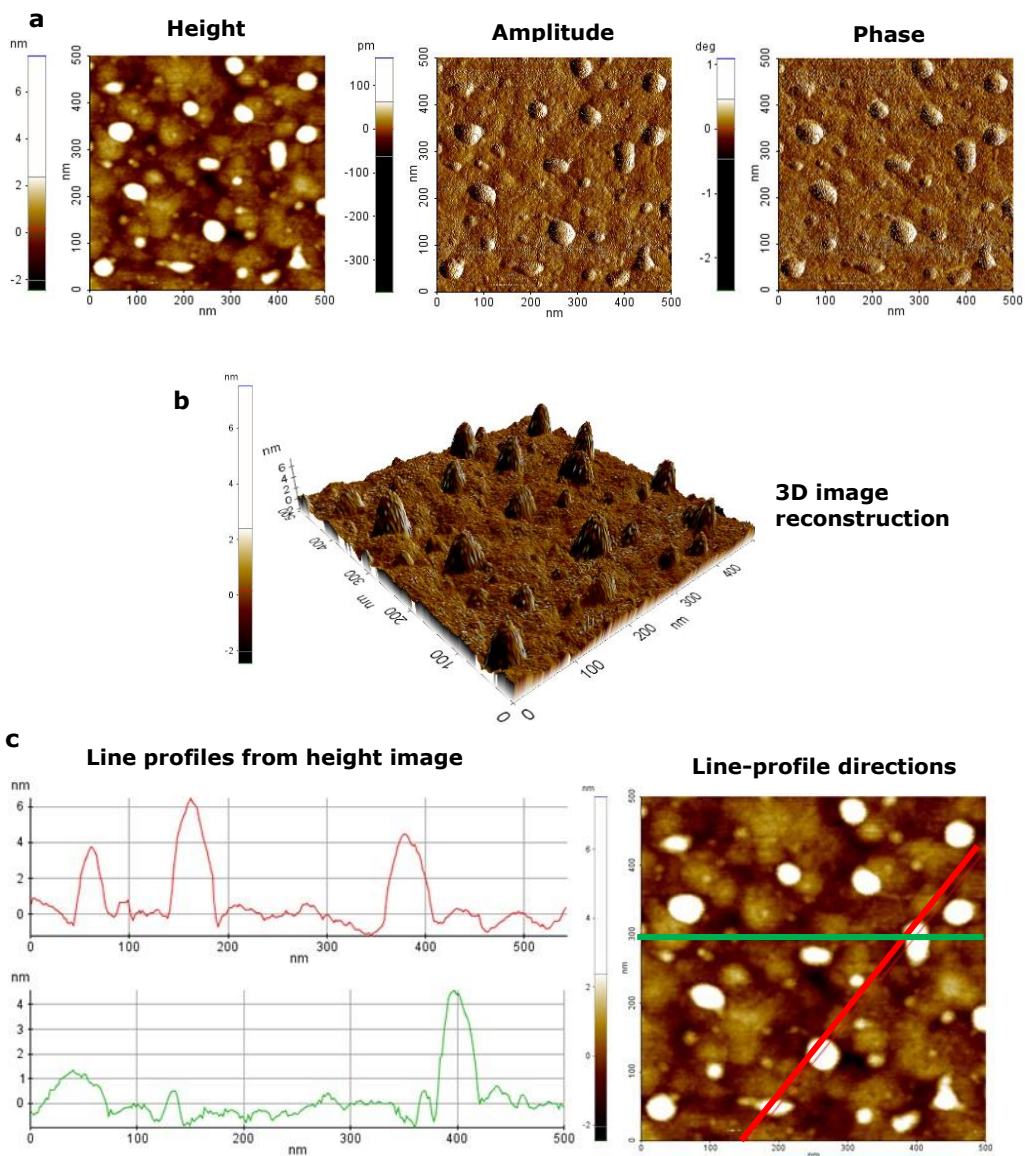


**Fig. 6.2. NC-AFM measurement on gold.** Nominal spring constant of cantilever 40 N/m. Scan size:  $0.5 \times 0.5 \mu\text{m}^2$ , RMS: 1.13 nm. **(a)** Height, amplitude and phase images; **(b)** Three dimensional representation and; **(c)** Line profiles, RMS red line profile: 1.68 nm and green line profile: 1.04 nm.

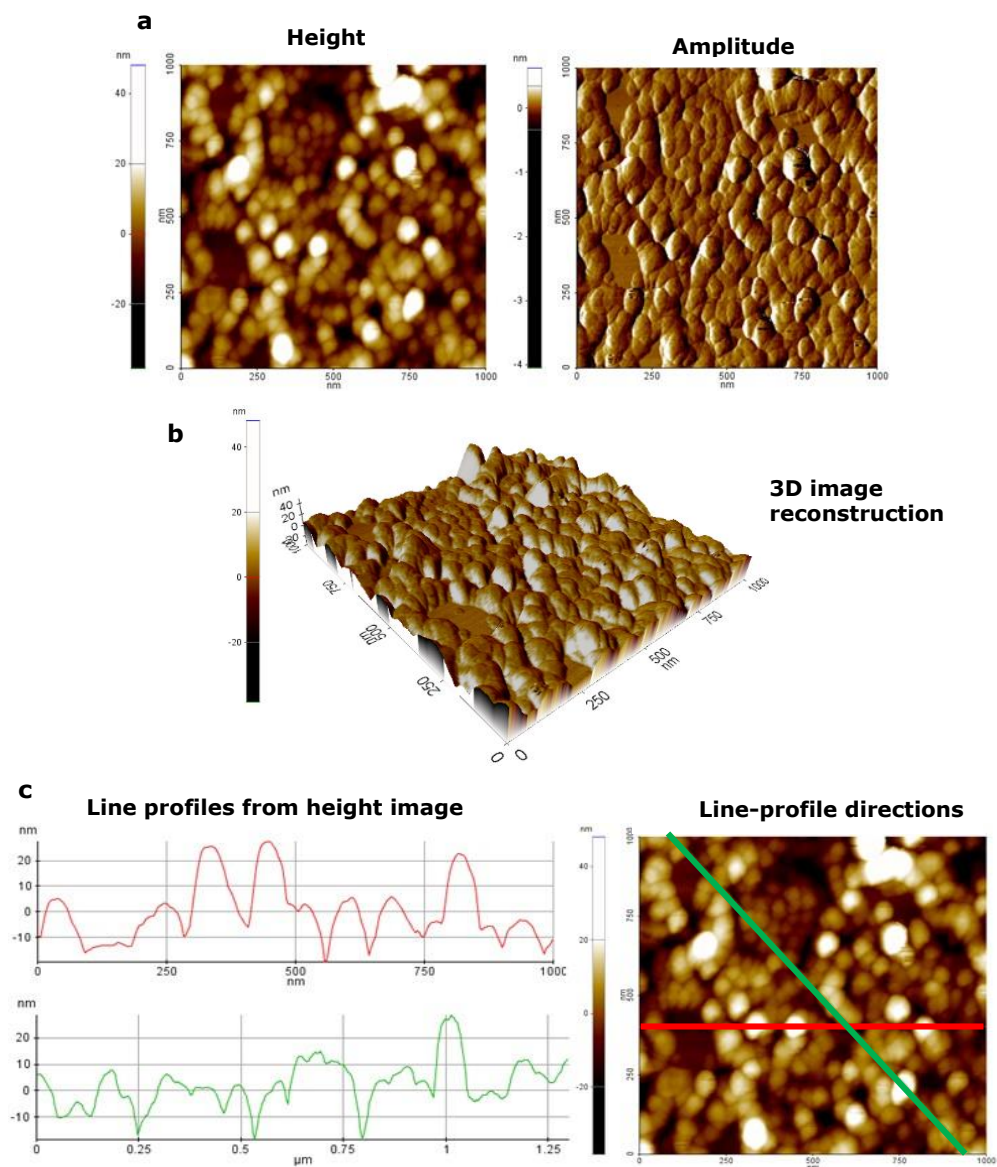


**Fig. 6.3. NC-AFM measurement on flame annealed gold.** Nominal spring constant of the cantilever: 40 N/m. Scan size:  $1 \times 1 \mu\text{m}^2$ , RMS: 10.20 nm. **(a)** Height and amplitude; **(b)** Three dimensional representation and; **(c)** Line profiles, RMS red line profile : 11.53 nm and green line profile: 8.55 nm.

## 6.1.2.3 After annealing and DNA-fullerene deposition (27 bp)

Moreover, a first experiment with our DNA-fullerene molecules (protocol 1) was performed on top of freshly annealed gold samples to test whether the DNA pattern could be localized. Molecules of DNA-fullerene were drop casted on the gold surface for a time span of 2 h. Then after washing the surface with milliQ water and drying with Nitrogen gas, the sample was imaged. Data obtained from **Fig. 6.4** indicate that no molecules can be differentiated from the substrate because the roughness is higher than the diameter of double stranded DNA.

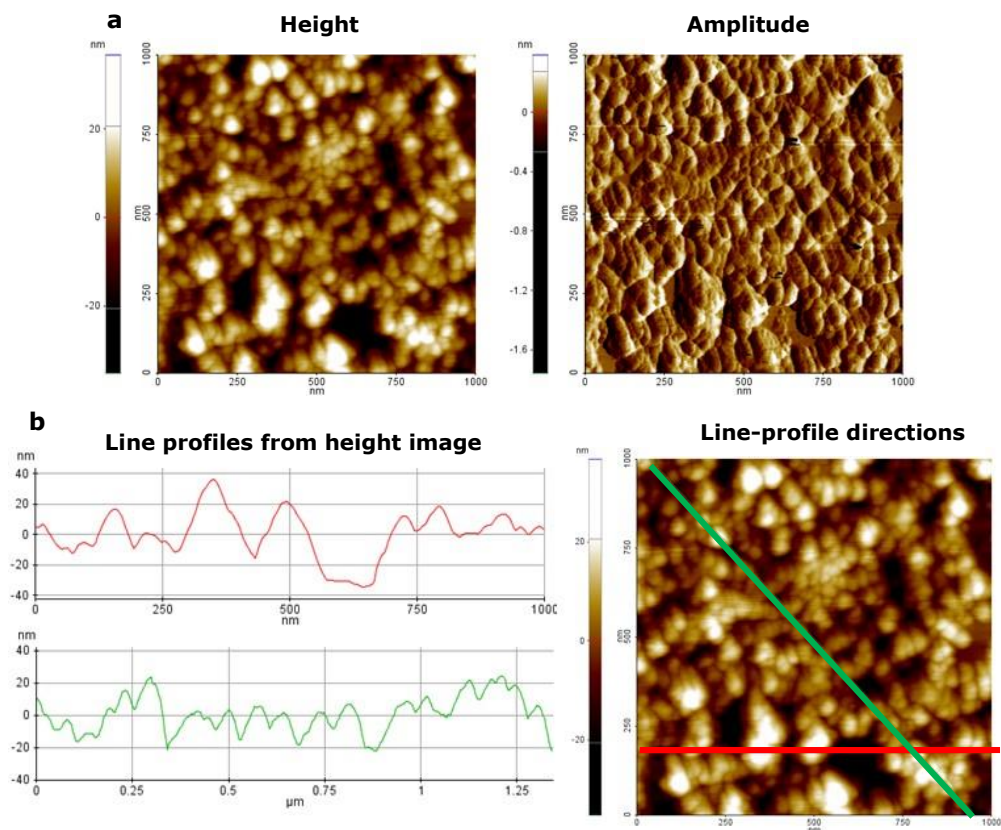


**Fig. 6.4. NC-AFM measurement on gold.** Nominal spring constant of the cantilever: 40 N/m. Scan size:  $1 \times 1 \mu\text{m}^2$ , RMS: 10.50 nm. **(a)** Height and amplitude and, **(b)** Line profiles, RMS red line profile: 15.32 nm and green line profile: 11.00 nm.



### 6.1.3 Commercial ultra-flat gold samples (Platypus)

In order to find a more appropriate ready to use flat substrate, we purchased “template stripped gold chips” (Platypus Technologies, LLC, USA). Their procedure is based on Hegner *et al.* [5]. The chips are fabricated by coating the flattest available silicon or mica substrates, with no adhesion layer. Then 1 cm<sup>2</sup> glass chips are epoxy-glued to the surface. The gold surface available for use is the one in contact with the silicon or mica substrate, so it is protected from the atmosphere and ultra-flat.

Prior to use, the chips were mechanically stripped from the surface. The AFM mode was changed from non-contact to contact mode due to the low RMS of the sample (20 times lower than flame annealed substrates). Previous attempts to visualize the sample with non-contact mode were unable to differentiate changes on the surface. Bare surface RMS values ranged between 0.34-0.5 nm, as shown in **Fig. 6.5** in contact mode.

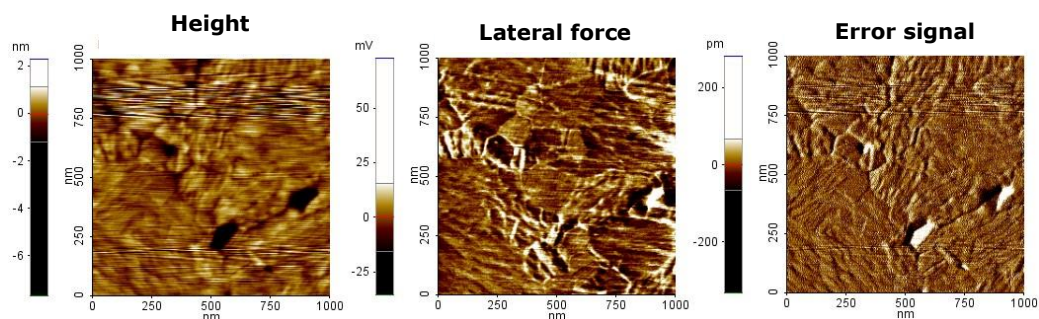


**Fig. 6.5.** Contact AFM measurement on ultra-flat gold. Scan size: 1 x 1 μm<sup>2</sup>, RMS: 0.34 nm. Height, lateral force and error signal.

#### 6.1.3.1 Imaging of Fullerene-DNA deposition (27 bp) on ultra-flat gold

Fullerene-DNA molecules were deposited onto the freshly stripped substrates (**Fig. 6.6**). A group of molecules are observed but it is evident that the functionalized DNA molecules require a further purification step because a number of different sized compounds (**Chapter 5**, protocol 1 = remaining salts

from the unreacted EDC, MES buffer) appear on the surface. Here two possible fullerene-DNA molecules can be differentiated on the line profiles (**Fig. 6.6b**).

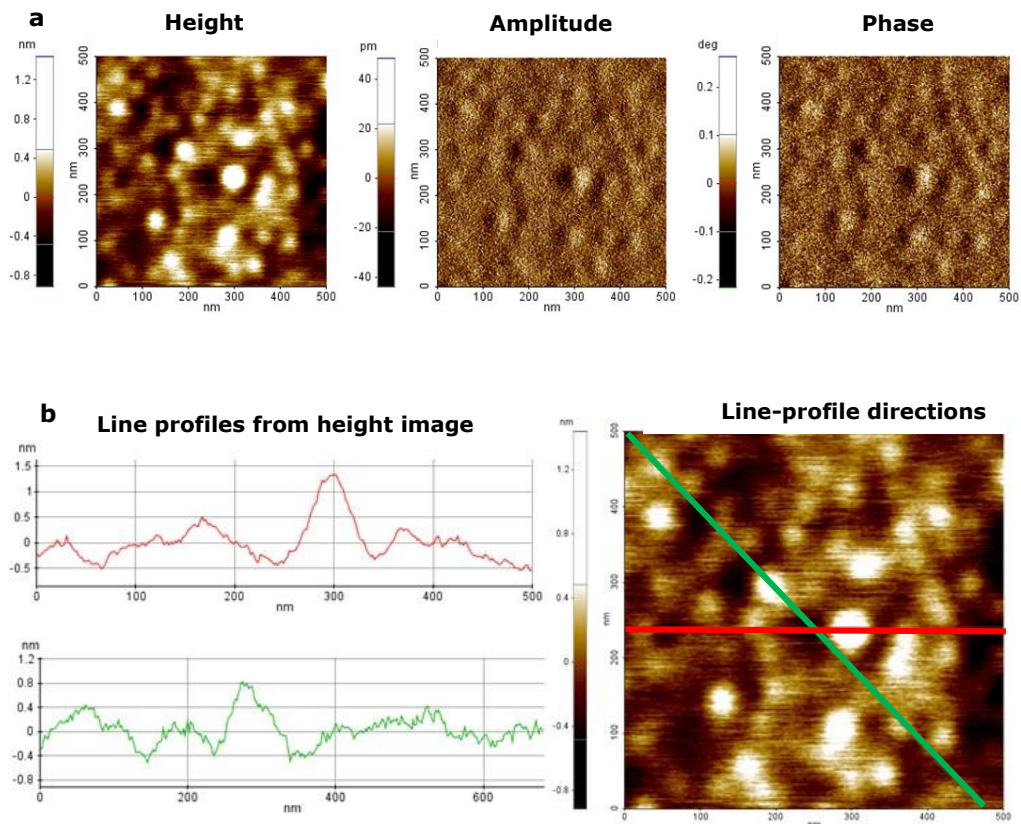


**Fig. 6.6. NC-AFM measurement on gold.** Scan size:  $0.5 \times 0.5 \mu\text{m}^2$ , RMS: 0.246 nm. **(a)** Height, amplitude and phase images and, **(b)** Line profiles, RMS red line profile: 0.391 nm and green line profile: 0.241 nm.

## 6.2 Elastic modulus and conductivity tests with the Park NX10 AFM

### 6.2.1 Conductive AFM (I-AFM) mode on silicon-gold sample

While the chemical process was optimized (**Chapter 5**, protocol 1 and 2), we tested the capabilities of the NX10 AFM to define the machine sensitivity on a standard conductive sample, composed of silicon covered with a gold layer (**Fig. 6.8**). As it was mentioned in **Chapter 4**, I-AFM requires to be in contact mode.

Some of the parameters that can be measured, besides topography (**Fig. 6.8**), are *i*) the material stiffness (Young's modulus): Deformation (Hertzian model, **Fig. 6.9**) or Indentation (Oliver and Pharr model, **Fig 6.10**) and; *ii*) sample conductivity via plotting changes of current with an applied bias voltage on the sample (**Fig. 6.11**).

It is important to mention that for the last measurements, the NX10 does not have any type of Faraday cage adaptation that isolates the sample from environmental interferences, which could lead to unreliable measurements, as observed in **Fig. 6.11**. A possible solution is placing the complete machine into a Faraday cage room but then the next problem was the assembly of the conductive AFM tip to the machine which was far from straightforward. Here the conductive tip had to be first glued to the cantilever with a small amount transparent adhesive, then the cable had to be glued with silver paste to the conductive tip using a small volume to avoid interference with the tip movement on the cantilever but strong enough to be elongated and connected to the machine voltage controller (**Fig. 6.7**). After all these steps, I-V spectroscopy could be performed but it was unclear how the current of the sample could be measured when the bias was changed through the tip, and the sample is placed on the chip holder, without any additional electrical connection to the machine in order to close the circuit or ground the sample. In any case, **Fig. 6.11** represents the attempts to perform these measurements.

The Hertzian model was used in order to study elastic deformation properties. In general, this elastic modulus is based on the classic rigid sphere on top of a flat surface model, for non-adhesive contact where no tension force is allowed to occur within the contact area, while van der Waals and contact adhesive interactions are neglected. For a detailed explanation, the reader can refer to reference [6]. **Figure 6.9** illustrates the application of the Hertzian model to our silicon-gold substrate at two neighbouring positions (P1 and P2). On the other hand, the Oliver and Pharr model is mainly used for nanoindentation or indentation hardness tests. Here, the mechanical properties of materials are tested for small amount of materials, where it is possible to determine the size of sub-micron indentations with high accuracy. For a more detailed explanation,

readers can consult references [8, 9]. Moreover, **Fig. 6.10** illustrates the use of the Oliver and Pharr model for the same substrate.



**Fig. 6.7.** Photograph of the cantilever adaptation to perform conductive measurements on the NX10 AFM.

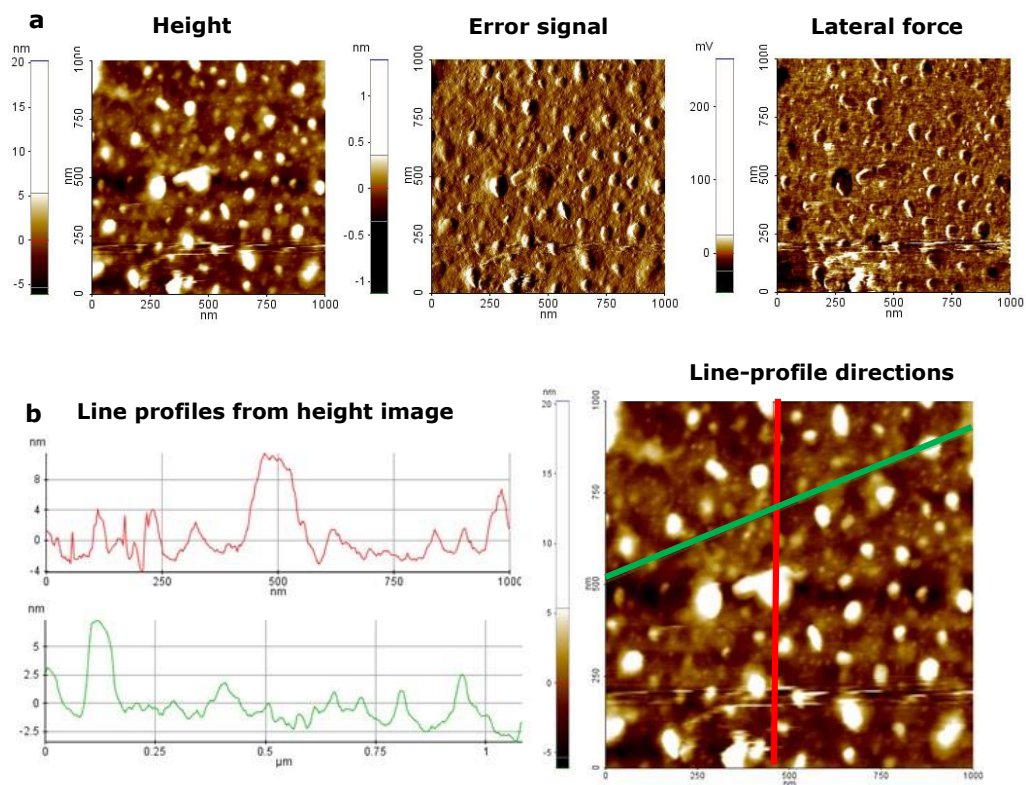


**Fig. 6.8.** C-AFM measurement on silicon-gold. Scan size:  $0.5 \times 0.5 \mu\text{m}^2$ , RMS = 0.246 nm. **(a)** Height, error signal and, lateral force; **(b)** Line profiles, RMS red line: 0.391 nm and green line: 0.241 nm, where peaks range between 7.5 and 12 nm height.

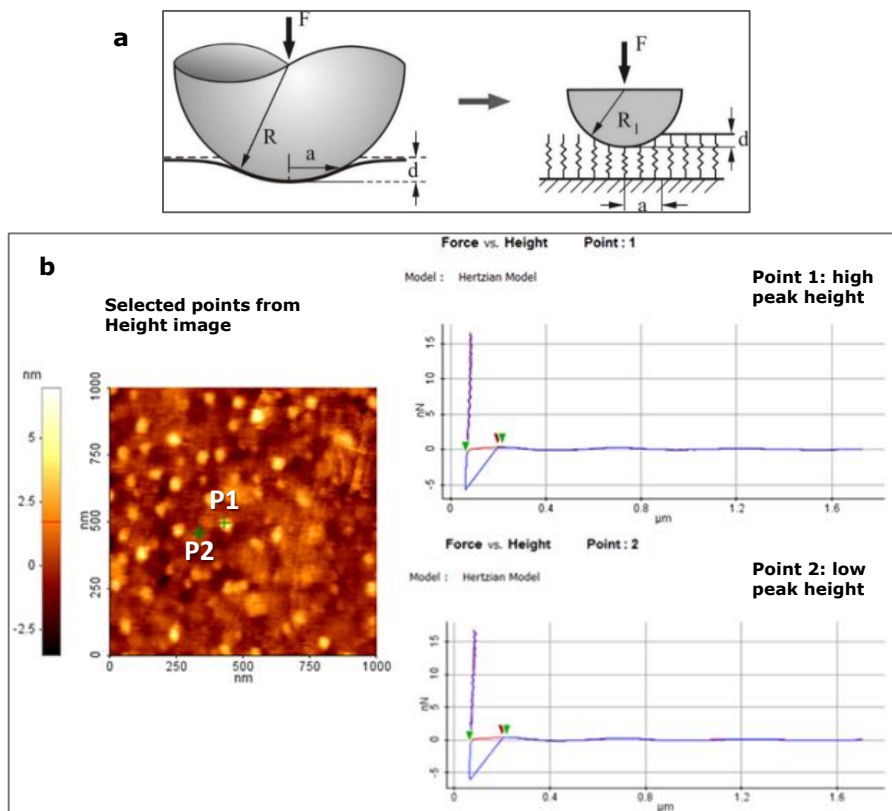


**Fig. 6.9.** (a) Illustration of the Hertz model principle [7]. (b) C-AFM measurement on Si-Gold. Scan size:  $1 \times 1 \mu\text{m}^2$ , RMS: 3.341 nm. Plots of force vs height for points 1 (P1, green cross) and 2 (P2, bold green cross). Here the light colour "dots" are hill type of structures sticking out from the silicon substrate and covered in gold. Hertzian model, where the tip depth reaches 151.05 and 152.84 nm, respectively for P1 and P2. Calculation of Young's modulus results in  $Y = 111.19 \text{ kPa}$  (P1) and  $88.77 \text{ kPa}$  (P2) indicate that the surface is rigid and changes on the Young modulus are just attributed to the silicon-gold peaks (hill or valley) on the selected area.

Typically a gold thin layer presents a Young's modulus of 79 GPa while bare silicon has a Young's modulus of 160 GPa [10]. We can observe that the Young modulus change from 111 to 89 kPa according to the Hertzian model for position 1 and 2 (**Fig. 6.9**), while it changes from 2.66 to 4.56 kPa for the same positions according to the Oliver and Pharr model (**Fig. 6.10**), obtained from exactly the same sample. Moreover, the elastic modulus values are similar in magnitude for both models. For soft samples, Hertz model is more appropriate while for hard samples the Oliver and Pharr model should provide more accurate

results. Here, the sample is a hard substrate, thus Oliver and Pharr would be the model of choice. After the successful study on the Young modulus, the conductivity mode was tested. Another region of the silicon-gold sample was selected with an area of  $1 \times 1 \mu\text{m}^2$  and subdivided into 16 squares ( $110 \times 110 \text{ nm}^2$ ) for a local I-V spectroscopy map (**Figure 6.11**), using bias voltages from -10 to +10 V, resulting in currents between nano- to pico-Amperes. From the figure, hysteresis and asymmetry are attributed to a short-cut or poor contact during the measurement.

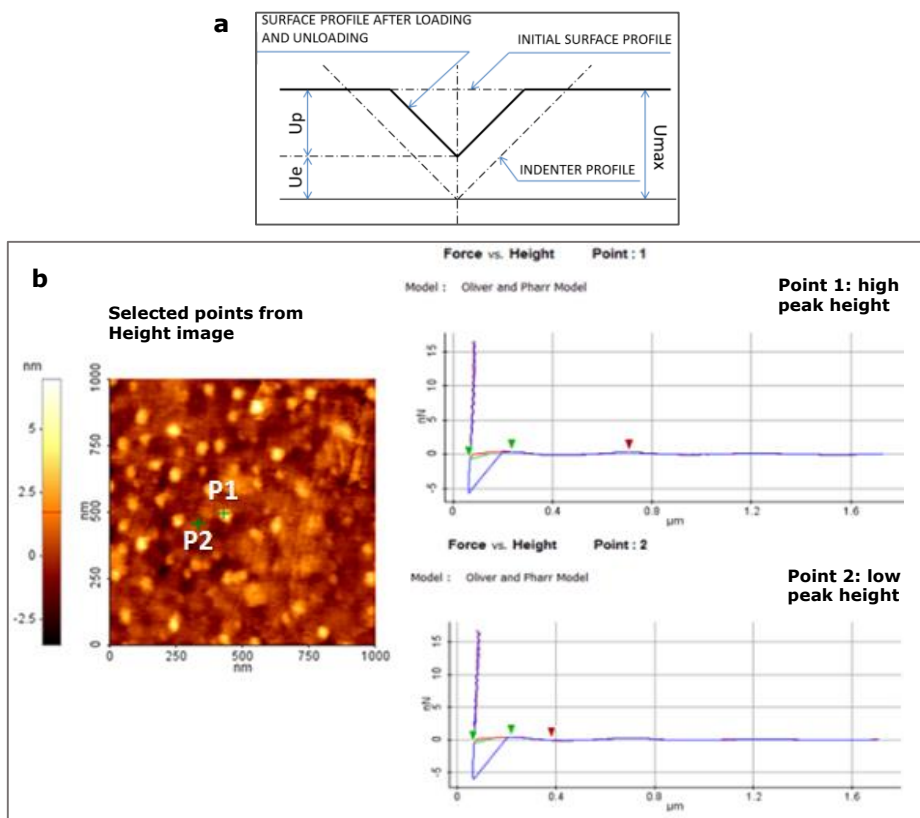


**Fig. 6.10. (a)** Illustration of the Oliver and Pharr model **(b)** Contact AFM measurement on Si-Gold. Scan size:  $1 \times 1 \mu\text{m}^2$ , RMS= 3.34 nm. Plots of force vs height for points 1 (P1) and 2 (P2). Oliver and Pharr model, where hardness is 131.11 and 233.71 Pa, respectively for P1 and P2. Contact depth is of 574.55 and 280.52 nm for P1 and P2. Calculation of Young's modulus is 2.66 kPa (P1) and 4.56 kPa (P2). Graph: approach curve is represented by the blue line, retrace by the red one and indentation within the graph is calculated by the green curve.

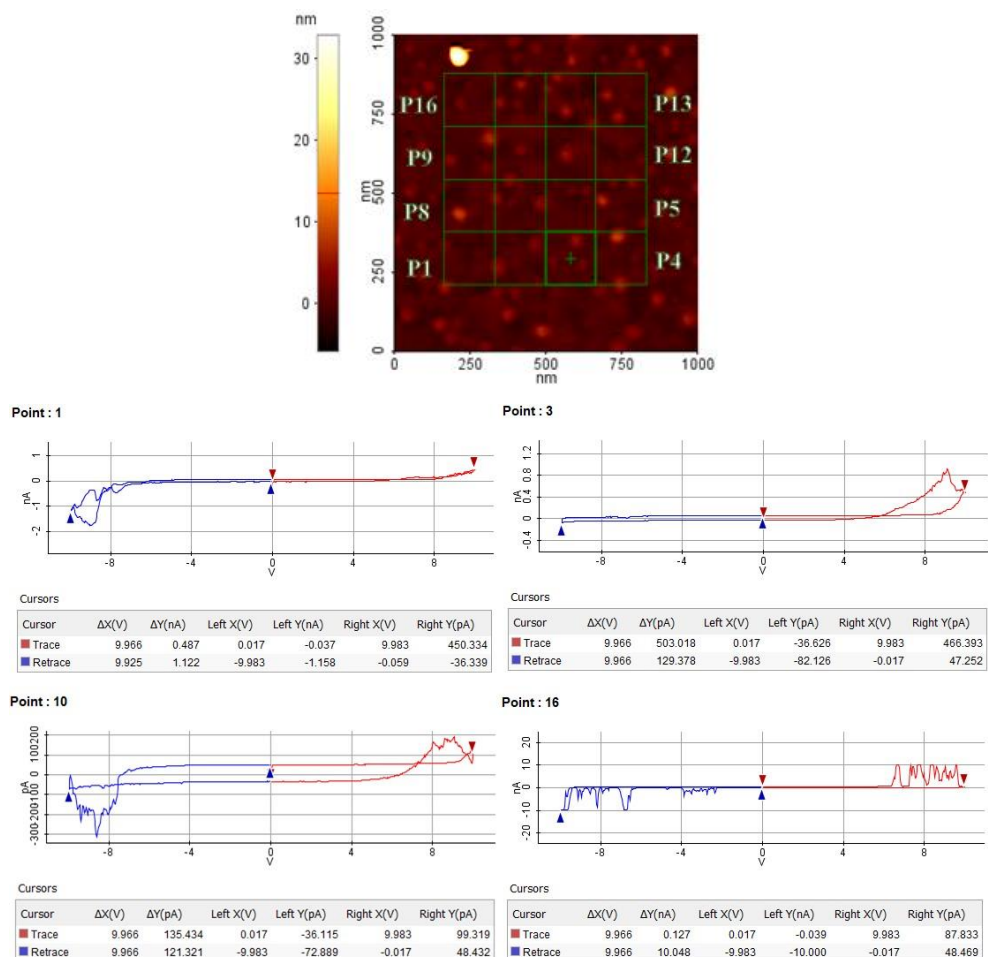


**Fig. 6.11. I-AFM measurement on Silicon-Gold.** Scan size:  $1 \times 1 \mu\text{m}^2$ , RMS is 2.73 nm. Plots of current vs sample bias. Diagram of  $4 \times 4$  squares.

### 6.3 Protocol 2. Image results with Park AFM

#### 6.3.1 DNA-fullerene (type 1, 27 bp) on ultra-flat gold

With the optimization of the synthesis protocol, type 1 fullerene-DNA molecules were prepared with protocol 2 (**Chapter 5**), with an additional milliQ-water washing step after deposition. Later, the samples were dried with a nitrogen flow and imaged with the AFM (**Fig. 6.12**). Small molecules were observed in between the bundles (length and height: 8.79 and  $\sim 2$  nm), thus we assume that single fullerene-DNA molecules may be the precursors of the long fibres

(fullerene-DNA bundles) displaying a length, height and width of 10  $\mu\text{m}$ , 1 and 4 nm, respectively.

From literature reports, the most similar result as **Fig. 6.12** is presented in the work of Cassell *et al.* [11] where they use a cationic type of fullerenes to cluster anionic charged DNA in a broader bundle than the fibers presented here. **Figure 6.13** shows a large number of small molecules adsorbed onto a 1 x 1  $\mu\text{m}^2$  surface ( $\sim 50$ -75). This means that if a conductive tip is approached, chances are that the tip will contact around 10-15 molecules, depending on the tip diameter (range between 5-30 nm in accordance to the coating). Therefore, tuning the sample dilution could provide a more spread coverage for single molecule measurements.

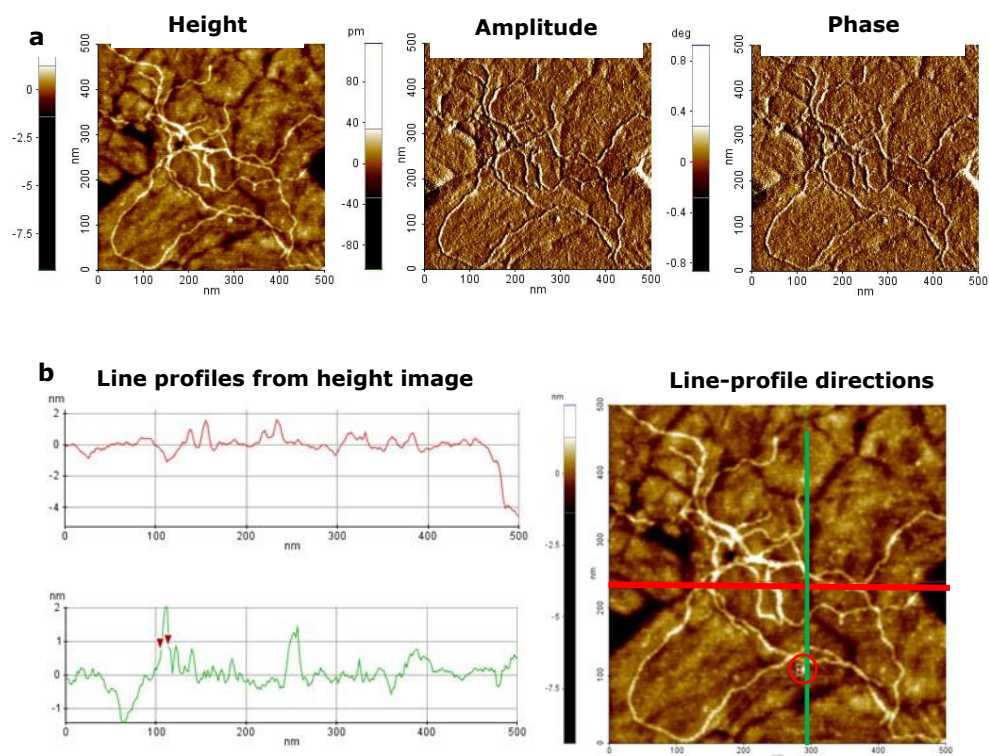


**Fig. 6.12. NC-AFM measurement on gold.** Si-Nitride AFM tip. Scan size: 0.5 x 0.5  $\mu\text{m}^2$ . (a) Height, amplitude and phase images; (b) Line profiles. Long strand length and height are of 4 and 1.8 nm and comparatively a small molecule length and height are of 8.79 and  $\sim 2$  nm.



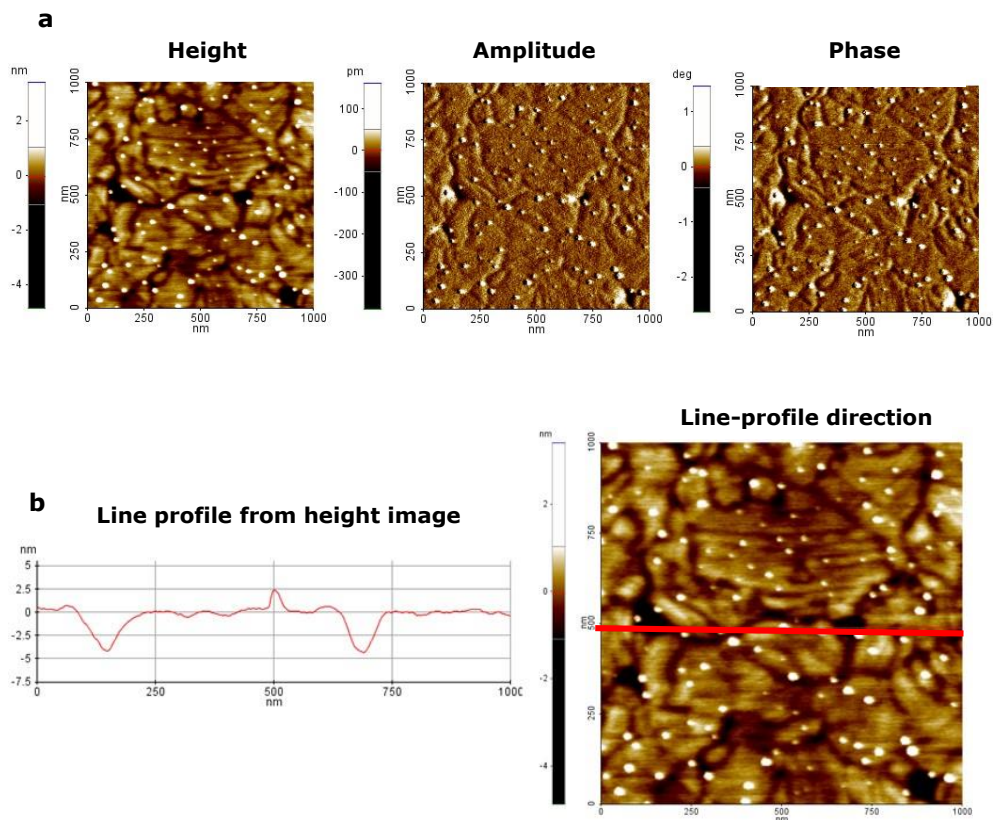


**Fig. 6.13. Non-contact AFM measurement on gold.** Scan size:  $1 \times 1 \mu\text{m}^2$ . (a) Height, amplitude and phase images; (b) Line profile with an RMS value of 1.25 nm.

#### 6.4 Conductivity test, with optimal molecules arrangement and gold AFM tip

Dilution to a final amount of 5-10 molecules (type 1, fullerene-DNA of 27 bp) per  $1 \times 1 \mu\text{m}^2$  was the most appropriate for our purpose. First the molecules were imaged with a standard AFM tip (MSNL, tip E. **Figs. 6.14-16**) and then, the tip was changed to a gold tip with the same spring constant (**Fig. 6.17**) for performing conductive AFM measurements.

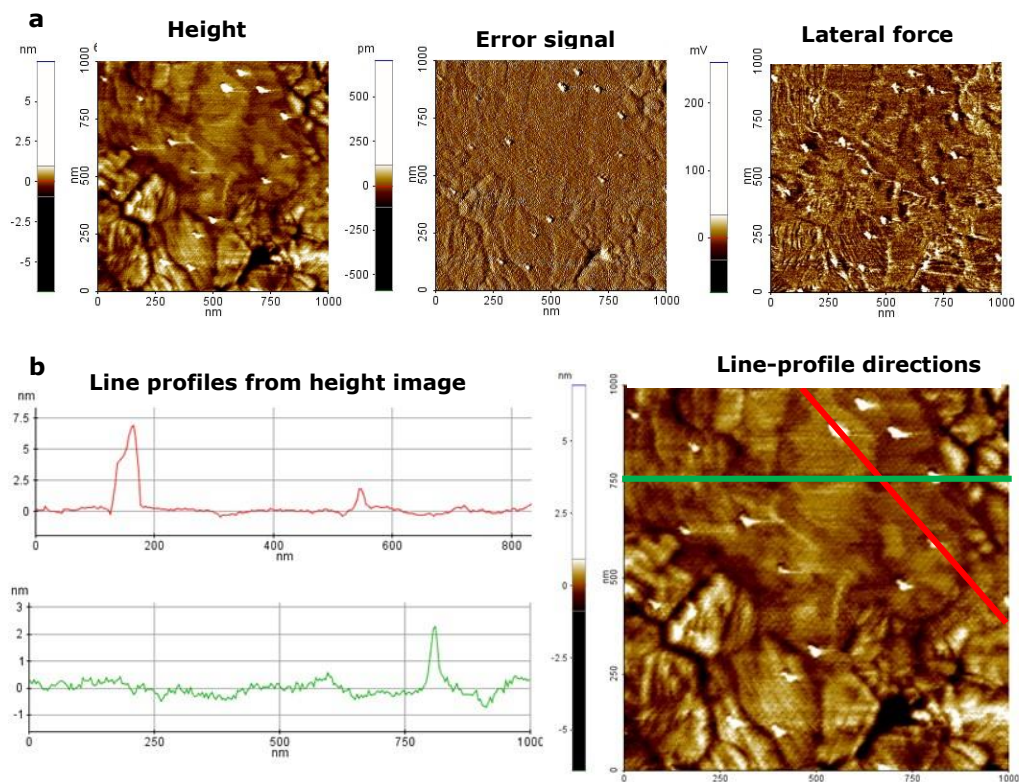


**Fig. 6.14. C-AFM measurement on ultra-flat gold.** MSNL AFM tip E. Spring constant: 0.1 N/m, scan size:  $1 \times 1 \mu\text{m}^2$ . (a) Height, Error Signal and Lateral force; (b) Line profiles show structures with heights of 2.5-5.0 nm heights.

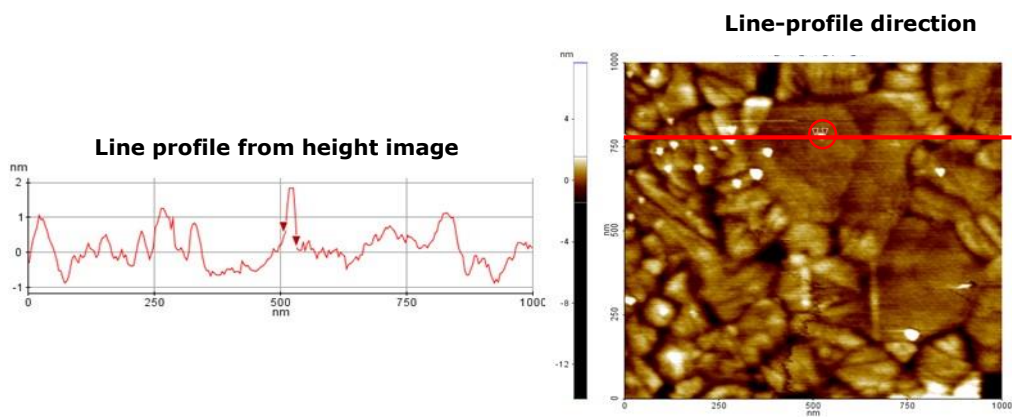


**Fig. 6.15. C-AFM measurement on ultra-flat Gold.** MSNL tip E. Scan size:  $1 \times 1 \mu\text{m}^2$ . Small molecule width and height of terrace are 25.39 and  $\sim 2$  nm respectively.

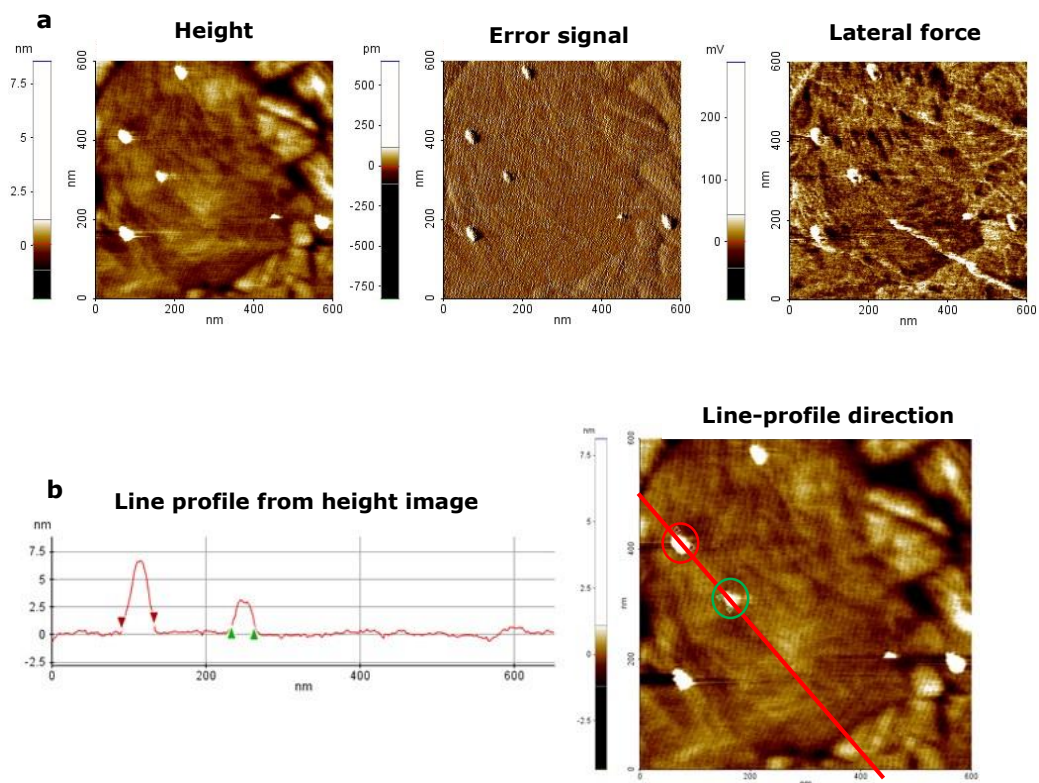


**Fig. 6.16. C-AFM measurement on ultra-flat Gold.** MSNL tip E. Scan size:  $0.6 \times 0.6 \mu\text{m}$ . (a) Height, error signal and lateral force; (b) The line profile of small molecules shows a width of 42.00 nm (red cursor, height: 6 nm) and 29.27 nm (green cursor, height: 2.5 nm).

The interaction between the fullerene groups and gold was expected but in this case even with a careful approach to the surface, the molecules readily attach to the gold tip and adsorb onto it. Furthermore, the tip thickness ( $\sim 5\text{-}10 \text{ nm}$ ) provides a large adsorption area for the fullerene-DNA complexes. Thus, another tip or approach was required.

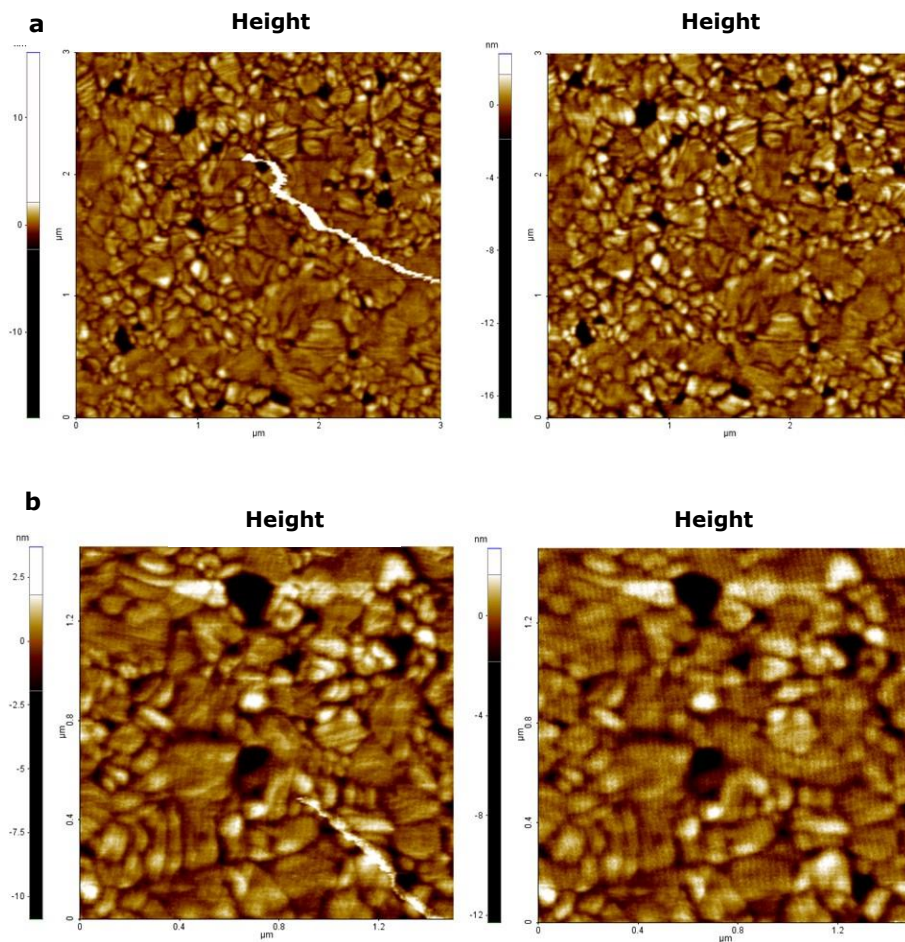


**Fig. 6.17. C-AFM measurement on ultra-flat gold with gold AFM tip. (a)** Scan size:  $3 \times 3 \mu\text{m}^2$ . Height images: Left image, molecule appears attached to the gold AFM tip and moving along with it (“crayon type of pattern”). The right image was taken immediately after, in the same area showing that the molecule is already adsorbed by the tip. **(b)** Another region of the substrate, scan size  $1.6 \times 1.6 \mu\text{m}^2$ . Height images: same fullerene-DNA behaviour (tip attachment) as above.

## 6.5 Additional characterization of DNA- fullerene molecules on top of mica

In the meantime, an addition characterization of the molecules was performed by contact AFM (C-AFM). Freshly cleaved mica was prepared by the scotch tape method. Then, DNA-fullerene molecules were deposited and, after drying under a nitrogen flow, the substrates were imaged.

### 6.5.1 C-AFM on mica

From **Fig. 6.18-19**, it is evident that C-AFM is not suitable for measurements on mica for these type of soft small biomolecules. This is especially because the only forces keeping the DNA molecules onto the hydrophilic surface are weak interactions from the DNA backbone. As a consequence, the molecules are susceptible to be displaced and adsorbed to an AFM tip that is very close, scanning the surface. **Figure 6.19** also show an indentation pattern (square) of the area.

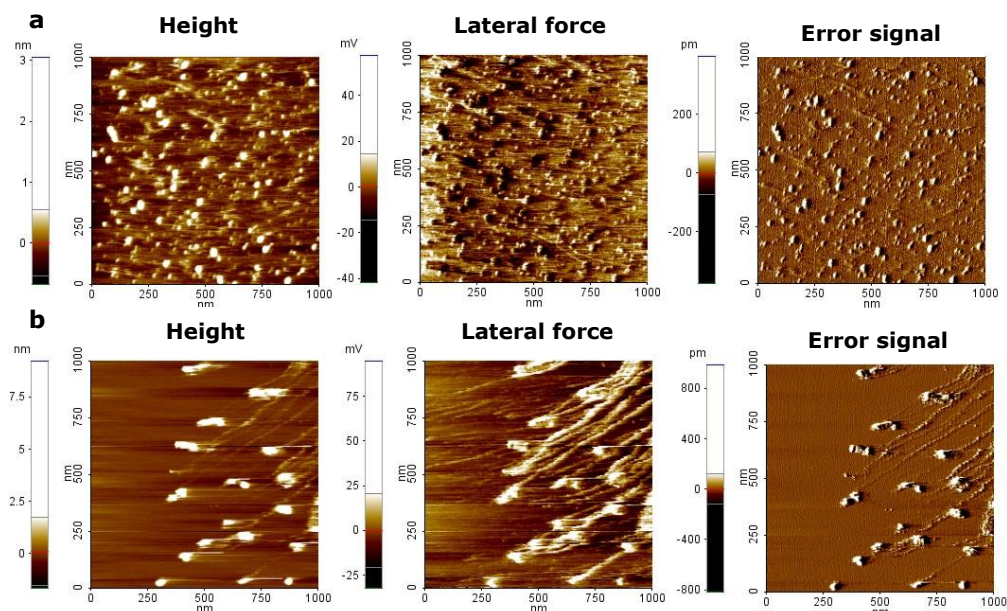


**Fig. 6.18. C-AFM measurement on mica (a-b)** MSNL tip E. Scan size:  $1 \times 1 \mu\text{m}^2$ . Height, lateral force and error signal. The white spots correspond to the Fullerene-DNA complexes.

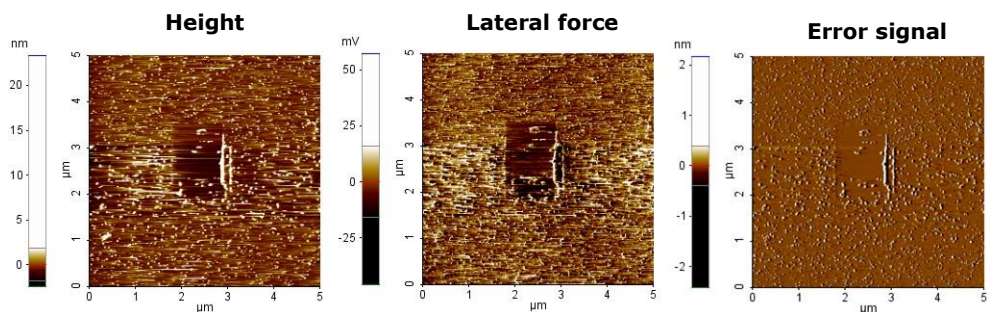


**Fig. 6.19. C-AFM measurement on mica.** Damage of the sample (indentation) can be seen. Scan size:  $5 \times 5 \mu\text{m}^2$ . Height, lateral force and error signal.

### 6.5.2 NC-AFM on mica

Consequently, a change of mode is necessary to avoid further damage of new mica-DNA substrates. The NC-AFM allowed to observe different patterns of the fullerene-DNA molecules, highly dependent on the concentration. **Fig. 6.20-22** show small aggregates in  $0.5 \times 0.5$  and  $1 \times 1 \mu\text{m}^2$ , with a dilution of about 100-150 molecules/ml, with maximum heights (line profile) of  $\sim 2$ -3 nm.

Moreover, higher concentrations produce more organized patterns, as seen in **Fig. 6.23-24**, where a homogeneous layer of height about 1.5 nm is formed, while individual molecules present heights of  $\sim 3$  nm and the large aggregates (circular white shape) present a standard height of  $\sim 7.5$  nm.

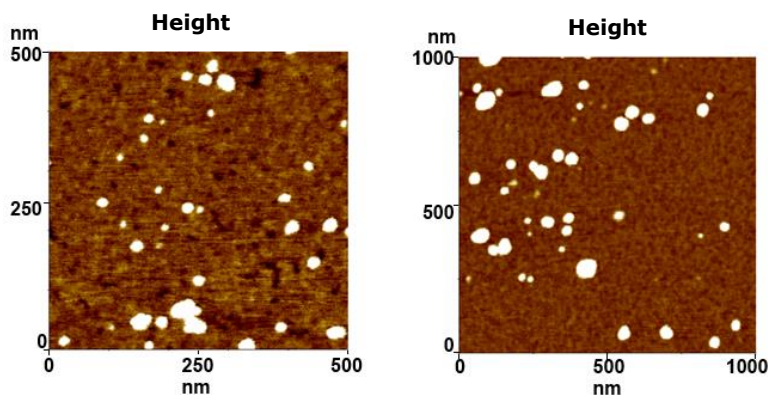


**Fig. 6.20. NC-AFM measurements on mica.** Left and right images: scan size of  $0.5 \times 0.5 \mu\text{m}^2$  and  $1 \times 1 \mu\text{m}^2$ .

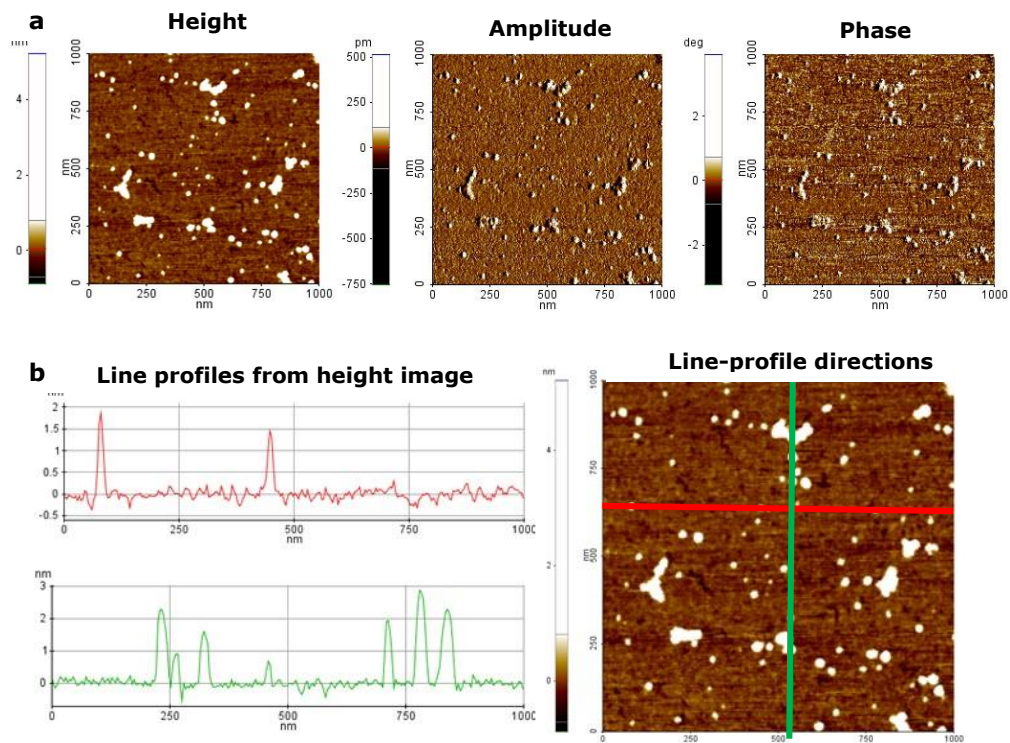


**Fig. 6.21. NC-AFM measurement on mica.** Scan size:  $1 \times 1 \mu\text{m}^2$ . (a) Height, Amplitude and Phase images; (b) Line profile, molecules height between 1-3 nm.

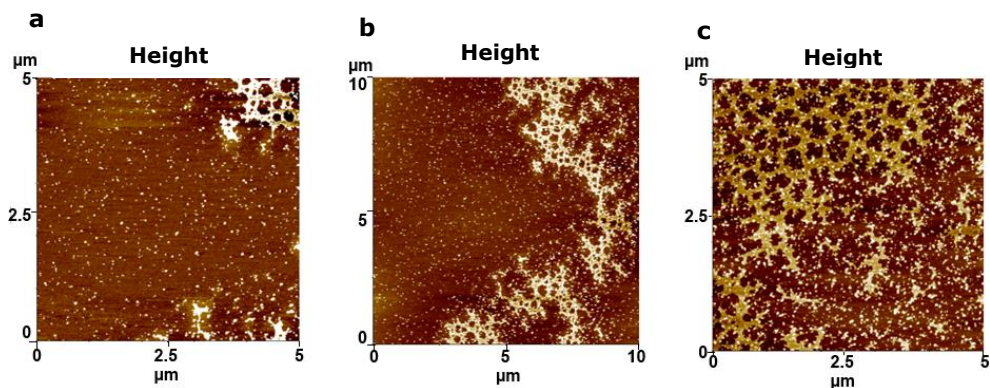


**Fig. 6.22. NC-AFM measurement on mica at different scan sizes.** (a-b) Scan at the same region, first at  $5 \times 5 \mu\text{m}^2$  and then at  $10 \times 10 \mu\text{m}^2$ . (c) Scan of  $5 \times 5 \mu\text{m}^2$  at the middle of the sample, where more molecules aggregate with a tendency to form networks.

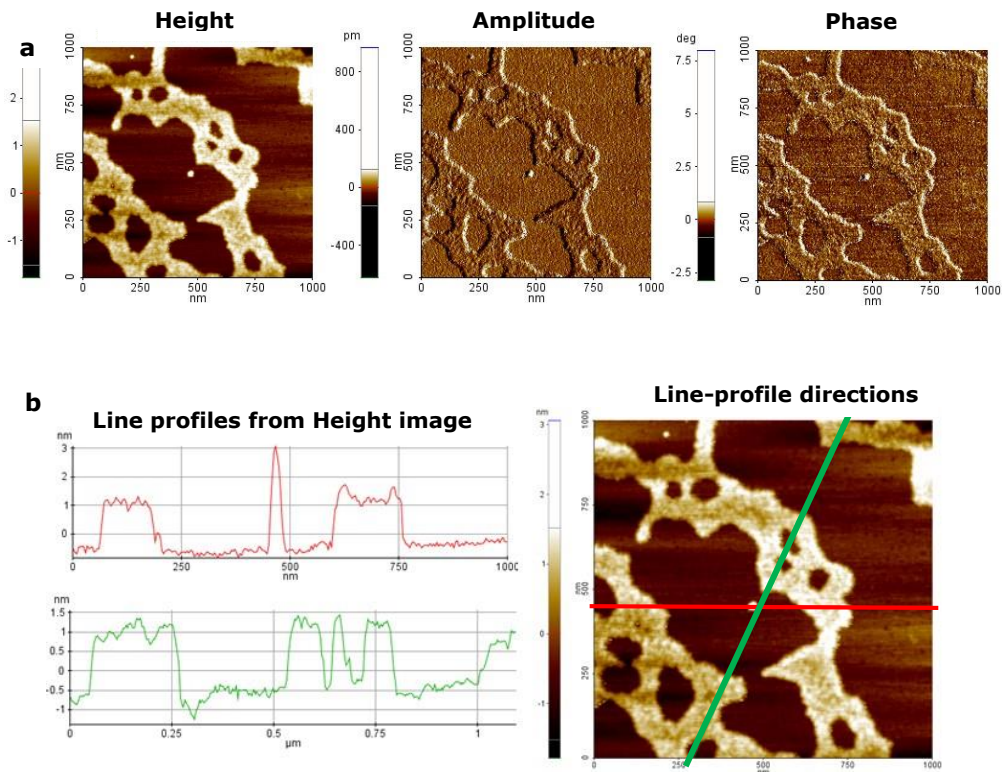


**Fig. 6.23. Non-Contact AFM measurement on mica.** Scan size:  $1 \times 1 \mu\text{m}^2$ . (a) Height, Amplitude and Phase images; (b) Line profile, large molecules height between 1.5 and 3 nm.

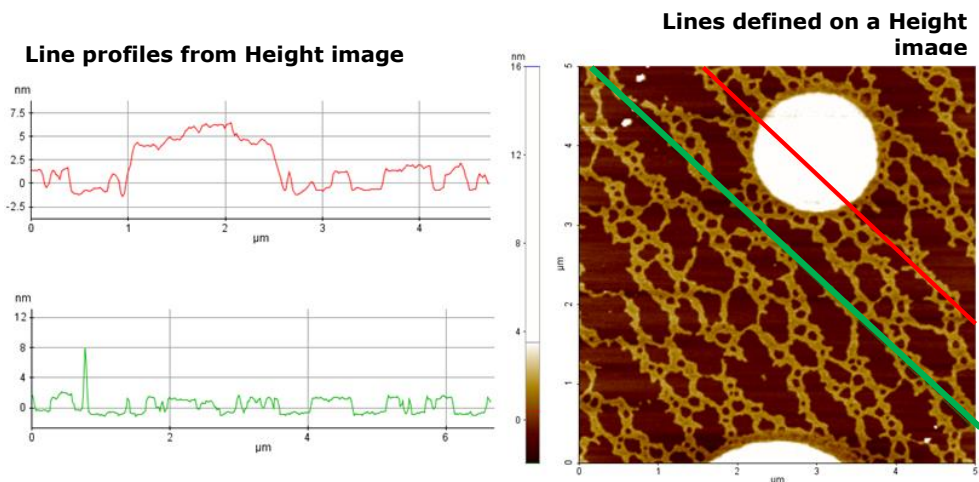


**Fig. 6.24. NC-AFM measurement on mica.** Line profile of DNA-fullerene networks and large aggregates at a scan size of  $5 \times 5 \mu\text{m}^2$ .



## 6.6 AFM studies on longer DNA fragments

### 6.6.1 Fullerene-DNA (102 bp) on ultra-flat gold

Analysis of our data indicates that, despite NX10 AFM produces high quality images in scan sizes between 0.5  $\mu\text{m}$  to 45  $\mu\text{m}$ , it does not provide enough resolution to analyse and measure small DNA molecules (27 bp). In smaller scan sizes, the resulting images tend to be noisy and inaccurate. Additionally, as earlier mentioned, the Conductive Mode (I-AFM) is not fully developed and the current cannot be isolated from external electrical interferences. Therefore, we decided to prepare larger molecules, with a length within the scan size resolution of a more specialized AFM (Bruker Multimode 8 AFM).

Prior to the deposition of the molecules, the gold substrate was scanned as shown in **Fig. 6.25** in order to be check that the surface was optimal for the deposition. Then, after the synthesis and deposition of the new molecules on ultra-flat gold, the surface was first characterized in the NX10 (**Fig. 6.26**), with the final purpose to produce high quality samples for the I-AFM measurements at the Bruker AFM.

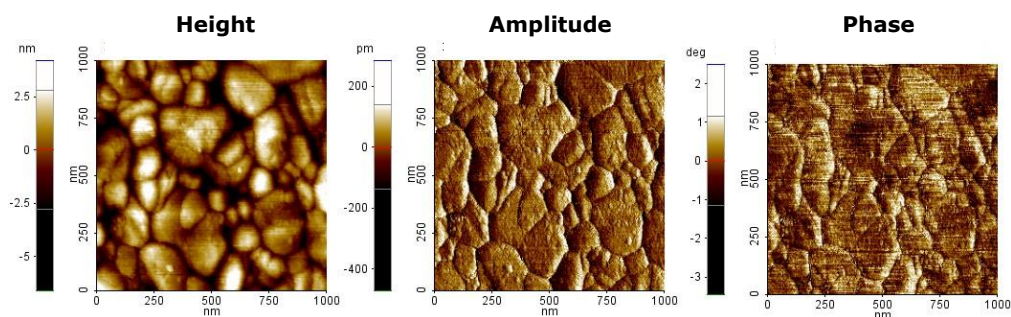


**Fig. 6.26. NC-AFM measurement on ultra-flat gold.** Scan size: 1 x 1  $\mu\text{m}^2$ . Height, amplitude and phase. Region RMS: 1.43 nm.

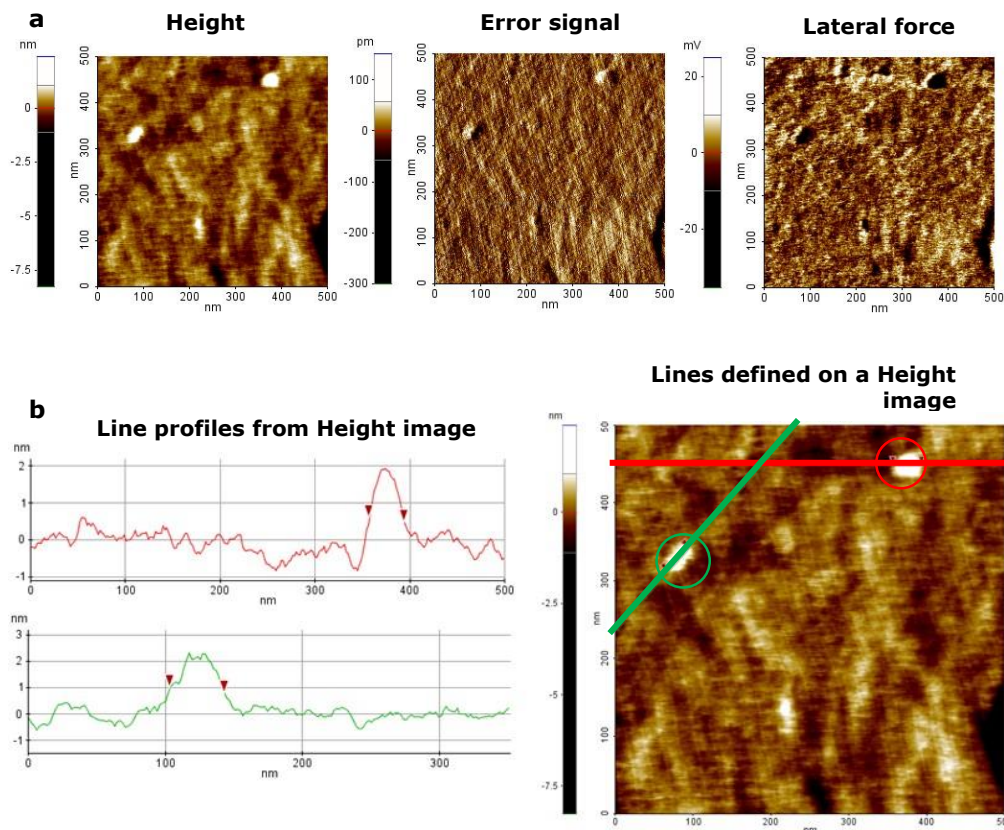


**Fig. 6.25. C-AFM measurement on gold.** Scan size:  $0.5 \times 0.5 \mu\text{m}^2$ . (a) Height, error signal and lateral force. (b) Line profile, sizes between 37.11 nm (red) and 40.34 nm (green).

## 6.7 Conclusion

- Surface analysis to perform single DNA-C61 molecule experiments was done on different substrates such as nanocrystalline diamond, home made flame annealed gold and commercial ultra-flat gold, rendering ultra-flat gold as the most suitable substrate.
- In order to study the electronic characteristics of DNA-C61 single molecules, it is necessary to use an AFM that is fully adapted to measure I-V curves in a

controlled platform and environment. For these experiments, the Bruker Multimode 8.

- The ideal molecules length size to perform AFM experiments on a dry surface was above 10 nm. Specifically for measuring on the Bruker Multimode 8 it is above 30 nm.

## 6.8 References

- [1] P. Christiaens, V. Vermeeren, S. Wenmackers, M. Daenen, K. Haenen, M. Nesládek, M. vandeVen, M. Ameloot, L. Michiels, and P. Wagner, "EDC-mediated DNA attachment to nanocrystalline CVD diamond films," *Biosens. Bioelectron.*, vol. 22, no. 2, pp. 170–177, 2006.
- [2] S. Wenmackers, V. Vermeeren, M. vandeVen, M. Ameloot, N. Bijmens, K. Haenen, L. Michiels, and P. Wagner, "Diamond-based DNA sensors: Surface functionalization and read-out strategies," *Phys. Status Solidi A*, vol. 206, no. 3, pp. 391–408, 2009.
- [3] B. van Grinsven, N. Vanden Bon, H. Strauven, L. Grieten, M. Murib, K. L. Jiménez-Monroy, S. D. Janssens, K. Haenen, M. J. Schöning, V. Vermeeren, M. Ameloot, L. Michiels, R. Thoelen, W. De Ceuninck, and P. Wagner, "Heat-transfer resistance at solid-liquid interfaces: A tool for the detection of single-nucleotide polymorphisms in DNA," *ACS Nano*, vol. 6, no. 3, pp. 2712–2721, 2012.
- [4] C. J. Chen, *Introduction to Scanning Tunneling Microscopy Second Edition*, 2nd ed. New York, USA.: Oxford University Press, 2008.
- [5] M. Hegner, P. Wagner, and G. Semenza, "Ultralarge atomically flat template-stripped Au surfaces for scanning probe microscopy," *Surf. Sci.*, 291, pp. 39-46, 1993.
- [6] K. L. Johnson, *Contact Mechanics*, 1st ed. New York, USA.: Cambridge University Press, 1985.
- [7] Reibungsphysik, "Contact between a sphere and an elastic half-space and one-dimensional replaced model," *Wikipedia: Contact Mechanics*. [Online]. Available: "WikipediabilderKap 4" by Reibungsphysik - Own work. Licensed under CC BY-SA 3.0 via Wikimedia Commons - [http://commons.wikimedia.org/wiki/File:WikipediabilderKap\\_4.jpg#/media/File:WikipediabilderKap\\_4.jpg](http://commons.wikimedia.org/wiki/File:WikipediabilderKap_4.jpg#/media/File:WikipediabilderKap_4.jpg). [Accessed: 17-May-2015].

- [8] W. C. Oliver and G. M. Pharr, "An improved technique for determining hardness and elastic-modulus using load and displacement sensing indentation experiments," *J. Mater. Res.*, vol. 7, no. 6, pp. 1564–1583, 1992.
- [9] W. C. Oliver and G. M. Pharr, "Measurement of hardness and elastic modulus by instrumented indentation: Advances in understanding and refinements to methodology," *J. Mater. Res.*, vol. 19, no. 01, pp. 3–20, 2004.
- [10] Benjamin Michael Dvorak, *Investigation of the near surface mechanical properties of gold-silicon thin films*. Oklahoma, U.S.A.: Oklahoma State University. Mechanical Engineering, 2008.
- [11] A. M. Cassell, W. A. Scrivens, and J. M. Tour, "Assembly of DNA/fullerene hybrid materials," *Angew. Chemie Int. Ed.*, vol. 37, no. 11, pp. 1528–1531, Jun. 1998.

## Chapter 7

# Electronic transport studies on DNA-fullerene complexes

### 7.1 I-V measurements on DNA-fullerene (type 2, 102 bp) Bruker AFM

The advantage of using the Bruker Multimode 8 AFM for conductivity measurements relies on the easy assembly of the sample and tip connection to the machine controllers. Also, it comes with an adaptation for sample grounding, leading to low-noise performance. This is by means of a contact between the SPM base and the metallic cover included with the low current head. When the cover made of can and the SPM base are electrically connected, the metallic cover works as a Faraday shield, reducing electrical noise level. These experiments were performed in collaboration with Dr. Jeroen Drijkonigen, at the IMO-IMOMEC institute of Hasselt University.

With this instrument, all AFM experiments were performed at room temperature, inside the Faraday isolator under a nitrogen environment (relative humidity < 6%), using a Pt-Ir AFM tip. In order to obtain single molecules of DNA-C61, we diluted the original stock in milliQ water, drop casted it into a flat gold surface and dried it under N<sub>2</sub> flow, yielding ~ 10 molecules per  $\mu\text{m}^2$  (PBS final concentration: 1.5 nM). The sample was left in a desiccator for 24 h before performing any type of measurement in order to avoid any water contamination (milliQ water resistivity,  $\rho = 18.2 \text{ M}\Omega\cdot\text{cm}$  at 25 °C) during our experiments.

For each measurement, the fullerene-DNA (C61-DNA) molecules were verified to correspond to a single molecule of 102 base pairs in the standard *B*-form (height ~ 2.5 nm and total length ~ 39 nm, see **Fig. 7.1-2**).

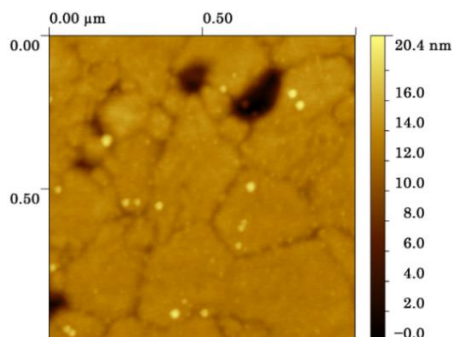


**Figure 7.1. C-AFM characterization of single fullerene-DNA molecules on top of ultra-flat gold:** Height image of multiple molecules (seen as light yellow dots), scan size  $1 \times 1 \mu\text{m}^2$ .

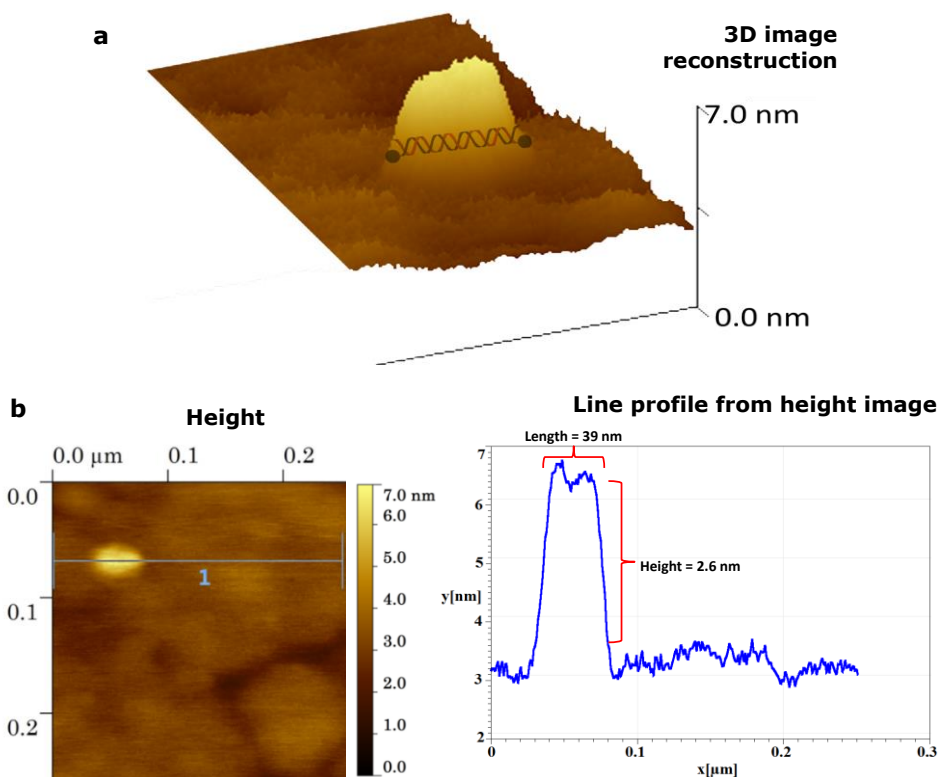


**Figure 7.2. Contact-AFM characterization of single fullerene-DNA molecules on top of ultra-flat gold:** (a) 3-dimensional representation of the fullerene-DNA molecule on the surface, scan size  $0.25 \times 0.25 \mu\text{m}^2$ . (b) Left: Topography of one fullerene-DNA molecule, scan size  $0.25 \times 0.25 \mu\text{m}^2$ , Right: Line profile of the fullerene-DNA molecule.

Note that a typical DNA-fullerene molecule has a length and width of 39 and 2.5 nm respectively. In addition, the conductive AFM tip that makes contact with the molecule has a diameter of about 5 nm. As a consequence, a cylindrical type of structure is observed due to a tip geometric convolution effect. With the use of a smaller AFM tip a more defined wire shape could be possible to observe but this is not available for standard conductive AFM tips.

### 7.1.1 I-AFM experiments on ultra-flat gold

It is important to mention that the work function for this particular Pt-Ir AFM tip was previously measured with Kelvin probe force microscopy (KPFM) on a bare gold surface and gave a value of 5.2 eV (**Eq. 7.1**), very close to the work function of Gold (5.1 eV). Generally, KPFM measures a contact potential difference (CPD) between the sample surface and the tip, and produces local contact potential difference images (LCPD). However, KPFM is mainly used for electrical characterization of metallic nanostructures and some semiconductor surfaces but for our small molecules it proved to be insufficient. Further experiments with AFM on DNA-C61 were performed only with I-AFM mode.

$$V_{CPD} = \frac{\Phi_{tip} - \Phi_{sample}}{-e} \quad (\text{Equation 7.1})$$

Here  $\Phi_{sample}$  and  $\Phi_{tip}$  are the work function of the sample and tip, and  $e$  is the electronic charge. When an AFM tip is brought close to the sample surface, an electrical force is generated between the tip and sample surface, due to the differences in their Fermi energy levels.

The first conductivity experiment was performed on a bare gold substrate as a control (**Fig. 7.3**), where a very steep Ohmic curve was seen. From this data, the resistance was determined 4.7 M $\Omega$ . Also, it can be seen flat plateaus between -0.5 to +0.5 V are artefacts corresponding to the limit of detection from the AFM amperometer (Picoamp Boost Box).

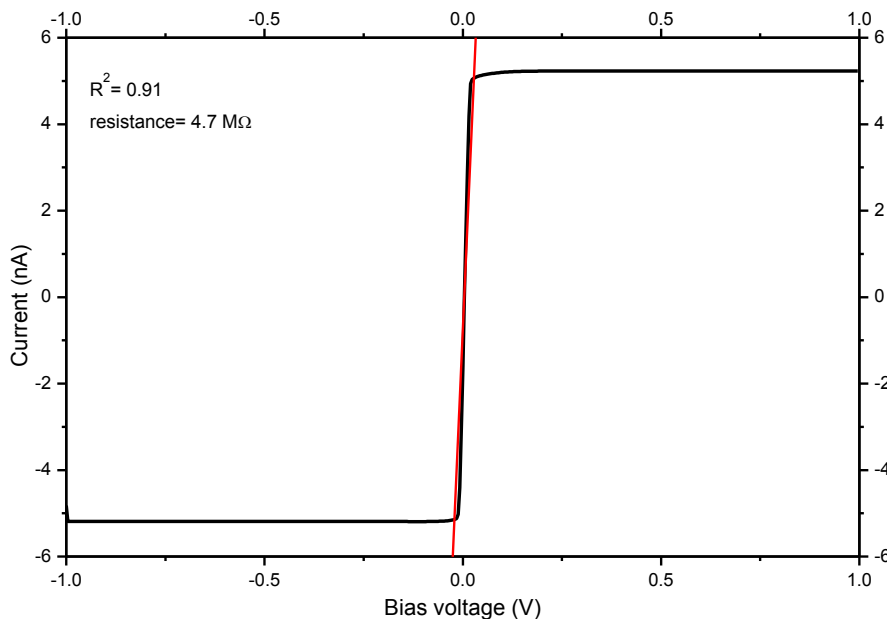
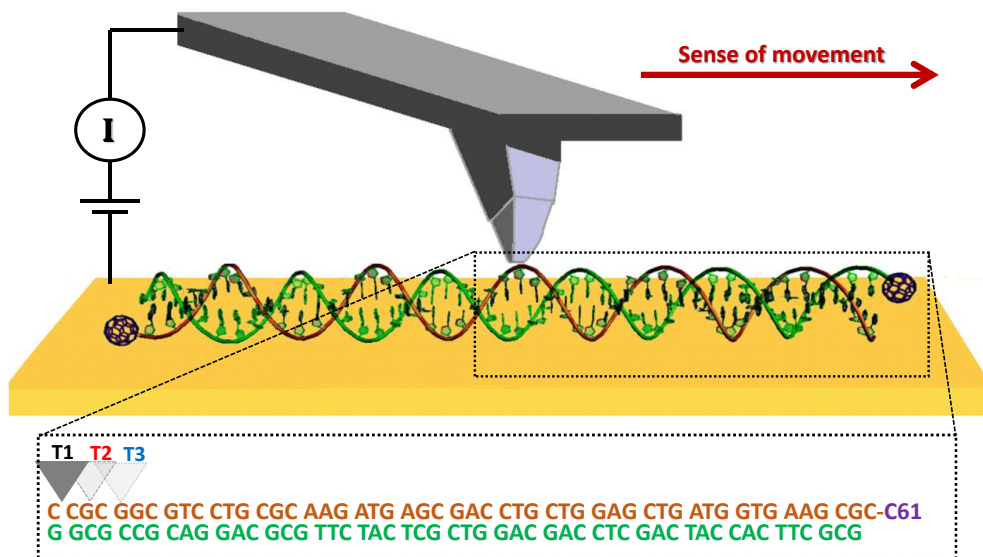


**Figure 7.3. I-V spectrum on bare ultra-flat gold substrate.** The obtained curve shows Ohmic behaviour, where a small gold area that is in contact with the AFM tip has a contact resistance of 4.7 M $\Omega$ .

Next, several current-voltage (I-V) measurements were performed on top of a DNA-fullerene molecule, as illustrated in **Fig. 7.4**. In this representation, the AFM tip is located approximately at the middle of the structure and moved towards the fullerene ends. The total number of steps, from this point until the AFM tip was out of the sample, was 31. Furthermore, we confirmed that the tip was out of the sample because the I-V curve returned to the original values as for bare gold (**Fig. 7.3**).

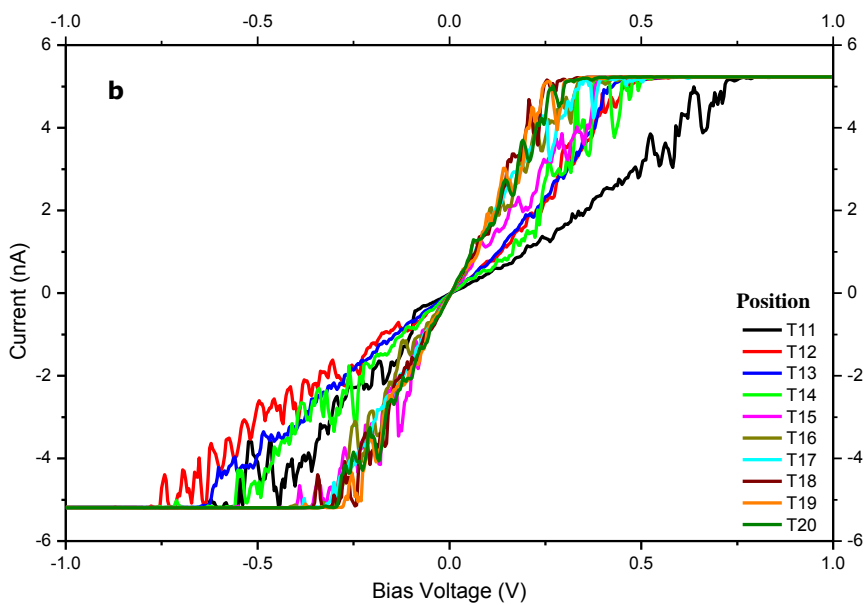
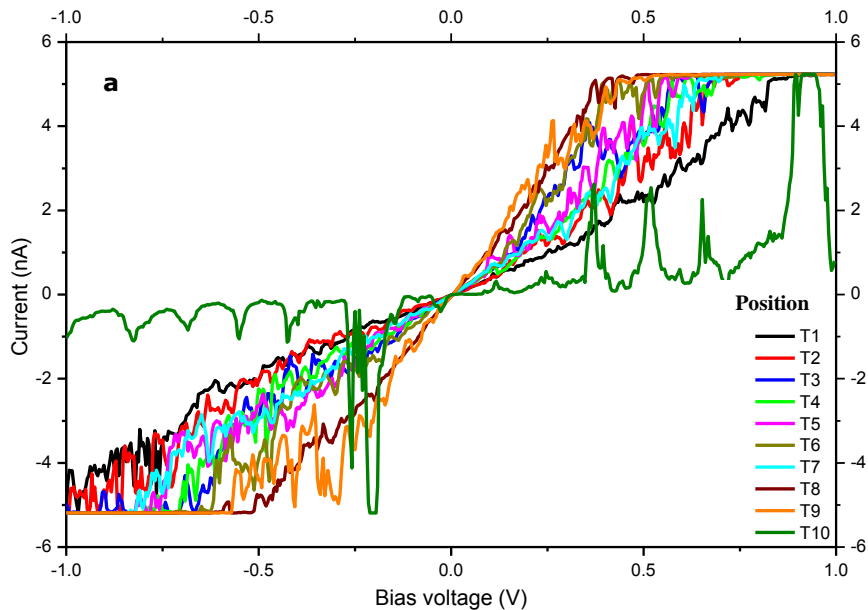
At this point, a new topography image was taken, demonstrating that the area under the tip was clean. Measurements on different molecules at different starting positions indicated that the small I-V step movements (0.65 nm) along the molecule render reproducible graphs and over-compression of the DNA structure (DNA-tip contact) can be avoided.





**Figure 7.4. Schematic representation of the Conductive-AFM experiment.** A Pt-Ir tip is approached to the fullerene-DNA molecule. Once the tip is on top of the molecule a voltage range between -1 to +1 V is applied. We measured stepwise I-V curves every 0.65 nm.

In addition, the I-V curves obtained for **Fig. 7.4** are displayed in **Figure 7.5.a-c** where all curves belong to different positions on one molecule. Further I-AFM experiments were performed on more DNA-C61 molecules (in total 22 single molecules) at different starting positions confirming the reproducibility of the acquired data for 19 out of 22 molecules. Changes of position and conductance are shown in **Table 1**. Also, from **Fig. 7.5a**, the I-V curve at position T10 shows a decrease in conductivity that related to a higher amount of adenine content in contact with the conductive AFM tip, which appears to be reflected on a lower efficiency of the hole transport. This effect was observed on other 3 particles at approximately the same position. The set of graphs presented here (**Fig. 7.5 a-c**) were the most representative for one consecutive measurement on a DNA-C61 wire and for that reason; the complete experimental results are displayed in here.



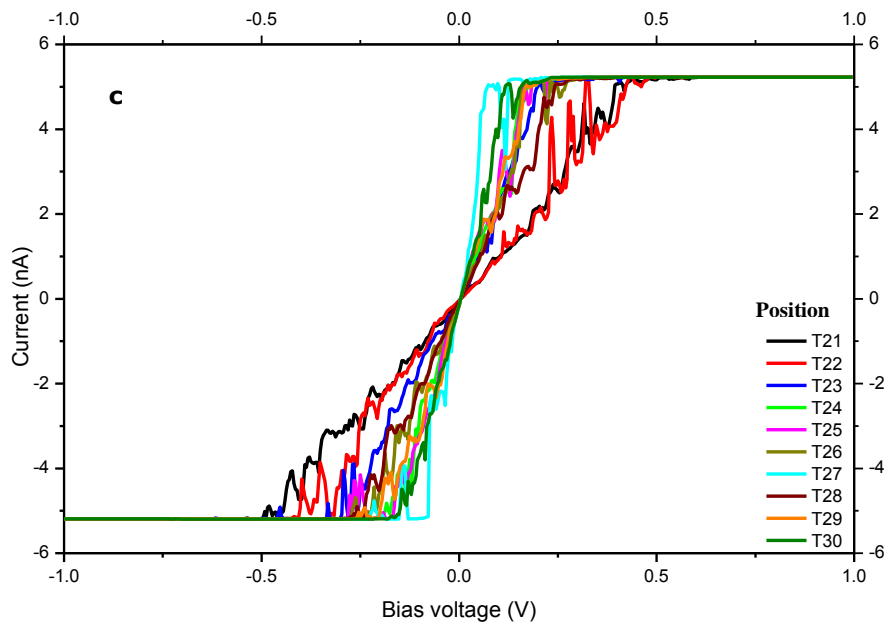


**Figure 7.5. I-AFM (a-c):** All thirty curves for DNA-C61 (PBS 1.5 nM) deposited on a gold substrate. Note the slope change when the AFM tip is moved from the middle position of DNA-C61 (T1) towards the fullerene end of the molecule (T30).

**Table 7.1. Conductance ( $dI/dV$ ) values.** For every measured I-V curve (T1-T30), the conductance was calculated, as shown below.

	D (Angstroms)	$dI/dV(S)$			D (Angstroms)	$dI/dV(S)$
<b>T1</b>	194.75	4.04E-09		<b>T16</b>	97.25	1.48E-08
<b>T2</b>	188.25	5.50E-09		<b>T17</b>	90.75	1.42E-08
<b>T3</b>	181.75	6.76E-09		<b>T18</b>	84.25	1.71E-08
<b>T4</b>	175.25	5.65E-09		<b>T19</b>	77.75	1.81E-08
<b>T5</b>	168.75	6.79E-09		<b>T20</b>	71.25	1.70E-08
<b>T6</b>	162.25	7.32E-09		<b>T21</b>	64.75	1.11E-08
<b>T7</b>	155.75	6.29E-09		<b>T22</b>	58.25	1.21E-08
<b>T8</b>	149.25	1.11E-08		<b>T23</b>	51.75	1.90E-08
<b>T9</b>	142.75	1.34E-08		<b>T24</b>	45.25	2.63E-08
<b>T10</b>	136.25	1.56E-09		<b>T25</b>	38.75	2.34E-08
<b>T11</b>	129.75	7.64E-09		<b>T26</b>	32.25	2.17E-08
<b>T12</b>	123.25	7.90E-09		<b>T27</b>	25.75	5.73E-08
<b>T13</b>	116.75	8.80E-09		<b>T28</b>	19.25	1.94E-08
<b>T14</b>	110.25	9.49E-09		<b>T29</b>	12.75	2.67E-08
<b>T15</b>	103.75	1.28E-08		<b>T30</b>	6.25	3.29E-08

### 7.1.2 I-AFM experiments on ultra-flat gold with desalted DNA-fullerene molecules.

Finally, we decided to test the effect of removing all salts from the DNA-fullerene structure by means of a gel extraction kit (Agarose Gel DNA extraction kit, Roche Diagnostics) and final dissolution in milliQ water. The results are displayed in **Fig 7.6**, where the conductance values (**Table 7.2**) are about 10-100 times lower compared to the standard DNA-C61 molecules (**Table 7.1**). This could be attributed to disturbances on  $\pi$ - $\pi$  stacking and change of distances between base pairs, where no salt is involved in stabilizing the structure in an inert environment. Additionally, when compared to **Fig. 7.4.a**, over-compression appears to also have a negative effect on the DNA structure, lowering the conductance values, as observed in position T10.

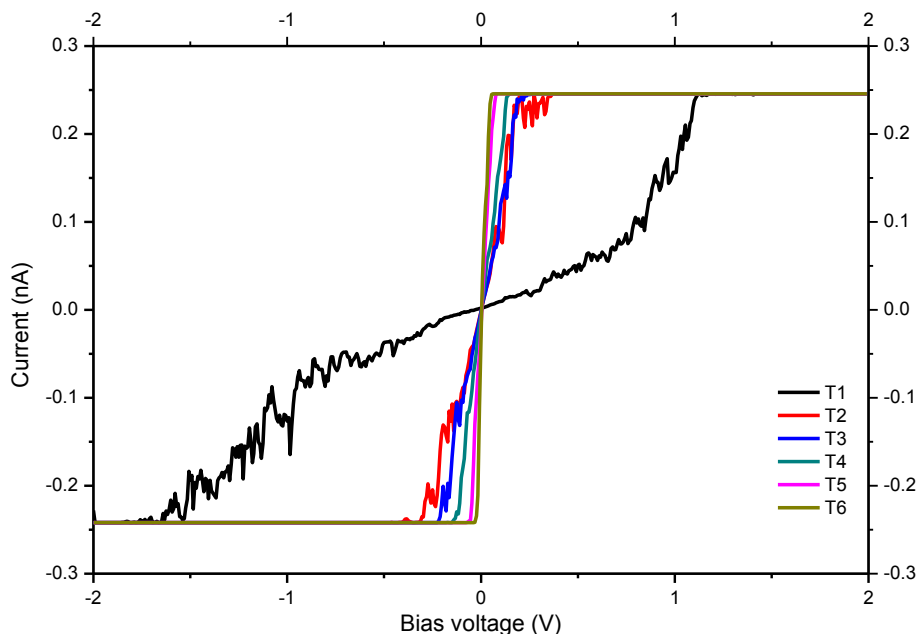


**Figure 7.6. I-AFM on ultra-flat gold for desalted DNA-C61.** Note that the device range sensitivity was changed to  $-0.25$  to  $+0.25$  nA, compared to the previous experiments ( $-5$  to  $+5$  nA). Here, complete desalting of the DNA-C61 molecule shows 20 times lower current ranges than the standard DNA-C61 molecules ( $1.5$  nM PBS) at the same voltage range.

**Table 7.2. Conductance ( $dI/dV$ ) values for desalted DNA-C61.** For every measured I-V curve (T1-T6), the conductance was calculated, as shown below.

	<b>D (Angstroms)</b>	<b><math>dI/dV</math> (S)</b>
<b>T1</b>	32.50	1.36E-10
<b>T2</b>	26.00	7.68E-10
<b>T3</b>	19.50	1.10E-09
<b>T4</b>	13.00	1.73E-09
<b>T5</b>	6.50	3.24E-09
<b>T6</b>	0.00	4.51E-09

### 7.1.3 Scanning Tunneling Microscopy (STM)

These measurements were performed in collaboration with Dr. Koen Schouteden at the KU Leuven Laboratory for Solid State Physics and Magnetism. In this experiment an Omicron Nanotechnology STM was used under ultrahigh vacuum conditions (base pressure below  $5 \times 10^{-11}$  mbar). In addition, for these experiments we used Au (111) substrates prepared at KU Leuven. Measurements were performed at room temperature and ultrahigh vacuum, using Pt-Ir (10% Ir) tips. Here, it was observed that DNA-C61 molecules do not have a very high contact (tunneling) with the gold substrate *in situ* (**Fig. 7.7 a-b**).

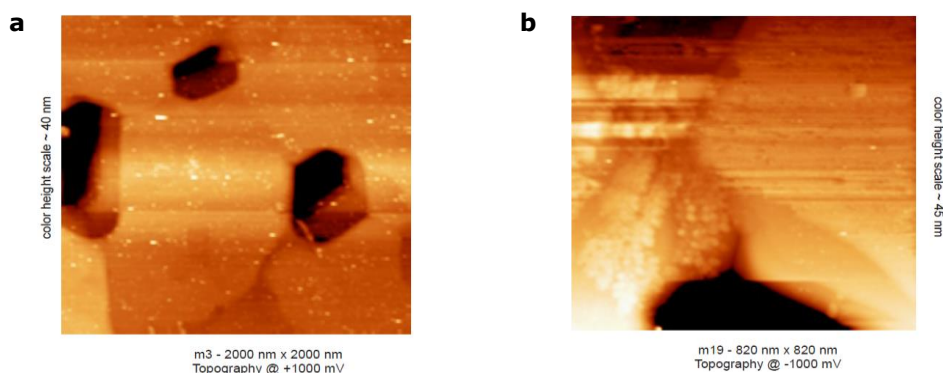


**Figure 7.7. Scanning Tunneling Microscopy.** Before annealing: DNA-C61 molecules tend to form clusters, observed at (a) scan size: 2000 x 2000 nm and (b) scan size: 820 x 820 nm, where the molecules seem to move along with the Pt-Ir tip.

Under this condition, a cluster of molecules was able to be measured and changes on the tunneling behaviour of gold were observed but after a set of voltage changes, the molecule seems to explode, possibly related to overcharging the particle with the STM tip (**Fig. 7.8**).

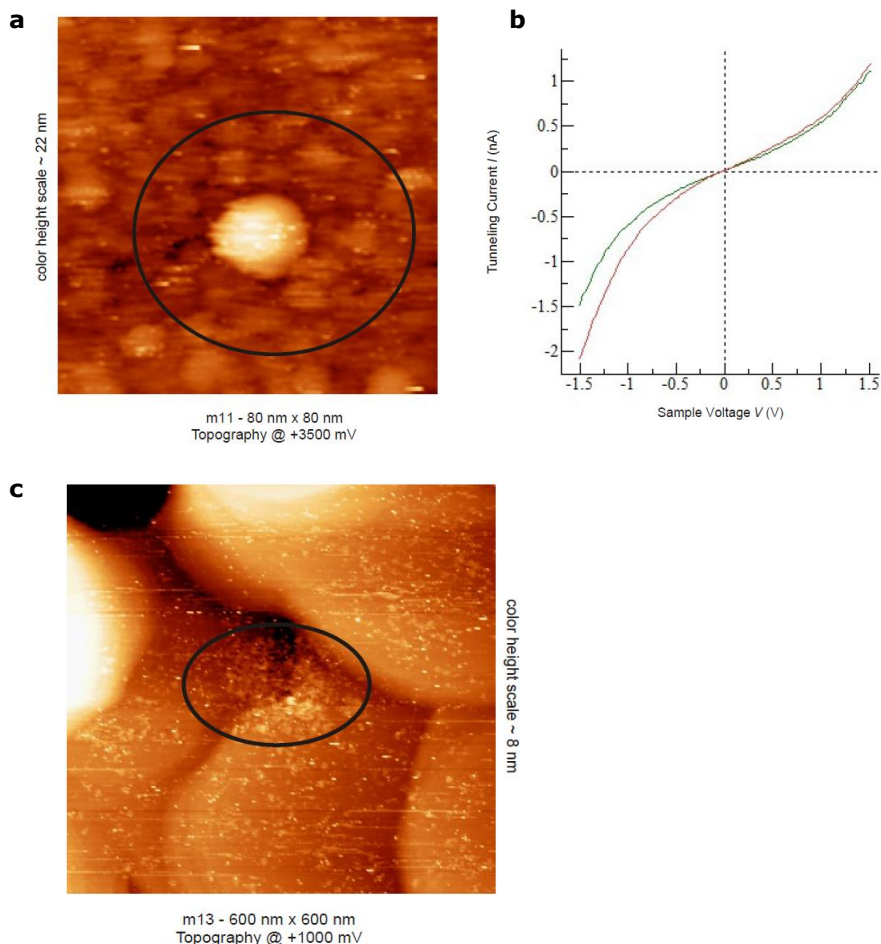


**Figure 7.8. Scanning Tunneling Microscopy.** (a) A small aggregate of molecules (height > 10 nm) was able to be measured, scan size of 80 x 80 nm<sup>2</sup>, (b) shows a slightly suppressed tunneling current on the particles (green curve), compared to the surrounding gold surface (red curve). (c) An example of the exploded particles is shown; scan size 600 x 600 nm<sup>2</sup>.

In order to increase the C61-gold interaction it is necessary to anneal the samples (up to ~ 350°C). Unfortunately, this annealing induces DNA degradation, as shown in **Figure 7.9**, where a clean gold substrate can be visualized from the background pattern and small spherical structures (presumably C60 and C61) are surrounded by burned organic material (DNA).

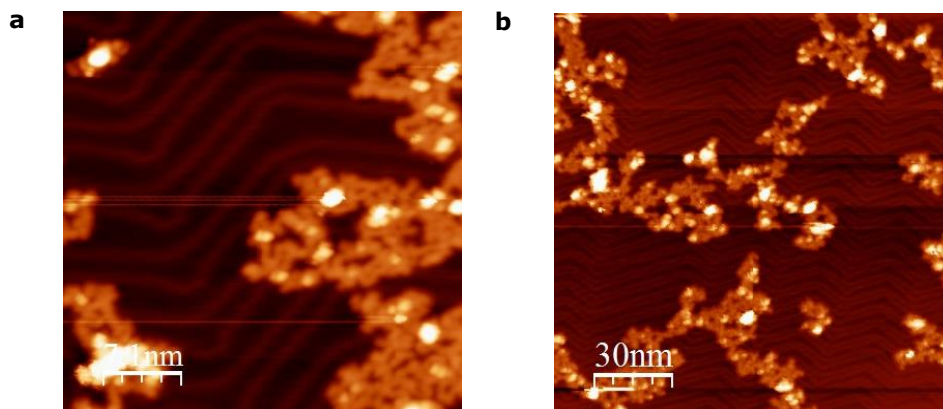


**Figure 7.9. Scanning Tunneling Microscopy.** After annealing: (a) and (b) illustrates the presence of decomposed organic material surrounding C60 and C61 molecules (lighter colour) on top of a very clean gold surface, seen in the herringbone ridge pattern.

## 7.2 Comparison with theoretical models

We compared visually our results to the literature reports, where 3 out of the 27 molecules showed an initial semiconductor slope with an average voltage gap of 1 V, similar to reference [1], possibly related to over-compression of the molecules, increasing the  $\pi$ - $\pi$  orbital overlap but also increasing the inter-base distances (twisting vs stretching) [2–4]. An example is shown in **Figure 7.10**, using the same procedure described at the beginning of this chapter, the AFM tip was placed close to the middle of the molecule and moved towards the fullerene ends.



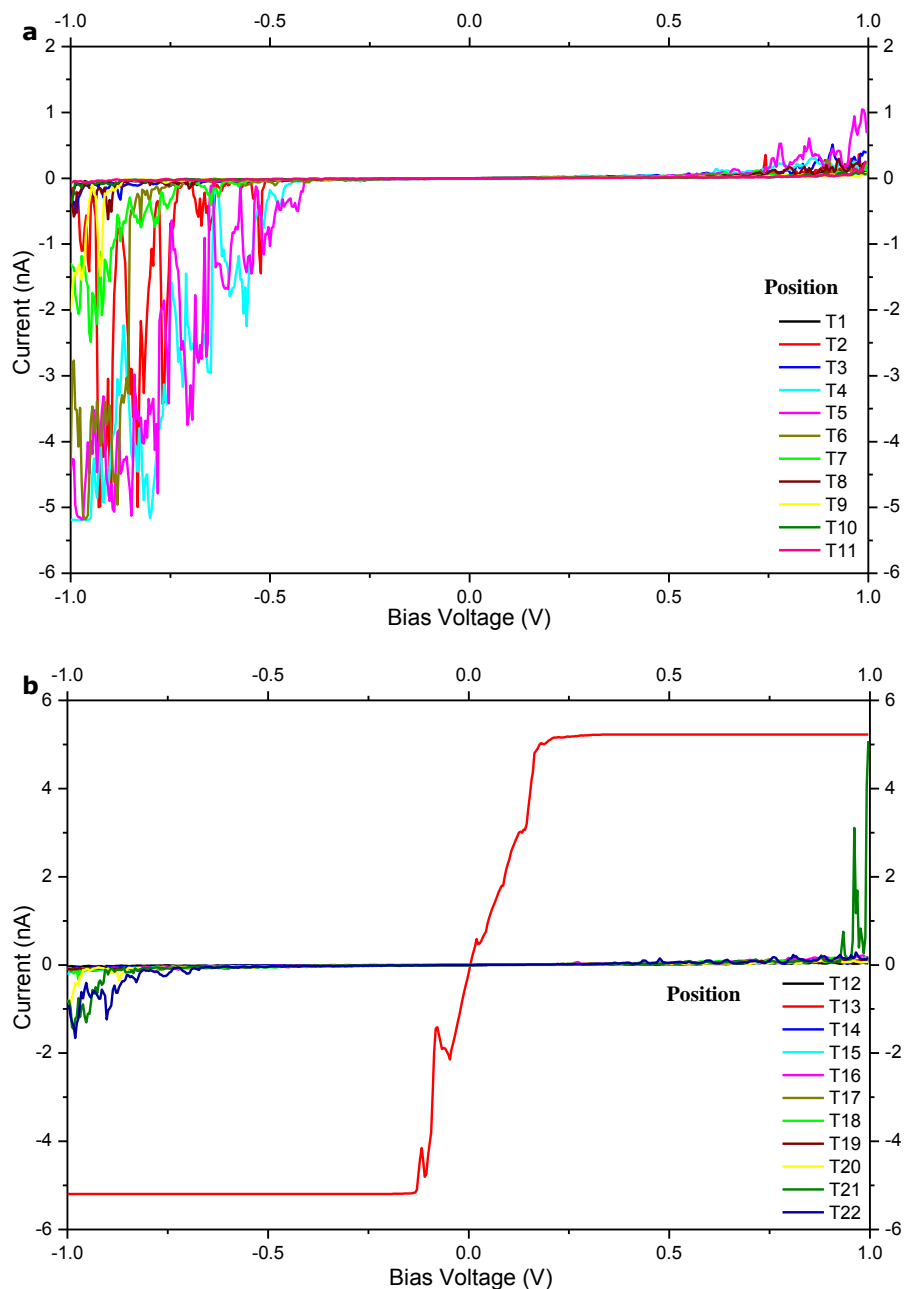


**Figure 7.10. "Anomalies" on the I-V experiments for Fullerene-DNA complexes:** (a) and (b) represent the curves of one of the three measured molecules that displayed a semiconductor type of behaviour.

Furthermore, in order to understand the main type of charge transfer mechanism involved in our experiments we contacted the group of Prof. Dr. Ferdinand Grozema, Prof. Dr. Laurens Siebbeles and Dr. Nicolas Renaud, at the TU Delft Department of Chemical Engineering.

There, they performed kinetic calculations for charge transfer simulations with a home-built algorithm. The first model considered a sequential tunneling mechanism while the following model assumed a multistep charge hopping mechanism.

### 7.2.1 Coherent charge transport for charge tunneling

Coherent charge tunnelling, also known as sequential tunnelling, assumes that charges are transferred from the tip to the surface via the DNA. In this approach the conductance of the system is given by **Eq. 7.2** [5]:

$$g = \frac{e^2}{\pi\hbar} T(E_F) \quad (\text{Equation 7.2})$$

Where  $T(E_F)$  is the transmission coefficient of the junction. This transmission coefficient can be calculated using the usual non-equilibrium Green's function approach (NGEF) [6]. Due to the large number of atoms in the system studied here, we employed a simple tight-binding model to compute the transmission coefficient.

As DNA is generally a HOMO conductor, we only consider the HOMO levels of each base pair in this model. These levels were taken as isoenergetic with an energy of  $E_{bp} = -2$  eV. This energy roughly corresponds to the difference between the ionization potential of the adenine (IP = 7.62 eV) or guanine (IP = 6.84 eV) and the Fermi energy of gold at about  $E_f = -5$  eV [7]. An electronic coupling between the neighbouring base pair was taken as  $V_{bp} = 50$  meV in agreement with electronic structure calculations [8]. The energy of the fullerene was taken as  $E_f = -2.6$  eV, corresponding to an ionization potential of 7.6 eV [9]. The coupling between the terminal base pair and the neighbouring fullerene was set to  $V_f = 5$  meV to account for the relatively long distance separating these two fragments. A self-energy of  $\Gamma = 25$  meV, was added to the fullerene

energies and to the base pair in contact with the tip to simulate the coupling with the electrodes. Additionally a small self-energy term of  $\Gamma_{bp}$  was eventually added to each base pair to represent their own coupling with the surface. The transmission coefficient was then calculated using the NEGF formalism in **Eq. 7.3**:

$$T(E) = \text{Tr}[\Gamma_S G(E) \Gamma_T G^\dagger(E)] \quad (\text{Equation 7.3})$$

Here  $\Gamma_{S/T}$  represents the coupling between the DNA and the surface/tip and  $G(E) = (E - H + i0^+)^{-1}$  is the Green's function of the DNA with  $H$  its model Hamiltonian. As for the kinetic scheme presented above, we have calculated the electronic transmission of the system for different positions of the tip, progressively moving it away from one terminal fullerene toward the middle position of DNA. The results of this calculation are represented in **Fig. 7.11**.

Two cases were considered:  $\Gamma_{bp} = 0$  and  $\Gamma_{bp} = 10$  meV. In the former case, only tunneling through the system is considered and a strong exponential decay with the distance between the tip and the fullerene is observed. This strong distance dependence is in clear contradiction with the experimental results showing a weak decay of the conductance. Therefore pure tunneling is rejected as a potential mechanism mediating the charge transfer in our experiment. The effect of introducing a direct coupling between each base pair and the surface leads to a flattening of the conductance for long distances between the tip and the final fullerene. However, the distance dependence of the conductance would be then equal to zero, which is also in contradiction with our experimental results. A direct injection between the base pair and the surface cannot be responsible of the charge transfer. This last conclusion is reinforced by previous experimental results showing very little to no current tunneling directly from the tip to the gold surface, in the voltage range employed here [1].

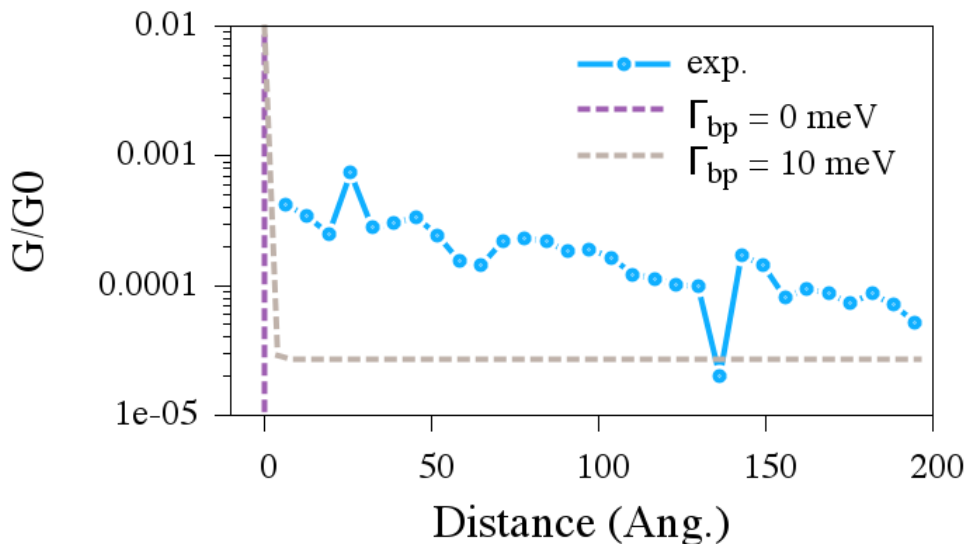


**Figure 7.11. Sequential tunneling: conductance vs distance.** The case with (purple curve) and without (grey curve) direct coupling between the base pairs and the surface are represented. A disagreement between our experimental data (blue curve) and this model can be clearly observed.

### 7.2.2 Kinetic scheme for multistep charge hopping

After demonstrating that no sequential tunneling takes place in our experiments, an alternative model was implemented: The multistep charge hopping model, also known as incoherent tunneling. Here, we assume that charges hop between the different molecular fragments. The hopping rates were adapted from literature or estimated on base of intermolecular distances. Then, the steady state approximation [10] was used to compute the charge transfer rate between the tip and the surface and subsequently the conduction of the junction.

This hopping model is illustrated in **Fig. 7.12**. As seen in the figure, we consider that a charge localized on a given base pair can hop to a neighbouring one at a rate  $k_{bp} = \tau_{bp}^{-1}$  with  $\tau_{bp} = 30$  ps. Such hopping rate is in good agreement with experimental and theoretical values giving hopping times ranging between 10

and few hundred ps [11]. We therefore do not account for the exact nature of each base pair, which could lead to a static disorder in the values of the different hopping rates.

Due to the long distance separating the final base pairs and the C60, we have considered that the hopping rate between these two fragments to be much smaller than between two base neighbouring base pairs with  $k_f = 0.005 \text{ ps}^{-1}$ . Finally the injection rate from each fullerene into the surface was taken as  $\Gamma = 0.05 \text{ ps}^{-1}$ . As seen in **Fig. 7.11** we also account for a possible direct charge injection from each base pair directly to the surface. Several values of this hopping rate,  $\Gamma_{bp}$ , will be considered in the following.

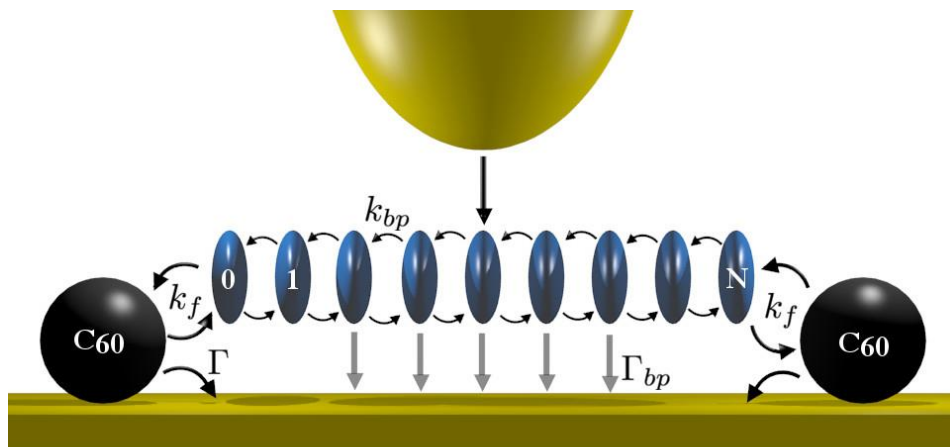


**Figure 7.12. Multistep charge hopping along the DNA.** Graphical representation of the kinetic scheme used to model charge hopping along the DNA–fullerene system.

A kinetic scheme was then considered to simulate the propagation of charge along the DNA (details can be found in **Chapter 3**). The population of each site of the system follows then a differential equation [10]. The evolution of the base pairs charge population is given by **Eq. 7.4**:

$$\frac{dP_n}{dt} = -(2k_{bp} + \Gamma_{bp})P_n(t) + k_{bp}(P_{n+1}(t) + P_{n-1}(t)) \quad (\text{Equation 7.4})$$

$$\text{for } n = 1, N - 1.$$

The population of the two terminal base pairs is given by a similar differential equation that accounts for the hopping to the neighbouring fullerene (**Eqs. 7.5-6**):

$$\frac{dP_0}{dt} = -(k_{bp} + k_f + \Gamma_{bp})P_n(t) + k_{bp} P_1(t) + k_f P_{fL}(t) \quad (\text{Equation 7.5})$$

$$\frac{dP_N}{dt} = -(k_{bp} + k_f + \Gamma_{bp})P_n(t) + k_{bp} P_{N-1}(t) + k_f P_{fR}(t) \quad (\text{Equation 7.6})$$

Finally the differential equations relative to the population of the left (or right) fullerene is given by **Eq. 7.7**:

$$\frac{dP_{fL(R)}}{dt} = -(k_f + \Gamma)P_{fL(R)}(t) + k_{fL(R)} P_{0(N)}(t) \quad (\text{Equation 7.7})$$

In the steady state limit, *i.e.* when a steady state current has been established between the tip and the surface, this population must have reached equilibrium, thus we impose  $\frac{dP_X}{dt} = 0$ .

Furthermore, we suppose that the current flows from the tip to the DNA surface and that the centre of the tip is located above the *i*-th base pair of the sequence with  $i = 1 - N$ . We hence impose  $P_i = 1$ , to simulate the constant injection of charge from the tip to the initial base pair. The system of linear equations can then be solved using usual techniques to obtain the steady state population of the different base pairs. The steady state injection rate was then calculated with **Eq. 7.8**:

$$k_{SS} = \Gamma(P_{fL} + P_{fR}) + \sum_{n=1}^N \Gamma_{bp} P_n \quad (\text{Equation 7.8})$$

This rate captures the time required for a charge to transfer from the DNA to the fullerene once the steady state has been reached. The product of this rate with the total electronic charge that is consequently transferred gives the final current in **Eq. 7.9**:

$$I(V) = (-e)N_e k_{SS} \quad (\text{Equation 7.9})$$

Here,  $N_e$  is the total number of charge that are available for transfer at a given bias voltage. The conductance is therefore given by **Eq. 7.10**:

$$g = \frac{dI}{dV} = (-e) \frac{dN_e}{dV} k_{SS} = (-e) \rho(E_F) k_{SS} \quad (\text{Equation 7.10})$$

Where  $\rho(E_F)$  is the density of electronic states of the tip expressed here in number of states/eV. We have considered that in the bias voltage window explored in the experiment, *i.e.* between -1 V to +1 V, the density of state is constant and equal to the density of states at the unbiased Fermi energy. *Ab-initio* electronic structure calculations have showed that  $\rho(E_F) = 0.3$  electrons/eV/atom for bulk gold [12].

Extrapolating this result to a cluster of 2 nm of diameter representing the tip we arrived to  $\rho(E_F) = 10 - 100$  states/eV for the tip. This result is in good agreement with *ab-initio* calculations performed for gold clusters with 2 nm of diameter [13].

Using the kinetic scheme presented above, we have calculated the theoretical values of the conductance in two different situations:  $\Gamma_{bp} = 0$  and  $\Gamma_{bp} = 0.01$  ns<sup>-1</sup>. Similarly to the experiment we have continuously moved the tip from one end of the fullerene to the middle of the DNA sequence and calculated the conductance for each position of the tip. The values of the conductance that we have obtained are represented in **Table 7.1**.

**Figure 7.13** demonstrates that the multistep charge hopping model captures correctly the distance dependence of the conduction for  $\Gamma_{bp} = 0$ . The variation of the conduction with the distance separating the initial base pair and the terminal fullerene follows then a power law, *i.e.*  $g \propto N_{bp}^{-1}$ . Accounting for a direct charge injection from each base pair to the surface leads, even for  $\Gamma_{bp} = 0.1$  ns<sup>-1</sup>, to a much flatter distance dependence that does not capture the decay observed experimentally. The theoretical analysis presented above

demonstrates that our experimental results can be explained by a hopping type mechanism along the DNA structure, without direct charge injection from the base pair to the surface. This consequently indicate that the current measured in our experiment is supported by a very long range multistep hopping charge transfer along the DNA over a distance up to 200 Å.

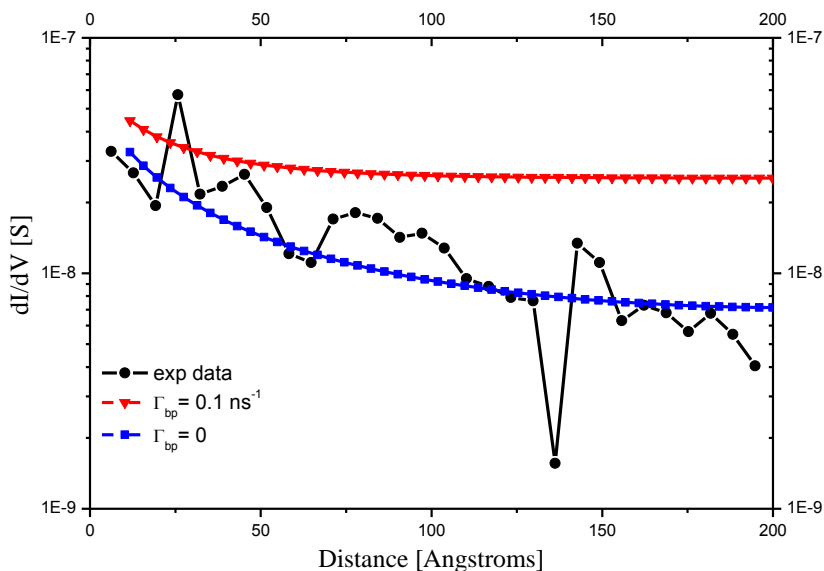


**Figure 7.13. Comparison of theoretical predictions vs experiment**, based on a multistep hopping type of mechanism: i) for the distance dependence of the conduction with (red curve) and, ii) without (blue curve) direct charge injection from the base pair to the surface. Experimental data is shown here in black solid dots.

### 7.3 Conclusions

- These data suggests that a small molecule, such as fullerene can provide a good anchor for single molecules of DNA towards a gold surface, where at a dry surface:
  - Structural fluctuations appear to be minimized (*e.g.* dynamic disorder).
  - Measurements are stable at room temperature and inert environment (glovebox).



- A careful design of hopping sites within a DNA duplex containing all type of base pairs, allowed to favour a mechanism of charge hopping in a low voltage range (-1 V to +1 V).
- Previous literature reports of local measurements on DNA, placed in flat geometries as presented here, have a common feature: when a voltage range between -1 V to +1 V is applied, a very small (pA) or no change in the current is detected and a characteristic large-bandgap semiconductor is observed.
- On the other hand, our results exhibit a characteristic Ohmic feature in the range of nA for a single molecule. The differences on this experimental approach as compared to previous literature can be enumerated as follows:
  - Structure of DNA: for every measurement the molecule dimensions were verified to correspond to a typical horizontal *B-DNA* helix.
  - The symmetry on the I-V curves is related to the coupling between the fullerene-DNA molecule and the gold surface
  - No charge injection barrier was observed in the majority of our experiments, which was supported by the theory
  - Changes on the conductance depend weakly on the distance, indicating that a multistep charge hopping mechanism takes place in these fullerene-DNA molecules. In contrast, the possibility of sequential tunneling was discarded due to the lack of congruence with our data.
- We show here that multistep charge hopping without a charge injection barrier is responsible for charge transfer along this type of fullerene-DNA molecules.
- In general terms, single fullerene-DNA molecules could be used as nanowires to connect molecular electronic devices at room temperature and at low voltages. This approach offers the following advantages:

- A large amount of these fullerene-DNA molecules can be synthesized per procedure.
- These molecules can be readily used on gold nanostructures and no additional processing is required after assembly.
- In this context, fullerene-DNA molecules offer a cost-effective solution to produce stable electronic devices, where a complex arrangement of integrated circuits can be easily produced (molecular level), and more computing processes can be achieved with a low voltage supply.

#### 7.4 References

- [1] E. Shafir, H. Cohen, A. Calzolari, C. Cavazzoni, D. A. Ryndyk, G. Cuniberti, A. Kotlyar, R. Di Felice, and D. Porath, "Electronic structure of single DNA molecules resolved by transverse scanning tunneling spectroscopy.," *Nat. Mater.*, vol. 7, pp. 68–74, 2008.
- [2] A. Y. Kasumov, D. V. Klinov, P.-E. Roche, S. Guéron, and H. Bouchiat, "Thickness and low-temperature conductivity of DNA molecules," *Appl. Phys. Lett.*, vol. 84, no. 6, pp. 1007–1009, 2004.
- [3] B. Song, M. Elstner, and G. Cuniberti, "Anomalous conductance response of DNA wires under stretching.," *Nano Lett.*, vol. 8, no. 10, pp. 3217–20, 2008.
- [4] F. C. Grozema, L. D. A. Siebbeles, Y. A. Berlin, and M. A. Ratner, "Hole mobility in DNA: effects of static and dynamic structural fluctuations.," *Chemphyschem*, vol. 3, no. 6, pp. 536–9, 2002.
- [5] R. Landauer, "Spatial variation of currents and fields due to localized scatterers in metallic conduction," *IBM J.*, pp. 223–231, 1957.
- [6] S. Datta, *Electronic transport in mesoscopic systems. Cambridge Studies in Semiconductor Physics and Microelectronic Engineering*. Cambridge University Press, 1995.
- [7] D. Mishra and S. Pal, "Ionization potential and structure relaxation of adenine, thymine, guanine and cytosine bases and their base pairs: A quantification of reactive sites," *J. Mol. Struct. Theochem*, vol. 902, pp. 96–102, 2009.
- [8] F. C. Grozema, S. Tonzani, Y. A. Berlin, G. C. Schatz, L. D. A. Siebbeles, and M. A. Ratner, "Effect of structural dynamics on charge transfer in

- DNA hairpins," *J. Am. Chem. Soc.*, vol. 130, no. 15, pp. 5157–5166, 2008.
- [9] D. L. Lichtenberger, K. W. Nebesny, C. D. Ray, D. R. Huffman, and L. D. Lamb, "Valence and core photoelectron spectroscopy of C<sub>60</sub>, buckminster fullerene," *Chem. Phys. Lett.*, vol. 176, no. 2, pp. 203–208, 1991.
- [10] D. Segal, A. Nitzan, W. B. Davis, M. R. Wasielewski, and M. A. Ratner, "Electron transfer rates in bridged molecular systems 2. A steady-state analysis of coherent tunneling and thermal transitions," *J. Phys. Chem. B*, vol. 104, no. 16, pp. 3817–3829, 2000.
- [11] C. Wan, T. Fiebig, O. Schiemann, J. K. Barton, and A. H. Zewail, "Femtosecond direct observation of charge transfer between bases in DNA.," *Proc. Natl. Acad. Sci. U. S. A.*, vol. 97, pp. 14052–14055, 2000.
- [12] M. G. Ramchandani, "Energy band structure of gold," *J. Phys. C Solid State Phys.*, vol. 3, pp. S1–S9, 1970.
- [13] H.-C. Weissker, H. B. Escobar, V. D. Thanthirige, K. Kwak, D. Lee, G. Ramakrishna, R. L. Whetten, and X. López-Lozano, "Information on quantum states pervades the visible spectrum of the ubiquitous Au<sub>144</sub>(SR)<sub>60</sub> gold nanocluster.," *Nat. Commun.*, vol. 5, p. 3785, 2014.



## Chapter 8

# Prospective research: DNA-fullerene complexes as photoactivable anticancer drugs

### 8.1 Introduction

The general electron donor-acceptor characteristics of fullerene molecules are described in **Chapter 5**. Taking into account fullerenes can be easily excited from their ground state by UV or visible light irradiation, it makes them interesting candidates for biomedical applications, with particular interest in photodynamic therapies. Photodynamic therapy (PDT) is a non-surgical and minimum invasive treatment related to photo-chemotherapy. It requires the presence of a photosensitizer, activating light of the proper wavelength and molecular oxygen (*e.g.* present in aqueous solutions) in order to produce a localized therapeutic effect (**Fig. 8.1**) [1]. In this chapter, we will focus on the cytotoxic therapeutic effect of inducing tumoral cell apoptosis or necrosis. Moreover, in order to consider a compound as a photosensitizer for PDT, it should fulfil the following criteria [2]:

- Chemical stability,
- Water-solubility,
- High quantum yield of  $^1\text{O}_2$  generation (rendering Reactive Oxygen Species, ROS),
- No cytotoxicity in the dark,
- Tumour selectivity,
- Rapid accumulation in targeted tumour tissues,
- Rapid clearance from patients and,
- A high molar absorption coefficient ( $\epsilon$ ) in the long wavelength (600-800 nm) that can penetrate deeper tissues.

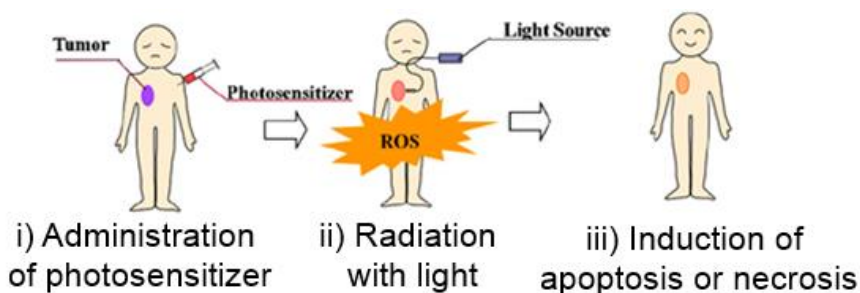


**Figure 8.1.** Cartoon of a Photodynamic therapy (PDT) treatment [2].

Pristine fullerenes fulfil most of these requirements with exception of the water solubility and their molar absorptivity range ( $\sim 532$  nm). On the other hand, fullerene derivatives (e.g. PEGylated-fullerenes and fullerene-DNA complexes) can increase their solubility in aqueous media and shift their absorption spectra closer to the red region ( $\sim 600$  nm). Furthermore, the photoinduced biological activity of fullerenes occurs by two main ways: (i) energy transfer to molecular oxygen and/or (ii) direct electron transfer to the fullerene and subsequent reaction with oxygen [3]. For both ways the formation of cytotoxic species will follow, such as single oxygen atoms and superoxide radical anions, thus inducing physiologically oxidative damage as illustrated in **Fig. 8.2**. Note that this is interesting for targeted cancer treatments, where malign tumours possess increased sensitivity to oxidative stress linked with the changes in generation of reactive oxygen species (ROS) [4].

However, in order to study the biological properties of DNA-fullerene complexes for prospective therapies, it is necessary to have a general overview of their behaviour under physiological conditions: (i) conformational changes depending on pH, (ii) mechanisms related to their cell uptake and the (iii) toxicity that they could present for normal cells or tissues, which is described below in more detail.

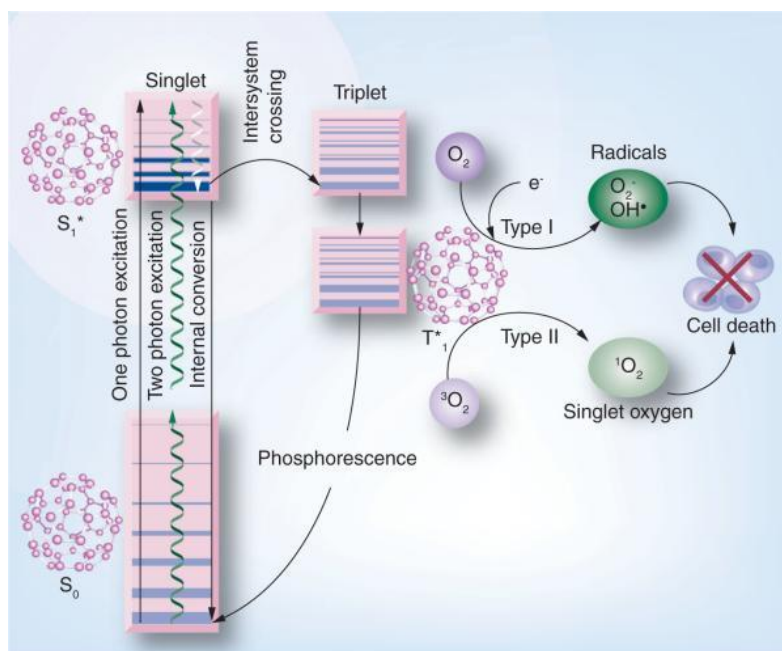


**Figure 8.2.** Jablonski diagram for fullerene and fullerene derivatives upon light irradiation in aqueous solutions [5].

### 8.1.1 Conformation as a function of pH

In the quest to produce DNA nanomachines, the group of Kim *et al.* [6, 7] synthesized fullerene-DNA complexes and studied their molecular motor functions (conformational changes) upon pH changes. For ssDNA-fullerene compounds (C60 attached to both end-sides of DNA), they observed that at mildly acidic conditions (pH = 5) the molecule adopts a compact, folded *i*-motif conformation, while at more basic values (pH = 8) the DNA opens and forms a random coil. Moreover, an *i*-motif conformation involves a non-canonical base pair, formed between one neutral cytosine and one protonated cytosine (C-C<sup>+</sup> bp) by means of three hydrogen bonds, rendering a quadruplex structure (**Fig. 8.3**).

On the other hand, when ssDNA-fullerene molecules are hybridized with their complementary strand, the conformational switch from *i*-motif to duplex *B*-motif occurs at higher pH values (pH = 6.14) than their corresponding non-functionalized DNA structures (pH = 5.01) [7].

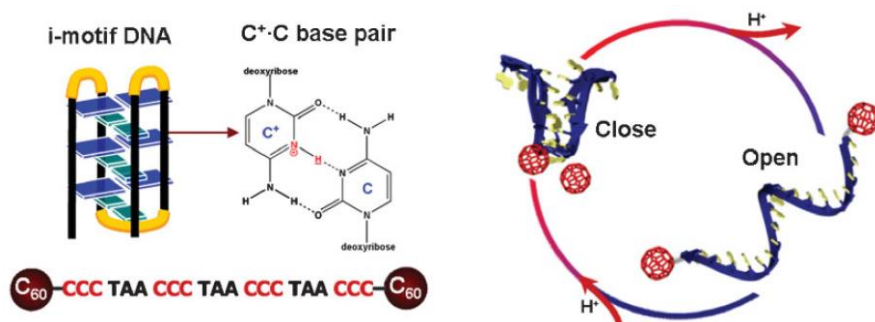


**Figure 8.3.** (a) Representation of an *i*-motif DNA and oligonucleotide sequence with functionalized fullerenes at both end-sites of DNA. The C<sup>+</sup>:C hemiprotonated base pairs are the “building blocks” for quadruplex formation. The contraction is induced by the folding of the oligonucleotides that contain six C<sup>+</sup>:C hemiprotonated bps. (b) Representative models of a fullerene-DNA nanomachine and the working switching cycle mediated only by protons via changing the ambient pH value [6].

### 8.1.2 Cellular uptake

The next question that can be asked is: how exactly the fullerene-DNA complexes will produce selective cellular apoptosis? In this context, multiple studies [2, 8–10] indicate that an endocytosis mechanism is responsible. Moreover, for internalized fullerene-DNA complexes, the fullerene moiety shows a protective function against DNA degradation by enzymes (*e.g.* exonucleases I, [11]).

Other points to consider are the size of the complex (< 150 nm to be efficiently internalized), density of charges around the molecule and the molecular weight of the compound [12]. In this context, the major uptake mechanism in non-immune eukaryotic cells is: (i) clathrin-mediated endocytosis, (ii) lipid raft/caveolae-mediated endocytosis and (iii) macropinocytosis. From experiments by Raof *et al.* on liver cancer cells [9] the most relevant mechanism for cellular uptake of fullerene-derivatives is macropinocytosis, where the internalized complex tends to accumulate at the cell nucleus.



Finally, to have an impression of the type of conformation that DNA-fullerenes could adopt at the different cellular compartments, the standard organelles pH values are presented in **Table 8.1** [13].

**Table 8.1.** List of cellular compartments and their corresponding pH values [13].

<b>Organelle</b>	<b>pH</b>
Mitochondria	8.0
Peroxisome	7.0
Secretary granule	5.5
Early endosome	6.3
Late endosome	5.5
Lysosome	4.7
Cytosol	7.2
Nucleus	7.2

### 8.1.3 Toxicity of fullerene nanoparticles

Fullerene compounds are not capable of producing ROS when they are kept in a dark environment because it requires light to produce their excited species [3]. Preliminary toxicological studies indicate that fullerene derivatives are not toxic *in vivo* but more experiments are required to allow their medical applications [14]–[17].

In any case, the general precautions to handle these type of molecules involve: protective glasses, gloves, lab coat and face mask to avoid inhalation or skin

contact with this nanoparticles. Additionally, some of the most common assays to test cell viability (number of viable cells after treatment with cytotoxic substances) are MTT and Alamar Blue.

#### 8.1.3.1. MTT (3-(4, 5-dimethylthiazol-2-yl)-2-5-diphenyltetrazolium bromide) reduction assay

This is a cell viability assay based on the reduction of the tetrazolium group. The MTT dye must be added to cells in culture and should be incubated between 1 to 4 hours. Next, a plate reader spectrophotometer needs to be used in order to determine the number of viable cells by means of changes in the optical absorbance of formazan at 570 nm. In this way, formazan can be quantified, providing indirect information about the number of viable cells.

Due to the metabolic activity of viable cells (particularly at the mitochondria), they are able to reduce the yellow MTT dye into a purple coloured product (formazan). On the other hand, dead cells cannot reduce MTT, thus no colour change will be observed. Because of the difference between dead and living cells, the production of formazan is a convenient marker to measure viable cells [18].

#### 8.1.3.2. Alamar Blue (7-Hydroxy-3H-phenoxazin-3-one 10-oxide)

Resazurin or Alamar Blue, is a blue dye that turns to pink or red colour (resorufin) upon reduction. This protocol is based on a fluorometric/colourimetric redox indicator of metabolic activity. It fluoresces and changes of colour in response to chemical reduction of the growth medium, consequence of the cell growth. In addition, because the compound indicator is water soluble, there is no need of additional washing/fixing steps.

Alamar Blue behaves as an intermediate between the final reduction of O<sub>2</sub> and cytochrome oxidase without disturbing the respiratory chain. Alamar Blue is reduced by the removal of oxygen and its replacement by hydrogen. Moreover,

data can be collected using either fluorescence (excitation at 530-560 nm and emission at 590 nm) or absorbance (between 570 and 600 nm).

## 8.2 Experimental design

Our objective here was to study the potential use of fullerene-DNA complexes as photosensitizers against cancer cells. For this purpose, we used the pulmonary cancer cell line A549 (adenocarcinomic human alveolar basal epithelial cells, Sigma Aldrich Co.) kindly provided by Sarah Deville. The experiments were done at the facilities of Prof. Dr. Veerle Somers and the setups from Prof. Dr. Marcel Ameloot, at the Biomedical Institute of the Hasselt University.

The A549 cells were cultured with DMEM (Dulbecco's Modified Eagle's Medium – high glucose) supplemented with 2 mM glutamine, 10% foetal bovine serum, 1% antibiotic/antimicotic (penicillin/streptomycin) in a humidified incubator with 5% CO<sub>2</sub> at 37°C.

### 8.2.1 PDT treatment and cell viability assays

A549 cells were cultured in 96-well plates at a density of  $10 \times 10^3$  cells per well for 24 h. Due to the novelty of our fullerene-DNA complex ("drug"), its optimal excitation wavelength and time of activation needed to be determined. For experiments related to light activation, the fullerene-DNA molecules were first diluted in the above mentioned cell medium to a final concentration of 47 nM. Depending on the number of wells required for the experiment, 100 µl of the solution/well were placed separately in black 96-well plates and with the use of the corresponding excitation filter, the sample is excited at a given wavelength by means of a high-energy xenon flash lamp.

After the light activation procedure, we co-incubated the cells with the "drug" for 24 h at 37°C in the dark with 5% CO<sub>2</sub>. After removing the culture medium, the cells were rinsed with fresh medium. Cytotoxicity was evaluated using either a MTT or Alamar Blue assay, and analysed by a plate reader spectrophotometer (FLUOstar Optima, BMG, Labtech GMBH; Offenburg, Germany).

### 8.2.1.1 MTT assay

Typically, the time range to perform this protocol is 4 days:

- Day 1: Cell seeding.
- Day 2: Activation of the drug sample (47 nM) and incubation for 24 h: Two incubation conditions were tested for the cell viability assay: (i) dark and (ii) light condition (3 excitation wavelengths exposed for 5 minutes).
  - For the dark condition there were two controls and one experiment: 1) Blank (which contained just medium), 2) Positive control (exposed to SDS) and 3) Drug (no light activation).
  - Also for the light measurement five conditions we prepared: 1) Blank, 2) Positive Control, 3) Drug excited at 355 nm, 4) Drug excited at 485 nm and 5) Drug excited at 570 nm.

In the positive control we expect that SDS will produce cellular death in most of the cells, thus the cell viability will be the lowest in this part.

- Day 3: MTT test

The cell medium was removed and the wells were washed with fresh medium for three times and then three times with colourless medium to remove any traces of phenol red (original medium). Next, 10  $\mu$ l of MTT solution were added to each well and incubated for 4 hours at 37°C. After this time, we added 100  $\mu$ l SDS-HCl to dissolve the formazan crystals. Then, we incubated the plate for 18 hours in a humidified chamber at 37°C with 5% CO<sub>2</sub>.

- Day 4: Measurement with the plate reader

Before quantification, the cell suspension was homogenised in the wells and transferred to a black 96-well plate. Here we observed that the medium of living cells had a dark, brown colour, while the medium dead cells were still

yellow (no reduction). At this point, absorbance was recorded at 570 nm (Fig. 8.4).

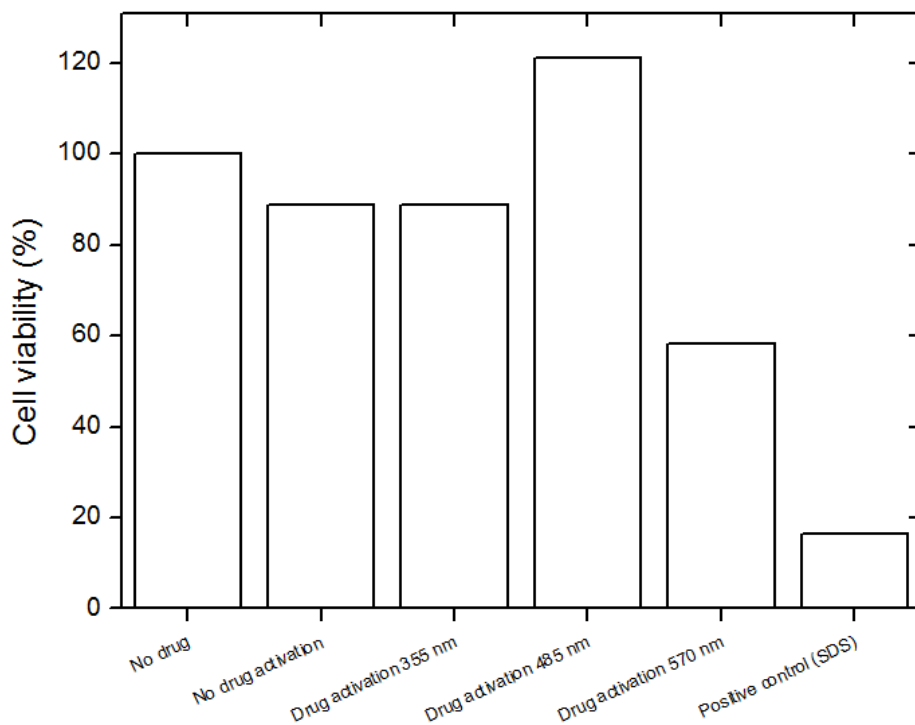


**Figure 8.4. MTT assay of cell viability at different light or dark conditions.** From left to right: A549 cells (i) No drug: blank, (ii) No drug activation: dark condition, (iii) Drug activation at 355 nm, (iv) Drug activation at 488 nm, (v) Drug activation at 570 nm and, (vi) Positive control: SDS. Note that this experiment was done only as an indicator whether the cells would respond or not to the drug activation, thus no triplicate experiment was done for statistical analysis. As a consequence, the column corresponding to the excitation wavelength of 485 nm appears at higher value than the blank.

The disadvantage of using MTT is that it is highly sensitive on the cell division stage, thus if the cells in a well are about to perform a cell division and the cells in the control are delayed, it will be easily reflected on the viability assays. As a consequence, to obtain more reliable results we performed the next experiments by triplicate and with the Alamar Blue protocol.

### 8.2.1.2 Alamar Blue assay

This protocol also requires 4 days and it was done exactly in the same way as MTT until Day 3.

- Day 1: Cell seeding.
- Day 2: Activation of the drug sample (47 nM) and incubation for 24 h.
- Day 3: Alamar Blue test.

The cell medium was removed and the wells were washed with fresh medium for three times and then three times with colourless medium to remove any traces of phenol red (original medium). Next, 100  $\mu$ l colourless media were applied to the cells and then 10  $\mu$ l of the Alamar Blue dye. After mixing, the cells were incubated for 24 hours in a humidified chamber at 37°C with 5% CO<sub>2</sub>.

- Day 4: Measurement with the plate reader

The cell solution was mixed and transferred to a black 96-well plate. Here, we observed that the medium of living cells had a shift from blue to pink colour, while dead cells were still blue. At this point, absorbance was recorded at 570 nm (**Fig. 8.5**).

From these results, the light excitation for 5 min at 570 nm wavelength displayed the best results for both cell viability assays, decreasing the population of cancer cells by  $\sim$  40% and  $\sim$  20% for MTT or Alamar Blue respectively.

The final round of experiments was performed in order to determine the optimal activation time, using the 570 nm excitation wavelength. Here the same protocol with the Alamar Blue assay was performed for different times: 5, 10, 15 and 30 minutes of light activation (**Fig. 8.6**).

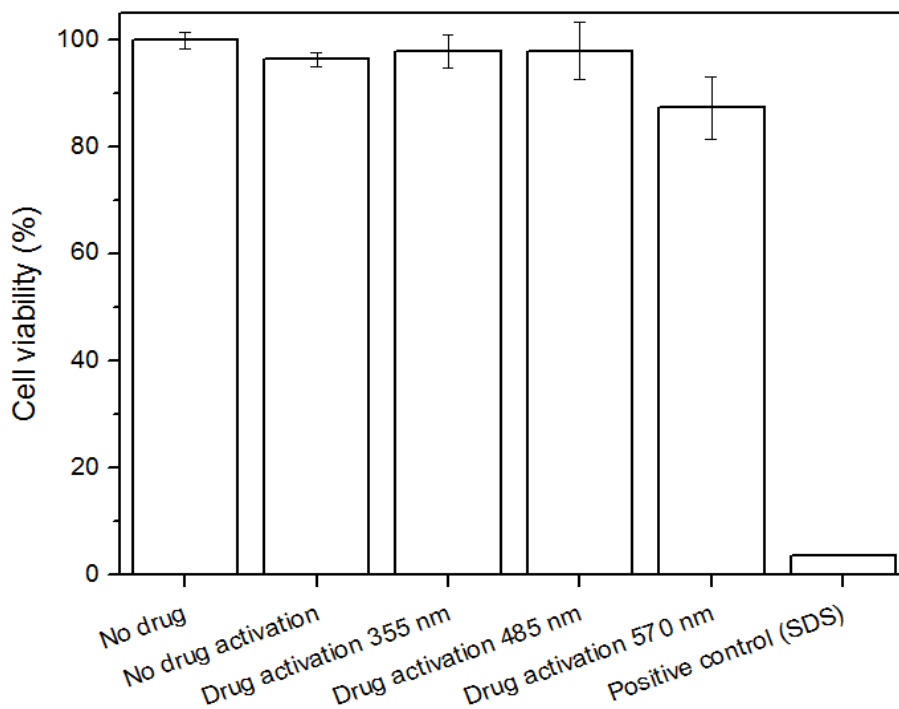


**Figure 8.5. Alamar Blue assay of cell viability at different light or dark conditions.**

From left to right: A549 cells (i) No drug: blank, (ii) No drug activation: dark condition, (iii) Drug activation at 355 nm, (iv) Drug activation at 488 nm, (v) Drug activation at 570 nm and, (vi) Positive control: SDS. Here activation was done for 5 minutes and a 10% of cellular dead can be clearly observed for the drug activation at 570 nm.

Until this moment, different fullerene adducts [5, 14, 15, 17, 19–21] have been studied as prospective photosensitizers for photodynamic therapies. Some examples are: i) *in vitro* antitumor activity of glycoconjugated fullerenes at “drug” concentrations between 1–10  $\mu\text{M}$  and excitation wavelength between 340–400 nm [8], ii) or glycoconjugated fullerenes for *in vivo* tests with a dosis of 424  $\mu\text{g}/\text{kg}$  at laser excitation of 400–505 nm [22] and iii) apoptosis of HeLa cells related to encapsulated C60 or C70 cyclodextrin complex, at 20  $\mu\text{M}$  concentration and excitation at 543 nm [23].

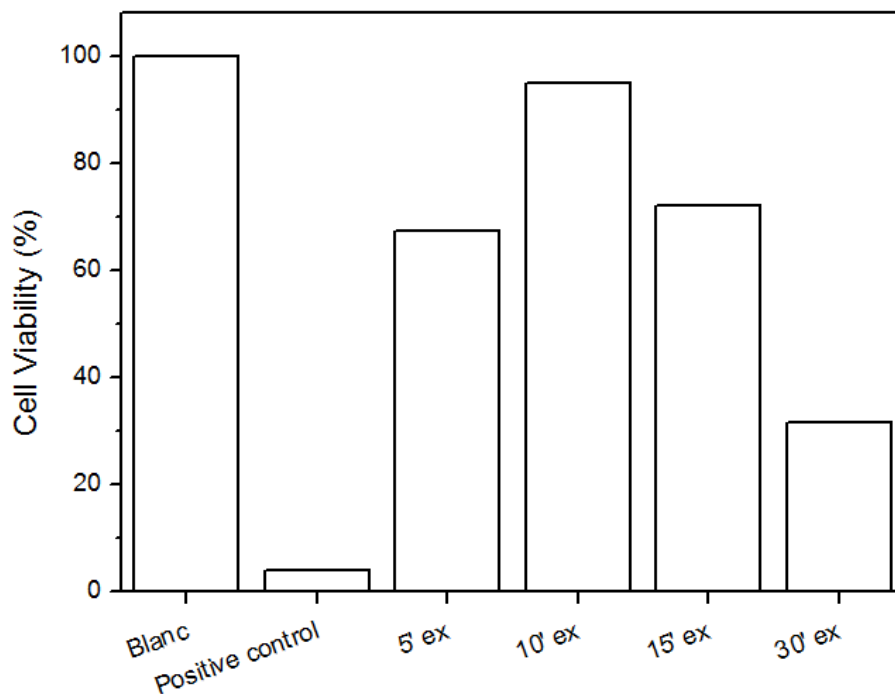


**Fig. 8.6.** . Alamar Blue assay of cell viability at different time activation at 570 nm. This experiment was also performed once as indicator, thus no statistical value was obtained but a clear decrease on the cell viability can be observed for 30 minutes light activation.

On the other hand, fullerene-DNA complexes have been studied for inducing DNA cleavage [11, 24] or for study DNA interactions [6, 25–27] but there is no record of fullerene-DNA complexes for prospective drugs applicable at photodynamic therapies, therefore it is difficult to compare our preliminar results with literature reports.

### 8.3 Conclusions

- These results indicate that fullerene-DNA complexes are promising candidates for further studies as photosensitizers at photodynamic therapies.



- Although these results are preliminary, they suggest that these molecules act as photoactivatable drugs at concentrations as low as 47 nM as compared with other fullerene based drugs (between 1-20  $\mu$ M).
- More experiments should target to identify their biologically active critical concentration, toxicity for normal neighbouring cells, and a time lapse study about how long these molecules produce cellular apoptosis after activation.
- Finally, a study of the ROS production via a ROS selective dye could provide information on the cellular localization of these fullerene-DNA complexes.
- We point out that these future experiments are challenging because they would involve labelling the complexes with fluorescent dyes, which can possibly interfere with the conformation of the drug, its activity and the uptake by the cells.

#### 8.4 References

- [1] R.-M. Ion, "Photodynamic Therapy (PDT): A Photochemical Concept with Medical Applications," *Rev. Roum. Chim.*, vol. 52, no. 12, pp. 1093–1102, 2007.
- [2] S. Yano, S. Hirohara, M. Obata, Y. Hagiya, S. I. Ogura, A. Ikeda, H. Kataoka, M. Tanaka, and T. Joh, "Current states and future views in photodynamic therapy," *J. Photochem. Photobiol. C Photochem. Rev.*, vol. 12, pp. 46–67, 2011.
- [3] D. M. Guldi and M. Prato, "Excited state properties of C60 fullerene derivatives," *Acc. Chem. Res.*, vol. 33, pp. 695–703, 2000.
- [4] A. P. Burlaka, Y. P. Sidorik, S. V. Prylutska, O. P. Matyshevska, O. A. Golub, Y. I. Prylutsky, and P. Scharff, "Catalytic system of the reactive oxygen species on the C60 fullerene basis.," *Exp. Oncol.*, vol. 26, no. 4, pp. 326–327, 2004.
- [5] S. K. Sharma, L. Y. Chiang, and M. R. Hamblin, "Photodynamic therapy with fullerenes in vivo: reality or a dream?," *Nanomedicine*, vol. 6, no. 10, pp. 1813–25, 2011.

- [6] S. R. Shin, K. S. Jin, C. K. Lee, S. I. Kim, G. M. Spinks, I. So, J. H. Jeon, T. M. Kang, J. Y. Mun, S. S. Han, M. Ree, and S. J. Kim, "Fullerene attachment enhances performance of a DNA nanomachine," *Adv. Mater.*, vol. 21, pp. 1907–1910, 2009.
- [7] K. S. Jin, S. R. Shin, B. Ahn, S. Jin, Y. Rho, H. Kim, S. J. Kim, and M. Ree, "Effect of C60 fullerene on the duplex formation of *i*-Motif DNA with complementary DNA in solution," *J. Phys. Chem. B*, vol. 114, no. 14, pp. 4783–4788, 2010.
- [8] E. Otake, S. Sakuma, K. Torii, A. Maeda, H. Ohi, S. Yano, and A. Morita, "Effect and mechanism of a new photodynamic therapy with glycoconjugated fullerene," *Photochem. Photobiol.*, vol. 86, pp. 1356–1363, 2010.
- [9] M. Raof, Y. Mackeyev, M. A. Cheney, L. J. Wilson, and S. A. Curley, "Internalization of C60 fullerenes into cancer cells with accumulation in the nucleus via the nuclear pore complex," *Biomaterials*, vol. 33, no. 10, pp. 2952–2960, 2012.
- [10] E. M. Eropkina, E. V. Ilyinskaya, E. V. Litasova, M. Y. Eropkin, L. B. Piotrovsky, M. A. Dumpis, and O. I. Kiselev, "Effect of different water-soluble forms of fullerene C60 on the metabolic activity and ultrastructure of cells in culture," *Biophysics*, vol. 57, no. 3, pp. 343–349, 2012.
- [11] X. Yang, X. Meng, B. Li, Z. Chen, D. Zhao, X. Tan, and Q. Yu, "Inhibition of in vitro amplification of targeted DNA fragment and activity of exonuclease I by a fullerene-oligonucleotide conjugate," *Biologicals*, vol. 36, pp. 223–226, 2008.
- [12] B. Sitharaman, T. Y. Zakharian, A. Saraf, P. Misra, J. Ashcroft, S. Pan, Q. P. Pham, A. G. Mikos, L. J. Wilson, and D. A. Engler, "Water-soluble fullerene (C60) derivatives as nonviral gene-delivery vectors," *Mol. Pharm.*, vol. 5, no. 4, pp. 567–578, 2008.
- [13] J. R. Casey, S. Grinstein, and J. Orlowski, "Sensors and regulators of intracellular pH," *Nat. Rev. Mol. Cell Biol.*, vol. 11, pp. 50–61, 2010.
- [14] P. Mroz, G. P. Tegos, H. Gali, T. Wharton, T. Sarna, and M. R. Hamblin, "Photodynamic therapy with fullerenes," *Photochem. Photobiol. Sci.*, vol. 6, no. 11, pp. 1139–1149, 2007.
- [15] R. Bakry, R. M. Vallant, M. Najam-ul-Haq, M. Rainer, Z. Szabo, C. W. Huck, and G. K. Bonn, "Medicinal applications of fullerenes.," *Int. J. Nanomedicine*, vol. 2, no. 4, pp. 639–49, 2007.
- [16] C. M. Sayes, A. A. Marchione, K. L. Reed, and D. B. Warheit, "Comparative pulmonary toxicity assessments of C60 water suspensions

- in rats: Few differences in fullerene toxicity *in vivo* in contrast to *in vitro* profiles," *Nano Lett.*, vol. 7, pp. 2399–2406, 2007.
- [17] T. Da Ros and M. Prato, "Medicinal chemistry with fullerenes and fullerene derivatives," *Chem. Commun.*, pp. 663–669, 1999.
- [18] T. Mosmann, "Rapid colourimetric assay for cellular growth and survival: application to proliferation and cytotoxicity assays," *J. Immunol. Methods*, vol. 65, pp. 55–63, 1983.
- [19] M. A. Orlova, T. P. Trofimova, A. P. Orlov, and O. A. Shatalov, "Perspectives of fullerene derivatives in PDT and radiotherapy of cancers," *Br. J. Med. Med. Res.*, vol. 3, no. 4, pp. 1731–1756, 2013.
- [20] G. A. Burley, P. A. Keller, and S. G. Pyne, "[60]Fullerene amino acids and related derivatives," *Fuller. Sci. Technol.*, vol. 7, no. 6, pp. 973–1001, 1999.
- [21] R. R. Sahoo and A. Patnaik, "Binding of fullerene C60 to gold surface functionalized by self-assembled monolayers of 8-amino-1-octane thiol: a structure elucidation," *J. Colloid Interface Sci.*, vol. 268, no. 1, pp. 43–49, 2003.
- [22] Y. Tabata, Y. Murakami, and Y. Ikada, "Photodynamic effect of polyethylene glycol-modified fullerene on tumor," *Japanese J. Cancer Res.*, vol. 88, pp. 1108–1116, 1997.
- [23] A. Ikeda, M. Matsumoto, M. Akiyama, J. Kikuchi, T. Ogawa, and T. Takeya, "Direct and short-time uptake of [70]fullerene into the cell membrane using an exchange reaction from a [70]fullerene-gamma-cyclodextrin complex and the resulting photodynamic activity," *Chem. Commun.*, vol. 12, pp. 1547–1549, 2009.
- [24] A. S. Boutorine, M. Takasugi, C. Hélène, H. Tokuyama, H. Isobe, and E. Nakamura, "Fullerene–oligonucleotide conjugates: Photoinduced sequence-specific DNA cleavage," *Angew. Chemie Int. Ed. English*, vol. 33, pp. 2462–2465, 1995.
- [25] M. Bergamin, T. Da Ros, G. Spalluto, M. Prato, and A. Boutorine, "Synthesis of a hybrid fullerene–trimethoxyindole–oligonucleotide conjugate," *Chem. Commun.*, no. 1, pp. 17–18, 2001.
- [26] A. M. Cassell, W. A. Scrivens, and J. M. Tour, "Assembly of DNA/fullerene hybrid materials," *Angew. Chemie Int. Ed.*, vol. 37, no. 11, pp. 1528–1531, 1998.

- 
- [27] H. Isobe, S. Sugiyama, and K. Fukui, "Atomic force microscope studies on condensation of plasmid DNA with functionalized fullerenes," *Angew. Chemie Int. Ed.*, vol. 40, no. 18, pp. 3364–3367, 2001.

## Chapter 9

### General conclusions and outlook

The purpose of this thesis was to study the feasibility to construct molecular wires based on fullerene-DNA molecules for integrating complex molecular circuits or devices. Our results show the possibility to synthesize single molecule fullerene-DNA wires and that they display a charge hopping mechanism along the DNA helical structure at low voltage ranges [-1 V to +1 V] that, remarkably, takes place at room temperature. To perform this experiment, some requirements are needed to assure that no air disturbances will interfere with the measurement, such as a measuring setup located in an inert environment (AFM located inside a glovebox with nitrogen atmosphere, controlled humidity, including a Faraday isolator for reliable measurements). In addition, the possible salt concentration effect on the nature of the electronic transport was evaluated. Desalting DNA can lead to structure disturbances, such as base to base stretching and changes on the  $\pi$ -orbital stacking, favouring a sequential tunneling mechanism from the tip to the base pair, and from this to the metallic surface. In turn, we observed that if salts are completely removed from the structure, the conductance signal decreases 10-fold compared to the original single molecules containing  $\sim 1.5$  nM PBS buffer, but preserve the same trend as the one observed with salt-containing molecules thus confirming that charge transport through the fullerene-DNA wire is governed by a multistep hopping mechanism. Moreover, if the salt would be the responsible of the observed shape in I-V curves, then no changes of conductance would be displayed as the tip moves towards the fullerene end, instead, the shape of the I-V curves would be independent of the tip position on the molecule provided the salt content is the same all along the wire. In our case, it appears that charge hops mainly along the DNA wire towards to fullerene ends, which agrees nicely with the hopping mechanism we proposed for DNA.

Furthermore, using AFM we observed that the DNA-fullerene molecules appear as cylindrical shapes, due to a tip broadening effect. This effect is somehow expected considering that a 2 nm wide tip is making contact with a 2-2.5 nm diameter molecule with length of  $\sim 39$  nm. Moreover, supporting STM measurements confirmed that no sequential tunneling mechanism is involved in the results. Interestingly, a comparison between our data and theoretical charge hopping and sequential tunneling models confirms charge hopping only through the DNA  $\pi$ - $\pi$  orbitals and neither a charge injection barrier nor charge scattering.

Some of the main achievements in this project were: 1) DNA retained its native structure, as for every measurement the molecule dimensions were verified to correspond to a *B-DNA* helix; (2) The adsorption of fullerene to gold had a strong effect on the selective localization of the charges within the DNA-fullerene molecules (3) No charge injection barrier is observed in our experiments, therefore no bandgap is observed (4) Changes on the conductance depend weakly on the distance from the fullerenes. These results strongly suggest that a small molecule, such as fullerene can provide a good electron donor-acceptor moiety for single molecules of DNA, where DNA's structural fluctuations (*e.g.* dynamic disorder) appear to be minimized on a dry surface, at room temperature and in inert environment.

In summary, we have demonstrated the feasibility to use stable single fullerene-DNA molecules to connect molecular electronic devices in a cost-effective manner, in a reliable way at room temperature and at low voltages. Additional processing is not required and a large quantity of these molecules can be prepared per procedure. This work can be contemplated as a reference point for further experiments regarding the correlation between sequence nature and transport nature. Will a higher content of Adenines-Thymines favour a sequential tunneling mechanism or would the multistep charge hopping mechanism will remain in the structure along larger distances beyond *e.g.* 200 Å?

Apart from the fundamental viewpoint on electronic transport through DNA wires, we have also briefly explored the potential of these fullerene-DNA

molecules as new anti-cancer drugs based on photodynamic therapies. The switch on-off mechanism of fullerene-DNA molecules was investigated in presence of light in water based solutions. Cell viability experiments performed on cancer cell cultures (cell line A-549, endothelial lung cancer) with fullerene-DNA molecules showed a toxicity effect only after a specific wavelength activation. Preliminarily the best results regarding cell toxicity were found with an illumination wavelength of 570 nm expuse for 30 min. No final conclusions can be made from this experiment, due to factors involved in the reproducibility, but it serves as first indication on its perspective role as a photoactivable drug.





## Chapter 10

### AFM-Imaging for Contributed Publications

In this chapter the contributed work for publications is mainly on the framework of the newly developed "Heat Transfer Method", briefly introduced here. Non-Contact AFM (NC-AFM) was used as a supporting technique to assess changes of topography for either functionalized or non-functionalized substrates [1]. Moreover, patterns created by cells [2] or molecular imprints [3] on polymers can be also analysed through NC-AFM, providing information on the experimental procedure (*e.g.* amount of cell imprints on a surface), as well as lipid vesicles [4] and aptamers [5].

From:

- B. Van Grinsven, N. Vanden Bon, H. Strauven, L. Grieten, M. Murib, K. L. Jiménez-Monroy, S. D. Janssens, K. Haenen, M. J. Schöning, V. Vermeeren, M. Ameloot, L. Michiels, R. Thoelen, W. De Ceuninck, and P. Wagner, "Heat-Transfer Resistance at Solid-Liquid Interfaces: A Tool for the Detection of Single-Nucleotide Polymorphisms in DNA," *ACS Nano*, vol. 6, no. 3, pp. 2712–2721, 2012.
- K. Eersels, B. van Grinsven, A. Ethirajan, S. Timmermans, K. L. Jiménez-Monroy, J. F. J. Bogie, S. Punniyakoti, T. Vandenryt, J. J. A. Hendriks, T. J. Cleij, M. J. A. P. Daemen, V. Somers, W. De Ceuninck, and P. Wagner, "Selective Identification of Macrophages and Cancer Cells Based on Thermal Transport through Surface-Imprinted Polymer Layers," *ACS Appl. Mater. Interfaces*, vol. 5, no. 15, pp. 7258–7267, 2013.
- M. Peeters, S. Kobben, K. L. Jiménez-Monroy, L. Modesto, M. Kraus, T. Vandenryt, A. Gaulke, B. van Grinsven, S. Ingebrandt, T. Junkers, and P. Wagner, "Thermal detection of histamine with a graphene oxide based molecularly imprinted polymer platform prepared by reversible addition–

fragmentation chain transfer polymerization," *Sensors Actuators B Chem.*, vol. 203, pp. 527–535, 2014.

- P. Losada-Pérez, K. L. Jiménez-Monroy, B. van Grinsven, J. Leys, S. D. Janssens, M. Peeters, C. Glorieux, J. Thoen, K. Haenen, W. De Ceuninck, and P. Wagner, "Phase transitions in lipid vesicles detected by a complementary set of methods: Heat-transfer measurements, adiabatic scanning calorimetry, and dissipation-mode quartz crystal microbalance," *Phys. Status Solidi Appl. Mater. Sci.*, vol. 211, no. 6, pp. 1377–1388, 2014.
- B. van Grinsven, K. Eersels, M. Peeters, P. Losada-Pérez, T. Vandenryt, T. J. Cleij, and P. Wagner, "The heat-transfer method (HTM): a versatile low-cost, label-free, fast and user-friendly read-out platform for biosensor applications," *ACS Appl. Mater. Interfaces*, p. 140808135513004, 2014.

## 10.1 Introduction

The Heat-Transfer Method (HTM) consists of a read-out platform that detects changes of thermal transport through functional interfaces. Variations at the solid-liquid interface lead to differences in the thermal resistance ( $R_{th}$ ). It is a fast, label-free and sensitive technique that requires a minimum of instrumentation and can be used "on-the-bench". It was developed in 2012 by van Grinsven *et al.* [1] within the IMO-IMOMEC laboratory of Hasselt University, and can be used for a wide range of applications, including analysis of DNA mutations [1, 6, 7], quantification of DNA sequences of interest [7, 8], specific detection of neurotransmitters [3, 9, 10] or cells [2, 11], and to analyse lipid vesicle layers upon temperature-induced phase transitions [4].

The key feature on a HTM setup is the chip, where the heat flux will pass. This chip serves as an immobilization platform onto which the functional interface is applied. It is mechanically pressed with its backside onto a polished copper block which works as the heat provider. Moreover, the internal temperature of the copper block,  $T_1$ , is measured by a thermocouple and steered via a proportional-

integral-derivative controller (PID controller), connected to a power resistor. Possible heat-transfer losses between copper and silicon are minimized by conductive silver paste. Also, the front side of the functionalised chip is exposed to the medium which contains the target of interest. An O-ring seal defines a contact area of  $28 \text{ mm}^2$  between the sensing surface and the liquid. Except for minor heat losses along the seal, heat will mainly be transferred from the chip to the liquid. The temperature in the liquid,  $T_2$  is measured by a second thermocouple, positioned above the solid-liquid interface. To extract the heat-transfer resistance  $R_{\text{th}}$  ( $^{\circ}\text{C}/\text{W}$ ) quantitatively, the ratio of the temperature difference  $\Delta T = T_1 - T_2$  and the input power  $P$  according to  $R_{\text{th}} = \Delta T/P$  is analysed. The basic components on a HTM sensor set-up are illustrated in **Figure 10.1**.

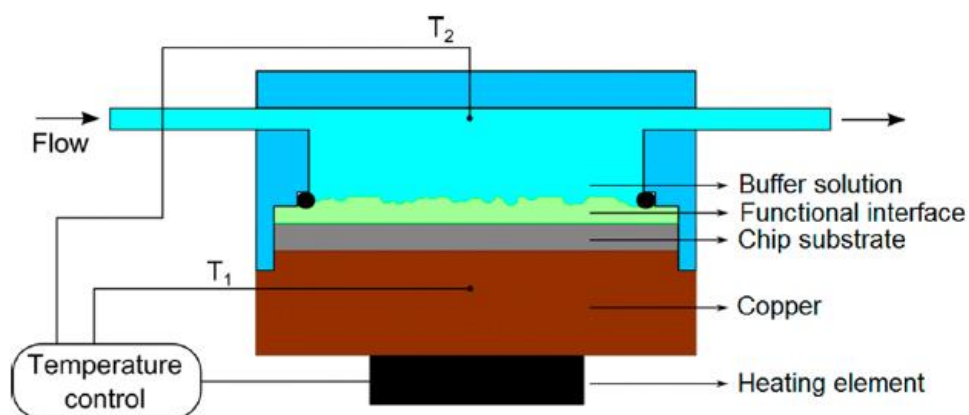


**figure 10.1. Schematic layout of the HTM setup.** The sensor chip is connected to a copper block with the functional interface facing a liquid flow cell. The temperature  $T_1$  of the copper backside contact is measured by a thermocouple and can be actively steered via a controller unit. The temperature  $T_2$  inside the liquid is recorded by using a second thermocouple. The heat transfer related parameters are the temperature difference  $T_1 - T_2$  and the input power  $P$  provided by the heating element, allowing the user to monitor the thermal resistance of the solid-liquid interface in real time [12].

## 10.2 Applications

### 10.2.1 Single Nucleotide Polymorphisms in DNA fragments

Biosensors that can measure in real-time mutations of DNA especially able to detect single nucleotide polymorphisms (SNPs), are of great interest for the pharmaceutical industry. HTM was originally developed in order to solve this particular issue in a cost-effective way.

The interface through which the thermal transport was analysed consisted of a silicon chip coated with a thin layer of boron-doped, nanocrystalline diamond (NCD). This diamond layer served as an immobilization platform suitable for DNA attachment. Here, the diamond surface (**Fig. 10.2a**) was first photochemically functionalized with a fatty acid linker (**Fig. 10.2b**) and then, by means of an EDC coupling reaction, single stranded DNA molecules (probes, **Fig. 10.2c**) were covalently immobilized on the chip [1, 13]. The final step was hybridization with their complementary single stranded DNA sequences (targets) to form brushes of double stranded DNA (dsDNA, **Fig 10.2d**).

The roughness of the surface is given by means of Ra or root mean square average roughness over a  $10 \times 10 \mu\text{m}^2$  area. From these images, nanocrystalline diamond exhibits a rough surface due to the diamond grains. After addition of the fatty acid, the Ra decreased due to a smoothing effect caused by the homogeneous coverage of fatty acid on the surface. Then, with the addition of ssDNA, values of Ra increased as a consequence of the structural curl-up of DNA into irregular structures. Finally, after hybridization with its complementary DNA strand, dsDNA is formed and it appears standing upright on the substrate with a stiffer structural shape.

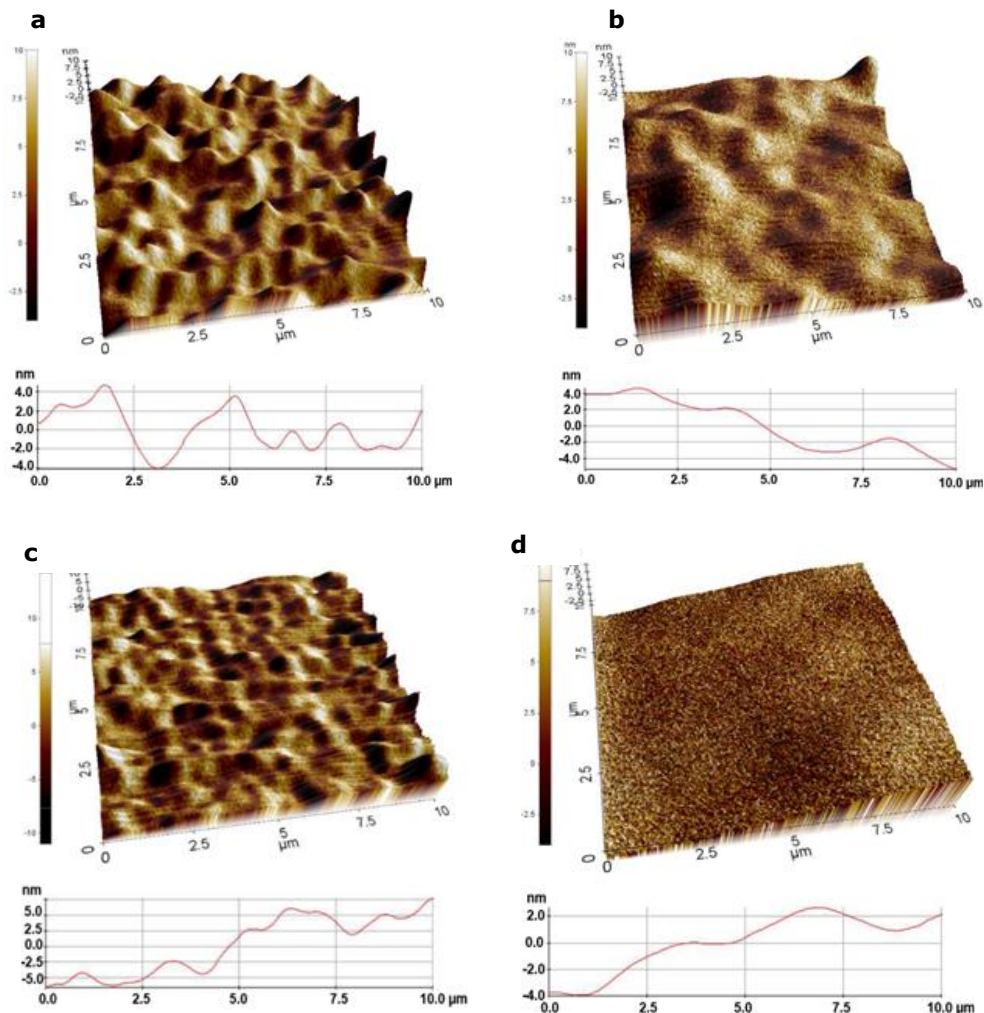


**Figure 10.2. NC-AFM** images of  $10 \times 10 \mu\text{m}^2$  size, representing the different functionalization steps. Measurements were performed at room temperature and dry state, using an AFM tip with a spring constant of 25–27 N/m. **(a)** Hydrogen-terminated NCD surface,  $R_a = 2.7$  nm, **(b)** Fatty-acid cross-linked to the surface,  $R_a = 2.2$  nm, **(c)** Grafting ssDNA layer increases roughness to  $R_a = 3.2$  nm. **(d)** The final hybridization with target DNA generated stiff molecular brushes with  $R_a = 4.4$  nm [1].

Once the chip is incorporated into the device, analysis of hybridization and denaturation processes can be performed with either fully-complementary targets or targets with mismatches. The results indicate that the setup is highly sensitive for mismatches, even for the same type of mismatches located at

different positions (**Fig. 10.3**) and more important, reproducible for several measurements on the same chip and on different chips.

From **Fig. 10.3** can be observed that the  $R_{th}$  increase upon denaturation is due to the higher surface coverage of ss-DNA. Single-stranded DNA curls up in irregular structures, which are wider than the stiff and upright ds-DNA.

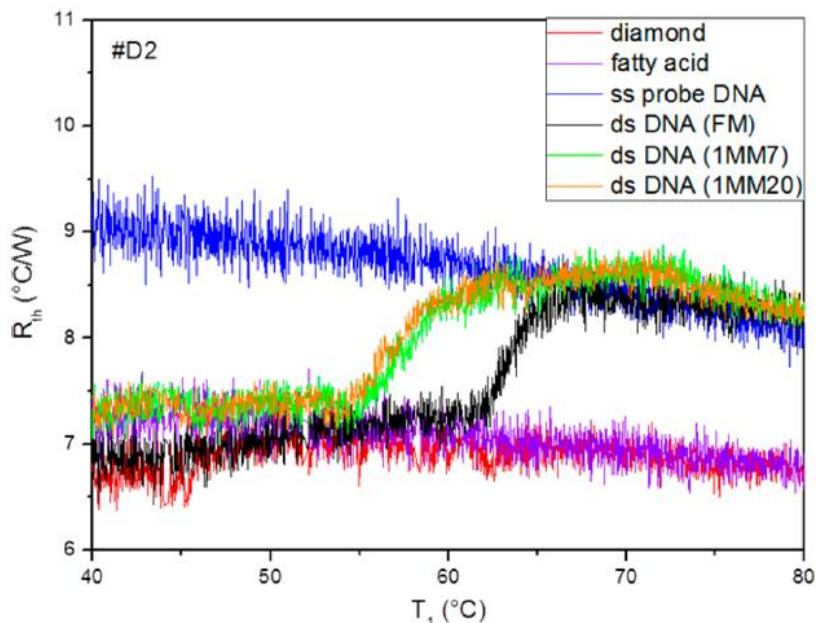


**Figure 10.3.** Heat-transfer resistance  $R_{th}$  as a function of temperature. The unmodified electrode (red line) and the electrode with covalently attached fatty acid linkers (purple line) are stable at  $R_{th}$  of  $\sim 7$  °C/W. In the configuration with attached DNA probes (blue line), the heat-transfer resistance present an evident increase to 9 °C/W, indicating an efficient thermal insulation by the highly flexible single stranded DNA fragments. The  $R_{th}$  of double-stranded DNA (black line for the complementary duplexes) is comparable to the non-modified surface at low temperatures and switches to the single stranded DNA behaviour upon denaturation with a midpoint temperature  $T_{\text{midpoint}} = 63.0 \pm 0.1$  °C. Repeating the experiment with defective DNA duplexes results in a clear shift of  $T_{\text{midpoint}}$  to lower temperatures: for the duplex with CC mismatch at BP7 (green line), a  $T_{\text{midpoint}} = 57.6$  °C  $\pm 0.1$  °C, and for the same mismatch at BP 20 (orange line), this is  $56.8 \pm 0.1$  °C [1].

### 10.2.2 Specific Cell Detection

For this application, surface imprinted polymers (SIPs) become the sensor interface of HTM in order to identify cell types. The functional interfaces were prepared by coating aluminium chips ( $10 \times 10 \mu\text{m}^2$ ) with semi cured polyurethane. Then, cell-covered polydimethylsiloxane (PDMS) stamps were gently pressed into this polymer layer. After curing of the layer, the stamp was removed, resulting in a pattern of micro cavities on the surface of the polymer. The functional and morphological complementarity between these cavities and the template cells makes it possible for cells to rebind to their receptor in a selective and specific manner. **Figure 10.4** illustrates the detection principle. Additionally, thermal resistance of an empty SIP is determined by the thickness of the polyurethane layer, indicating that the  $R_{th}$  of the micro cavities is lower in comparison to the thicker non-imprinted areas of the SIP. These micro cavities will therefore act as preferential heat channels (**Fig. 10.4a**). Rebinding of cells into these cavities will result in an increase in  $R_{th}$  at the solid-liquid interface (**Fig. 10.4b**).

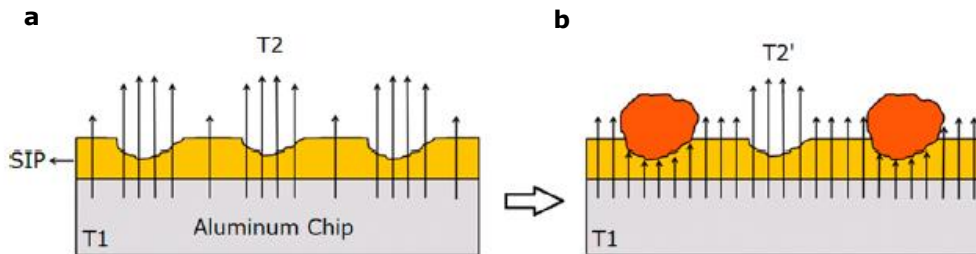


**Figure 10.4. Concept of heat transfer** through SIP layers. The arrows indicate the heat-transfer direction. **(a)** The thermal resistance of an empty SIP is determined by the thickness of the polyurethane layer. Therefore, most of the heat will dissipate through the micro cavities. **(b)** Cells binding block the heat transfer through the imprints, causing the thermal resistance at the solid-liquid interface to increase [2].

Characterization techniques, such as optical microscopy (**Fig. 8.5a**) and NC-AFM (**Fig. 10.5b**) provided additional information on the cell imprints, such as the optimal cell concentration on the PDMS stamp to produce individual micro cavities, avoiding formation of agglomerates that could induce non-specific binding. An example is shown in **Figure 10.5** for MCF-7 imprints, were mostly

individual cavities are produced with a typical depth of approximately 750 nm (line profile).

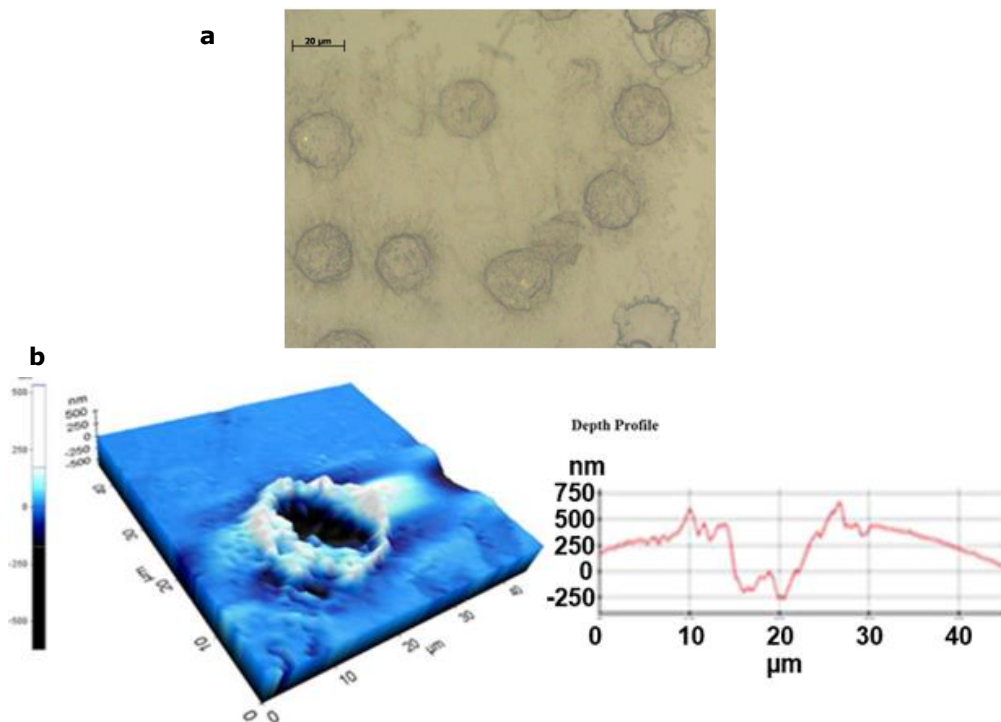


**Figure 10.5. Structural analysis of a SIP**, imprinted for human MCF-7 cells. **(a)** Optical micrograph of a typical SIP imprint for MCF-7. **(b)** NC-AFM 3D image of a single MCF-7 imprint micro cavity, together with a cross sectional depth profile of the imprint [2].

In this context, changes of the  $R_{th}$  were studied for the specific detection of cancer cells in buffer solution. The experimental setup was able to discriminate between breast-cancer cells (MCF-7 cells), immortalized T-lymphocytes associated with leukaemia (Jurkat cells) and a mixed population of healthy blood cells (peripheral blood mononuclear cells, PBMCs). An example of the results is shown in **Fig 10.6**, where a selective binding (increase of  $R_{th}$  signal) was observed for MCF7 cells at the SIP imprinted with MCF7 cells. Analogous patterns were observed with Jurkat imprints exposed to solutions containing Jurkat, MCF-7 and PBMC cells.



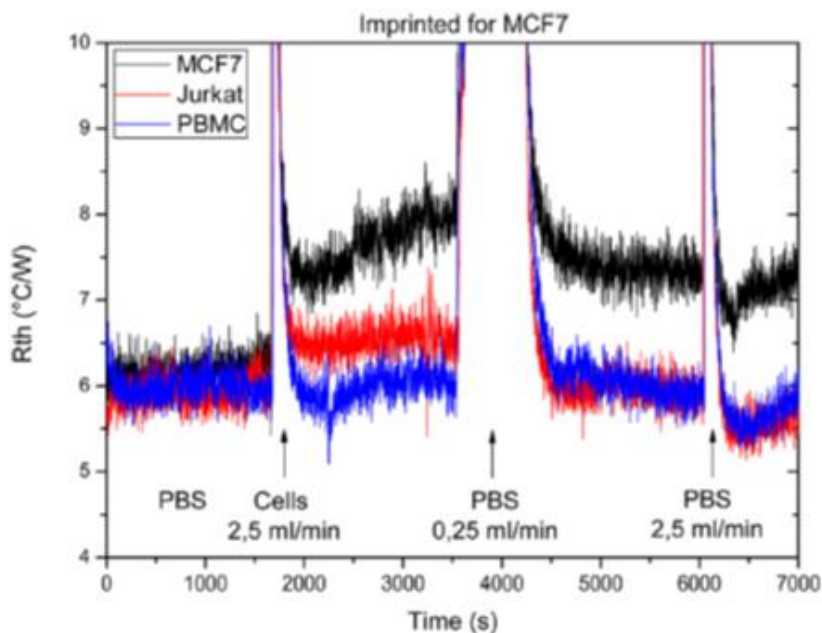


**Figure 10.6.** Heat-transfer resistance as a function of time shown for MCF-7 imprinted SIP towards MCF-7 cells (black line), Jurkat cells (red line) and PBMC (blue line). Mild rinsing with cell-free PBS brings to cross-selective response for non-targeted cells back to the baseline [2].

### 10.2.3 Specific Detection of small molecules (e.g. histamine).

As mentioned before, the sensor interface can be prepared with imprinted polymers. For this specific work, molecularly imprinted polymers (MIPs) were grafted onto graphene oxide (GO) in order to enhance together the binding capacity, and the sensitivity of MIPs. Furthermore, reversible addition-fragmentation chain transfer (RAFT) polymerization was the technique of choice to produce a histamine MIP-GO hybrid. NC-AFM assessed the selective formation of a polymer around GO, with particles covered with a homogeneous  $\sim 2.4$  nm thick layer (**Fig. 10.7a**). In contrast, non-functionalized GO samples showed amorphous layers all over the surface with dispersed GO particles (**Fig. 10.7b**).

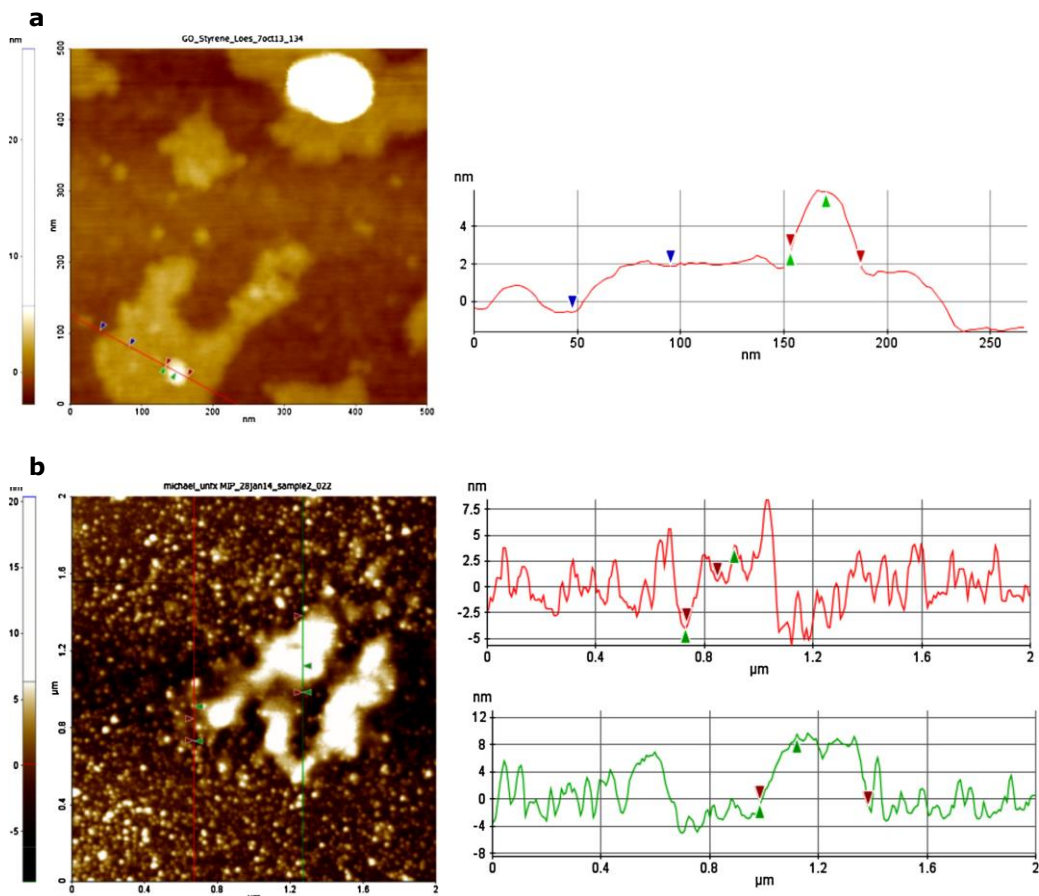


**Figure 10.7. NC-AFM height images (a)** MIP grafted on graphene oxide with scan size of  $0.5 \times 0.5 \mu\text{m}^2$ . MIP grafted on GO. The line profile indicates the formation of a MIP-GO hybrid structure of 34.2 nm length and 3.1 nm height. The polymer layer shows a homogeneous height of 2.4 nm around GO. **(b)** Scan size =  $2 \times 2 \mu\text{m}^2$ . For comparison, a bulk polymer (not grafted on GO), produce large aggregates of GO particles and of the polymer. For this reason, we tested first small scan sizes ( $0.5 \times 0.5 \mu\text{m}^2$ , data not shown) and continued with larger scan sizes in order to characterize the real sensor surface.

Finally, the MIP-GO sensor was installed in the HTM setup, proving the high selectivity of the MIP-GO structure towards histamine (**Fig. 10.8**) and negligible response to the structurally related competitor molecule histidine.

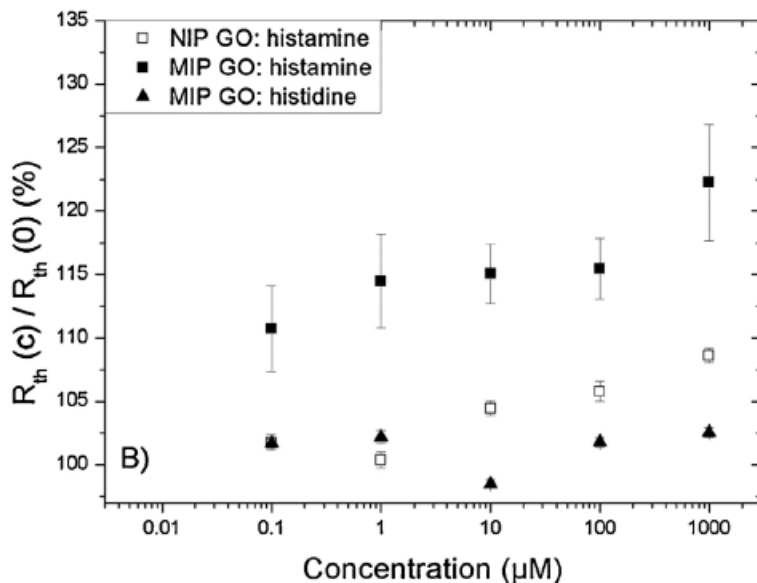


**Figure 10.8. HTM applied for GO-MIPs.** Graph of the corresponding dose response-curves for the MIP and NIP (non imprinted polymer) exposed to histamine. To test the binding selectivity, the effect on the MIP towards histidine was tested. For each concentration, the  $R_{th}$  was divided by the value of the baseline-level, thus normalizing the signal. The error bars are obtained by comparing three separate measurements.

#### 10.2.4 Detection of phase transitions on supported lipid vesicle layers

Another HTM-based application is the detection of phase transitions of model lipid membranes, study that has been mostly carried out in literature for vesicle dispersions in bulk. The aim of this experiments was to investigate whether HTM could detect phase transitions by measuring  $R_{th}$  across a lipid layer, previously deposited onto a hydrogenated NCD film in contact with a liquid environment. Particularly, dipalmitoylphosphatidylcholine (DPPC) was the selected lipid for this study because of its rich phase behaviour combined with an experimentally accessible temperature range. Within an aqueous environment, the main phase transition between the ripple phase to liquid disordered phase is expected at 41 °C [4]. The lipid vesicle deposition onto a surface is illustrated in **Fig. 10.9**.

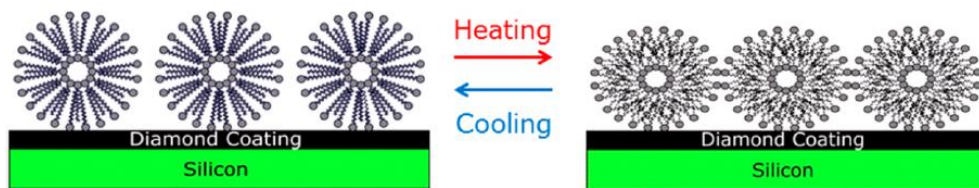


**Figure 10.9.** Schematic representation of a layer of DPPC SUVs applied onto a silicon chip covered with hydrogenated NCD. Phase transitions are induced in the lipid vesicle layer by heating and cooling off the substrate, changing the thermal resistance at the solid-liquid interface [4].

The sensor surface was also characterized by NC-AFM (**Fig. 10.10**), where hydrogenated-NCD presented difficulties to differentiate the small vesicles from the diamond grains (**Fig. 10.10b**). Therefore, more appropriate surfaces (ultra-flat gold substrates) were used to simply determine the typical height of the lipid vesicles. This information is relevant to differentiate between the formation of a lipid bilayer or mainly vesicles as seen in **Fig. 10.10d**.

Finally, the advantage of using the HTM setup is the possibility to perform characterization of solid supported lipid layers without the need for fluorescent labels (label-free), which could interfere with the actual phase transition behaviour of the layer. An example of the phase transition detection is shown in **Figure 10.11**. Here, the phase transition was indeed found at the expected temperature with a clear hysteresis effect between heating- and cooling runs, as expected for a first-order phase transition.

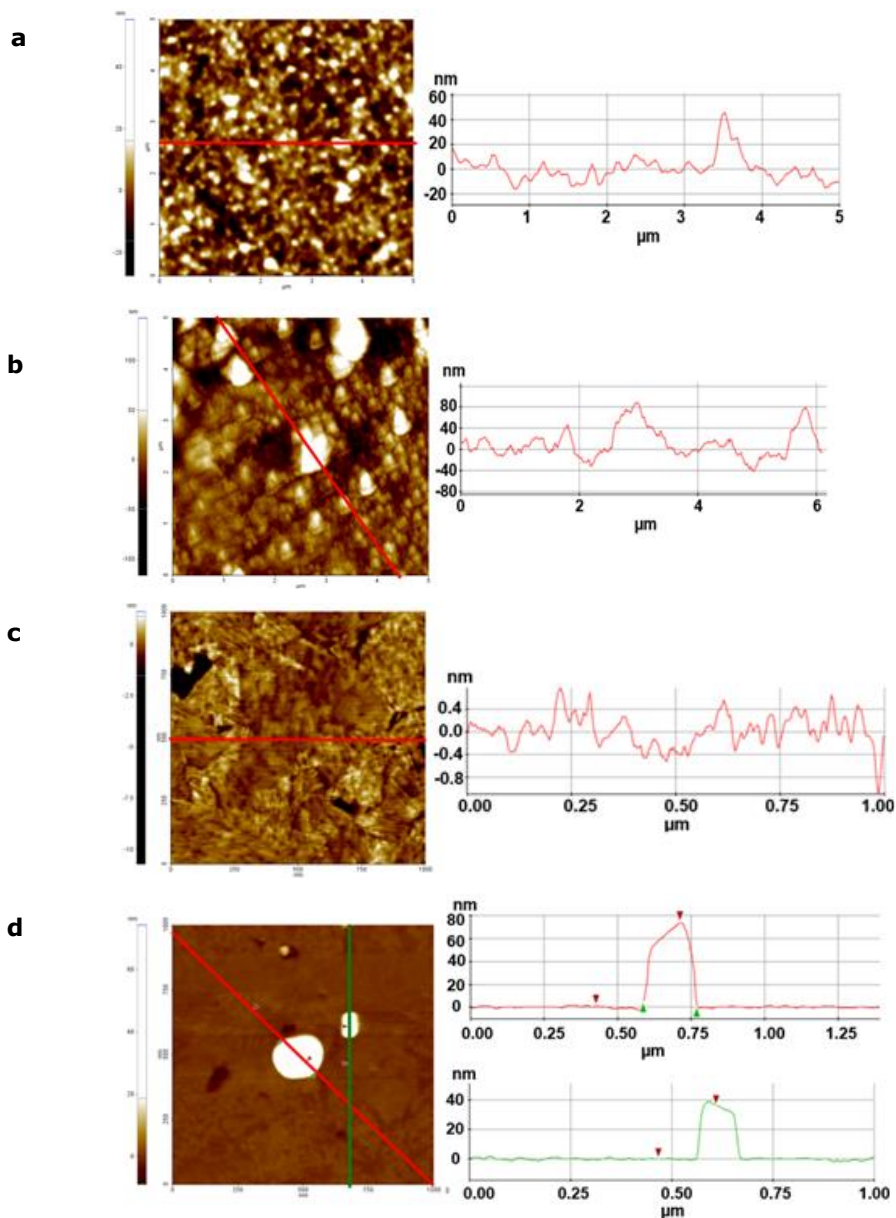


**Figure 10.10.** NC-AFM measurements of a hydrogenated-NCD substrate **(a)** before and **(b)** after lipid vesicle deposition, where vesicles height was between 40-60 nm. Due to the issues to identify lipid vesicles on this rough substrate, more accurate measurements were done on top of ultra-flat gold substrates: **(c)** before and **(d)** after lipid vesicles deposition, where the vesicles height was found to be about 40-75 nm.

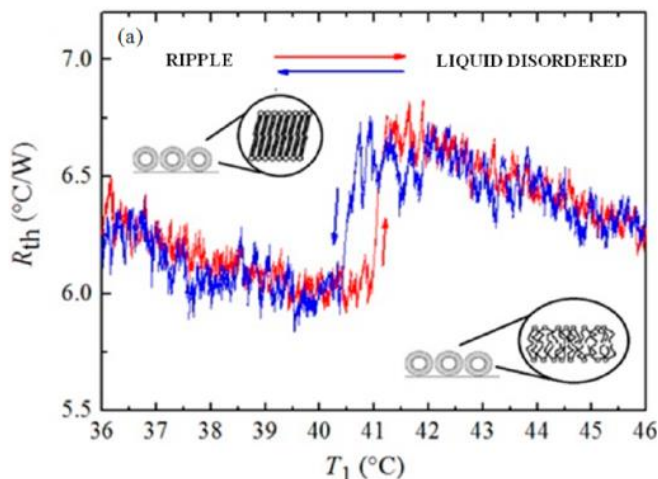


**Figure 10.11.** Temperature profile of the heat transfer resistance  $R_{th}$  during the main phase transition from the ripple-to the liquid-disordered phase of a DPPC supported vesicle layer adsorbed on a NCD. The arrows indicate the sense of the temperature run: heating (red solid line) and cooling (blue solid line) [4].

### 10.3 References

- [1] B. van Grinsven, N. Vanden Bon, H. Strauven, L. Grieten, M. Murib, K. L. Jiménez-Monroy, S. D. Janssens, K. Haenen, M. J. Schöning, V. Vermeeren, M. Ameloot, L. Michiels, R. Thoelen, W. De Ceuninck, and P. Wagner, "Heat-transfer resistance at solid-liquid interfaces: A tool for the detection of single-nucleotide polymorphisms in DNA," *ACS Nano*, vol. 6, no. 3, pp. 2712–2721, 2012.
- [2] K. Eersels, B. van Grinsven, A. Ethirajan, S. Timmermans, K. L. Jiménez-Monroy, J. F. J. Bogie, S. Punniyakoti, T. Vanderyt, J. J. A. Hendriks, T. J. Cleij, M. J. A. P. Daemen, V. Somers, W. De Ceuninck, and P. Wagner, "Selective identification of macrophages and cancer cells based on thermal transport through surface-imprinted polymer layers," *ACS Appl. Mater. Interfaces*, vol. 5, no. 15, pp. 7258–7267, 2013.
- [3] M. Peeters, S. Kobben, K. L. Jiménez-Monroy, L. Modesto, M. Kraus, T. Vanderyt, A. Gaulke, B. van Grinsven, S. Ingebrandt, T. Junkers, and P. Wagner, "Thermal detection of histamine with a graphene oxide based molecularly imprinted polymer platform prepared by reversible addition-fragmentation chain transfer polymerization," *Sensor Actuat. B-Chem.*, vol. 203, pp. 527–535, 2014.

- [4] P. Losada-Pérez, K. L. Jiménez-Monroy, B. van Grinsven, J. Leys, S. D. Janssens, M. Peeters, C. Glorieux, J. Thoen, K. Haenen, W. De Ceuninck, and P. Wagner, "Phase transitions in lipid vesicles detected by a complementary set of methods: Heat-transfer measurements, adiabatic scanning calorimetry, and dissipation-mode quartz crystal microbalance," *Phys. Status Solidi A*, vol. 211, no. 6, pp. 1377–1388, 2014.
- [5] M. Peeters, K. L. Jimenez-Monroy, C. Libert, Y. Eurlings, W. Cuypers, G. Wackers, S. Duchateau, P. Robaey, M. Nesládek, B. van Grinsven, E. Pérez-Ruiz, J. Lammertyn, P. Losada-Perez, and P. Wagner, "Real-time monitoring of aptamer functionalization and detection of Ara H1 by electrochemical impedance spectroscopy and dissipation-mode quartz crystal microbalance," *J. Biosens. Bioelectron.*, vol. 05, no. 03, 2014.
- [6] N. Vanden Bon, B. van Grinsven, M. S. Murib, W. S. Yeap, W. De Ceuninck, P. Wagner, M. Ameloot, V. Vermeeren, and L. Michiels, "Heat-transfer-based detection of SNPs in the PAH gene of PKU patients," *Int. J. Nanomedicine*, vol. 9, pp. 1629–1640, 2014.
- [7] K. Bers, B. Van Grinsven, T. Vandenryt, M. Murib, W. Janssen, B. Geerets, M. Ameloot, K. Haenen, L. Michiels, W. De Ceuninck, and P. Wagner, "Implementing heat transfer resistivity as a key element in a nanocrystalline diamond based single nucleotide polymorphism detection array," *Diam. Relat. Mater.*, vol. 38, pp. 45–51, 2013.
- [8] P. Cornelis, T. Vandenryt, G. Wackers, E. Kellens, P. Losada-Pérez, R. Thoelen, W. De Ceuninck, K. Eersels, S. Drijkoningen, K. Haenen, M. Peeters, B. van Grinsven, and P. Wagner, "Heat transfer resistance as a tool to quantify hybridization efficiency of DNA on a nanocrystalline diamond surface," *Diam. Relat. Mater.*, vol. 48, pp. 32–36, 2014.
- [9] M. Peeters, P. Csipai, A. Weustenraed, B. van Grinsven, R. Thoelen, J. Gruber, W. De Ceuninck, T. J. Cleij, F. J. Troost, and P. Wagner, "Heat-transfer-based detection of L-nicotine, histamine, and serotonin using molecularly imprinted polymers as biomimetic receptors," *Anal. Bioanal. Chem.*, vol. 405, no. 20, pp. 6453–6460, 2013.
- [10] G. Wackers, T. Vandenryt, P. Cornelis, E. Kellens, R. Thoelen, W. De Ceuninck, P. Losada-Pérez, B. Van Grinsven, M. Peeters, and P. Wagner, "Array formatting of the heat-transfer method (HTM) for the detection of small organic molecules by molecularly imprinted polymers," *Sensors*, vol. 14, pp. 11016–11030, 2014.
- [11] K. Bers, K. Eersels, B. Van Grinsven, M. Daemen, J. F. J. Bogie, J. J. A. Hendriks, E. E. Bouwmans, C. Püttmann, C. Stein, S. Barth, G. M. J. Bos, W. T. V Germeraad, W. De Ceuninck, and P. Wagner, "Heat-transfer resistance measurement method (HTM)-based cell detection at trace levels using a progressive enrichment approach with highly selective cell-

- binding surface imprints," *Langmuir*, vol. 30, no. 12, pp. 3631–3639, 2014.
- [12] B. van Grinsven, K. Eersels, M. Peeters, P. Losada-Pérez, T. Vandenryt, T. J. Cleij, and P. Wagner, "The heat-transfer method (HTM): a versatile low-cost, label-free, fast and user-friendly read-out platform for biosensor applications," *ACS Appl. Mater. Interfaces*, vol. 16, no. 6, pp. 13309-13318, 2014.
- [13] S. Wenmackers, V. Vermeeren, M. vandeVen, M. Ameloot, N. Bijmens, K. Haenen, L. Michiels, and P. Wagner, "Diamond-based DNA sensors: Surface functionalization and read-out strategies," *Phys. Status Solidi Appl. Mater. Sci.*, vol. 206, no. 3, pp. 391–408, 2009.



# Appendix 1

## Publications and Conference contributions

### Publications:

- K. L. Jiménez-Monroy, N. Renaud, J. Drijkoningen, K. Schouteden, D. Cortens, G. Degutis, W. Guedens, C. van Haesendonck, J. Manca, L. D. A. Siebbeles, F. C. Grozema and P. Wagner. "Fullerene groups enhance long-range charge hopping on single DNA molecules". Article submitted for publication.
- K. Eersels, B. van Grinsven, T. Vandenryt, K. L. Jiménez-Monroy, M. Peeters, V. Somers, C. Püttmann, C. Stein, S. Barth, G. M. J. Bos, W. T. V. Germeraad, H. Diliën, T. J. Cleij, R. Thoelen, W. De Ceuninck and P. Wagner. "Improving the sensitivity of the heat transfer method (HTM) for cancer cell detection with optimized sensor chips". *Physica Status Solidi A*, vol. 212, no. 6, pp.1320-1326, 2015.
- M. Peeters, B. van Grinsven, T. J. Cleij, K. L. Jiménez-Monroy, P. Cornelis, E. Pérez-Ruiz, G. Wackers, R. Thoelen, W. De Ceuninck, J. Lammertyn, P. H. Wagner. "Label-free protein detection based on the heat-transfer method –a case study with the peanut allergen Ara h1 and aptamer-based synthetic receptors". *ACS Appl. Mater. Interfaces*, vol. 7, no. 19, pp. 10316–10323, 2015.
- M. Peeters, S. Kobben, K. Jimenez-Monroy, L. Modesto, M. Kraus, T. Vandenryt, A. Gaulke, B. van Grinsven, S. Ingebrandt, T. Junkers, P. Wagner. "Thermal detection of histamine with a graphene oxide based molecularly imprinted polymer platform prepared by reversible addition–fragmentation chain transfer polymerization". *Sensors and Actuators B Chemical*, vol. 203, pp. 527-535, 2014.

- P. Losada-Pérez, K. L. Jiménez-Monroy, B. van Grinsven, J. Leys, S. D. Janssens, M. Peeters, C. Glorieux, J. Thoen, K. Haenen, W. De Ceuninck, P. Wagner. "Phase transitions in lipid vesicles detected by a complementary set of methods: heat-transfer measurements, adiabatic scanning calorimetry, and dissipation-mode quartz crystal microbalance". *Physica Status Solidi A*, vol. 211, nr. 6, 1377-1388, 2014.
- M. Van Gompel, B. Conings, K.L. Jiménez-Monroy, J. D'Haen, K. Gilissen, M. D'Olieslaeger, M.K. Van Bael, P. Wagner. "Preparation of epitaxial films of the transparent conductive oxide Al/ZnO by reactive high-pressure sputtering in Ar/O<sub>2</sub> mixtures". *Physica Status Solidi A*, vol. 210, nr. 5, pp. 1013-1018, 2013.
- K. Eersels, B. van Grinsven, A. Ethirajan, S. Timmermans, K. L. Jiménez-Monroy, J. F. J. Bogie, S. Punniyakoti, T. Vandenryt, J. J. A. Hendriks, T. J. Cleij, M. J. A. P. Daemen, V. Somers, W. De Ceuninck, P. Wagner. "Selective identification of macrophages and cancer cells based on thermal transport through surface-imprinted polymer layers". *ACS Applied Materials & Interfaces*, vol. 5, nr. 15, pp. 7258-7267, 2013.
- K.L. Jiménez-Monroy, A. Kick, K. Eersels, B. van Grinsven, P. Wagner, M. Mertig. "Surface plasmon resonance-based DNA microarrays: Comparison of thiol and phosphorothioate modified oligonucleotides". *Physica Status Solidi (a)*, vol. 210, nr. 5, 918-925, 2013.
- B. van Grinsven, N. Vanden Bon, H. Strauven, L. Grieten, M. Murib, K. L. Jiménez-Monroy, S. Janssens, K. Haenen, M. Schöning, V. Vermeeren, M. Ameloot, L. Michiels, R. Thoelen, W. De Ceuninck, P. Wagner. "Heat-transfer resistance at solid-liquid interfaces: a tool for the detection of single-nucleotide polymorphisms in DNA". *ACS Nano*, vol. 6, nr. 3, pp. 2712-21, 2012.

Conference contributions:

- Engineering of Functional Interfaces (EnFI 2014). Aachen University of Applied Sciences. Aachen, Germany (July 14-15, 2014).  
Presentation and poster: "Electrical characterization of molecular wires based on DNA".
- General Scientific Meeting of the Belgian Physical Society (BPS) 2014. IMEC, KU Leuven, Belgium (May 28, 2014).  
Poster: "DNA electrical behavior at room temperature: I-V measurements on single molecules".
- Engineering of Functional Interfaces (EnFI 2013). Hasselt University, Hasselt, Belgium (July 8-9, 2013).  
Presentation and poster: "Surface plasmon resonance-based DNA microarrays: A hybridization study with different target sizes".
- Biomedica 2013. The European Life Sciences Summit. Eurogress Center, Aachen, Germany (June 19, 2013).  
Poster: "DNA microarrays based on surface plasmon resonance: Target size effect on probes hybridization".
- General Scientific Meeting of the Belgian Physical Society (BPS) 2013. Université Catholique de Louvain (UCL), Louvain-la-Neuve, Belgium (May 22, 2013).  
Poster: "DNA microarrays based on surface plasmon resonance: Target size effect on probes hybridization".
- Engineering of Functional Interfaces (EnFI 2012). University of Applied Sciences Kaiserslautern, Zweibrücken, Germany (July 16-17, 2012).  
Presentation and poster: "Lab-on-a-chip: Highly stable modified probes immobilized on the surface of a DNA chip based on surface plasmon resonance".

- General Scientific Meeting of the Belgian Physical Society (BPS) 2012. Vrije Universiteit Brussel, Belgium (May 30, 2012).  
Poster: "Lab on a chip: effective immobilization of PT-modified oligonucleotides on the gold surface of DNA chips based on surface plasmon resonance".
- The European Life Sciences Summit, Biomedica 2012. Palais des Congrès, Liège, Belgium (April 18-19, 2012).  
Poster: "Lab on a chip: effective immobilization of PT-modified oligonucleotides on the gold surface of DNA chips based on surface plasmon resonance".

## Appendix 2

### List of abbreviations

#### Chapter 1

<i>B-DNA</i>	Native structure of DNA (right handed)
CMOS	Complementary metal-oxide semiconductor
STM	Scanning tunneling microscope
AFM	Atomic force microscope
SAMs	Self-assembled monolayers
I-AFM	Conductive probe AFM
FET	Field effect transistors
S	Source
D	Drain
G	Gate
$I_S$	Current entering at S
$I_D$	Current entering at D
$V_{DS}$	Drain-to-source voltage
$V_G$	Voltage applied at G
MOSFET	Metal-oxide-semiconductor FET
EDT-TTF	Ethylene-dithio-tetrathiafulvalene
TIE	Tetra-iodoethylene
SEL	Single-electron logic
SET	Single electron transistor
QCA	Quantum cellular automata
CAENs	Chemically assembled electronic nano-computers

#### Chapter 2

$G_L$	Landauer quantum conductance
D	Donor
A	Acceptor
ssDNA	Single stranded DNA
A base	Adenine (purine)
T base	Thymine (pyrimidine)
G base	Guanine (purine)
C base	Cytosine (pyrimidine)
<i>A-DNA</i>	Under wound <i>B-DNA</i> (right handed)
<i>Z-DNA</i>	Superhelical DNA (left handed)
$\lambda$ -DNA	DNA extracted from <i>Enterobacteria phage</i> $\lambda$ (bacteriophage)
LEEPS	Low-energy electron point source microscope
DAP <sup>2+</sup>	Diazapyrenium dichloride
Poly(dA-dT) <sub>2</sub>	Synthetic analogue of <i>B-DNA</i> : Poly(deoxyadenylic-deoxythymidylic) acid sodium salt
Poly(dG-dC) <sub>2</sub>	Synthetic analogue of <i>Z-DNA</i> : poly(deoxyguanylic-deoxycytidylic) acid sodium salt
Dppz	dipyrido[3,2-a:2',3'-c]phenazine
HeLa cells	Cervical cancer cells (donor: Henrietta Lacks)
<i>M-DNA</i>	Complex between divalent metal ions and <i>B-DNA</i>

**Chapter 3**

ET	Electron transfer
$R_0$	Distance between donor and acceptor
$\beta$	Fall-off parameter or coupling decay parameter
$T_{DA}$	Electronic coupling matrix element
FWCDS	Franck-Condon weighted density of states
$\Delta G^0$	Reaction driving force
$\lambda$	Reorganization energy
HOMO	Highest occupied molecular orbital
LUMO	Lowest unoccupied molecular orbital
$k_{ET}$	Rate of charge transfer
$H_{AB}$	Electronic coupling between the donor and acceptor groups
$E_{tun}$	Tunneling energies
SCE	Standard calomel electrode
$k_{SS}$	Rate of steady states phases
$g$	Junction conductance
$E_F$	Fermi energy
NEGF	Non-equilibrium Green function
IP	Ionization potential
$k_{hop}$	Hopping rate
$\eta$	Acceptor-direction biased random walk process
$P_n$	Population at site n

**Chapter 4**

UV-vis	Ultraviolet-visible spectroscopy
IR	Infrared spectroscopy
FTIR	Fourier transformed IR
E	Electric field
B	Magnetic field
$q$	Charge of a molecule
$I$	Transmitted intensity
$I_0$	Incident intensity
T	Transmittance
A	Absorbance
FFT	Fast Fourier transformation
KBr	Potassium bromide
DTGS	Deuterated triglycine sulphate
C60	Fullerene
$\alpha$	Polarizability
J	Single moment of inertia
K	Quantum number
$f_v$	Friction force
SPM	Scanning probe microscopy
PSPD	Position sensitive photodiode
C-AFM	Contact-AFM
NC-AFM	Non-Contact-AFM

**Chapter 5**

C61	C60-CHCOOH
EDC	1-Ethyl-3-(3-dimethyl-aminopropyl)-carbodiimide
NHS	N-Hydroxysuccinimide
S <sub>0</sub>	Ground state
S <sub>1</sub>	Singlet excited state
S <sub>2</sub>	Intermediate state
T <sub>1</sub>	Triplet excited state
MES	2-N-morpholino-ethane sulfonic acid
PBS	Phosphate saline buffer
Hp	Hairpin
Fwd	Forward
Bwd	Backward
MWCO	Molecular weight cut off
RMS	Root mean square roughness
NCD	Nanocrystalline diamond

**Chapter 6-7** (same as Ch. 3-5).**Chapter 8**

PDT	Photodynamic therapy
ROS	Reactive oxygen species
MTT	3-(4,5-dimethylthiazol-2-yl)-2,5-diphenyltetrazolium bromide
Alamar blue	7-Hydroxy-3 <i>H</i> -phenoxazin-3-one 10-oxide
A549 cells	Adenocarcinomic human alveolar basal epithelial cells
DMEM	Dulbecco's Modified Eagle's Medium-high glucose
SDS	Sodium dodecyl sulphate

**Chapter 9** (same as Ch. 3-8).**Chapter 10**

R <sub>th</sub>	Thermal resistance
PID	Proportional-integral derivative controller
SNPs	Single nucleotide polymorphisms
SIPs	Surface imprinted polymers
PDMS	polydimethylsiloxane
MCF-7 cells	Breast cancer cells
Jurkat cells	T-lymphocytes related with leukaemia
PBMCs	Peripheral blood mononuclear cells
MIPs	Molecularly imprinted polymers
GO	Graphene oxide
DPPE	Dipalmitoylphosphatidylcholine